

---

# **SIXTH RECENT ADVANCES IN QUANTITATIVE REMOTE SENSING**

Auditori de Torrent, Spain  
19 – 23 September 2022

Editor

**José A. Sobrino**  
Global Change Unit  
Universitat de València, Spain

Published by  
Publicacions de la Universitat de València.  
C/ Arts Gràfiques, 134  
46010 València  
gespuv@uv.es

## **SIXTH RECENT ADVANCES IN QUANTITATIVE REMOTE SENSING**

Edited by  
José A. Sobrino  
Universitat de València, Spain

Publication: G. Sòria

Copyright © 2024 by the Authors

This is an open Access article under the Creative Commons Attribution (CC BY-NC-ND)  
<https://creativecommons.org/licenses/by-nc-nd/4.0/>



**ISBN: 978-84-9133-712-6**  
<https://doi.org/10.7203/PUV-OA-712-6>

## *Preface*

The Sixth International Symposium on Recent Advances in Quantitative Remote Sensing was held in Torrent, Spain from 19 to 23 September 2022. It was sponsored and organized by the Global Change Unit (GCU) from the Image Processing Laboratory (IPL), University of Valencia (UVEG), Spain. Other sponsors include:

- City Council of Torrent (Spain);
- L'Auditori Torrent (Spain);
- European Space Agency (ESA);
- National Aeronautics and Space Administration (NASA);
- EOLAB;

This Symposium addressed the scientific advances in quantitative remote sensing in connection with real applications. Its main goal was to assess the state of the art of both theory and applications in the analysis of remote sensing data, as well as to provide a forum for researcher in this subject area to exchange views and report their latest results. In this book 35 of the 188 contributions presented in both plenary and poster sessions are arranged according to the scientific topics selected. The papers are ranked in the same order as the final programme.

To conclude, I would particularly like to thank the participants who have contributed to constructive discussions and the members of the International Scientific Committee, who greatly contributed to select the papers presented at the Symposium providing an attractive scientific programme. The success is also due to the efforts made by the Organizing Committee. Many thanks to all of them.

José A. Sobrino  
Symposium Chairperson  
Global Change Unit,  
Universitat de València

Valencia, 2023

## International Scientific Committee:

### Chairperson:

J. A. Sobrino University of Valencia, Spain

### Members:

G. Asrar	University of Maryland, USA
F. Baret	INRAE, Avignon, France
G. Chehbouni	IRD, France
G. Dedieu	CESBIO, Toulouse, France
M. Drinkwater	European Space Agency, The Netherlands
D. Ghent	University of Leicester, UK
A. Gillespie	University of Washington, USA
R. O. Green	NASA, JPL, Pasadena, USA
G. Gutman	NASA, Washington, D. C., USA
O. Hagolle	CESBIO, Toulouse, France
S. Hook	NASA, JPL, USA
A. Huete	University of Technology, Sydney Australia
G. Hulley	NASA, JPL, USA
Y. Kerr	CESBIO, Toulouse, France
B. Koetz	European Space Agency, Italy
Z.-L. Li	University of Strasbourg, France
S. Liang	University of Maryland, USA
M. Menenti	Delft University of Technology, The Netherlands
J. Moreno	University of Valencia, Spain
F. Nerry	University of Strasbourg, France
A. Olivos	INRAE, Avignon, France
F. Prata	NILU, Norway
J. Privette	NOAA, NCDC, USA
S. Quegan	University of Sheffield, UK
M. Rast	ISSI, Switzerland
H. Ren	Peking University, China
J.-L. Roujean	CESBIO, Toulouse, France
A. Royer	University of Sherbrooke, Canada
Z. Su	University of Twente, The Netherlands
B.-H. Tang	IGSNRR/CAS, Beijing, China
C. J. Tucker	NASA, USA
E. Vermote	NASA, USA
J. P. Wigneron	INRAE, Bordeaux, France
Y. Yu	NOAA, USA
P.J. Zarco-Tejada	University of Melbourne, Australia

## Organizing Committee:

### Chairperson:

P. Gómez Symposium, Torrent, Spain

### Members:

J. C. Jiménez	D. Skoković	I. Moletto-Lobos	S. Gimeno
G. Sòria	S. García-Monteiro	B. Mollà-Bononad	A. Ruescas
Y. Julien	R. Llorens	M. Sánchez-Torres	D. Salinas
B. Franch	V. Crisafulli	A. Sobrino-Gómez	



# CONTENTS

## Preface

iii

<b>Earth Surface Temperature evolution during the years 2003-2020 from MODIS data</b>	<b>1</b>
J. A. Sobrino, S. García-Monteiro, Y. Julien	
<b>Lake Surface Water Temperature evolution in the world's largest lakes during the years 2003-2020 from MODIS data</b>	<b>7</b>
J. A. Sobrino, S. García-Monteiro, Y. Julien	
<b>Exploring spatio-temporal spectral and functional variability in Mediterranean grasslands</b>	<b>12</b>
M. Pilar Martín, Vicente Burchard-Levine, Rosario González-Cascón, Javier Pacheco-Labrador, David Riaño	
<b>Exploring the capabilities of Sentinel-2 reflectance to predict soil organic carbon in Spain</b>	<b>16</b>
S. Sánchez-Ruiz, M. Campos-Taberner, M. Chiesi, F. Maselli, B. Martínez, F. J. García-Haro, M. A. Gilabert	
<b>First Applications of High Resolution BRDF Algorithm (HABA) for reflectance normalization on a fusion dataset from the Sen2Like processor</b>	<b>20</b>
Moletto-Lobos I., Franch B., Saunier S., Louis J., Cadau E., Debaecker V., Pflug B., De Los Reyes R., Boccia V., Gascon F.	
<b>Assessing and improving the consistency between the AVHRR/Metop and SEVIRI/MSG vegetation products</b>	<b>26</b>
Francisco Javier García-Haro, Manuel Campos-Taberner, Beatriz Martínez, Sergio Sánchez-Ruiz, María Amparo Gilabert, Jorge Sánchez-Zapero, Fernando Camacho, Enrique Martínez-Sánchez	
<b>Carbon fluxes estimation combining SEVIRI/MSG products, machine learning and in situ data</b>	<b>30</b>
Manuel Campos-Taberner, Beatriz Martínez, Sergio Sánchez-Ruiz, Francisco Javier García-Haro, María Amparo Gilabert	
<b>Estimation of surface energy and CO<sub>2</sub> fluxes through remote sensing in a Juniper tree ecosystem at the National Park of Doñana</b>	<b>34</b>
Pedro J. Gómez-Giráldez, Jordi Cristóbal, Héctor Nieto, Ricardo Díaz-Delgado	
<b>Evaluation of an operational multiple resolution evapotranspiration algorithms over a temperate basin on Chiloé Island mounted on a WebGIS platform</b>	<b>39</b>
Moletto-Lobos I., Mattar C., Acuña-Ruz T., Amézquita L., Sanyer W., Muñoz R., Áviles F., Bono, L., Garate, P. Olea-Encina, P., Troncoso, R., Arce, S., Neira H.,	
<b>Building and validating NOAA-AVHRR orbital drift correction methods by using MSG-SEVIRI temperature data</b>	<b>44</b>
Y. Julien, J. A. Sobrino	
<b>ECOSTRESS products for drought monitoring over different land covers</b>	<b>48</b>
J. C. Jimenez, G. Cottier, J. A. Sobrino, D. Skokovic, G. Sòria, Y. Julien, B. Franch, S. García, R. Llorens	

<b>Mediterranean Climate Zones, Time Series Analysis from 2010 to 2022: 100 Biophysical Indices, 300 Algorithms and 6 Satellites</b>	<b>52</b>
F-E. Ezzaher, N. Ben Achhab, H. Naciri, J. A. Sobrino, N. Raissouni	
<b>Mediterranean Basin Vegetation Forecasting Approaches: Accuracy Analysis &amp; Climate-Land Cover-Sensor nexus Impacts</b>	<b>58</b>
H. Naciri, N. Ben Achhab, F-E. Ezzaher, J. A. Sobrino, N. Raissouni	
<b>Estimation of fire severity using Sentinel-2 spectral indices in the 2020 Galicia forest fires</b>	<b>63</b>
Rafael Llorens, José Antonio Sobrino, Cristina Fernández, José M. Fernández-Alonso, José A. Vega	
<b>Monitoring winter barley within-field yield using PolSAR, backscatter coefficients and surface reflectance data</b>	<b>69</b>
B. Mollà-Bononad, B. Franch, I. Moletto-Lobos, J. M. López-Sánchez, J. Cintas, M. J. Sánchez-Torres, A. San Bautista, C. Rubio	
<b>Yield forecast models and nitrogen content management in rice crops in Valencia.</b>	<b>74</b>
M.J. Sánchez-Torres, B. Franch, A. San Bautista, C. Rubio, C. Domingo	
<b>Analysis of Surface Urban Heat Island effect during 2021 using automatic classification of Spanish cities with Deep Learning algorithms</b>	<b>80</b>
Salinas-González, Daniel, Skoković, Drazen, Sobrino, José A	
<b>Inter-annual trends of FAPAR and FVC SEVIRI/MSG climate data records along the period 2005-2020</b>	<b>85</b>
B. Martínez, S. Sánchez-Ruiz, M. Campos-Taberner, F.J. García-Haro, M.A. Gilabert	
<b>Spatiotemporal evolution of the land cover over Deception Island, Antarctica, its impact on albedo and its relationship with meteorological variables</b>	<b>89</b>
Javier F. Calleja, Susana Fernández, Rubén Muñiz, Jaime Otero, Francisco Navarro, Alejandro Corbea-Pérez, Carleen Reijmer, Miguel Ángel de Pablo	
<b>Long-term Dynamics of Land Surface Temperature over Europe: Towards a Daytime normalized AVHRR Land Surface Temperature Product</b>	<b>93</b>
Philipp Reiners, Stefanie Holzwarth, Sarah Asam, Ursula Gessner, Claudia Kuenzer	
<b>Evaluation of repeat-pass interferometric coherence from Sentinel-1 as a vegetation index for crop monitoring</b>	<b>98</b>
Arturo Villarroja-Carpio, Juan M. Lopez-Sanchez, Marcus Engdahl	
<b>Study of Effects of Different Vegetation Model Parameter Settings on Quantitative CFD Simulation of Urban Spatial Air Temperature and Wind-field</b>	<b>104</b>
Chen Fei, Hongyuan Huo, Jing Tao, Zhaofang Wang, Li Guo, Xiangtian Bai, Zhao-Liang Li	
<b>Simulation of Canopy Urban Heat Island at a Block Scale Based on Local Climate Zones and Urban Weather Generator</b>	<b>111</b>
Wenzhi Zhang, Hongyuan Huo, Xiaowei Geng, Jing Tao, Ping Zhou, Li Guo	
<b>Simulation of UFZ Air Temperature Based on GF-2 Remotely Sensed Data and UWG: A Case Study of Beijing, China</b>	<b>116</b>
Xiaowei Geng, Hongyuan Huo, Yunlong Chen, Wenzhi Zhang, Li Guo, Zhao-Liang Li	
<b>3D Spatial wind and thermal environment simulation of modern gardens in North and South China and its comparative analysis based on CFD and High remote sensing data</b>	<b>122</b>
Jing Tao, Hongyuan Huo, Xiaowei Geng, Wenzhi Zhang, Li Guo, Zhao-Liang Li	
<b>Ensemble Learning methods for Soil Moisture Retrieval from Radar Images</b>	<b>128</b>
Liguo Wang, Ya Gao, Geji Zhong, Yitong Wang	
<b>Assessment of water stress of major river basins in China for Sustainable Development Goals</b>	<b>133</b>
Jing Lu, Li Jia	
<b>Retrieval of vegetation water content with multi-frequency passive microwave sensor AMSR-E data</b>	<b>139</b>
Cunxin Cui and Bo-Hui Tang	

<b>Identification of tea plantations in plateau areas based on Sentinel-1/2 active and passive remote sensing data</b>	<b>145</b>
Shanchuan Gao and Bo-Hui Tang	
<b>The use of temporal sample migration to explore crop type from remotely sensed data</b>	<b>151</b>
Shibo Zhang, Jingya Yang, Jing Sun, Qiong Hu, Pei leng, Miao Lu, Yuman Ma, Hongyang Wang, Wenbin Wu, Qian Song	
<b>Estimation of gross primary productivity of Xishuangbanna tropical seasonal rainforest based on VPM correction model</b>	<b>155</b>
Siqi Feng and Bo-Hui Tang	
<b>Estimating the downwelling surface longwave radiation under all-sky conditions from FengYun-4A Data</b>	<b>161</b>
Yun Jiang, Bo-Hui Tang and Huanyu Zhang	
<b>Estimation of all-weather land surface temperature based on deep neural network by combining AMSR2 and MODIS data</b>	<b>167</b>
Zhong Peng, Ronglin Tang, Yazhen Jiang, Meng Liu, Zhao-Liang Li	
<b>Influence of hyperspectral thermal infrared sensor channel selection on land surface temperature and emissivity inversion accuracy</b>	<b>172</b>
Xiujuan Li, Hua Wu, Zhaoliang Li, Ni Li	
<b>Retrieval of apparent fluorescence quantum efficiency from FLEX–FLORIS 500-780 nm</b>	<b>176</b>
Shari Van Wittenberghe, Ana Belen Pascual, Adrian Perez, Eatidal Amin, Carolina Tenjo, Neus Sabater, Jose Moreno	
<b>AUTHOR INDEX</b>	<b>181</b>



# Earth Surface Temperature evolution during the years 2003-2020 from MODIS data

J. A. Sobrino, S. García-Monteiro, Y. Julien

*Global Change Unit. Image Processing Laboratory, University of Valencia. C/ Catedrático José Beltrán, 2. 46980 Paterna, Valencia, Spain.*

sobrino@uv.es; susana.garcia-monteiro@uv.es; yves.julien@uv.es

**ABSTRACT** - *The present work shows the estimation of the surface temperature of Planet Earth with MODIS Terra and Aqua Land (LST) and Sea Surface Temperature (SST) products for the years 2003-2021. The results corroborate the temperature anomalies retrieved from climate models and show a rate of warming higher than 0.2 °C per decade. Furthermore, the MODIS surface temperature retrievals are compared with the NOAA's NCDC air temperature estimations, showing high correlations for the global EST (0.96), LST (0.93) and SST (0.94). As an specific application, Lake Surface Water Temperature (LSWT) is estimated for ten of the largest lakes in the world by using MODIS Level 3 SST Thermal IR 8 Day 4km Version 2019.0 product at a high precision during the timespan 2003-2020. The selected lakes are the Caspian Sea, Superior, Victoria, Huron, Michigan, Tanganyika, Baikal, Great Slave Lake, Erie and Ontario lakes. LSWT trends show positive warming rates for every lake, with values ranging between 0.012°C/yr for Victoria Lake and 0.083°C/yr for Baikal Lake. Our LSWT estimations have been validated in the Laurentian Great Lakes, obtaining correlations between 0.96-0.99 respect Moukomla and Blanken (2016) research, which used the MOD11L2 LST product considering the years 2003-2014.. Despite MODIS SST product used is designed to retrieve SST by applying a specific SST algorithm, it also provides accurate information about freshwater extension and this work has demonstrated its functionality for estimating LSWT.*

**Keywords** - *MODIS, trend, global warming, Sea Surface Temperature, Land Surface Temperature, Lake Surface Water Temperature*

## 1. INTRODUCTION

The IPCC's Fifth Assessment Report provided the scientific input into the Paris Agreement (Field et al., 2014), which aims to strengthen the global response to the threat of climate change by holding the increase in the global average temperature to well below 2 °C above pre-industrial levels and to pursue efforts to limit the temperature increase to 1.5 °C above pre-industrial levels. For this reason, estimating both Sea Surface Temperature (SST) and Land Surface Temperature (LST) in an accurate way is a priority task to achieve the IPCC's Report objective.

Traditionally, surface temperature has been measured by using in situ instruments, which are irregularly distributed and differently calibrated (Sobrino et al., 2020a). This means that adjustments must be made in an attempt to homogenize temperature data from such varied sources. On the other hand, in situ instruments have the advantage of measuring data directly, without a column of air in between the water and instrument, as in the satellite case.

In contrast to the measurements provided by in situ sources, satellites make global and continuous observations of the planet surface (Sobrino et al., 2020b; Garcia-Monteiro, et al., 2022). by the same

thermal sensor of a known uncertainty. This means no residual uncertainties are going to be carried due to different calibration methods or instrument uncertainties.

The following work aims to give an overall view of the evolution of the EST, SST and LST during the years 2003-2021, estimated from MODIS retrievals, to compare results with the NOAA'S NCDC widely used air temperature dataset and to highlight the value of satellite thermal observations in their application to climate studies.

On the other hand, Lake Surface Water Temperature (LSWT) is an Essential Climate Variable recognized by the Global Observing System for Climate (GCOS) and it is an indicator of how climate change is affecting worldwide lake physical dynamics and ecosystems Ten large lakes have been selected for developing this study: the Caspian Sea, Superior, Victoria, Huron, Michigan, Tanganyika, Baikal, Great Slave Lake, Erie and Ontario lakes in order to retrieve their LSWT, in absolute and trend terms.

LSWT will be retrieved for the ten lakes mentioned above by using MODIS Level 3 SST Thermal IR 8 Day 4km V2019.0 product in order to show how it functions when estimating surface temperature of freshwater extensions non-connected to the open water. Our results will be validated by a previous study focused on

the Laurentian Great Lakes and which uses an LST MODIS product (Moukomla and Blanken, 2016). Furthermore, LSWT trends will be estimated to analyse the behaviour of this parameter during the last years.

## 2. MATERIAL AND METHODS

### 2.1. Study sites (lakes)

Ten large lakes have been selected for developing this study: the Caspian Sea, the only saline lake included; the Superior, Michigan, Huron, Ontario and Erie Lakes, called the Great Lakes, which occupy part of the territory of the United States of America and Canada; the Victoria and Tanganyika lakes, located in the African continent; the Baikal lake in Russia and the Slave lake in Canada (table 1) (Dumont, 2003; United States Environmental Protection Agency, 2022; Swain and Shannon, 1980; Verburg, P. et al., 2003; Zimmerman et al., 2006).

*Table 1. Metric characteristics of the ten lakes considered in the study.*

Lake	Cont	Area (km <sup>2</sup> )	Vol (km <sup>3</sup> )	Max. depth (m)
Caspian Sea	Asia	371,0	78,2	1,025
Superior	America	82,1	12,1	406,3
Victoria	Africa	68,9	2,8	84
Huron	America	59,6	3,5	229
Michigan	America	58,0	4,9	281
Tanganyika	Africa	32,6	18,9	1,470
Baikal	Asia	31,5	23,6	1,620
Slave	America	27,0	1,6	614
Erie	America	25,7	489	64
Ontario	America	18,9	1,639	244

### 2.2. Data sets

The SST product used in this study is MODIS Level 3 SST Thermal IR 8 Day 4km V2019.0, which is freely available in <https://podaac.jpl.gov>. 8-days composites have been considered as ideal for this work, as they allow both to save storage capacity and to reduce computational costs.

3450 images have been computed for the years 2003-2020 (1723 images associated to MODIS-Terra and 1727 images associated to MODIS-Aqua). Each image is a global dataset with a spatial resolution of 4.63 km and 8640x4320 pixels dimensions. A mask has been applied in order to consider only the area corresponding to each lake, step that will be explained with more detail in the methodology section.

The algorithm of the MODIS SST product used in this work uses seven latitudinal bands in 20° intervals from 0° to 60° and then, a single interval from 60° to the poles (Kilpatrick et al, 2019; Jia, 2019; Jia and Minnett, 2020) for setting coefficients for the different atmospheric regions at a certain month of the year. These coefficients are continuously updated and validated by the Rosenstiel School of Marine and Atmospheric Science (RSMAS) at the University of Miami (Brown and Minnett, 1999). The product applies the long-wave algorithm, which considers MODIS bands 31 and 32 at 11 µm and 12 µm, respectively (Goddard Space Flight Center, 2014)

When referring to errors, the product's Algorithm Technical Background Document (ATBD) establishes an uncertainty of 0.45K at nadir and 0.56K at 45°. Several researchers have validated the MODIS SST product at global and regional scales: Sobrino et al. (2020a) estimated de global Sea Surface Temperature (SST) with a median evaluated uncertainty of 0.10 in the period 2003-2016; Reinart and Reinhold (2008) obtained errors of 0.40°C when applying the product to Swedish lakes by using MODIS-Terra images and considering the period 2001-2003.

For LST retrieval, the product selected is MOD11C2 (MODIS-Terra) and MYD11C2 (MODIS-Aqua), 8-days composites at 0.05° resolution. Uncertainties range between 0.88K and 1.63K depending on the observation angle and water vapour content (Wan, 2004). A total of 3497 images have been processed (1748 images from MODIS-Terra and 1749 images from MODIS-Aqua).

### 2.3. Methodology

The methodology applied is based on the one proposed by Sobrino et al. (2020b) to estimate SST at a global level and which has been shown to be valid at regional scales too (García-Monteiro et al., 2022).

SST means are estimated by following equation 1, where  $SST_{mean}^t$  is the SST for each area considered at a certain time,  $t$ ;  $SST_{ij}^t$ , the SST for each pixel  $ij$  at a time  $t$ ;  $m$  is the column pixel dimension and  $n$ , the row pixel dimension;  $A_{ij}$ , is the area of every pixel of  $i,j$  dimensions and  $A_{lake}$ , the total area of each lake, only considering cloud free pixels.

$$SST_{mean}^t = \frac{1}{A_{total}} \sum_{i=1}^m \sum_{j=1}^n A_{ij} SST_{ij}^t$$

For each 8-day period, four observations are considered, Terra and Aqua, daytime and nighttime, whose passing times are the following: 10:30, 13:30, 22:30 and 01:30. For each pixel, the four data average has been calculated according to Eq. 2. (Mao et al., 2017). The timespan selected starts in the year 2003

because, despite Terra provides data since 2001, Aqua was launched in 2002 and did not make data available until the year 2003. Therefore, the first complete year, with four measures per image is 2003.

$$SST_{MODIS} = \left( \frac{SST_{mean}^{(10:30)} + SST_{mean}^{(13:30)} + SST_{mean}^{(22:30)} + SST_{mean}^{(01:30)}}{4} \right)$$

The product ATBD assesses the pixel quality through the Quality Control variable. We have taken this information into account and only included on computations those pixels of good or acceptable quality, meaning Quality Control values of 0 and 1, respectively. Furthermore, an additional filter has been applied to results with the aim of removing outliers based on the Z-score method. Linear regressions have been used to estimate trends and develop validations. In addition, the Sen's slope method and Mann-Kendall test have been run out to estimate trends with an associated level of confidence.

For each lake, monthly and annual SST means have been computed as shown in Eq. 1. A mask for each lake considered has been elaborated and applied, in order to include in computations only the study sites selected. Once the different regions of interest are cropped, the SST is estimated applying the methodology mentioned above.

### 3. RESULTS & DISCUSSION

#### 3.2. Earth Surface Temperature

MODIS EST, SST and LST global estimations are compared with NOAA's NCDC air temperature merged land-ocean, land and ocean surface temperature measurements in figure 1.

For EST, the linear trends estimated are of  $0.0202 \pm 0.0008^\circ\text{C/yr}$  for MODIS EST and  $0.022^\circ\text{C/yr}$  for NOAA NCDC anomalies. Results show a high correlation between MODIS EST estimations and NOAA NCDC air temperature global data, interpolated from in situ sources, with a 0.96 value. MODIS EST trend has also been estimated by the Sen's slope method, obtaining  $0.020^\circ\text{C/yr}$ , as for the linear method, with a confidence level of 99.9%, showing the high potential of MODIS thermal infrared satellite data as a source of input data for global surface temperature estimations and for global change studies.

In the LST case, the correlation is of 0.93 between both data sets with a significance higher than 99.9%. Linear trends are defined as  $0.025 \pm 0.001^\circ\text{C/yr}$  for the MODIS LST and  $0.032^\circ\text{C/yr}$  for the NOAA's NCDC anomalies. As for EST, the Sen's slope trend has also been calculated, with a similar resulting value,  $0.023^\circ\text{C/yr}$  and a Mann-Kendall significance of 99.7%.

For the SST variable, the correlation between NOAA NCDC anomalies and MODIS retrievals is 0.94, slightly improving the LST results. The SST trend is  $0.018^\circ\text{C/yr}$  in both cases, confirmed by the Sen's slope method with a 99.7% of confidence. The trend uncertainty for the MODIS linear estimation is  $0.0008^\circ\text{C/yr}$ .

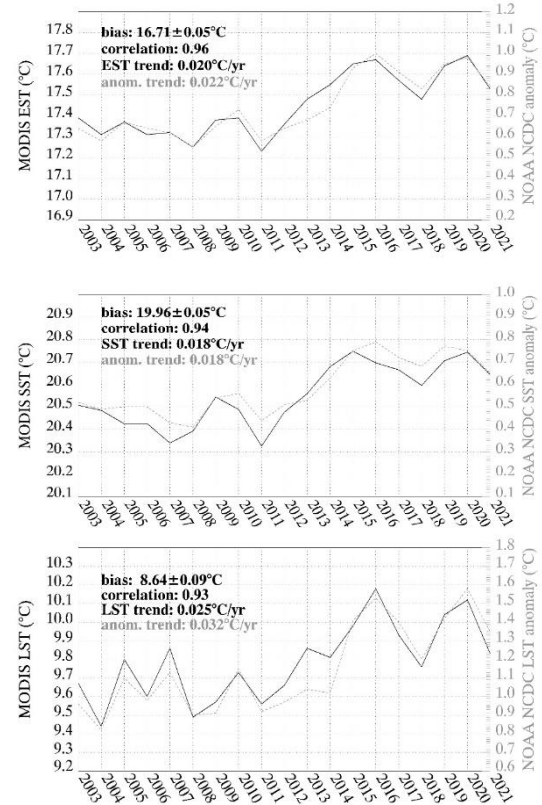


Figure 1. MODIS and NOAA's NCDC air temperature comparison for EST, SST and LST.

Global surface temperature trend maps, as well as the Mann-Kendall significance map, are shown in figure 2. The global trends are  $0.020^\circ\text{C/yr}$  for EST,  $0.018^\circ\text{C/yr}$  for SST and  $0.023^\circ\text{C/yr}$  for LST, given at a confidence level higher than 99%.

For the LST variable, positive trends are found for large areas of the central and Eastern Europe, Scandinavia and Siberia. In the American continent, peninsulas of California and Florida, and in northeastern Brazil and Patagonia. Negative trends appear mainly in the Indian Peninsula and in eastern longitudes of Antarctica.

In the SST case, negative trends are found in the North Atlantic Ocean, Greenland, in the North Pacific, the Sea of Japan, the Yellow Sea and in the Southern Ocean. On the other hand, positive trends are irregularly distributed along NH low and mid-latitudes and in the Atlantic and Pacific Oceans, next to the

North American and Australian Continent and the Arctic Circle.

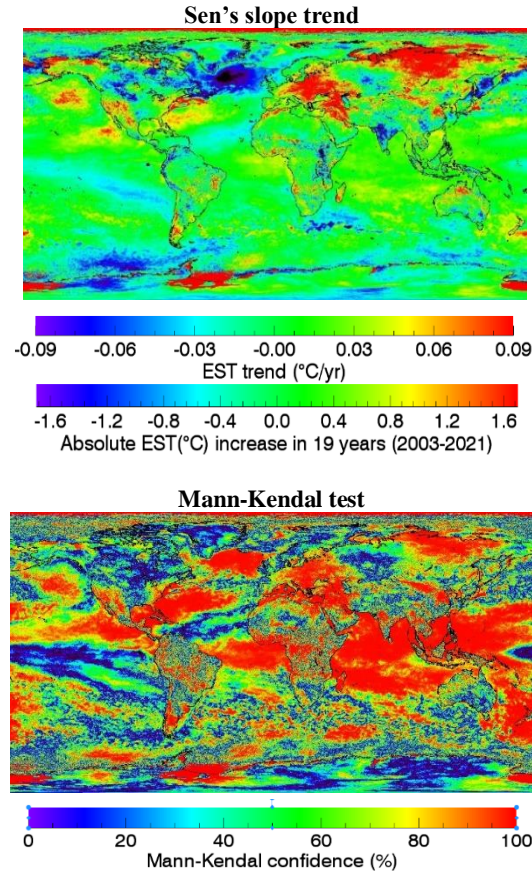


Figure 2. Sen's slope trend and Mann-Kendal confidence level in maps

### 3.3. Lake Surface Water Temperature validation

Our MODIS results have been validated with Moukomla and Blanken (2016) results. They estimated the Great Lakes Surface Temperature from the 6<sup>th</sup> of July 2001 and the 31<sup>st</sup> of December 2014 by merging skin temperature derived from the MODIS Land Surface Temperature (MOD11L2) and the MODIS Cloud product (MOD06L2). They validated their temperature estimations with *in situ* data from buoys belonging to the NOAA National Data Buoy Center, obtaining R-squared values ranging from 0.4975 to 0.9560 from regressions.

Figure 3 shows the regressions carried out considering our results respect the Moulomla and Blanken (2016) paper results. Correlations between both data sets are

in the interval of 0.962-0.998, demonstrating, on one hand, that the retrievals of both products are in the same line and on the other, that our methodology is capable of generating valid SST estimations in lake water surfaces.

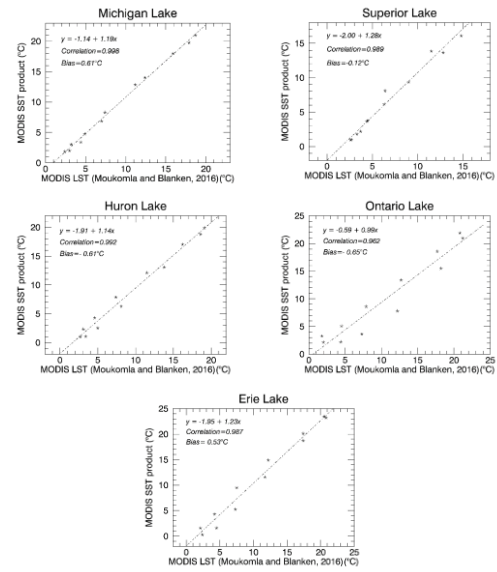


Figure 3. Results validation. MODIS SST products monthly estimations are compared with the results of Moukomla and Blanken (2016) for the Great Leaks. The timespan considered is 2003-2014. The correlation coefficients obtained ranges between 0.962 and 0.998.

### 3.4. Lake Surface Water Temperature in ten of the largest lakes of the world

Once the reliability of the MODIS SST product for LSWT estimations has been established, LSWT trends for the years 2003-2020 have been estimated for the Caspian Sea, Superior, Victoria, Huron, Michigan, Tanganyika, Baikal, Great Slave Lake, Erie and Ontario by both the linear and Sen's slope methods. The confidence level is offered by carrying out the Mann-Kendal test. The mean LSWT for the whole timespan is also provided (table 2).

The MODIS Level 3 SST Thermal IR 8 Day 4km V2019.0 provides complete data (including four daily measures) from 2003 onwards. AVHRR enables a more comprehensive data period for both LST and SST variables but, in contrast, their satellites induce variability due to their orbital drift (Price, 1990; Sobrino et al., 2008 Julien and Sobrino, 2012). For this reason, MODIS time series have been selected for this study in detriment of AVHRR.

Positive trends are found in the ten lakes analysed (table 2) for both the linear and Sen's slope trend



estimation methods. The higher LSWT trend estimated is found for Lake Baikal, 0.083°C/yr at a 99.79% confidence level, whereas the lower trend is found in Lake Victoria, 0.012°C/yr. Results show a high Mann-Kendall level (>95%) in the case of the Tanganyika and Erie lakes, with warming rates of 0.017°C/yr and 0.058°C/yr, respectively.

From the absolute LSWT values, the Tanganyika and Victoria lakes are the warmer lakes among the lakes considered and show the lower data variability through time, established by their standard deviations. These absolute LSWT are 25.76±0.18°C for the Victoria Lake and 26.95±0.16°C for the Tanganyika Lake. On the other hand, the colder lakes are represented by the Baikal Lake, 6.3±0.6°C, and the Superior Lake, 6.8±0.8°C.

*Table 2. Annual trends estimated for the lakes analysed during the years 2003-2020 by the linear and Sen's slope methods. The results' confidence is given by the Mann-Kendal test (significant results are highlighted in bold).*

Lake	Mean LSWT (°C)	Linear trend (°C)	Sen's slope (°C)	Mann-Kendal (%)
Caspian Sea	16.3±0.5	0.037	0.044	87.97
Superior	6.8±0.8	0.002	0.013	37.76
Victoria	25.76±0.18	0.012	0.012	72.85
Huron	9.1±0.6	0.031	0.029	69.37
Michigan	9.9±0.8	0.025	0.029	61.64
Tanganyika	26.95±0.16	0.015	<b>0.017</b>	<b>96.93</b>
Baikal	6.3±0.6	0.082	<b>0.083</b>	<b>99.79</b>
Slave	6.9±0.7	0.041	0.056	78.88
Erie	11.7±0.5	0.043	<b>0.058</b>	<b>95.53</b>
Ontario	10.5±0.7	0.043	0.047	65.64

Sobrinho et al. (2020b) established a global SST trend of 0.019°C/yr for the years 2003-2019. Assuming this value for the present timespan and attending to the Sen's slope trends estimated in this paper, seven of the ten lakes analysed exceed this value: Caspian Sea (0.044°C/yr), Huron (0.029°C/yr), Michigan (0.029°C/yr), Baikal (0.083°C/yr), Slave Lake (0.056°C/yr), Erie (0.058°C/yr) and Ontario (0.047°C/yr). In this way, the general overview shows that lakes are warming at a higher rate than the global water surfaces.

#### 4. CONCLUSIONS

The comparison between the planetary MODIS Earth Surface Temperature (EST) presented in this work and the NOAA-NCDC air temperature data shows a correlation coefficient of 0.96 between the two databases, demonstrating the high potential of thermal infrared satellite data to provide accurate data for

climatic and meteorological studies. Satellite data are essential in the monitoring of SST, LST and EST as a solid source of continuous data in space and time.

The global EST trend is 0.020 °C/yr, 0.018°C/yr for SST trends and 0.025°C/yr for the LST parameter. SST shows less variability in time than LST and a higher influence on EST, as sea surface extension dominates over the land surface extension. This proceeding has covered not only the trends observed from satellites but also the current estimations of air temperature. We consider that satellite data used be used to estimate anomalies of the average temperature of the Earth's surface and be included in the IPCC assessment reports. When referring to lakes, they are freshwater enclosed extensions in which there is no exchange with open waters. For this reason, the initial hypothesis of this work was that they could suffer to a greater extent from the effect of global warming. Results show positive LSWT trend for the ten lakes considered: the Caspian Sea, Superior, Victoria, Huron, Michigan, Tanganyika, Baikal, Great Slave Lake, Erie and Ontario lakes.

Furthermore, when considering the current SST warming rate, established in 0.018°C/yr for the whole sea surfaces, seven of these ten lakes exceed this trend. The sample size is limited enough to prevent generalizing that LSWT is warming at a higher rate than SST, but it can be affirmed that the LSWT of seven of the largest lakes of the world is increasing at an accelerated rate. The highest LSWT is found for Lake Baikal, with 0.083°C/yr, nearly five times the global SST trend, whereas the lowest trend is associated to Victoria Lake, with 0.012°C/yr.

The MODIS Level 3 SST Thermal IR 8 Day 4km V2019.0 achieves SST retrieval by applying a specific SST algorithm. However, it also provides information about freshwater extension and this paper has demonstrated its functionality in this type of ecosystems. The validations carried out show correlations between 0.96 and 0.99 with results provided by previous literature.

Remote sensing is a valuable technology which provides homogeneous and periodic data from the whole Earth's surface. Its main disadvantage is the impossibility of collecting data below clouds. This weakness is overcome by the satellite temporal resolution that means 4 passes per day. The low uncertainty of results confirms its reliability, strengthened by the validation that has been carried out. The LSWT is positioned as a parameter of climatic interest, already recognized as an Essential Climate Variable by the World Meteorological Organization, which reflects global warming in an amplified way. As for other ECVs, such as SST, the LSWT must be continuously monitored, as it is an indicator of the behaviour of the surface temperature of the planet.

## REFERENCES

- Brown, B and Minnett, P.J. 1999. MODIS Infrared Sea Surface Temperature Algorithm. Algorithm Theoretical Basis Document. Version 2.0. University of Miami, Miami, United States of America.
- De Santis, D, Del Frate, F., Schiavon, G. 2022. Analysis of Climate Change Effects on Surface Temperature in Central-Italy Lakes Using Satellite Data Time-Series. *Remote Sensing*, **14**, 117. <https://doi.org/10.3390/rs14010117>
- Gamito, R., Teixeira, C.M., Costa, M.J., Cabral, H.N. Are regional fisheries' catches changing with climate? *Fisheries Research*, **161**, pp. 207-216, ISSN 0165-7836, <https://doi.org/10.1016/j.fishres.2014.07.014>.
- García-Monteiro, S; Sobrino, J.A.; Julien, Y.; Sòria, G.; Skokovic, D. 2021. Surface Temperature trends in the Mediterranean Sea from MODIS data during years 2003-2019. *Regional Studies in Marine Science*, **49** (2022) 102086. <https://doi.org/10.1016/j.rsma.2021.102086>
- Goddard Space Flight Center. NASA, Ocean Ecology Laboratory, Ocean Biology Processing Group; (2014): MODIS-Terra Ocean Color Data. Available in <https://modis.gsfc.nasa.gov/data/dataproduct/mod28.php>
- Jia, C. 2019. Satellite Infrared Retrievals of Sea Surface Temperature at High Latitudes. MS Thesis, Meteorology and Physical Oceanography. University of Miami. Miami. FL, USA. pp. 79.
- Jia, C. and Minnett, P.J. 2020. High Latitude Sea Surface Temperatures Derived from MODIS Infrared Measurements. *Remote Sensing of Environment*, **251**, 112904.
- Kilpatrick, K. A., P. Minnett, B. Luo. 2019. Validation of NASA MODIS R2019.0 reprocessed SST Products. The 18th International GHRSSST Science Team Meeting (GHRSSST XVIII) – Frascati Italy- 6th to 10th June 2019.
- Lindsay, R. and Dahlman, L. 2009. Climate Variability: North Atlantic Oscillation. Last update: October 2021. Available in <https://www.climate.gov/news-features/understanding-climate/climate-variability-north-atlantic-oscillation>
- McPhaden, M.J.; Zebiak, S.E.; Glantz, M.H. 2006. ENSO as an integrating concept in Earth Science. *Science*, **314** (5806), pp. 1740-1745. Doi: 10.1126/science.1132588
- Physical Oceanography Distributed Active Archive Center (PO.DAAC). 2018. Available online [<https://podaac.jpl.nasa.gov/>] from NASA EOSDIS PO.DAAC, Pasadena, CA, Accessed January 5, 2021.
- Sobrino, J.A.; Julien, Y.; García-Monteiro, S., 2020a. Surface Temperature of the Planet Earth from Satellite Data. *Remote Sensing*, **12**, 218.
- Sobrino, J.A.; García-Monteiro, S.; Julien, Y. 2020b. Surface Temperature of the Planet Earth from Satellite Data over the period 2003-2019. *Remote Sens.* **12**(12), 2036. Doi: 10.3390/rs12122036
- Wan, Z.; Zhang, Y.; Zhang, Q.; Li, Z.-L. 2004. Quality assessment and validation of the MODIS global land surface temperature. *Int. J. Remote Sensing*, **25**, 261–274

# Lake Surface Water Temperature evolution in the world's largest lakes during the years 2003-2020 from MODIS data

J. A. Sobrino, S. García-Monteiro, Y. Julien

*Global Change Unit. Image Processing Laboratory, University of Valencia. C/ Catedrático José Beltrán, 2. 46980 Paterna, Valencia, Spain.*

sobrino@uv.es; susana.garcia-monteiro@uv.es; yves.julien@uv.es

**ABSTRACT** - Lake Surface Water Temperature (LSWT) is an Essential Climate Variable recognized by the Global Observing System for Climate (GCOS). In this work, LSWT is estimated for ten of the largest lakes in the world by using MODIS Level 3 SST Thermal IR 8 Day 4km Version 2019.0 product at a high precision during the timespan 2003-2020. The selected lakes are the Caspian Sea, Superior, Victoria, Huron, Michigan, Tanganyika, Baikal, Great Slave Lake, Erie and Ontario lakes. Absolute LSWT values have been estimated for each lake, obtaining the minimum average for Baikal lake ( $6.6 \pm 0.6^\circ\text{C}$ ) and the maximum for Tanganyika Lake ( $26.95 \pm 0.16$ )  $^\circ\text{C}$ . LSWT trends show positive warming rates for every lake, with values ranging between  $0.012^\circ\text{C/yr}$  for Victoria Lake and  $0.083^\circ\text{C/yr}$  for Baikal Lake. Our LSWT estimations have been validated in the Laurentian Great Lakes, obtaining correlations between 0.96-0.99 respect Moukomla and Blanken (2016) research, which used the MOD11L2 LST product considering the years 2003-2014. Sentinel 2 estimations have also been included in the validation, represented by sensor SLSTR retrievals for the Issyk-Kul Lake during the year 2020. In this case, the correlation is 0.99 between MODIS and SLSTR estimations, with a  $0.33^\circ\text{C}$  bias, lower MODIS' SST uncertainties at nadir. Despite MODIS SST product used is designed to retrieve SST by applying a specific SST algorithm, it also provides accurate information about freshwater extension and this work has demonstrated its functionality for estimating LSWT.

**Keywords** - Lake Surface Water Temperature, MODIS, trend, global warming.

## 1. INTRODUCTION

Lake Surface Water Temperature (LSWT) is recognized as an Essential Climate Variable (ECV) by the Global Observing System for Climate (GCOS, 2016), working as an indicator of how climate change is affecting worldwide lake physical dynamics and ecosystems. It has been proved that the behaviour of this ECV conditions several processes, such as the fisheries' presence and catches (Gamito et al., 2015), the alternation between rainy and dry seasons (Liu et al., 2020; Zhang et al., 2001) or the climatic oscillations dynamics (McPhaden et al., 2006; Lindsey and Dahlman, 2009). For this reason, it is crucial to monitor ECVs, in order to better understand these processes, among others, and be prepared to face the changes they may face.

LSWT has traditionally been estimated by using *in situ* instruments, heterogeneous, irregularly distributed and differently calibrated (De Santis et al., 2021; Sobrino et al., 2020a). Remote sensing solves these *in situ* measurements disadvantages and provides continuous temporal series data, retrieved from the same sensor observations, with a given uncertainty, the identical for each observation.

As a consequence, it is becoming increasingly common to find in the literature studies whose objective is to analyze the LSWT from satellite data (Ghasemifar et al., 2019; Zhang et al., 2014; Crosman and Horel, 2009).

It is clear that LSWT is a variable to consider when studying lakes and has more implications than simple variations in lake temperatures. For this reason, we propose to develop a study that considers the most representative lakes in the world, to know their LSWT behaviour during the last years, from 2003 to 2020, by using MODIS data. The lakes selected are the Caspian Sea, Superior, Victoria, Huron, Michigan, Tanganyika, Baikal, Great Slave, Erie and Ontario lakes.

The aim of this contribution is to retrieve the LSWT of the ten lakes mentioned above by using MODIS Level 3 SST Thermal IR 8 Day 4km V2019.0 product in order to show how it functions when estimating surface temperature of freshwater extensions non-connected to the open water.

Our results will be validated by a previous study focused on the Laurentian Great Lakes and which uses an LST MODIS product (Moukomla and Blanken, 2016). Furthermore, LSWT trends will be estimated to analyse the behaviour of this parameter during the last years.

## 2. MATERIAL AND METHODS

### 2.1. Study sites

Ten large lakes have been selected for developing this study: the Caspian Sea, the only saline lake included; the Superior, Michigan, Huron, Ontario and Erie Lakes, called the Great Lakes, which occupy part of the territory of the United States of America and Canada; the Victoria and Tanganyika lakes, located in the African continent; the Baikal lake in Russia and the Slave lake in Canada (table 1) (Dumont, 2003; United States Environmental Protection Agency, 2022; Swain and Shannon, 1980; Verburg, P. et al., 2003; Zimmerman et al., 2006).

*Table 1. Metric characteristics of the ten lakes considered in the study.*

Lake	Cont	Area (km <sup>2</sup> )	Vol (km <sup>3</sup> )	Max. depth (m)
Caspian Sea	Asia	371,0	78,2	1,025
Superior	America	82,1	12,1	406.3
Victoria	Africa	68,9	2,8	84
Huron	America	59,6	3,5	229
Michigan	America	58,0	4,9	281
Tanganyika	Africa	32,6	18,9	1,470
Baikal	Asia	31,5	23,6	1,620
Slave	America	27,0	1,6	614
Erie	America	25,7	489	64
Ontario	America	18,9	1,639	244

### 2.2. Data sets

The product used in this study is MODIS Level 3 SST Thermal IR 8 Day 4km V2019.0, which is freely available in <https://podaac.jpl.gov>. 8-days composites have been considered as ideal for this work, as they allow both to save storage capacity and to reduce computational costs.

3450 images have been computed for the years 2003-2020 (1723 images associated to MODIS-Terra and 1727 images associated to MODIS-Aqua). Each image is a global dataset with a spatial resolution of 4.63 km and 8640x4320 pixels dimensions. A mask has been applied in order to consider only the area corresponding to each lake, step that will be explained with more detail in the methodology section.

The algorithm of the MODIS SST product used in this work uses seven latitudinal bands in 20° intervals from 0° to 60° and then, a single interval from 60° to the poles (Kilpatrick et al, 2019; Jia, 2019; Jia and Minett, 2020) for setting coefficients for the different atmospheric regions at a certain month of the year. These

coefficients are continuously updated and validated by the Rosenstiel School of Marine and Atmospheric Science (RSMAS) at the University of Miami (Brown and Minnett, 1999). The product applies the long-wave algorithm, which considers MODIS bands 31 and 32 at 11 µm and 12 µm, respectively (Goddard Space Flight Center, 2014).

When referring to errors, the product's Algorithm Technical Background Document (ATBD) establishes an uncertainty of 0.45K at nadir and 0.56K at 45°. Several researchers have validated the MODIS SST product at global and regional scales: Sobrino et al. (2020a) estimated de global Sea Surface Temperature (SST) with a median evaluated uncertainty of 0.10 in the period 2003-2016; Reinart and Reinhold (2008) obtained errors of 0.40°C when applying the product to Swedish lakes by using MODIS-Terra images and considering the period 2001-2003.

### 2.3. Methodology

The methodology applied is based on the one proposed by Sobrino et al. (2020b) to estimate SST at a global level and which has been shown to be valid at regional scales too (García-Monteiro et al., 2022).

As a first step, a mask for each lake considered has been elaborated and applied, in order to include in computations only de study sites selected. Once the different regions of interest are cropped, the SST is estimated applying the methodology mentioned above. For each lake, the monthly and annual SST have been computed as shown in Eq. 1, where  $SST_{lake}^t$  is the SST for each lake at a certain time,  $t$ ;  $SST_{ij}^t$ , the SST for each pixel  $ij$  at a time  $t$ ;  $m$  is the column pixel dimension and  $n$ , the row pixel dimension;  $A_{ij}$ , is the area of every pixel of  $i,j$  dimensions and  $A_{lake}$ , the total area of each lake, only considering cloud free pixels.

$$SST_{lake}^t = \frac{1}{A_{lake}} \sum_{i=1}^m \sum_{j=1}^n A_{ij} SST_{ij}^t$$

For each 8-day period, four observations are considered, Terra and Aqua, daytime and nighttime, whose passing times are the following: 10:30, 13:30, 22:30 and 01:30. For each lake, the four data average has been calculated according to Eq. 2. (Mao et al., 2017). The timespan selected starts in the year 2003 because, despite Terra provides data since 2001, Aqua was launched in 2002 and did not made data available until the year 2003. Therefore, the first complete year, with four measures per image is 2003.

$$SST_{MODIS} = \left( \frac{SST_{mean}^{(10:30)} + SST_{mean}^{(13:30)} + SST_{mean}^{(22:30)} + SST_{mean}^{(01:30)}}{4} \right)$$

The product ATBD assesses the pixel quality through the Quality Control variable. We have taken this information into account and only included on computations those pixels of good or acceptable quality, meaning Quality Control values of 0 and 1, respectively. Furthermore, an additional filter has been applied to results with the aim of removing outliers based on the Z-score method. Linear regressions have been used to estimate trends and develop validations. In addition, the Sen's slope method and Mann-Kendall test have been run out to estimate trends with an associated level of confidence.

### 3. RESULTS & DISCUSSION

#### 3.1. Validation

Our MODIS results have been validated with Moukomla and Blanken (2016) results. They estimated the Great Lakes Surface Temperature from the 6<sup>th</sup> of July 2001 and the 31<sup>st</sup> of December 2014 by merging skin temperature derived from the MODIS Land Surface Temperature (MOD11L2) and the MODIS Cloud product (MOD06L2). They validated their temperature estimations with *in situ* data from buoys belonging to the NOAA National Data Buoy Center, obtaining R-squared values ranging from 0.4975 to 0.9560 from regressions.

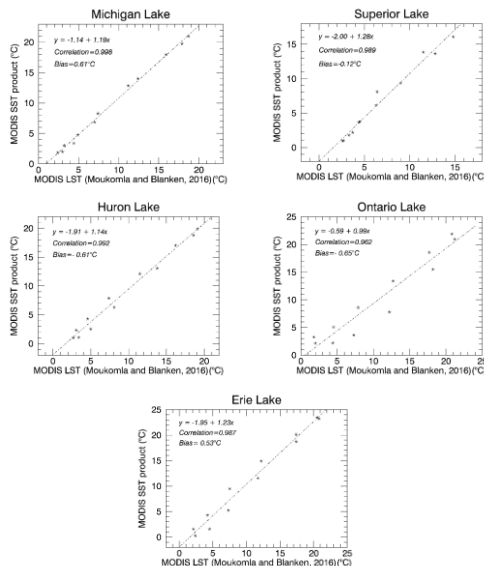


Figure 1. Results validation. MODIS SST products monthly estimations are compared with the results of Moukomla and Blanken (2016) for the Great Leaks. The timespan considered is 2003-2014. The correlation coefficients obtained ranges between 0.962 and 0.998.

Figure 1 shows the regressions carried out considering our results respect the Moukomla and Blanken (2016) paper results. Correlations between both data sets are in the interval of 0.962-0.998, demonstrating, on one hand, that the retrievals of both products are in the same line and on the other, that our methodology is capable of generating valid SST estimations in lake water surfaces.

Our validation is extended by considering Hernández-Galindo (2022) work which uses Sentinel's 3 SLSTR data to estimate monthly LSWT of the Issyk-Kul lake, in Kyrgyzstan for the year 2020 (figure 2). We have reproduced their methodology to estimate the lake's LSWT but using MODIS SST product data. As the SLSTR observations are made between 10 and 11 a.m., only Terra's diurnal images have been used, whose passing time is 10:30 a.m.

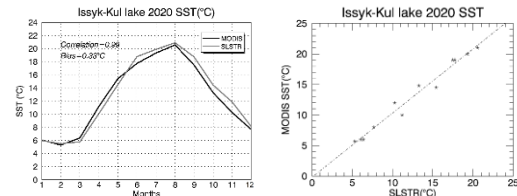


Figure 2. Monthly LSWT for the Issyk-Kul lake in the year 2020 for the MODIS and SLSTR SST estimations (left). Linear regression for both products (right).

#### 3.2. Lake Surface Water Temperature in ten of the largest lakes of the world

Once the reliability of the MODIS SST product for LSWT estimations has been established, LSWT trends for the years 2003-2020 have been estimated for the Caspian Sea, Superior, Victoria, Huron, Michigan, Tanganyika, Baikal, Great Slave Lake, Erie and Ontario by both the linear and Sen's slope methods. The confidence level is offered by carrying out the Mann-Kendall test. The mean LSWT for the whole timespan is also provided (table 2).

The MODIS Level 3 SST Thermal IR 8 Day 4km V2019.0 provides complete data (including four daily measures) from 2003 onwards. AVHRR enables a more comprehensive data period for both LST and SST variables but, in contrast, their satellites induce variability due to their orbital drift (Price, 1990; Sobrino et al., 2008 Julien and Sobrino, 2012). For this reason, MODIS time series have been selected for this study in detriment of AVHRR.

Positive trends are found in the ten lakes analysed (table 2) for both the linear and Sen's slope trend estimation methods. The higher LSWT trend estimated is found for Lake Baikal, 0.083°C/yr at a 99.79% confidence level, whereas the lower trend is found in Lake Victoria, 0.012°C/yr. Results show a high Mann-Kendall level (>95%) in the case of the Tanganyika and

Erie lakes, with warming rates of 0.017°C/yr and 0.058°C/yr, respectively.

From the absolute LSWT values, the Tanganyika and Victoria lakes are the warmer lakes among the lakes considered and show the lower data variability through time, established by their standard deviations. These absolute LSWT are 25.76±0.18°C for the Victoria Lake and 26.95±0.16°C for the Tanganyika Lake. On the other hand, the colder lakes are represented by the Baikal Lake, 6.3±0.6°C, and the Superior Lake, 6.8±0.8°C.

*Table 2. Annual trends estimated for the lakes analysed during the years 2003-2020 by the linear and Sen's slope methods. The results' confidence is given by the Mann-Kendal test (significant results are highlighted in bold).*

Lake	Mean LSWT (°C)	Linear trend (°C)	Sen's slope (°C)	Mann-Kendal (%)
Caspian Sea	16.3±0.5	0.037	0.044	87.97
Superior	6.8±0.8	0.002	0.013	37.76
Victoria	25.76±0.18	0.012	0.012	72.85
Huron	9.1±0.6	0.031	0.029	69.37
Michigan	9.9±0.8	0.025	0.029	61.64
Tanganyika	26.95±0.16	0.015	<b>0.017</b>	<b>96.93</b>
Baikal	6.3±0.6	0.082	<b>0.083</b>	<b>99.79</b>
Slave	6.9±0.7	0.041	0.056	78.88
Erie	11.7±0.5	0.043	<b>0.058</b>	<b>95.53</b>
Ontario	10.5±0.7	0.043	0.047	65.64

Sobrinho et al. (2020b) established a global SST trend of 0.019°C/yr for the years 2003-2019. Assuming this value for the present timespan and attending to the Sen's slope trends estimated in this paper, seven of the ten lakes analysed exceed this value: Caspian Sea (0.044°C/yr), Huron (0.029°C/yr), Michigan (0.029°C/yr), Baikal (0.083°C/yr), Slave Lake (0.056°C/yr), Erie (0.058°C/yr) and Ontario (0.047°C/yr). In this way, the general overview shows that lakes are warming at a higher rate than the global water surfaces.

#### 4. CONCLUSIONS

Lakes are freshwater enclosed extensions in which there is no exchange with open waters. For this reason, the initial hypothesis of this work was that they could suffer to a greater extent from the effect of global warming. Results show positive LSWT trend for the ten lakes considered: the Caspian Sea, Superior, Victoria, Huron, Michigan, Tanganyika, Baikal, Great Slave Lake, Erie and Ontario lakes.

Furthermore, when considering the current SST warming rate, established in 0.018°C/yr for the whole sea surfaces, seven of these ten lakes exceed this trend.

The sample size is limited enough to prevent generalizing that LSWT is warming at a higher rate than SST, but it can be affirmed that the LSWT of seven of the largest lakes of the world is increasing at an accelerated rate. The highest LSWT is found for Lake Baikal, with 0.083°C/yr, nearly five times the global SST trend, whereas the lowest trend is associated to Victoria Lake, with 0.012°C/yr.

The MODIS Level 3 SST Thermal IR 8 Day 4km V2019.0 achieves SST retrieval by applying a specific SST algorithm. However, it also provides information about freshwater extension and this paper has demonstrated its functionality in this type of ecosystems. The validations carried out show correlations between 0.96 and 0.99 with results provided by previous literature.

Remote sensing is a valuable technology which provides homogeneous and periodic data from the whole Earth's surface. Its main disadvantage is the impossibility of collecting data below clouds. This weakness is overcome by the satellite temporal resolution that means 4 passes per day. The low uncertainty of results confirms its reliability, strengthened by the validation that has been carried out. The LSWT is positioned as a parameter of climatic interest, already recognized as an Essential Climate Variable by the World Meteorological Organization, which reflects global warming in an amplified way. As for other ECVs, such as SST, the LSWT must be continuously monitored, as it is an indicator of the behaviour of the surface temperature of the planet.

#### REFERENCES

- Brown, B and Minnett, P.J. 1999. MODIS Infrared Sea Surface Temperature Algorithm. Algorithm Theoretical Basis Document. Version 2.0. University of Miami, Miami, United States of America.
- De Santis, D, Del Frate, F., Schiavon, G. 2022. Analysis of Climate Change Effects on Surface Temperature in Central-Italy Lakes Using Satellite Data Time-Series. *Remote Sensing*, **14**, 117. <https://doi.org/10.3390/rs14010117>
- Gamito, R., Teixeira, C.M., Costa, M.J., Cabral, H.N. Are regional fisheries' catches changing with climate? *Fisheries Research*, **161**, pp. 207-216, ISSN 0165-7836, <https://doi.org/10.1016/j.fishres.2014.07.014>.
- García-Monteiro, S; Sobrinho, J.A.; Julien, Y.; Sòria, G.; Skokovic, D. 2021. Surface Temperature trends in the Mediterranean Sea from MODIS data during years 2003-2019. *Regional Studies in Marine Science*, **49** (2022) 102086. <https://doi.org/10.1016/j.rsma.2021.102086>

- Goddard Space Flight Center. NASA, Ocean Ecology Laboratory, Ocean Biology Processing Group; (2014): MODIS-Terra Ocean Color Data. Available in <https://modis.gsfc.nasa.gov/data/dataproduct/mod28.php>
- Jia, C. 2019. Satellite Infrared Retrievals of Sea Surface Temperature at High Latitudes. MS Thesis, Meteorology and Physical Oceanography. University of Miami. Miami. FL, USA. pp. 79.
- Jia, C. and Minnett, P.J. 2020. High Latitude Sea Surface Temperatures Derived from MODIS Infrared Measurements. *Remote Sensing of Environment*, **251**, 112904.
- Kilpatrick, K. A., P. Minnett, B. Luo. 2019. Validation of NASA MODIS R2019.0 reprocessed SST Products. The 18th International GHRSSST Science Team Meeting (GHRSSST XVIII) – Frascati Italy- 6th to 10th June 2019.
- Lindsay, R. and Dahlman, L. 2009. Climate Variability: North Atlantic Oscillation. Last update: October 2021. Available in <https://www.climate.gov/news-features/understanding-climate/climate-variability-north-atlantic-oscillation>
- McPhaden, M.J.; Zebiak, S.E.; Glantz, M.H. 2006. ENSO as an integrating concept in Earth Science. *Science*, **314** (5806), pp. 1740-1745. Doi: 10.1126/science.1132588
- Physical Oceanography Distributed Active Archive Center (PO.DAAC). 2018. Available online [<https://podaac.jpl.nasa.gov/>] from NASA EOSDIS PO.DAAC, Pasadena, CA, Accessed January 5, 2021.
- Sobrino, J.A.; Julien, Y.; García-Monteiro, S., 2020a. Surface Temperature of the Planet Earth from Satellite Data. *Remote Sensing*, **12**, 218.
- Sobrino, J.A.; García-Monteiro, S.; Julien, Y. 2020b. Surface Temperature of the Planet Earth from Satellite Data over the period 2003-2019. *Remote Sens.* **12**(12), 2036. Doi: 10.3390/rs12122036

# Exploring spatio-temporal spectral and functional variability in Mediterranean grasslands

M. Pilar Martín <sup>(1,\*)</sup>, Vicente Burchard-Levine <sup>(1)</sup>, Rosario González-Cascón <sup>(2)</sup>, Javier Pacheco-Labrador <sup>(3)</sup>, David Riaño <sup>(1,4)</sup>

<sup>(1)</sup> *Environmental Remote Sensing and Spectroscopy Laboratory (SpecLab), Spanish National Research Council (CSIC), Madrid, Spain.*

<sup>(2)</sup> *Department of Environment, National Institute for Agriculture and Food Research and Technology (INIA), Spanish National Research Council (CSIC), Madrid, Spain.*

<sup>(3)</sup> *Max Planck Institute for Biogeochemistry, Department Biogeochemical Integration, Hans-Knöll-Str. 10, D-07745 Jena, Germany.*

<sup>(4)</sup> *Center for Spatial Technologies and Remote Sensing (CSTARS), University of California, Davis, USA*

\*Email: mpilar.martin@cchs.csic.es

**ABSTRACT-** Close-range and satellite remote sensing data have been widely used to estimate vegetation properties (e.g., biomass, leaf area index, or chlorophyll and nitrogen contents) and characterize ecosystem functioning. However, the estimation of plant functional traits from spectral information in Mediterranean and semi-arid grasslands remains challenging. These ecosystems can be highly biodiverse, featuring numerous species that dynamically overlap in space and time. Such mixtures reduce the potential generalization of empirical models and complicate the usage of physically-based approaches. This study explores the spatio-temporal spectral and functional variability of a drought-prone Mediterranean wooded grassland where spectral measurements were acquired using an ASD FieldSpec® 3 spectroradiometer (Analytical Spectral Devices Inc., Boulder, CO, USA) with a spectral range between 350 and 2500 nm, in a 1 ha study site over plots sampled in 23 campaigns from 2017 to 2019. Concomitant destructive sampling provided grass functional properties (leaf area index, pigments, and water content). Five phenological phases (phenophases) were identified in this ecosystem: summer drought, autumn-winter regrowth, spring (biomass peak), and beginning of grass decay, plus an additional flowering phase. Spectral Angle Mapper technique classified each sampled plot into the five phenophases. Multiple linear regression (MLR) was used to estimate LAI from in-situ data and spectral vegetation indices (VIs) calculated from ASD and compare annual vs phenological models. Results revealed a spatio-temporal disagreement between classification and the general phenology of the ecosystem and showed promising improvement in the estimation of LAI for autumn-winter regrowth and beginning of grass decay phenophases.

## 1 INTRODUCTION

Semi-arid grasslands can be highly biodiverse, featuring numerous species that overlap and change in space and time. Such diversity implies dynamic and heterogeneous vegetal mixtures featuring different spectral and functional properties such as green vegetation, senescing vegetation, litter, or flowers. These mixtures confound the relationships between the averaged spectral and functional properties of patches (or pixels) observable at proximal or remote ranges and the retrieval of vegetation properties using physical models (Darvishzadeh et al., 2008; Pacheco-Labrador et al., 2021). This study explores spatio-temporal spectral and functional variability of a drought-prone Mediterranean wooded grassland under extensive livestock use (<0.3 cows/ha) located in

western Spain aiming to answer the following research questions:

1. How many phenophases can we observe in a semi-arid Mediterranean grasslands?
2. Do they have a "typical" spectral behaviour?
3. Can pheno-spectral characterization of these ecosystems help to improve the estimation of plant traits?

## 2 STUDY SITE AND DATASETS

The study site (western Spain, 39°56'25" N, 5°46'29" W) is a typical Spanish *dehesa* (wooded grassland) with 20% tree fraction cover, 25 trees/ha density, 46 cm mean DBH, and 150-200 years mean tree age. The climate is characterized by dry and hot summers with 16.6 °C mean annual temperature and 600mm mean annual precipitation. The soils are poorly drained



stagnic alisols over arkose with low organic matter contents. This ecosystem is composed of two vegetation strata with very different biophysical and phenological characteristics. The tree stratum is mainly composed of holm oaks (*Quercus Ilex*). The herbaceous layer covers almost the entire study area, except for some dirt paths and small lakes, and comprehends a wide variety of annual species, *Tolpis barbata* (L.) Gaertn., *Chamaemelum mixtum* (L.) All., *Plantago lagopus* L., *Echium plantagineum* L., *Cynodon dactylon* (L.) Pers., etc. (Martín, et al., 2020). The grassland's strong seasonal and inter-annual variabilities (Luo et al., 2020) (Fig. 1) relate to their superficial roots and, thus, dependence on rain and shallow soil water availability.

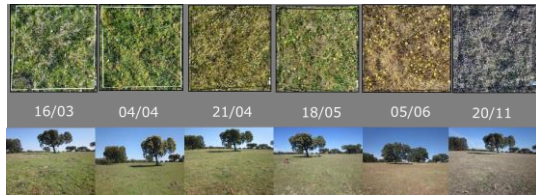


Figure 1. Field pictures showing the phenological cycle of the herbaceous layer in the study site (2017).

*In-situ* measurements were collected in 15 field campaigns distributed throughout the various phenological phases of the ecosystem between 2017 and 2019. These measurements include information on plant traits and hemispherical conical reflectance factors (HCRF) of the herbaceous layer. The latter

were measured with an ASD spectroradiometer FieldSpec® 3 (Analytical Spectral Devices Inc., Boulder, CO, USA) with a spectral range between 350 and 2500 nm and a nominal field of view of 25°. A total of 391 spectra plus RGB pictures were acquired on 1x1m quadrants. Destructive sampling in the central 25x25cm area of the same quadrants was performed by ground-level cutting of all rooted vegetation (green and/or dry plants). The samples were processed in the laboratory to estimate key variables, such as the leaf area index (LAI, m<sup>2</sup> / m<sup>2</sup>) -both total and green fractions-, pigments, water, and dry matter content.

### 3 METHODS

Temporal series analysis of Normalized Difference Vegetation Index (NDVI) from Moderate Resolution Imaging Spectroradiometer (MODIS) images in Melendo-Vega et al. (2018), along with visual inspection of field pictures, allowed to define in the study site's four phenological stages or phenophases (Fig. 2a-c): summer drought, autumn- winter regrowth, spring (biomass peak), and beginning of grass decay. A flowering phase was additionally defined in this study due to the spectral diversity induced by these mixtures (e.g., green/dry grass combined with white/yellow/red flowers). These diverse combinations leads to spectral differences that can be related to the state of the grass or to the flowers' color and density (Fig. 2e).

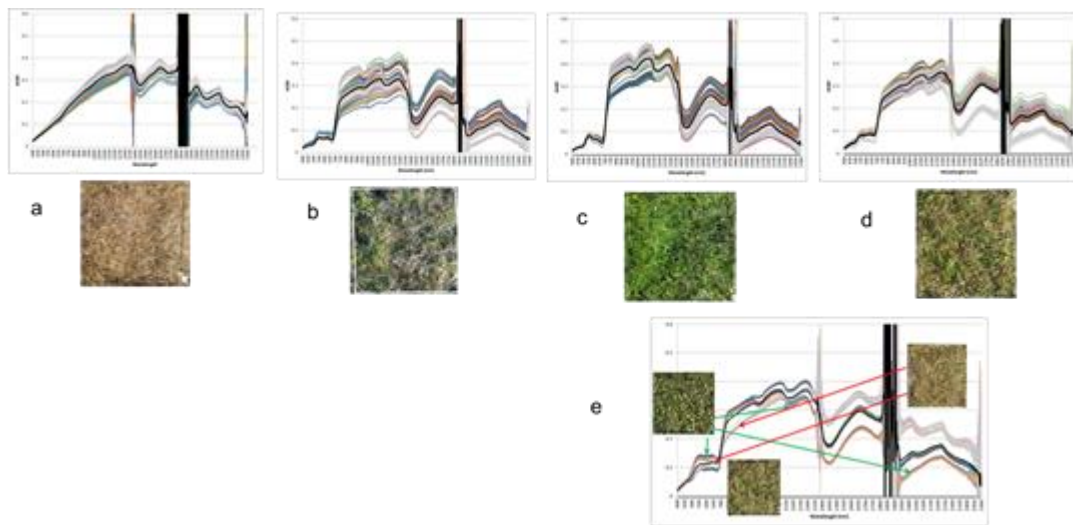


Figure 2. Phenophases identified on the herbaceous layer in the study site: a) summer drought, b) autumn- winter regrowth, c) spring (biomass peak), d) beginning of grass decay and e) flowering phase. Hemispherical conical reflectance factors (HCRF) measured with a field spectroradiometer and field pictures representative of each phenophase are presented.

Twenty "pure" spectra of the different phenophases obtained as average values of spectra acquired in representative sampling plots were used as endmembers to classify the remaining spectra with Spectral Angle Mapper (SAM) hyperspectral classifier. SAM is a classification algorithm that calculates the angular distance between spectral signatures in an  $n$ -dimensional space where  $n$  is the number of bands (Kruse et al., 1993). One of the main advantages of this method is that it is rather insensitive to illumination conditions since the angle between the vectors is independent of its length. This is relevant in our study as illumination conditions can vary in the different field campaigns due, among others, to seasonal changes in solar elevation.

The SAM classification allowed to conduct an exploratory analysis to estimate LAI (total and green fractions) from *in-situ* data and spectral vegetation indices (VIs) calculated from ASD and compare annual vs fenological models. Seventeen spectral vegetation indices (VIs) were calculated from ASD Fieldspec 3 HCRF and multiple linear regression (MLR) models were generated for each phenophase (plots classified with SAM) and the whole study period both using all data and a random sample of ~25% of all sampling plots. Model performance was evaluated using  $R^2$  and standard errors of the estimates.

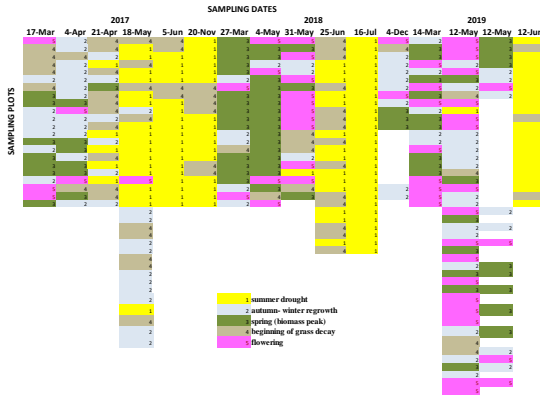


Figure 3. SAM classification of sampling plots in 5 phenophases. Color represents each phenophase: yellow) summer drought, grey) autumn- winter regrowth, green) spring (biomass peak), brown) beginning of grass decay and pink) flowering phase.

#### 4 RESULTS

A total of 371 spectra were classified and assigned to the 5 phenophases previously identified. As it can be observed in Fig.3, plots sampled the same day were assigned to different phenophases. 30% of the plots were assigned to the summer drought phenophase and between 16 and 20 % to the autumn- winter regrowth,

spring (biomass peak) or beginning of grass decay phenophases. 13% of the plots were assigned to the flowering phenophase mainly in spring campaigns but with some plots also in winter.

MLR analysis generated different models for each phenophase with  $R^2$  values for the total LAI models ranging from 0.39 for the flowering phenophase to 0.60 for the autumn- winter regrowth; and from 0.41 for the beginning of grass decay to 0.66 for the autumn- winter regrowth for the green-LAI models (Table 1).  $R^2$  values reached higher values for the annual models: 0.56 and 0.69 for total and green-LAI models respectively using the whole dataset and 0.57 and 0.67 when only a random sample of approximately 25% of the dataset was used (Table 1). However, the standard error of the estimates were lower in the fenological models for three out of five phenophases: autumn- winter regrowth and beginning of grass decay, which are specially problematic for the estimation of plant traits using annual models due to the mixture of green and senesced material.

Table 1. Summary of the statistics for the different multiple linear regression models predicting total (LAI) and green (green-LAI) leaf area index from a selection of 17 spectral vegetation indices calculated from ASD *in-situ* data.

Phenophase	n	$R^2$		Adjusted $R^2$		Std Error of the estimate	
		LAI	Green LAI	LAI	Green LAI	LAI	Green LAI
Summer drought	115	.450	.582	.367	.514	.299	.205
Autumn-winter regrowth	72	.600	.663	.484	.565	.287	.255
Spring (biomass peak)	66	.457	.485	.279	.317	.499	.470
Beginning of grass decay	62	.411	.570	.202	.418	.398	.236
Flowering	49	.397	.459	.095	.189	.506	.464
All	364	.565	.691	.545	.676	.393	.331
Random ~25%	82	.570	.672	.464	.588	.418	.355

#### 5 DISCUSSION AND CONCLUSIONS

Results showed a disagreement between spectral-based classification and the described general phenology of the ecosystem (NDVI time series analysis and visual inspection of field pictures). Consequently, plots sampled during the same campaign were often assigned to different spectral phenophases. This might result from the spatial variability of grass phenology, which can be driven by several factors, such as microtopography (Julitta et al., 2013) or the influence of livestock grazing. In addition, the spatial variability of vegetation properties (functional diversity) or the mixture of different canopy elements could inflate grass spectral variability, challenging classification. However, the fraction of spatial trait variability unexplained by phenological diversity remains unclear. Previous works showed that accounting for phenology (using

simulated spectral data from radiative transfer models) improved the retrieval of plant functional traits since it reduced the variability of the relationships between both datasets (Martín et al., 2020).

This study reveals that spatial variability should also be considered when accounting for phenology to fit and apply empirical or semi-empirical models to minimize the variability of the correlation patterns. Spatial variability can be especially relevant at field scales, from medium to high spatial resolution images, including those acquired from planes or drones.

## 6 ACKNOWLEDGEMENTS

The research received funding from the Spanish Ministry of Science through the BIOSPEC CGL2008-0230, the Ministry of Economy and Competitiveness through FLUXPEC CGL2012-34383 and SynerTGE CGL2015-G9095-R (MINECO/FEDER, UE) projects and the Ministry of Innovation through DiverSpec-TGA (PID2019-108313RB-C32). We would like to thank all people involved during the field campaigns throughout the years from different institutions: CSIC, INIA, UAH, CEAM, MPI-BGC, UEX and UNIZAR.

## 7 REFERENCES

- Darvishzadeh, R., Skidmore, A., Schlerf, M., and Atzberger, C., 2008, Inversion of a radiative transfer model for estimating vegetation LAI and chlorophyll in a heterogeneous grassland. *Remote Sensing of Environment*, 112, 2592-2604
- Julitta, T., Cremonese, E., Migliavacca, M., Colombo, R., Galvagno, M., Siniscalco, C., Rossini, M., Fava, F., Cogliati, S., Morra di Cella, U., and Menzel, A., 2014, Using digital camera images to analyse snowmelt and phenology of a subalpine grassland. *Agricultural and Forest Meteorology*, 198–199, 116-125
- Kruse, F. A., Lefkoff, A. B., Boardman, J. W., Heidebrecht, K. B., Shapiro, A. T., Barloon, P. J. and Goetz, A. F. H., 1993, The spectral image processing system (SIPS)—interactive visualization and analysis of imaging spectrometer data. *Remote Sensing of Environment* 44(2), 145-163.
- Luo, Y., El-Madany, T., Ma, X., Nair, R., Jung, M., Weber, U., Filippa, G., Bucher, S.F., Moreno, G., Cremonese, E. and Carrara, A., 2020, Nutrients and water availability constrain the seasonality of vegetation activity in a Mediterranean ecosystem. *Global Change Biology*, 26(8), 4379-4400.
- Martín, M.P., Pacheco-Labrador, J., González-Cascón, R., Moreno, G., Migliavacca, M., García, M., Yebra, M., Riaño, D., 2020, Estimation of essential vegetation variables in a dehesa ecosystem using reflectance factors simulated at different phenological stages. *Revista de Teledetección*, 55, 31-48.
- Pacheco-Labrador, J., El-Madany, T. S., van der Tol, C., Martín, M. P., Gonzalez-Cascon, R., Perez-Priego, O., ... and Migliavacca, M., 2021, senSCOPE: Modeling mixed canopies combining green and brown senesced leaves. Evaluation in a Mediterranean Grassland. *Remote Sensing of Environment*, 257, 112352.

# Exploring the capabilities of Sentinel-2 reflectance to predict soil organic carbon in Spain

S. Sánchez-Ruiz<sup>1\*</sup>, M. Campos-Taberner<sup>1</sup>, M. Chiesi<sup>2</sup>, F. Maselli<sup>2</sup>, B. Martínez<sup>1</sup>,  
F. J. García-Haro<sup>1</sup>, M. A. Gilabert<sup>1</sup>

<sup>1</sup> Environmental Remote Sensing Group (UV-ERS), Departament de Física de la Terra i Termodinàmica, Facultat de Física, Universitat de València, 46100-Burjassot, Spain

<sup>2</sup> Istituto per la BioEconomia, Consiglio Nazionale delle Ricerche, 50019-Sesto Fiorentino, Italy

\* [sergio.sanchez@uv.es](mailto:sergio.sanchez@uv.es)

**ABSTRACT** -Soil organic carbon (SOC) is the greatest carbon reservoir in terrestrial ecosystems. Encouraged by the good performance of hyperspectral reflectance in estimating SOC in the laboratory, the current study aims at estimating SOC in Spain from multispectral satellite reflectance. 113 SOC samples from the LUCAS database measured during the 2015 campaign were taken as reference, including bare lands, croplands, grasslands, shrublands, and woodlands. Sentinel-2 tiles during the 01/04/2017-31/03/2018 period with 10 % cloud cover or less were downloaded through Google Earth Engine. Reflectance from bands 2 (blue), 3 (green), 4 (red), 5 (red edge), 6 (red edge), 7 (red edge), 8 (near infrared), 8A (narrow near infrared), 11 (shortwave infrared) and 12 (shortwave infrared) of dates coincident to all sampling locations were used as predictors. General and land cover dependent models were trained through Random Forests to predict SOC. Their performances were evaluated through leave-one-out cross-validation. Considering all land covers together, relative mean bias error (rMBE) of 2 % and relative root mean square error (rRMSE) of 63 % were found. Most important predictors were reflectance from band 11 (B11) measured on day of year (DOY) 291, B8A on DOY = 36, B7 on DOY = 36, B12 on DOY = 166 and B2 on DOY = 291. Results generally improved with land cover dependent models. Minimum rMBE (−0.9 %) and minimum rRMSE (28 %) were respectively found for grasslands and bare lands; whereas maxima rMBE (−4 %) were found for bare lands, shrublands and woodlands, and maximum rRMSE (61 %) was found for shrublands.

## 1 INTRODUCTION

Among terrestrial ecosystems, soil is the greatest reservoir of organic carbon. Particularly, soil organic carbon (SOC) is at least twice the amount of carbon stored in vegetation in the form of biomass at global scale (Batjes, 2016; Eswaran et al., 1993). Soil acts as a carbon sink, which helps mitigating global warming. However, this behaviour is already in danger due to degradation and deforestation (IPCC, 2014). Therefore, the necessity of monitoring the amount of carbon stored in soil has increased.

In this context, remote sensing is a suitable tool for this task. Actually, the combination of hyperspectral measurements in the 400-2500 nm spectral range with machine learning methods has already achieved very good results when estimating SOC in Europe (Odebiri et al., 2021; Padarian et al., 2019; Singh & Kasana, 2019). However, the majority of these studies used hyperspectral spectra measured in the laboratory. The estimation of SOC from multispectral sensors on board satellites remains yet a challenging task (Odebiri et al., 2021).

The current is a preliminary study to start filling this gap and proposes to estimate SOC in Spain from Sentinel-2 multispectral reflectance using Random Forests.

## 2 DATA

### 2.1 Soil organic carbon

A total of 113 SOC samples from the Land Use and Cover Area frame Survey (LUCAS) database measured during the 2015 campaign (LUCAS 2015 Topsoil Survey) were taken as reference SOC, including bare lands, croplands, grasslands, shrublands, and woodlands (Jones et al., 2020). LUCAS is a panEuropean initiative that took around 20 000 samples throughout the whole European Union distributed along the intersections of a 2 km × 2 km regular grid. Each sample consists of 5 subsamples: one in the location point and the other 4 at a distance of 2 m following the cardinal directions. SOC was estimated in laboratory after dry combustion (<https://www.iso.org/standard/18782.html>). The 113

samples used in the current study were selected as a compromise to include all 5 land covers in regions with similar ecoclimatic features (*Región de Murcia* and *Comunitat Valenciana*) and to match the same dates with the used satellite data (see section 2.2). Table 1 summarizes the basic statistics of SOC reference data.

Table 1. Minimum (MIN), maximum (max), average (AVG), and standard deviation (STD), all expressed in  $g\ kg^{-1}$ , of reference SOC by land cover (LC): bare lands (BRL), crop lands (CRO), grasslands (GRA), shrublands (SHR), and woodlands (WDL). N indicates the number of samples.

LC	MIN	MAX	AVG	STD	N
BRL	5.00	18.00	12.03	3.78	12
CRO	1.80	28.80	11.76	7.09	50
GRA	6.30	30.90	16.46	7.10	18
SHR	11.60	88.70	37.18	25.17	12
WDL	17.50	104.20	47.90	25.03	21
All	1.80	104.20	21.95	20.44	113

## 2.2 Sentinel-2 reflectance

Sentinel-2 Level-2A product was downloaded through Google Earth Engine (GEE) (Gorelick et al., 2017). It is computed running sen2cor atmospheric correction toolbox and called S2\_SR in GEE ([https://developers.google.com/earth-engine/datasets/catalog/COPERNICUS\\_S2\\_SR](https://developers.google.com/earth-engine/datasets/catalog/COPERNICUS_S2_SR)). Only reflectance from bands 2 (blue), 3 (green), 4 (red), 5 (red edge), 6 (red edge), 7 (red edge), 8 (near infrared), 8A (narrow near infrared), 11 (shortwave infrared) and 12 (shortwave infrared) were selected from tiles with cloud cover equal or less than 10 % during the 01/04/2017-31/03/2018 period. Bands with spatial resolution coarser than 10 m were resampled to 10 m.

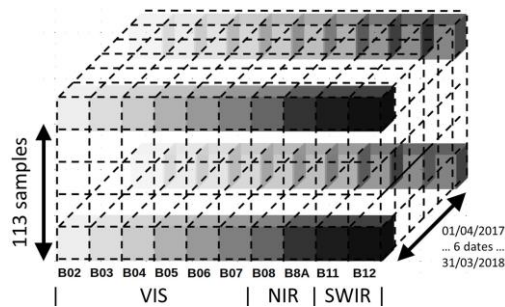


Figure 1. Diagram of used Sentinel-2 observations. VIS refers to visible, NIR to near infrared, and SWIR to shortwave infrared.

Copernicus Sentinel-2 mission consists of two polar-orbiting satellites placed in the same sun-synchronous orbit. Its revisit time is 5 days at the

equator and 2-3 days at mid-latitudes (<https://sentinel.esa.int/web/sentinel/missions/sentinel-2>). Thus, a total of 6 dates were available under maximum 10 % cloud cover for the 113 selected sampling points. Figure 1 schematizes the used Sentinel-2 observations.

## 3 METHODOLOGY

Different models to predict SOC from Sentinel-2 reflectance were trained with Random Forests (Breiman, 2001). Random Forests is a decision tree ensemble learning method that combines bootstrap aggregating (Breiman, 1996) with a random selection of a subset of predictors in each decision. Bagging consists in dividing the initial training dataset in several subsets of the same size. Their sample units are chosen randomly with replacement, that is, the same sample unit can be selected in different subsets. Then a different model is trained for each training data subset and, finally, all models are combined to obtain predictions.

In the current study, the reflectances of the 10 selected bands in the 6 available dates (see section 2.2) were used as predictors (60 predictors). 500 trees, i.e. training data subsets were sampled with replacement. For each of the training subsets, a decision tree was grown with 4 (the square root of one third of the 60 predictors, rounded down) randomly selected predictors in each node. And, since Random Forests was used in regression mode, all decision trees were combined to obtain final estimations through average.

Due to the size of the sample (113 samples), the methodology was evaluated through leave-one-out cross-validation. It consists in fitting as many models as samples are available. In each iteration, one sample is used as test set, while the remaining samples are used for training. Then the performance of the models is evaluated as the average of the test statistics of all iterations. In the current study, mean bias error (MBE) and root mean square error (RMSE) were calculated, as well as their relative values (i.e. divided by the mean of all samples).

This procedure was carried out both considering all land covers together and independently for each land cover.

## 4 RESULTS

### 4.1 All land covers

When considering all land covers together, the following results were obtained ( $r$  indicates relative, see section 3): MBE =  $0.53\ g\ kg^{-1}$ , rMBE = 2 %, RMSE =  $14\ g\ kg^{-1}$ , and rRMSE = 63 %.

A subset of best performing predictors was also identified, as shown in Figure 2. In each of the 113 iterations, predictor importance was obtained for all predictors used and the 5 predictors with the greatest predictor importance were selected, forming a reduced subset. Then, the 5 best performing predictors were identified by counting the times they appeared in the reduced subset. This resulted in the reflectance of band 11 (B11) measured on day of year (DOY) 291, followed by B8A on DOY = 36, B7 on DOY = 36, B12 on DOY = 166 and B2 on DOY = 291.

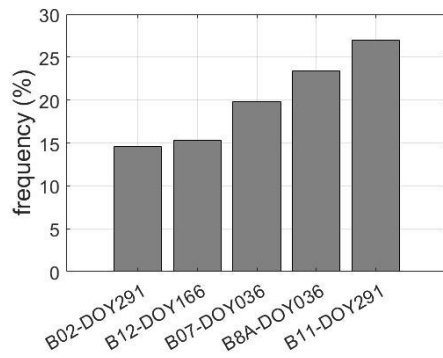


Figure 2. Best 5 predictors in terms of normalized frequency of appearance. DOY refers to day of year. Bands are described in section 2.2.

#### 4.2 By land cover

The results of training different models for each land cover are summarized in Table 2. In comparison to training only one model for all land covers together, relative RMSE (rRMSE) was reduced in all land covers. However, relative MBE (rMBE) was reduced (in absolute value) only in croplands and grasslands. Its sign changed from positive to negative in all land covers but croplands, though.

Table 2. Errors of predicted SOC by land cover (LC): bare lands (BRL), croplands (CRO), grasslands (GRA), shrublands (SHR), and woodlands (WDL). *r* indicates relative (see section 3).

LC	MBE (g kg <sup>-1</sup> )	rMBE (%)	RMSE (g kg <sup>-1</sup> )	rRMSE (%)
BRL	-0.50	-4.14	3	28
CRO	0.11	0.96	6	52
GRA	-0.15	-0.88	5	33
SHR	-1.42	-3.82	23	61
WDL	-1.89	-3.94	22	45

## 5 DISCUSSION AND CONCLUSIONS

Random Forests algorithm was used to estimate soil organic carbon using reflectance from Sentinel-2 and results were validated against LUCAS database. When

training a single model for all considered land covers (bare lands, crop lands, grasslands, shrublands, and woodlands) together, low MBE and high RMSE were obtained. Additionally, the reflectance measured in near and shortwave infrared along different periods of the year were identified as the best performing predictors.

When training different models for each land cover, results generally improved. While absolute value of relative MBE was only reduced for croplands and grasslands, relative RMSE was reduced for all land covers, mainly for bare lands and grasslands (up to 35 percent points). This might be due to the sensor directly observing the soil in bare lands and doing so at least during some period of the year in grasslands. Shrubbylands and woodlands, instead, present a permanent cover during the whole year (at least, a woody one), so the models are trying to indirectly estimate SOC from vegetation state. Some crops present bare soil during some periods of time too. But, since no further classification was performed, the croplands samples might contain very different types of crops presenting different structures, including trees.

In comparison to other studies using similar spectral data, the current study obtained higher errors. For example, Odebiri et al. (2020) obtained relative RMSE around 20 % over a range of algorithms including Random Forests. However, that study concerned a single and controlled land cover, i.e. a commercial forest plantation. Wang et al. (2022) found that shortwave infrared reflectance was key for airborne and spaceborne sensors to estimate SOC in bare soils, which is in agreement with the best performing predictors identified in the present study.

Some alternatives that could improve the current results were identified from previous studies (mostly performed with laboratory spectra): (i) preprocessing of the spectral data such as the generation of spectrograms (Padarian et al., 2019) or the first-order derivative (Wang et al., 2022), (ii) using spectral indices as predictors instead of solely spectral reflectance (Odebiri et al., 2020), (iii) using more sophisticated algorithms to train the prediction models, e.g. convolutional neural networks or long short-term memory networks (Odebiri et al., 2021; Padarian et al., 2019; Singh & Kasana, 2019), (iv) training different models for different types of soil instead of different land covers (Wang et al., 2022).

## ACKNOWLEDGEMENTS

This research was supported by grant PID2020-118036RB-I00 (Project ECCE EO) funded by MCIN/AEI/10.13039/501100011033 and by “ERDF A way of making Europe”.



## REFERENCES

- Batjes, N. H. (2016). Harmonized soil property values for broad-scale modelling (WISE30sec) with estimates of global soil carbon stocks. *Geoderma*, 269, 61–68. <https://doi.org/10.1016/j.geoderma.2016.01.034>
- Breiman, L. (1996). Bagging predictors. *Machine Learning*, 24(2), 123–140. <https://doi.org/10.1007/BF00058655>
- Breiman, L. (2001). Random forests. *Machine Learning*, 45(1), 5–32. <https://doi.org/10.1023/A:1010933404324>
- Eswaran, H., Berg, E. Van Den, & Reich, P. (1993). Division S-5 Notes. *Soil Science of America Journal*, 57(1), 192–194.
- Gorelick, N., Hancher, M., Dixon, M., Ilyushchenko, S., Thau, D., & Moore, R. (2017). Google Earth Engine: Planetary-scale geospatial analysis for everyone. *Remote Sensing of Environment*, 202, 18–27. <https://doi.org/10.1016/j.rse.2017.06.031>
- IPCC. (2014). *Climate Change 2014: Synthesis Report. Contribution of Working Groups I, II and III to the Fifth Assessment Report of the Intergovernmental Panel on Climate Change*.
- Jones, A., Fernandez-Ugalde, O., & Scarpa, S. (2020). *LUCAS 2015 Topsoil Survey. Presentation of dataset and results*. <https://doi.org/10.2760/616084>
- Odebiri, O., Mutanga, O., Odindi, J., Peerbhay, K., & Dovey, S. (2020). Predicting soil organic carbon stocks under commercial forest plantations in KwaZulu-Natal province, South Africa using remotely sensed data. *GIScience and Remote Sensing*, 57(4), 450–463. <https://doi.org/10.1080/15481603.2020.1731108>
- Odebiri, O., Odindi, J., & Mutanga, O. (2021). Basic and deep learning models in remote sensing of soil organic carbon estimation: A brief review. *International Journal of Applied Earth Observation and Geoinformation*, 102(June), 102389. <https://doi.org/10.1016/j.jag.2021.102389>
- Padarian, J., Minasny, B., & McBratney, A. B. (2019). Using deep learning to predict soil properties from regional spectral data. *Geoderma Regional*, 16, e00198. <https://doi.org/10.1016/j.geodrs.2018.e00198>
- Singh, S., & Kasana, S. S. (2019). Estimation of soil properties from the EU spectral library using long short-term memory networks. *Geoderma Regional*, 18, e00233. <https://doi.org/10.1016/j.geodrs.2019.e00233>
- Wang, S., Guan, K., Zhang, C., Lee, D. K., Margenot, A. J., Ge, Y., Peng, J., Zhou, W., Zhou, Q., & Huang, Y. (2022). Using soil library hyperspectral reflectance and machine learning to predict soil organic carbon: Assessing potential of airborne and spaceborne optical soil sensing. *Remote Sensing of Environment*, 271(December 2021), 112914. <https://doi.org/10.1016/j.rse.2022.112914>

# First Applications of High Resolution BRDF Algorithm (HABA) for reflectance normalization on a fusion dataset from the Sen2Like processor

Moletto-Lobos I.<sup>1</sup>, Franch B.<sup>1</sup>, Saunier S.<sup>2</sup>, Louis J.<sup>2</sup>, Cadau E.<sup>3</sup>, Debaecker V.<sup>2</sup>, Pflug B.<sup>4</sup>, De Los Reyes R.<sup>4</sup>, Boccia V.<sup>5</sup>, Gascon F.<sup>5</sup>

<sup>1</sup> University of Valencia, Global Change Unit, Image Processing Laboratory, Paterna, 46980 Valencia, Spain

<sup>2</sup> Telespazio France, Satellite System and Operation, 26 avenue JF Champollion, BP 52309, 31023 Toulouse Cedex 1, France

<sup>3</sup> Serco Italia S.p.A - Via Sciadonna 24-26, 00044 Frascati (RM)

<sup>4</sup> German Aerospace Center (DLR), Remote Sensing Technology Institute, Photogrammetry and Image Analysis, Oberpfaffenhofen, 82234 Weßling, Germany

<sup>5</sup> European Space Agency, Directorate of Earth Observation Programmes, Largo Galileo Galileo 1, 00044 Frascati (Roma), Italy

[italo.moletto@uv.es](mailto:italo.moletto@uv.es), [belen.franch@uv.es](mailto:belen.franch@uv.es), [sebastien.saunier@telespazio.com](mailto:sebastien.saunier@telespazio.com), [jerome.louis@telespazio.com](mailto:jerome.louis@telespazio.com), [vincent.debaecker@telespazio.com](mailto:vincent.debaecker@telespazio.com), [enrico.cadau@esa.int](mailto:enrico.cadau@esa.int), [bringfried.pflug@dlr.de](mailto:bringfried.pflug@dlr.de), [raquel.delosreyes@dlr.de](mailto:raquel.delosreyes@dlr.de), [valentina.boccia@esa.int](mailto:valentina.boccia@esa.int), [ferran.gascon@esa.int](mailto:ferran.gascon@esa.int)

**ABSTRACT** - Normalized Bidirectional Adjusted Reflectance (NBAR) is a key parameter for a consistent time series monitoring over non-lambertian surfaces. The Sen2Like is a Virtual Constellation (VC) which harmonizes and fuses Landsat 8 / Landsat 9 & Sentinel 2 dataset giving out a higher spatial and temporal resolution surface reflectance. However, for adequate monitoring of land surface is necessary the correction of sun and sensor angle view across the VC acquisitions. The High resolution Adjusted BRDF Algorithm (HABA) provides 10m NBAR product retrieved from the disaggregation of the Bidirectional Reflectance Distribution Function (BRDF) parameters based on the VJB disaggregation. The model was evaluated on stable sites, such as Sahara Desert and Amazonian Forest by comparing the impact of View Zenith Angle (VZA) and Solar Zenith Angle (SZA) of directional reflectance, a static NBAR model and HABA for NIR and red spectrum. Also, the Sen2Like performance was assessed on dynamic sites with a mosaic of land covers across the Belgium, calculating the difference per-tile in a 5-day window. The results of stable sites show a decline of linear dependency on the Amazon VZA from  $R^2$  0.57 (directional) to 0.37 (HABA) in NIR and  $R^2$  0.04 (directional) to 0.0 (HABA) in red. The Sahara Desert showed a correction of 4% of linear dependency of SZA versus reflectance. Finally, in Belgium, HABA corrected up to 12,74 % the directional effect on the time series. This work contributes to develop a dynamic and operationalization of NBAR correction method based on pixel scale for high resolution datasets.

## 1 INTRODUCTION

The Sentinel-2 (S2) mission managed by the European Space Agency (ESA) has been fully operational since June 2017 with a constellation of two polar orbiting satellite units. Both the Sentinel-2A (S2A) and Sentinel-2B (S2B) satellites are equipped with an optical imaging sensor, namely the Multi-Spectral Instrument (MSI), which acquires high spatial resolution images with ground sampling distances (GSDs) of 10 to 60 m depending on the wavelength (Drusch et al., 2012). Currently, the understanding and characterization of time-varying land changes at fine spatial scale is becoming a real concern. The challenge

is to maximize revisit frequency irrespective of the Earth location, such as over equatorial and high latitude regions, and thus reduce the effect of limiting factors such as persistent cloud coverage. The combination of the Sentinel-2A/2B (S2A/B) and Landsat-8/9 (LS8/LS9) sensors together already provides a global median average revisit of 2.3 days (Li et al., 2020). These products combined can provide a Virtual Constellation (VC), but for retrieve an adequate magnitude of reflectance correction is mandatory performe such corrections such as the spectral band adjustment factor (SBAF) (Teillet et al., 2007) and correcting the noise of the data due to the Bi-Directional Reflectance Function (BRDF) angular dependency.



Regarding the BRDF correction, Landsat and Sentinel-2 sampling characteristics provide nearly constant observation geometry and low illumination variation within each scene. However, when a surface reflectance time series combining measurements from both sensors is created, variations due to differences in view geometry between them arise. In extreme cases, the differences in the view zenith angle for a ground target can reach  $20^\circ$  from adjacent orbits only a few days apart. Additionally, variations in the seasonal illumination also impact the surface reflectance value. Gao et al (2014) concluded that for Landsat-like narrow swath sensors, the major BRDF effect arises from the day of year effect, and can cause variations of 0.04–0.06 reflectance compared to mid-summer observations. Such angular effects can be corrected using a Bidirectional Reflectance Distribution Function (BRDF) model. However, the narrow angular sampling of moderate resolution sensors such as Landsat and Sentinel 2 complicates the BRDF parameters retrieval. In this paper, we describe the adaptation of the method of Franch et al. (2014, 2018) called High resolution Adjusted BRDF Algorithm (HABA) for HLS BRDF normalization and applied to testing on test sites.

The application of BRDF normalization algorithms such as HABA or C-Factor (Roy et al., 2016) is mandatory evaluate the performance of the correction of angular dependency. For this reason, the aim of this work is to validate the BRDF correction of HABA and C-Factor algorithms compared to the bidirectional reflectance over time series in different stable and unstable sites around the world.

## 2. MATERIAL AND METHODS

For evaluate the Sen2Like series, we used 2019 dataset for evaluate two different methods for BRDF corrections were implemented based on the literature survey. This evaluation was performed on two stable sites such as Amazon Forest and Sahara Desert, and also a mosaic of different land covers over Belgium area (Figure 1). The HABA is the only algorithm that estimates the BRDF parameters at S2 spatial resolution including a disaggregation of the BRDF parameters estimated from the MODIS surface reflectance product (M{O, Y}D09) at  $0.01^\circ$  spatial resolution and using the Vermote Justice Bréon (VJB) method (Vermote et al., 2008). A global method based on a static set of coefficients issued in Roy et al. (2016, 2017) and a scene dependent set based on BRDF dynamic characterization (Franch et al., 2014). The two methods were selected to fulfill the accuracy requirements of users. The first approach proposed by Roy et al. (2016, 2017) is widely adopted in the community to correct S2/LS8 data (observations performed close to nadir) due to its simplicity and relatively good performance

depending on the land cover. The results are in general more accurate with the HABA, which provides HR characterization, and the correction is performed at the S2 pixel level. However, the HABA implementation is more complex and requires more processing resources.

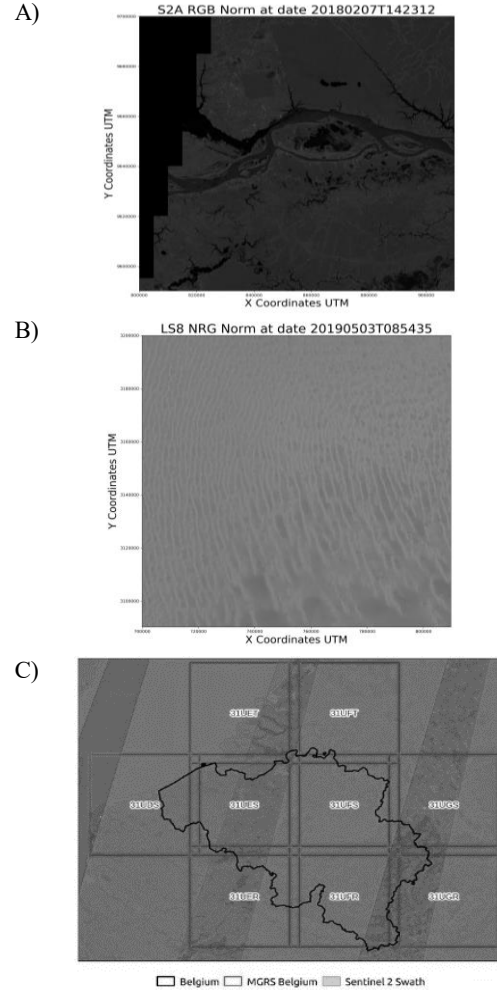


Figure 1. Study Area. A) Amazon, B) Sahara Desert C) Belgium

As shown in Figure 2, the two methods were implemented within the same configurable processing. Regarding the normalization step specifically, there are two major differences between the two methods. On one hand, Roy et al. (2016) provides a single set of coefficients called C-factor. On the other hand, the HABA provides per pixel values, estimated by using the NDVI parameter as proxy value. Furthermore, HABA requires as input a MGRS tile-dependent BRDF characterization. The BRDF calibration for those parameters is shown in the Equation (1). In order to evaluate the performance, we studied the impact of the

solar zenith angle (SZA) variation through the year over two homogeneous sites and d the impact of the view zenith angle (VZA) variation. For Belgium we analysed the impact of the swath overpass over all tiles using a 5-day time window and determining the absolute difference between different VZA over the study area.

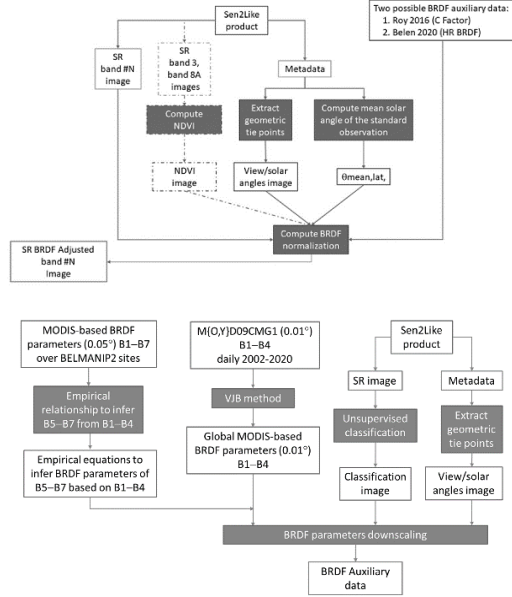


Figure 2. S2L BRDF correction workflow. Figure 2A) shows the correction on S2L parameter, and 2B) represent the disaggregation parameter in the BRDF parametrization for HABA method

In summary we performed two tests:

Test 1: Evaluation normalized and directional reflectance against the corresponding solar and view geometry (SZA & VZA) over two stable sites 20MRB (Amazon Forest) 34RGS (Libya Desert).

Test 2: Evaluate Absolute difference of adjacent Sentinel-2 orbits within a 5-day time window vs VZA variation over multiple tiles in Belgium through 2019.

### 2.1 Software used

The software used in this algorithm was Python version 3.6 based on the Sen2Like environment available in Github (<https://github.com/senbox-org/sen2like>).

### 2.2 Equations

$$R^N(\theta_{mean,lat}, 0, 0, \Delta) = R(\theta_{mean,lat}, v, \phi, \Delta) \cdot \frac{1 + V(\Delta)K_{vol}R^N(\theta_{mean,lat}, 0, 0) + R(\Delta)K_{geo}(\theta_{mean,lat}, 0, 0)}{1 + V(\Delta)K_{vol}(\theta_{mean,lat}, v, \phi) + R(\Delta)K_{geo}(\theta_{mean,lat}, v, \phi)} \quad (1)$$

Where:  $K_{vol}$ ,  $K_{geo}$  (Li et al., 1986, Maignan et al., 2004, Schaaf et al., 2002) are derived based on the pixel-based solar and view angles,

$V$  and  $R$  are the volume and the roughness parameters that describe the BRDF shape,

The  $\theta, v, \phi$  parameters are the solar/viewing, zenith and the relative azimuth,

The  $\Delta$  parameter is related to the spectral band taken into consideration for this calculation.

## 3. RESULTS

BRDF-normalized using C-Factor, HABA and directional reflectance versus solar zenith angle for each day of the year (DOY) considered in the time series (2019). Results are shown for (a) the red band, (b) the near infrared (NIR) band, (c), and (d) the SZA for each observation (Figure 3) over a stable surface (evergreen forest) from Amazon Forest, where the linear dependency from NIR is reduced from  $R^2$  0.43 (C-Factor) to 0.37 (HABA).

The figure 4 shows the directional (red), BRDF-normalized using C-Factor, HABA and surface reflectance versus the SZA in the Sahara. The SZA of this site shows a greater variation during the year (from 10 to 60 degrees) compared to the previous site (from 20 to 45 degrees). Despite this, the directional reflectance barely shows any dependency with the SZA. However, the C-Factor BRDF-normalized data shows a high dependency with higher values for high SZA and lower values for low SZA (increased  $R^2$  from directional red 0.08 to 0.42 and NIR 0.08 to 0.21). This is not the case when applies HABA, that shows more stable surface reflectance values (red  $R^2$  0.06 and NIR 0.04).

Regarding the BRDF processing, comparisons between different observations from adjacent swath overpasses to cover different observation geometries and illumination conditions over Belgium during 2019 were carried out (Figure 5). Figure 11 shows the absolute differences for bands B02, B03, B04, B8A, B11 and B12 regarding the directional reflectance (DIR) without BRDF correction, the C-factor correction (Roy et al., 2016) and the HABA correction applied for different view zenith angles (VZAs). The results were obtained from the comparison of 964 million cloud-free pixels for each date. The number of overlapping pixels varies between 9% and 36% for VZAs from  $0^\circ$  to  $2^\circ$  depending on the swath for each MGRS tile and the acquisition date. For VZAs between  $2^\circ$  to  $4^\circ$ , the percentage of overlapping data represented between 28% and 45% of the tiles. Additionally, for VZAs between  $4^\circ$  and  $6^\circ$ , the number of analyzed pixels represented between 13% and 25%. Finally, for the largest VZA observations ( $>6^\circ$ ), the analyzed pixels represent between 12% and 42%.

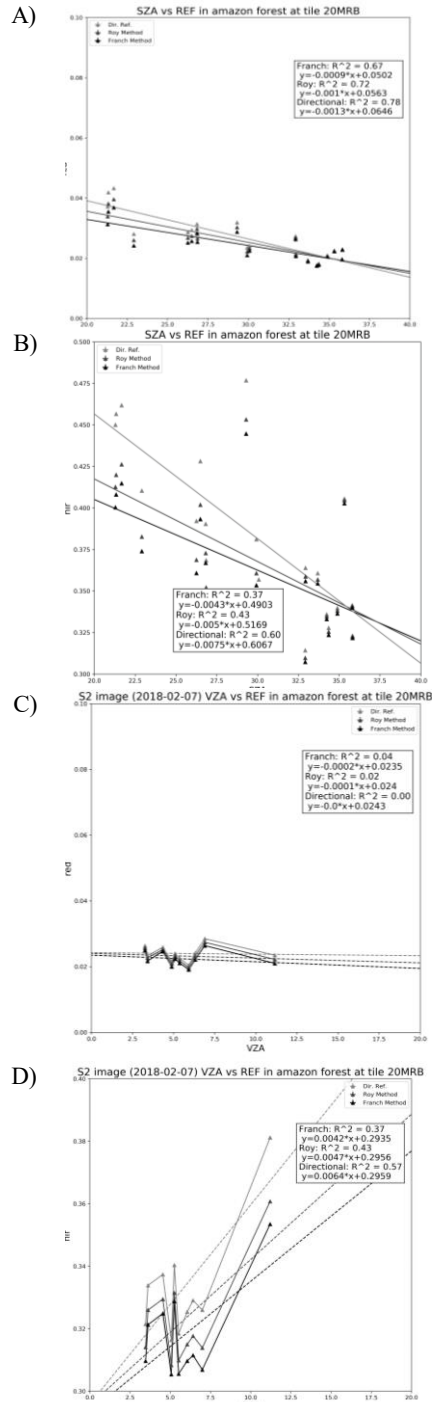


Figure 3. SZA and VZA evaluation over amazon forest

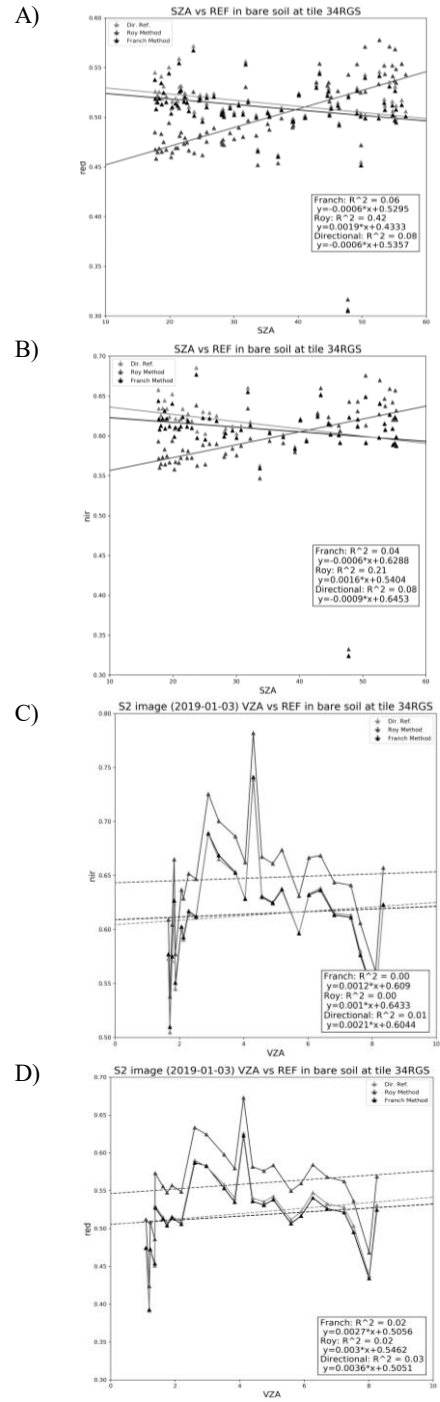


Figure 4. SZA and VZA evaluation over Sahara Desert. Table 4 summarizes the metrics obtained from the analysis, demonstrating that the HABA correction decreases the absolute difference up to 13% (in the SWIR bands) compared to the directional product.

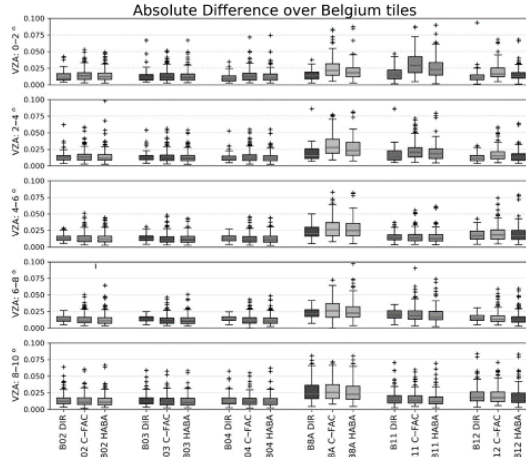


Figure 5. VZA evaluation over Belgium based on different threshold on 5-day window.

Band Method	Mean	Std	% Corr
B02 DIR	0.01297	0.01174	
C-FACTOR	0.01482	0.01402	14.24%
HABA	0.01213	0.01139	-6.45%
B03 DIR	0.01179	0.01207	
C-FACTOR	0.01397	0.01460	18.56%
HABA	0.01062	0.01185	-9.90%
B04 DIR	0.01144	0.01318	
C-FACTOR	0.01357	0.01552	18.58%
HABA	0.01051	0.01279	-8.19%
B8A DIR	0.01994	0.02038	
C-FACTOR	0.02431	0.02213	21.96%
HABA	0.01742	0.02002	-12.60%
B11 DIR	0.01424	0.01842	
C-FACTOR	0.01753	0.02012	23.03%
HABA	0.01243	0.01791	-12.74%
B12 DIR	0.02621	0.01686	
C-FACTOR	0.03134	0.01851	19.58%
HABA	0.02442	0.01614	-6.82%

Table 1. Summary of difference of S2L bands over Belgium MGRS tiles, considering a window of 1 to 5 days. Columns shown are the mean, standard deviation and correction percentage of NBAR algorithms. Positive and negative values represent increase and decrease of errors, respectively.

The separation of intervals of absolute difference in the boxplot (Figure 11) shows that the metrics in the visible spectrum (B02, B03, B04) yielded the lowest errors with a median under 0.01 and a low variability for all methods and the observation geometries. Besides, the impact of the BRDF correction in B8A, B11 and B12 depends on the observation geometry (VZA) and on the BRDF correction method. For VZA lower than 4°, the directional reflectance shows the lowest errors, while C-Factor and HABA show errors up 0.01. For VZA

over 6°, the C-Factor stills shows an overestimation in B8A reflectances, and HABA stabilizes the average value but still exhibits a higher variability than the directional reflectance. In the case of the SWIR bands (B11 and B12), the C-Factor and the HABA perform a better correction for the larger VZA acquisitions. The comparison shows that the HABA produced the lowest differences across all bands, while the C-factor correction showed larger discrepancies than the directional product for all VZA pixels aggregated.

#### 4. CONCLUSION

When applying the HABA method, the results show a decrease in the surface reflectance timeseries a decrease of the correlation coefficient with the SZA for the forest site, and little to no dependency on the desert site. In contrast, the C-Factor S2L BRDF normalization algorithm under-corrects the BRDF effects on the forests site, and increases the linear correlation on the desert site. In amazon forest is known that reflectance variation is mainly driven by directional effects on surface reflectance can be larger than the differences in reflectance along the year, and HABA performs well the correction over stable sites. In a mosaic crop area where exists unstable surfaces such as crop or deciduous forest areas mixed with stable surfaces (cities, evergreen forest and tree crops), all models performed a good performance, however C-factor tends to overcorrect on all bands. In future work, we can add this parameter and improve the quality assessment, evaluating the noise of time series with satellite azimuth data over areas in order to provide a new evaluation of linear dependencies on time series.

#### 5 REFERENCES

- Drusch, M.; Del Bello, U.; Carlier, S.; Colin, O.; Fernandez, V.; Gascon, F.; Hoersch, B.; Isola, C.; Laberinti, P.; Martimort, P.; et al. Sentinel-2: ESA's optical high-resolution mission for GMES operational services. *Remote Sens. Environ.* 2012, 120, 25–36.
- Franch, B.; Vermote, E.F.; Claverie, M. Intercomparison of Landsat albedo retrieval techniques and evaluation against in situ measurements across the US SURFRAD network. *Remote Sens. Environ.* 2014, 152.
- Franch, B.; Vermote, E.; Skakun, S.; Roger, J.-C.; Santamaria-Artigas, A.; Villaescusa-Nadal, J.L.; Masek, J. Toward Landsat and Sentinel-2 BRDF Normalization and Albedo Estimation: A Case Study in the Peruvian Amazon Forest. *Front. Earth Sci.* 2018, 6, 185.

- Gao, F.; He, T.; Masek, J.G.; Shuai, Y.; Schaaf, C.B.; Wang, Z. Angular Effects and Correction for Medium Resolution Sensors to Support Crop Monitoring. *IEEE J. Sel. Top. Appl. Earth Obs. Remote Sens.* 2014, 7, 4480–4489.
- Li, J.; Chen, B. Global Revisit Interval Analysis of Landsat-8 -9 and Sentinel-2A -2B Data for Terrestrial Monitoring. *Sensors* 2020, 20, 6631.
- Li, X.; Strahler, A.H. Geometric-optical bidirectional reflectance modeling of a conifer forest canopy. *IEEE Transactions on Geosci. Remote Sens.* 1986, GE-24, 906–919.
- Maignan, F.; Bréon, F.-M.; Lacaze, R. Bidirectional reflectance of Earth targets: Evaluation of analytical models using a large set of spaceborne measurements with emphasis on the Hot Spot. *Remote Sens. Environ.* 2004, 90, 210–220.
- Roy, D.P.; Zhang, H.K.; Ju, J.; Gomez-Dans, J.L.; Lewis, P.E.; Schaaf, C.B.; Sun, Q.; Li, J.; Huang, H.; Kovalsky, V. A general method to normalize Landsat reflectance data to nadir BRDF adjusted reflectance. *Remote Sens. Environ.* 2016, 176, 255–271.
- Roy, D.P.; Li, J.; Zhang, H.K.; Yan, L.; Huang, H.; Li, Z. Examination of Sentinel-2A multi-spectral instrument (MSI) reflectance anisotropy and the suitability of a general method to normalize MSI reflectance to nadir BRDF adjusted reflectance. *Remote Sens. Environ.* 2017, 199, 25–38.
- Schaaf, C.B.; Gao, F.; Strahler, A.H.; Lucht, W.; Li, X.; Tsang, T.; Strugnell, N.C.; Zhang, X.; Jin, Y.; Muller, J.-P.; et al. First operational BRDF, albedo nadir reflectance products from MODIS. *Remote Sens. Environ.* 2002, 83, 135–148.
- Teillet, P.M.; Fedosejevs, G.; Thome, K.J.; Barker, J.L. Impacts of spectral band difference effects on radiometric cross-calibration between satellite sensors in the solar-reflective spectral domain. *Remote Sens. Environ.* 2007, 110, 393–409.
- Vermote, E.; Justice, C.O.; Bréon, F.M. Towards a generalized approach for correction of the BRDF effect in MODIS directional reflectances. *IEEE Trans. Geosci. Remote Sens.* 2008, 47, 898–908.

# Assessing and improving the consistency between the AVHRR/Metop and SEVIRI/MSG vegetation products

Francisco Javier García-Haro<sup>\*1</sup>, Manuel Campos-Taberner<sup>1</sup>, Beatriz Martínez<sup>1</sup>, Sergio Sánchez-Ruíz<sup>1</sup>, María Amparo Gilabert<sup>1</sup>, Jorge Sánchez-Zapero<sup>2</sup>, Fernando Camacho<sup>2</sup>, Enrique Martínez-Sánchez<sup>2</sup>

<sup>1</sup>*Environmental Remote Sensing Group (UV-ERS), Earth Physics and Thermodynamics Department, Faculty of Physics, Universitat de València, Dr. Moliner 50, 46100 Burjassot, Spain.*

<sup>2</sup>*EOLAB, Paterna. Valencia, Spain.*

<sup>\*</sup>j.garcia.haro@uv.es

**ABSTRACT** - The EUMETSAT Satellite Application Facility on Land Surface Analysis (LSA-SAF) aims to be a Leading Centre for retrieval of information on Land Surfaces from Remote Sensing data. All LSA SAF products have been classified as essential and are distributed free of charge from the LSA SAF web page (<https://landsaf.ipma.pt/en>). Currently the LSA-SAF generates two operational lines of LSA SAF vegetation products. Unlike the approach to produce SEVIRI/MSG, which relies on stochastic spectral mixture and statistic methods, the EPS algorithm relies on a hybrid approach that blends the generalization capabilities offered by physical radiative transfer models with the accuracy and computational efficiency of machine learning methods. This work assesses the consistency among the two suites of LSA-SAF vegetation products and proposes methods to improve their consistency. Results demonstrate that these differences can be reduced through the adaptation of the EPS algorithm on SEVIRI/MSG data. This work will contribute to enhance the consistency among derived vegetation parameters, which is a priority task previous to the adaptation of the current algorithms to the new processing chains of future EUMETSAT sensors.

## 1 INTRODUCTION

The EUMETSAT Satellite Application Facility on Land Surface Analysis (LSA-SAF) aims to be a Leading Centre for retrieval of information on Land Surfaces from Remote Sensing data, with emphasis on EUMETSAT Satellites. The LSA-SAF provides near-real-time and offline products and user support for a wide range of land surface variables. All LSA SAF products are distributed according with EUMETSAT data policy and have been classified as essential and are distributed free of charge from the LSA SAF web page (<https://landsaf.ipma.pt/en>). Currently the LSA-SAF generates two operational lines of LSA SAF vegetation products.

### 1.1 The SEVIRI/MSG products

Firstly, a suite of product (FVC, LAI, FAPAR, GPP) derived from the geostationary SEVIRI (Spinning Enhanced Visible and Infrared Imager) on board MSG (Meteosat Second Generation) 1-4 (Meteosat 8-11) (see examples in figure 1). García-Haro et al. (2019) describes the algorithms and provide technical details about the products, including potential applications.

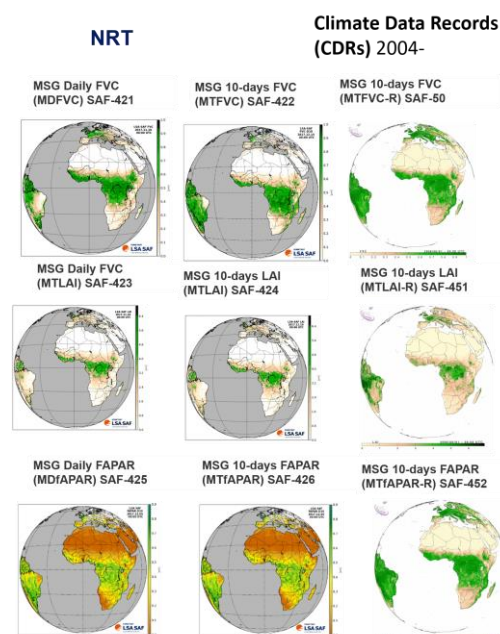


Figure 1. Examples of NRT and CDR MSG vegetation products along with their respective identifiers.



These products are generated and disseminated in Near-Real-Time (NRT) with a time lag of about six hours at two resolutions (daily and 10-day) over the geostationary Meteosat disk, covering Europe, Africa, the Middle East and parts of South America. The algorithms were reprocessed to generate the full archive of Climate Data Records (CDRs) for 10-days vegetation since 2004 onwards.

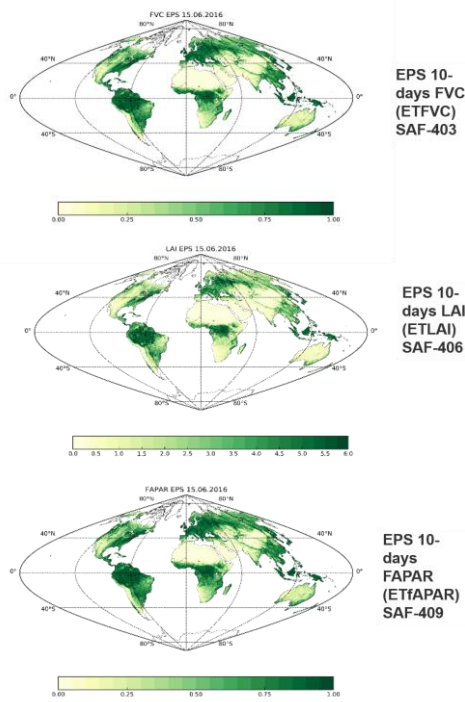


Figure 2. AVHRR/Metop FVC (top), LAI (middle) and FAPAR (bottom) LSA SAF product corresponding to the 15th of June 2016.

## 1.2 The AVHRR/Metop products

Secondly, a suite of global FVC, LAI and FAPAR vegetation products based on data from the AVHRR sensor on board MetOp-A, B and C satellites forming the EUMETSAT Polar System (EPS) is also disseminated. Unlike the approach to produce SEVIRI/MSG, which relies on stochastic spectral mixture and statistic methods, the EPS algorithm relies on a hybrid approach that blends the generalization capabilities offered by physical radiative transfer models with the accuracy and computational efficiency of machine learning methods. The 10-day vegetation products are level 3 full globe rectified images in sinusoidal projection, with a resolution of

1.1 km x 1.1 km and. The algorithms and practical information about the products characteristics are provided in García-Haro et al. (2018). The LSA-SAF plans to release a CDR of FVC, LAI, FAPAR EPS products (2007-present) that correspond to a back-processing of existing for NRT/operational products using the most recent algorithm version.

The LSA-SAF vegetation products are routinely validated through comparison with in situ measurements inter-comparison with other satellite derived vegetation products. The validation studies have revealed overall statistical good results compared with reference products (e.g. PROBA-V and MODIS) over a network of sites (García-Haro et al. 2018; Campos-Taberner et al. 2018).

The families of SEVIRI/MSG and AVHRR/Metop LSA SAF vegetation products are disseminated as a separate file coded in HDF5 format signed 16-bit integer variable, and include additional datasets and metadata attributes. Additional datasets include an estimate of the uncertainty assigned at each pixel and quality flag information to identify unreliable observations.

## 2 COMPARISON BETWEEN THE FAMILIES OF LSA SAF PRODUCTS

This work assesses the consistency among the two suites of LSA-SAF vegetation products and proposes methods to improve their consistency. A representative example of these differences is depicted in figure 3.

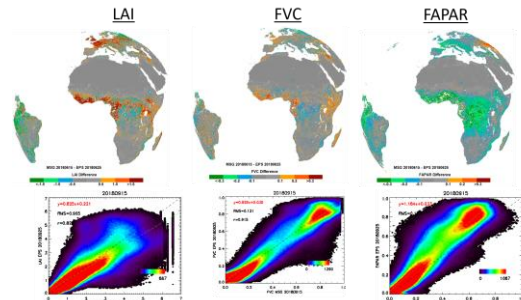


Figure 3. Difference maps and scatterplots between the actual MSG and EPS products corresponding to June 2018. To enable the comparison, EPS products were reprojected to the MSG grid.

While differences are not very considerable for FVC and LAI, both FAPAR products are significantly biased in forest regions showing MSG a clear negative bias regarding EPS. Although inputs of MSG and EPS algorithms are similar (i.e. atmospherically corrected cloud-cleared k0 BRDF product at three channels: red, NIR, MIR), discrepancies exist due to various spatial and temporal resolutions, processing lines and

differences in the algorithms used to retrieve both the BRDF parameters and the vegetation products. For example, the approach to retrieve SEVIRI/MSG vegetation products relies on stochastic spectral mixture and statistic methods. The FAPAR product presents a lower quality because it uses as input the three BRDF parameters ( $k_0$ ,  $k_1$ ,  $k_2$ ), with  $k_2$  presenting large uncertainties and noisy profiles on a short time scale, mainly in Western Africa. Conversely, the EPS algorithm jointly retrieves the suite of vegetation parameters using a hybrid approach that blends the generalization capabilities offered by physical radiative transfer models with the accuracy and computational efficiency of machine learning methods.

### 3 IMPROVING THE CONSISTENCY BETWEEN LSA SAF PRODUCTS

We propose a method to improve the consistency, which consists in the adaptation of the EPS algorithm on SEVIRI/MSG data. A synthetic database was thus generated using PROSAIL, considering diversity of vegetation types and soil background that can be found the MSG disk and taking into account the spectral wavebands of SEVIRI sensor. The MSG-like observations derived using this prototype were then compared with the actual observations of EPS (figure 4) and MSG (figure 5).

This comparison exercise shows an improved in the consistency regarding the LSA SAF. It should be clarified that the main source of differences between the new MSG prototype versus actual MSG values (figure 5) is that both products rely on different retrieval algorithms, whereas the differences versus EPS values (figure 4) are mainly due to the differences in the input, i.e. differences in the EPS and MSG BRDF algorithms (Geiger et al. 2016). This explains the considerable improvement in the consistency between LSA SAF FAPAR products in figure 4.

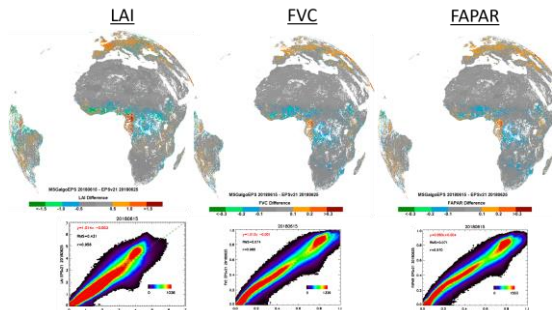


Figure 4. Difference maps and scatterplots between the EPS products and MSG prototyped using the EPS algorithm. Results correspond to June 2018. To enable the comparison, EPS products were reprojected to the MSG grid.

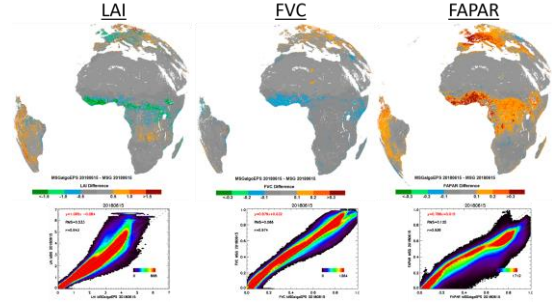


Figure 5. Difference maps and scatterplots between the actual MSG products and MSG prototyped using the EPS algorithm. Results correspond to June 2018.

### 4. CONCLUDING REMARKS

Currently the LSA-SAF generates two operational lines of LSA SAF NRT vegetation products. The algorithms were reprocessed to generate the full archive of Climate Data Records for 10-days vegetation products, offering nineteen years of homogeneous time series required for climate and environmental applications. The high frequency and good temporal continuity of SEVIRI products addresses the needs of near-real-time users and are also suitable for long-term monitoring of land surface variables. By its part, the EPS products provide global coverage and a good spatial completeness and temporal continuity in the tropical, subtropical and warm temperate regions, addressing deficiencies in current operational products over cloudy areas.

LSA-SAF has also developed recently two new products, SEVIRI/MSG GPP (Martínez et al. 2018; 2020) and AVHRR/Metop CWC (García-Haro et al. 2020). The future generation of new LSA-SAF products derived from the future Meteosat Third Generation (MTG) and EPS second generation (EPS-SG) satellites, with higher spatial and spectral resolution, will guarantee the continuity of the service.

This work has addressed the existing differences between the LSA SAF vegetation products derived from geostationary SEVIRI/MSG and polar orbit AVHRR/Metop LSA SAF vegetation products, which mainly affect FAPAR product, mainly due to inconsistencies in the retrieval algorithms. Results demonstrate that the adaptation of the EPS algorithm on MSG can reduce such differences. The proposed method will contribute to enhance the consistency among derived vegetation parameters, which is a priority task previous to the adaptation of the current algorithms to the new processing chains of future EUMETSAT sensors (FCI/MTG, VII/EPS-SG, and 3MI/EPS-SG) to ensure service continuity.



## ACKNOWLEDGMENTS

This work received funding support of LSA-SAF (EUMETSAT) and ESCENARIOS (CGL2016-75239-R) projects.

## REFERENCES

- García-Haro, F. J., Campos-Taberner, M., Muñoz-Marí, J., Laparra, V., Camacho, F., Sánchez-Zapero, J., Camps-Valls, G. 2018. Derivation of global vegetation biophysical parameters from EUMETSAT Polar System. *ISPRS Journal of Photogrammetry and Remote Sensing*, **139**, 57-74.
- García-Haro, F. J., Camacho, F., Martínez, B., Campos-Taberner, M., Fuster, B., Sánchez-Zapero, J., & Gilabert, M. A., 2019. Climate data records of vegetation variables from geostationary SEVIRI/MSG data: products, algorithms and applications. *Remote Sensing*, **11**(18), 2103
- García-Haro, F.J., Campos-Taberner, M., Moreno, A., Tagesson, T. Camacho, F. Martínez, B., Sánchez, S., Piles, M., Camps-Valls, G., Yebra, M., Gilabert, M.A., 2020. A global Canopy Water Content product from AVHRR/Metop. *ISPRS Journal of Photogrammetry and Remote Sensing*, **162**: 77-93.
- Geiger, B., Carrer, D., Hautecoeur, O., Franchistéguy, L., Roujean, J.-L., Catherine Meurey, X. C., Jacob, G., 2016. Algorithm Theoretical Basis Document (ATBD). Land Surface Albedo PRODUCTS: LSA-103 (ETAL). Retrieved from <https://landsaf.ipma.pt/GetDocument.do?id=641>.
- Campos-Taberner, M., García-Haro, F.J., Busetto, L., Ranghetti, L., Martínez, B., Gilabert, M.A., Camps-Valls, G., Camacho, F., Boschetti, M., 2018. A Critical Comparison of Remote Sensing Leaf Area Index Estimates over Rice-Cultivated Areas: From Sentinel-2 and Landsat-7/8 to MODIS, GEOV1 and EUMETSAT Polar System. *Remote Sensing*, **10**, 763.
- Martínez, B., Sanchez-Ruiz, S., Gilabert, M. A., Moreno, A., Campos-Taberner, M., García-Haro, F. J., Trigo, I.F., Aurela, M., Brümmer, C., Carrara, A., De Ligne, A., Gianelle, D., Grünwald, T., Limousin, J.M., Lohila, A., Mammarella, I., Sottocornola, M., Steinbrecher, R., Tagesson, T., 2018. Retrieval of daily gross primary production over Europe and Africa from an ensemble of SEVIRI/MSG products. *International journal of applied earth observation and geoinformation*, **65**, 124–136.
- Martínez, B.; Gilabert, M.A.; Sánchez-Ruiz, S., Campos-Taberner, M.C., García-Haro, F.J., Brümmer, C., Carrara, A., Feig, G., Grünwald, T., Mammarella, I., Tagesson, T, 2020. Evaluation of the LSA-SAF Gross Primary Production product derived from SEVIRI/MSG data (MGPP). *ISPRS Journal of Photogrammetry and Remote Sensing*, **129**:220-236.
- Trigo, I.F.; Dacamara, C.C.; Viterbo, P.; Roujean, J.-L.; Olesen, F.; Barroso, C., Camacho-de-Coca, F., Carrer, D., Freitas, S.C., García-Haro, F.J., B. Geiger, F. Gellens-Meulenberghs, N. Ghilain, J. Meliá, L. Pessanha, N. Siljamo, A. Arboleda, 2011, The Satellite Application Facility for Land Surface Analysis. *International Journal of Remote Sensing*, **32**, 2725–2744.

# Carbon fluxes estimation combining SEVIRI/MSG products, machine learning and in situ data

Manuel Campos-Taberner\*, Beatriz Martínez, Sergio Sánchez-Ruíz, Francisco Javier García-Haro<sup>1</sup>, María Amparo Gilabert

*Environmental Remote Sensing Group (UV-ERS), Earth Physics and Thermodynamics Department, Faculty of Physics, Universitat de València, Dr. Moliner 50, 46100 Burjassot, Spain.*

[\\*manuel.campos@uv.es](mailto:*manuel.campos@uv.es)

**ABSTRACT-** *The increasing number of EC towers distributed along the planet fosters the application of statistical regression approaches (machine learning) for carbon fluxes estimation. The Satellite Application Facility for Land Surface Analysis (LSA SAF) aims to take full advantage of EUMETSAT remotely sensed data to measure land surface variables. Among others, LSA-SAF provides products of downward radiation fluxes, land surface vegetation parameters, surface temperature, and evapotranspiration from observations acquired by the Spinning Enhanced Visible and InfraRed Imager (SEVIRI) on board the Meteosat Second Generation (MSG). This work aims at assessing the feasibility of estimating CO<sub>2</sub> fluxes such as the gross primary production (GPP), net ecosystem exchange (NEE), and ecosystem respiration (RESP) blending SEVIRI/MSG and EC data by means of machine learning methods. An ensemble of SEVIRI/MSG products were used as inputs for the model: Fraction of Vegetation Cover (FVC), Leaf Area Index (LAI), Fraction of Absorbed Photosynthetically Active Radiation (FAPAR), Downward Surface Shortwave Flux (DIDSSF), Evapotranspiration (DMET), Reference evapotranspiration (METREF), Land Surface Temperature (MLST), and the BRDF k0 parameter in the RED, NIR, and MIR SEVIRI/MSG bands. In addition, CO<sub>2</sub> fluxes from seven European EC towers were selected for pairing in situ data with the SEVIRI/MSG observations during the 2015-2019 period. Several machine learning regression methods were used for comparison including tree models (decision, bagging, boosting, and random forests), neural networks, and kernel methods (support vector regression, kernel ridge regression, and Gaussian process regression). The results show that the machine learning methods provide accurate and consistent estimates among them. The best performance is found in the case of random forests, in which correlations with GPP, NEE, and RESP reached 0.85, 0.61, and 0.89, respectively. These results encourage the use of data-driven approaches jointly with remote sensing data for carbon fluxes estimation.*

## 1 INTRODUCTION

The characterization of carbon exchanges between biosphere and atmosphere requires detailed information on both spatial and temporal behaviours of CO<sub>2</sub> fluxes. The assessment of these carbon fluxes is key to enhance our knowledge regarding the Earth's climate system modelling and understanding. Ground observations can be acquired by eddy-covariance (EC) towers, which are able to estimate CO<sub>2</sub> net exchanges at very high temporal resolutions. EC measure the net ecosystem exchange (NEE), that is the net balance between two gross CO<sub>2</sub> fluxes: the gross primary production (GPP), which accounts for the CO<sub>2</sub> uptake from atmosphere by photosynthesis, and the CO<sub>2</sub> released in the atmosphere by ecosystem respiration (RESP). EC data are available around the planet in multiple regional networks and initiatives such as the Integrated Carbon Observation System (ICOS) (<https://www.icos-cp.eu/>), the National Ecological

Observatory Network (NEON) (Keller, 2008), AmeriFlux (Novick et al., 2018), and Fluxnet (Pastorello et al., 2020).

Upscaling EC measurements from tower footprint to regional and global scales to better understand their spatial temporal dynamics. This can be achieved by combining EC data and remote sensing variables (Jung et al., 2020) using machine learning (ML) approaches. Statistical ML regression algorithms are able to generate adaptive and robust relationships among the predictors (remote sensing observations) and the response variables (GPP, NEE, and RESP). These algorithms can cope with the nonlinearity of the functional dependence between the CO<sub>2</sub> fluxes and some of the remote sensing signals. They are suitable for operational applications since are very fast to apply after the training (Campos-Taberner et al, 2016). There is a wide variety of machine learning models for regression and function approximation. Among them the most widely used belong to the families of tree

models, neural networks (shallow and deep learning), and kernel methods. Deep learning approaches usually outperform shallow ML; however, the understanding of these techniques is limited (Campos-Taberner et al., 2020).

This work aims at assessing the feasibility of estimating CO<sub>2</sub> fluxes (GPP, NEE, and RESP) by means of ML approaches using SEVIRI/MSG and EC data in the framework of the Satellite Application Facility on Land Surface Analysis (LSA SAF) (García-Haro et al., 2021).

## 2 MATERIALS

### 2.1 Eddy-covariance data and sites

In this work, we used daily data from seven ICOS EC towers located within the extension of the MSG/SEVIRI disk during the 2015-2019 period. Table 1 summarizes the main characteristics of the EC sites used in this study.

Table 1. EC sites.

Name	Code	Lat /long	Biome
Majadas del Tietar (South)	ES-LM2	39.93 / -5.77	SAV
Klingenberg	DE-Kli	50.89 / 13.52	CRO
Grillenburg	DE-Gri	50.95 / 13.51	GRA
Tharandt	DE-Tha	50.96 / 13.56	ENF
Gebesee	DE-Geb	51.09 / 10.91	CRO
Hyttiala	FI-Hyy	61.84 / 24.29	ENF
Monte Bondone	IT-MBo	46.01 / 11.04	GRA

### 2.2 Remote sensing data

A set of daily SEVIRI/MSG products were used as inputs for the regression algorithms: Fraction of Vegetation Cover (MDFVC), Leaf Area Index (MDLAI), Fraction of Absorbed Photosynthetically Active Radiation (MDfAPAR) (García-Haro et al., 2019), Downward Surface Shortwave Flux (DIDSSF) (LSA SAF, 2012), Evapotranspiration (DMET) and Reference evapotranspiration (METREF) (LSA SAF Team, 2016), Land Surface Temperature (MLST) (Trigo et al., 2009). In addition, an internal LSA SAF products were also used as predictors: the  $k_0$  parameter of the bidirectional reflectance distribution function (BRDF) in the RED, NIR, and MIR SEVIRI/MSG bands, respectively.

## 3 RETRIEVAL METHODOLOGY

For both *in situ* and remote sensing data only best quality data were used according with their quality flag. Several regression algorithms were built using the data set composed by the EC data and the

corresponding SEVIRI/MSG products (70% for training and 30% for validation). For instance, both single and ensembles of models based on decision trees were used. For the ensembles, different techniques such as bagging, boosting, and random forest (Belgiu and Drăguț, 2016) were used. In addition, neural networks, and kernel methods (Johnson et al., 2020) including support vector regression (SVR), kernel ridge regression (KRR), and Gaussian process regression (GPR) were also tested.

## 4 RESULTS

Time series of GPP, NEE, and RESP retrievals were obtained using independently all the algorithms. The time series correspond to the pixel where every EC tower is located in the MSG disk. The mean error (ME), root mean squared error (RMSE), mean absolute error (MAE), and the Pearson's coefficient of correlation (R) were computed for every case over the test set to assess the accuracy of the retrievals. Tables 2, 3 and 4 shows the accuracy metrics for every regression algorithm and estimated flux.

Table 2. Accuracy metrics for GPP.

Algorithm	ME	RMSE	MAE	R
RF	0.02	1.89	1.12	0.85
GPR	0.02	1.91	1.12	0.83
KRR	0.03	1.92	1.19	0.82
Boosting	0.03	1.99	1.20	0.80
Bagging	0.03	1.98	1.19	0.80
NN	0.05	2.05	1.29	0.75
Tree	0.05	2.25	1.28	0.74

Table 3. Accuracy metrics for NEE.

Algorithm	ME	RMSE	MAE	R
RF	0.03	1.37	0.76	0.61
GPR	0.03	1.37	0.77	0.60
KRR	0.03	1.39	0.77	0.61
Boosting	0.05	1.44	0.78	0.58
Bagging	0.05	1.45	0.78	0.55
NN	0.06	1.50	0.80	0.50
Tree	0.09	1.75	0.98	0.45

Table 4. Accuracy metrics for RESP.

Algorithm	ME	RMSE	MAE	R
RF	0.03	1.19	0.71	0.89
GPR	0.04	1.21	0.71	0.88
KRR	0.04	1.21	0.72	0.87
Boosting	0.05	1.23	0.75	0.81
Bagging	0.05	1.22	0.75	0.81
NN	0.05	1.35	0.77	0.75
Tree	0.07	1.40	0.81	0.69

RF outperformed the rest of the methods in all cases and metrics as shown in tables 1, 2 and 3. Figures 1, 2, and 3 show the scatter plots of the predicted fluxes with the RF over the validation set never used during the training.

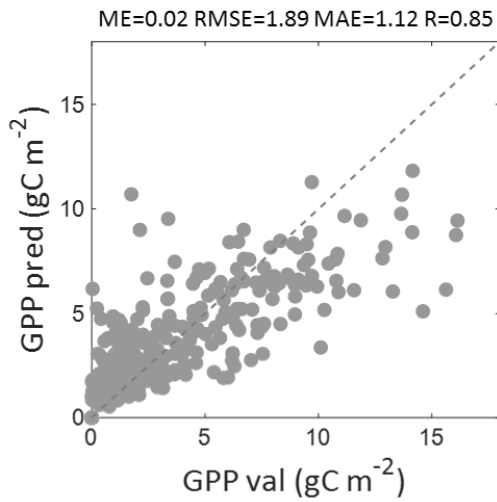


Figure 1. Scatter plot and accuracy metrics of estimated SEVIRI/MSG GPP values versus EC GPP.

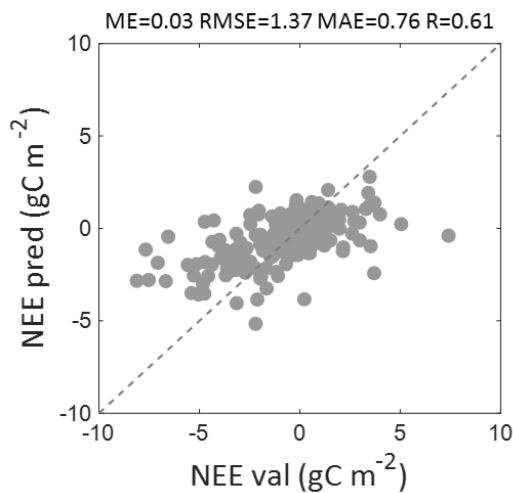


Figure 2. Scatter plot and accuracy metrics of estimated SEVIRI/MSG NEE values versus EC NEE.

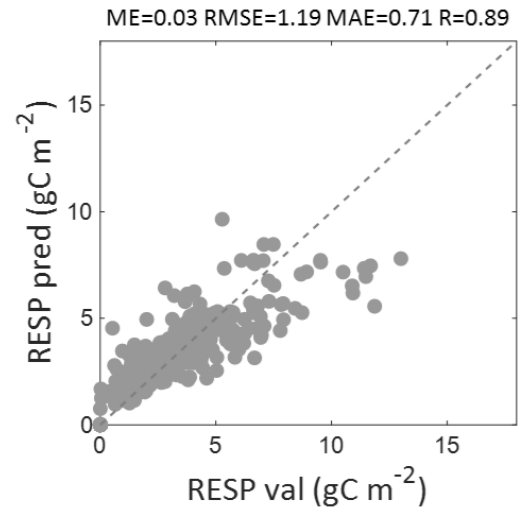


Figure 3. Scatter plot and accuracy metrics of estimated SEVIRI/MSG RESP values versus EC RESP.

In addition, RF provides the relevance of every predictor in the training (see figure 4). The DIDSSF is identified as the most relevant predictor, whereas de BRDF  $k_0$  parameter of the MIR band is the least relevant.

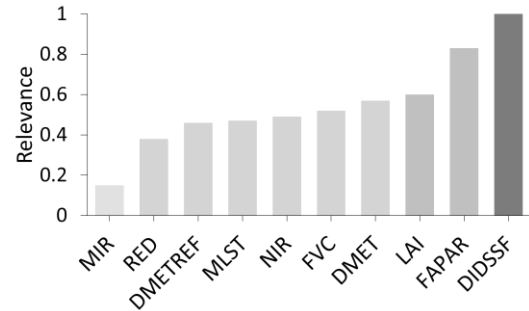


Figure 4. Relevance of the predictors (normalized to the maximum) as provided by the RF.

#### ACKNOWLEDGMENTS

This research was supported by the ECCE EO project (Grant PID2020-118036RB-I00 funded by MCIN/AEI/ 10.13039/501100011033 and by “ERDF A way of making Europe”).

## REFERENCES

- Belgiu, M., & Drăguț, L. (2016). Random forest in remote sensing: A review of applications and future directions. *ISPRS journal of photogrammetry and remote sensing*, 114, 24–31.
- Campos-Taberner, M., García-Haro, F. J., Camps-Valls, G., Grau-Muedra, G., Nutini, F., Crema, A., Boschetti, M. (2016). Multitemporal and multiresolution leaf area index retrieval for operational local rice crop monitoring. *Remote Sensing of Environment*, 187, 102–118.
- Campos-Taberner, M., García-Haro, F. J., Martínez, B., Izquierdo-Verdiguier, E., Atzberger, C., Camps-Valls, G., & Gilabert, M. A. (2020). Understanding deep learning in land use classification based on Sentinel-2 time series. *Scientific reports*, 10(1), 1–12.
- García-Haro, F. J., Camacho, F., Martínez, B., Campos-Taberner, M., Fuster, B., Sánchez-Zapero, J., Gilabert, M. A. (2019). Climate data records of vegetation variables from geostationary SEVIRI/MSG data: Products, algorithms and applications. *Remote Sensing*, 11(18), 2103.
- García-Haro, F. J., Campos-Taberner, M., Martínez, B., Sánchez-Ruiz, S., Camacho, F., & Gilabert, M. A. (2021, September). LSA SAF: a long-term service of vegetation variables for modelling terrestrial ecosystems at regional and global scales. In *Sensors, Systems, and Next-Generation Satellites XXV* (Vol. 11858, pp. 305-312). SPIE.
- LSA SAF Team. (2016). Algorithm Theoretical Basis Document for Reference Evapotranspiration (DMETREF): ATBD\_DMETREF, Product LSA-303.
- LSA SAF. (2012). Algorithm Theoretical Basis Document (ATBD) for Down-Welling Surface Shortwave Flux (DSSF). SAF/LAND/MF/ATBD\_DSSF/1.0
- Johnson, J. E., Laparra, V., Pérez-Suay, A., Mahecha, M. D., & Camps-Valls, G. (2020). Kernel methods and their derivatives: Concept and perspectives for the earth system sciences. *PloS one*, 15(10), e0235885.
- Jung, M., Schwalm, C., Migliavacca, M., Walther, S., Camps-Valls, G., Koirala, S., Reichstein, M. (2020). Scaling carbon fluxes from eddy covariance sites to globe: synthesis and evaluation of the FLUXCOM approach. *Biogeosciences*, 17(5), 1343–1365.
- Keller, M., Schimel, D. S., Hargrove, W. W., & Hoffman, F. M. (2008). A continental strategy for the National Ecological Observatory Network. *The Ecological Society of America*: 282–284.
- Novick, K. A., Biederman, J. A., Desai, A. R., Litvak, M. E., Moore, D. J., Scott, R. L., & Torn, M. S. (2018). The AmeriFlux network: A coalition of the willing. *Agricultural and Forest Meteorology*, 249, 444–456.
- Pastorello, G., Trotta, C., Canfora, E., Chu, H., Christianson, D., Cheah, Y. W., Law, B. (2020). The FLUXNET2015 dataset and the ONEFlux processing pipeline for eddy covariance data. *Scientific data*, 7(1), 1–27.
- Trigo, I., Freitas, S., Bioucas-Dias, J., Barroso, C., Monteiro, I., & Viterbo, P. (2009). Algorithm theoretical basis document for land surface temperature (LST). LSA-4 (MLST), 59

# Estimation of surface energy and CO<sub>2</sub> fluxes through remote sensing in a Juniper tree ecosystem at the National Park of Doñana

Pedro J. Gómez-Giráldez <sup>a1</sup>, Jordi Cristóbal <sup>b2</sup>, Héctor Nieto <sup>c3</sup>, Ricardo Díaz-Delgado <sup>a4</sup>

<sup>a</sup> Estación Biológica de Doñana (EBD-CSIC), C/ Americo Vespucio, s/n. 41092 Sevilla

<sup>b</sup> Programa de l'Ús Eficient de l'Aigua en l'Agricultura. IRTA, Fruitcentre, 25003, Lleida

<sup>c</sup> Instituto de Ciencias Agrarias (ICA-CSIC), C/ Serrano 115 bis, 28006 Madrid

<sup>1</sup> [pedro.gomez@ebd.csic.es](mailto:pedro.gomez@ebd.csic.es), <sup>2</sup> [jordi.cristobal@irta.cat](mailto:jordi.cristobal@irta.cat), <sup>3</sup> [hector.nieto@ica.csic.es](mailto:hector.nieto@ica.csic.es), <sup>4</sup> [ricardo.diaz@ebd.csic.es](mailto:ricardo.diaz@ebd.csic.es)

**ABSTRACT** Doñana National Park is located in the southwest of the Iberian Peninsula, with high heterogeneity ecosystems and where water scarcity is recurrent. In this study, we performed a first evaluation of the modeling of surface energy fluxes as well as carbon assimilation (GPP) with flux tower data. Surface energy fluxes were estimated through a two-source energy balance model (TSEB) while GPP was done through a LUE model. Both models used Terra/Aqua MODIS images during the period 2014-2015 in an experimental plot of Juniper woodlands (*Juniperus phoenicea*) in the Doñana Biological Reserve. TSEB yielded acceptable results, in the case of net radiation, latent heat, sensible heat and soil heat fluxes showing an average RMSE of 54, 47, 63 and 6 W·m<sup>-2</sup>, respectively. The LUE-model is based on the relationship between absorbed photosynthetically active radiation and its use by the plant defining a maximum value per species or plant functional types which is reduced by environmental conditions. We evaluated the LUE-model in two ways to reduce such maximum efficiency value: 1) by forcing it with meteorological variables; 2) by forcing it with both meteorological variables and a water stress index from TSEB evapotranspiration retrievals. Our assessment with flux data showed that although the application of the LUE with meteorological data had an acceptable error (~0.9 gC/m<sup>2</sup>), the use of the water stress index improved the results (0.7 gC/m<sup>2</sup>) due to a better fit in situations of scarcity of water.

## 1 INTRODUCTION

Monitoring of surface energy fluxes (net radiation, latent heat, sensible heat and soil heat fluxes) and CO<sub>2</sub> fluxes has important implications for global and regional climate modeling and the understanding of hydrological cycles, as well as for advising on environmental stress affecting agricultural and forest ecosystems. Remote sensing provides useful radiometric measurements to estimate these fluxes and to apply them in large areas in an economically viable way. Currently, a large part of the algorithms developed for the determination of energy and CO<sub>2</sub> fluxes have been developed and validated in crop areas (e.g. Padilla et al., 2012, Knipper et al., 2020), and their implementation in natural vegetation represents a major challenge for monitoring these variables and in improving the knowledge on water resources. This is particularly relevant in Mediterranean ecosystems due to its complexity including various layers of vegetation, low coverage and a great diversity of species. With this objective, the Singular Scientific and Technological Infrastructure of the Doñana Biological Reserve (ICTS-Doñana), has set up flux towers (Eddy Covariance systems, EC) to monitor the ecosystem functioning in 4 different ecosystems of the Doñana Natural Area (black juniper, shrubs wet and dry areas and marsh). Flux towers are an effective tool to quantify and validate

surface energy and carbon fluxes in natural land covers (Cristóbal et al., 2020).

This paper presents the first results and the assessment of the surface energy fluxes and CO<sub>2</sub> assimilation (gross primary production, GPP) models for the years 2014 and 2015 in a Juniper woodlands located at the Doñana Biological Reserve (RBD) using remote sensing MODIS products and flux towers.

## 2 METHODOLOGY

### 2.1 Study site and validation data

The flux tower, located at the RBD (lat: 36.99°, long: -6.51°) in the province of Huelva (Fig. 1), is a Juniper woodlands, with a vegetation cover of 50%, dominated by the black juniper (*Juniperus phoenicea* ssp. *turbinata*) and punctually accompanied by stone pine (*Pinus pinea*) and other Mediterranean shrub species.

The main instruments of the EC tower are installed at 7.5 m a.g.l (4 m above the juniper cover) and consist of all the necessary sensors to continuously measure the surface energy fluxes such as net radiation (R<sub>n</sub>), sensible heat (H), latent heat (LE), and soil heat fluxes (G) as well as carbon fluxes (NEE). The main sensors installed are a four-component radiometer, relative humidity and air temperature sensors, a 3D sonic anemometer, a water vapor and carbon dioxide open

path sensor, and soil moisture, temperature, and heat flux sensors. In addition, there are two radiometric temperature sensors on a juniper canopy and a bare soil (sandy soil).

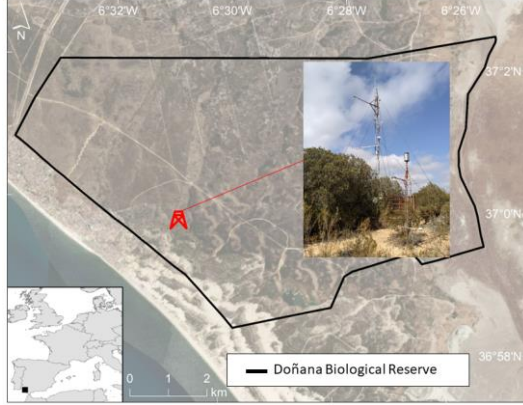


Figure 1. Location of the Juniper EC tower in the Doñana Biological Reserve.

## 2.2 Surface energy fluxes modeling with TSEB.

To estimate surface energy fluxes a Two-Source Energy Balance Model (TSEB) (Norman et al., 1995) was applied. This model is based on the partition of the radiometric temperature of the surface (Trad) in two components, soil ( $T_s$ ) and the canopy ( $T_c$ ) temperatures, through the fraction of vegetation cover observed by the thermal sensor given its angle of observation,  $f(\theta)$  (Eq. 1):

$$Trad = \{f(\theta)T_c^4 + (1 - f(\theta))T_s^4\}^{1/4} \quad (1)$$

With this information, TSEB evaluates the energy balance of the soil and the canopy separately, calculating the total energy fluxes and components, fulfilling the energy balance equation (Eq 2-6):

$$Rn_c = H_c + LE_c \quad (2)$$

$$Rn_s = H_s + LE_s + G \quad (3)$$

$$Rn = Rn_c + Rn_s \quad (4)$$

$$H = H_c + H_s \quad (5)$$

$$LE = LE_c + LE_s \quad (6)$$

where  $Rn$  is the net radiation,  $H$  the sensible heat,  $LE$  the latent heat and  $G$  the soil heat flux. The subscript  $c$  identifies the canopy fluxes and  $s$  the soil fluxes. All fluxes are measured in  $W \cdot m^{-2}$ .

Canopy and soil heat fluxes are evaluated by means of a temperature gradient through a series resistance model where  $T_c$ ,  $T_s$  and  $T_0$  (estimated aerodynamic temperature of the cover) are obtained. The extinction of  $Rn$  within the canopy ( $Rnc$ ) is approximated from the

Leaf Area Index (LAI), while  $G$  is set as a fraction (0.14) of the  $Rns$ . Through a modification of the Priestley-Taylor formulation (Priestley and Taylor, 1972), in which the estimation of the greenness fraction ( $fg$ ) is necessary, an initial estimate of the canopy transpiration ( $LEc$ ) is calculated, the which is iteratively reduced if signs of plant stress are detected in the soil-surface thermal component. Finally, the soil evaporation rate ( $LEs$ ) is calculated as a residual of the energy balance (Anderson et al., 2007).

This model was firstly applied at a local scale in order to calibrate it with EC data and later with remote sensing data for application at a regional scale. As input data for model calibration, we used meteorological data from the EC tower and the Trad derived from the MODIS LST product on board Terra and Aqua (MOD011/MYD011) at 1000 spatial resolution with a total of 96 and 109 images for 2014 and 2015. In the case of LAI, the MODIS product (MOD15A2) at 500 m spatial resolution was used, and for  $fg$  the NDVI and EVI indices at 500 m spatial resolution, derived from the surface reflectance products of MODIS (MOD09) according to Guzinski et al. (2013) and Cristóbal et al. (2020). Model assessment was carried out using EC data. Model agreement and error metrics were computed using the root mean square error (RMSE) and the determination coefficient ( $R^2$ ).

## 2.3 CO<sub>2</sub> assimilation by vegetation modeling.

CO<sub>2</sub> assimilation by vegetation (GPP), can be estimated by means of the Light Use Efficiency (LUE) models. These models relate the incident solar radiation with the photosynthetic activity of the plant through the LUE parameter ( $\epsilon$ ), which is the amount of biomass produced per unit of absorbed radiation. The GPP was estimated using an adaptation of the Monteith equation (1972) at daily scale and at 500 m spatial resolution:

$$GPP = FPAR \cdot PAR \cdot \epsilon \quad (7)$$

where GPP is measured in  $gC \cdot m^{-2}$ ,  $PAR$  ( $MJ \cdot m^{-2}$ ) is photosynthetically active radiation and  $FPAR$  (dimensionless) is the fraction of  $PAR$  absorbed by vegetation and  $\epsilon$  the LUE parameter ( $gC \cdot MJ^{-1}$ ).

The MODIS FPAR product (MCD15A3H) was used with a total of 157 images for the study period and was linearly interpolated to obtain daily values.

The  $PAR$  values were obtained from the flux tower radiation sensor, with a reduction factor of 0.48 according to Szeicz (1974).

For  $\epsilon$ , a maximum value of  $0.841 \text{ g C} \cdot \text{MJ}^{-1}$  was used ( $\epsilon_{max}$ ). This value was taken from Biome-Property-



Look-Up-Table (BPLUT) (Running y Zhao 2019) for open shrublands coverage, considered to be a fairly accurate estimate for ideal conditions of Juniper woodlands. This value were then decreased by two approaches:

1) Forced by meteorological variables (called from now on Meteo):  $\epsilon_{max}$  is modified according to the meteorological variables that reduce the efficiency of the plant, the minimum daily temperature (Tmin) and the vapor pressure deficit (VPD). In this approach, we fitted a scalar Tmin and VPD by means of simple linear functions between 0 and 1 derived from the daily values of Tmin and VPD (Fig. 2). These linear functions are obtained using threshold values, where the minimum and maximum values for Tmin are 0 and 1 of scalar Tmin (increasing function) respectively; and minimum and maximum value for VPD correspond to 1 and 0 values of scalar VPD (decreasing function) respectively

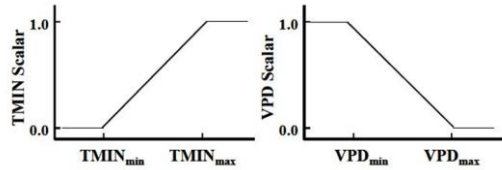


Figure 2 Scheme of linear equations for Meteo approach (Modified from Running y Zhao 2019).

Upper and lower threshold values were taken for both variables (-8 and 8.8 °C for Tmin; and 0.65 and 4.8 kPa for VPD). These values were also obtained from the BPLUT for open shrublands.

2) Forced by meteorological variables and a water stress index from TSEB evapotranspiration retrievals (called from now on WSI):  $\epsilon_{max}$  is reduced according to a water stress index between 0 to 1 (Eq. 8).

$$WSI = ETd/ETr \quad (8)$$

Where WSI is the water stress index (dimensionless), ETd is the daily evapotranspiration (mm) and ETr the evapotranspiration reference (mm).

The ETd was obtained by temporally upscaling instantaneous LE fluxes with solar radiation according to Cammalleri et al. (2014). ETr was estimated using FAO56 approximation (Allen et al 1998). Due to the non-linearity of the TSEB model, a shorter period of 141 days with ETd data was used, with no interpolation.

Results of the two LUE models were compared by calculating the RMSE (selection the same short period for both) where GPP was calculated as follows:

$$GPP = NEE - R_{eco} \quad (9)$$

where NEE is the net CO<sub>2</sub> exchange of the ecosystem obtained from the EC tower data and Reco is the respiration of the heterotrophic part of the ecosystem estimated using a flux partitioning algorithm (Lasslop et al., 2010) implemented in the package REdDyProc (Wutzler et al 2018).

### 3 RESULTS AND DISCUSSION

#### 3.1 TSEB model

Figure 3 shows the results obtained from the TSEB model vs. observed values. R<sup>2</sup> and RMSE values for instantaneous net radiation, latent heat, sensible heat flux and soil heat flux are shown in Table 1. TSEB evaluation results against EC data yielded similar results than those reported in other studies (Kalma et al., 2008), with average RMSE values for all fluxes below 50 W m<sup>-2</sup>. This RMSE value allows daily upscale LE fluxes with an accuracy of ca. 1 mm·day<sup>-1</sup>. However, we found an underestimation of the estimated energy fluxes (Figure 3). This may be due to the use of MODIS images of 1000 m spatial resolution and the heterogeneity of the cover within the pixel.

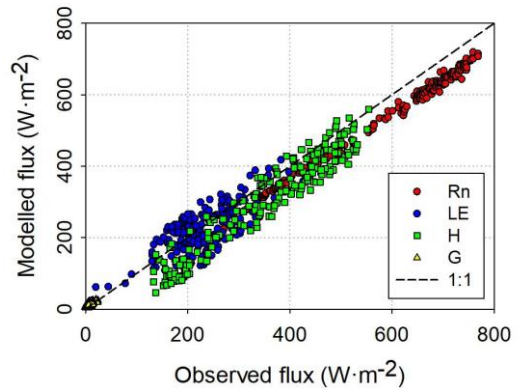


Figure 3. Modeled fluxes with TSEB vs Observed fluxes from EC tower.

Table 1. R<sup>2</sup> and RMSE between modeled and observed fluxes for the 204 images used.

Flux	R <sup>2</sup>	RMSE (W m <sup>-2</sup> )
Rn	0.99	54
LE	0.57	47
H	0.92	63
G	0.75	6



### 3.2 LUE model approaches.

Figure 4 shows the temporal evaluation of EC GPP and the two LUE model approaches during the study period. The  $R^2$  and RMSE are shown in Table 2.

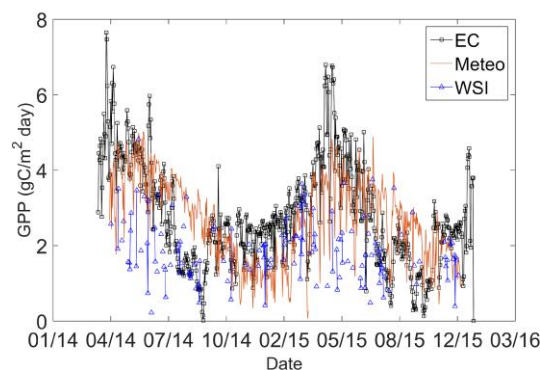


Figure 4. Temporal dynamics of GPP for EC and the two LUE-models.

The GPP values obtained using the LUE models were similar to those obtained for global scale studies (Gilabert et al., 2015). The RMSE obtained (Table 2) of  $0.9 \text{ g C m}^{-2} \text{ day}$  for Meteo and  $0.7$  for WSI were acceptable, although somewhat higher than those reported in natural Mediterranean ecosystems using more local scales (Gómez-Giraldez et al., 2018). On the other hand, the value of  $R^2$  obtained was low due to the overestimation of the model in the summer season for Meteo and an underestimation in the wet period for WSI.

Table 2.  $R^2$  and RMSE between modeled GPP from the two LUE-Models and observed GPP from EC. We show in brackets values for the coincident shorter time period of 141 days.

Approach	$R^2$	RMSE ( $\text{g C}^{-1} \text{ m}^{-2} \text{ day}$ )
Meteo	0.32 (0.26)	0.9 (0.85)
WSI	0.25	0.7

When results are compared for the shorter common period for both models of 141 days, results for Meteo are very similar and the WSI RMSE values are lower due to a better fit along the period of water scarcity. An example of the overestimation of Meteo can be seen in Figure 5, where both approaches are applied at regional scale on a summer day, where there is a elevated water stress in the study area.

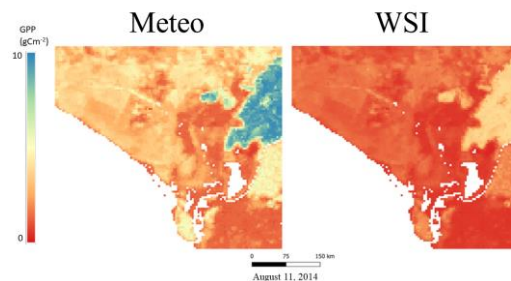


Figure 5. GPP maps for Meteo and WSI, August 11, 2014.

However, although WSI improves the RMSE, it shows a lower  $R^2$  value, mainly due to overall underestimation out of these periods of water scarcity. A better solution for this type of ecosystem would likely be a hybrid solution which uses the Meteo approach but including stress factors for drought periods which will be evaluated in further analysis.

### 4 CONCLUSIONS

The TSEB and LUE models yielded satisfactory results in terms of RMSE as a first approximation for estimating both surface energy and  $\text{CO}_2$  fluxes in a Juniper woodlands:

- 1- In the case of net radiation, latent heat, sensible heat and soil heat fluxes, evaluation results yielded an average RMSE of 54, 47, 63 and  $6 \text{ W} \cdot \text{m}^{-2}$ , respectively.
- 2- Application of the LUE with meteorological data also yielded acceptable results ( $0.9 \text{ gC} \cdot \text{m}^{-2}$ ). Finally, using the WSI improved the model results ( $0.7 \text{ gC} \cdot \text{m}^{-2}$ ) due to its best performance in water scarcity conditions.

Future studies will extend the time series in the juniper ecosystem and will extend to other ecosystems in the RBD to study the peculiarities of the different ecosystems present in the Doñana National Park, as well as the use of higher spatial resolution images.

### 5 ACKNOWLEDGMENTS

The SUMHAL project, which is financed by the Spanish Ministry of Science and Innovation, through the European Regional Development Funds (ERDF) [SUMHAL, LIFEWATCH-2019-09-CSIC-13, POPE 2014-2020]. Additional funds come from the project ET4Drough funded by the Spanish Ministry of Science and Innovation [PID2021-127345OR-C31]. Data from EC Towers and complementary sensors were kindly provided by ICTS-RBD (Doñana Biological Station, CSIC).

## 6 REFERENCES

- Allen, R.G.; Pereira, L.S.; Raes, D. and Smith, M. 1998. Crop Evapotranspiration-Guidelines for Computing Crop Water Requirements-FAO; *Irrigation and Drainage Paper 56*; FAO: Rome, Italy, 1998; Available online: <http://www.fao.org/3/x0490e/x0490e00.htm>
- Anderson, M.C., Kustas, W.P. and Norman, J.M. 2007. Upscaling Flux Observations from Local to Continental Scales Using Thermal Remote Sensing. *Agronomy Journal*, 99, 240-254
- Cristóbal J, Prakash A, Anderson MC, Kustas WP, Alfieri JG and Gens R. 2020. Surface Energy Flux Estimation in Two Boreal Settings in Alaska Using a Thermal-Based Remote Sensing Model. *Remote Sensing*, 12(24):4108.
- Gilabert, M.A., Moreno, A., Maselli, F., Martínez, B., Chiesi M., Sánchez-Ruiz, S., García-Haro, F.J., Pérez-Hoyos, A., Campos-Taberner, M., Pérez-Priego, O., Serrano-Ortiz, P. and Carrara, A. 2015. Daily GPP estimates in Mediterranean ecosystems by combining remote sensing and meteorological data. *ISPRS Journal of Photogrammetry and Remote Sensing*, 102, 184–197.
- Gómez-Giráldez, P.J., Carpintero, E., Ramos, M., Aguilar, C. and González-Dugo, M.P. 2018. Effect of the water stress on gross primary production modeling of a Mediterranean oak savanna ecosystem. *Proceedings of IAHS*, 95, 1–7.
- Guzinski, R., Andersson, M.C., Kustas, W.P., Nieto, H. and Sandholt, I. 2013. Using a thermal-based two source energy balance model with time-differencing to estimate surface energy fluxes with day–night MODIS observations. *Hydrology and Earth System Sciences*, 17, 2809–2825.
- Kalma, J.D., McVicar, T.R., McCabe and M.F. 2008. Estimating Land Surface Evaporation: A Review of Methods Using Remotely Sensed Surface Temperature Data. *Surveys in Geophysics*, 29, 421-469
- Knipper, K.R., Kustas, W.P., Anderson, M.C., Nieto, H., Alfieri, J.G., Prueger, J.H., Hain, C.R., Gao, F., McKee, L.G., Mar Alsina, M. and Sanchez, L. 2020. Using high-spatiotemporal thermal satellite ET retrievals to monitor water use over California vineyards of different climate, vine variety and trellis design. *Agricultural Water Management*, 241, 106361.
- Lasslop, G., Reichstein, M., Papale, D., Richardson, A., Arneth, A., Barr, A., Stoy, P. and Wohlfahrt, G. 2010. Separation of net ecosystem exchange into assimilation and respiration using a light response curve approach: critical issues and global evaluation. *Global Change Biology*, 16, 187-208.
- Monteith, J.L. 1972. Solar radiation and productivity in tropical ecosystems. *Journal of Applied Ecology* 9:747–766.
- Norman, J.M., Kustas, W.P. and Humes, K.S. 1995. Source Approach for Estimating Soil and Vegetation Energy Fluxes in Observations of Directional Radiometric Surface-Temperature. *Agricultural and Forest Meteorology*, 77, 263-293
- Padilla, F.L.M., Maas, S.J., González-Dugo, M.P., Mansilla, F., Rajan, N., Gavilán, P. and Domínguez, J. 2012. Monitoring regional wheat yield in Southern Spain using the GRAMI Model and satellite imagery. *Field Crops Research*. 130, 145-154.
- Priestley, C.H.B. and Taylor, R.J. 1972. On the assessment of surface heat flux and evaporation using large-scale parameters. *Monthly Weather Review*, 100, 81-92
- Running, S.W. and Zhao, M. 2019. *User's Guide Daily GPP and Annual NPP (MOD17A2H/A3H) and Year-end GapFilled (MOD17A2HGF/A3HGF) Products NASA Earth Observing System MODIS Land Algorithm (For Collection 6)*. <https://modis-land.gsfc.nasa.gov>
- Szeicz, G., 1974. Solar radiation for plant growth. *Journal of Applied Ecology*. 11, 617-637.
- Wutzler T., Lucas-Moffat A., Migliavacca M., Knauer J., Sickel K., Sigut, Menzer O. and Reichstein M. 2018. Basic and extensible post-processing of eddy covariance flux data with REddyProc. *Biogeosciences*, 15, 5015–5030.

## Evaluation of an operational multiple resolution evapotranspiration algorithms over a temperate basin on Chiloé Island mounted on a Web-GIS platform

Moletto-Lobos I.<sup>1,2</sup>, Mattar C.<sup>2</sup>, Acuña-Ruz T.<sup>2</sup>, Amézquita L.<sup>2</sup>, Sanyer W.<sup>3</sup>, Muñoz R.<sup>3</sup>, Áviles F.<sup>4</sup>, Bono, L.<sup>4</sup>, Garate, P.<sup>4</sup>, Olea-Encina, P.<sup>4</sup>, Troncoso, R.<sup>4</sup>, Arce, S.<sup>4</sup>, Neira H.<sup>4</sup>, *Global Change Unit, Image Processing Laboratory, Universitat de València, 46980 Valencia, Spain.*

*Laboratory for Analysis of the Biosphere (LAB), University of Chile, Santiago 1030000, Chile*

*AgroSpace SPA, Santiago, 7560908*

[italo.moletto@uv.es](mailto:italo.moletto@uv.es), [cmattar@uchile.cl](mailto:cmattar@uchile.cl), [tomas.acuna@ug.uchile.cl](mailto:tomas.acuna@ug.uchile.cl), [lucas.amezquita@ug.uchile.cl](mailto:lucas.amezquita@ug.uchile.cl), [vladimir@agrospace.cl](mailto:vladimir@agrospace.cl), [raul@agrospace.cl](mailto:raul@agrospace.cl), [felipe.aviles@sernageomin.cl](mailto:felipe.aviles@sernageomin.cl), [laura.bono@sernageomin.cl](mailto:laura.bono@sernageomin.cl), [paula.garate@sernageomin.cl](mailto:paula.garate@sernageomin.cl), [paula.olea@sernageomin.cl](mailto:paula.olea@sernageomin.cl), [rosa.troncoso@sernageomin.cl](mailto:rosa.troncoso@sernageomin.cl), [silvia.arce@sernageomin.cl](mailto:silvia.arce@sernageomin.cl), [hugo.neiras@sernageomin.cl](mailto:hugo.neiras@sernageomin.cl)

**ABSTRACT** - Evapotranspiration is a key parameter for water budget quantification over ecosystems and set up requirements for water balance modeling on temperate basins, such as the Chiloé Island. However, public institutions and stakeholders do not have enough instrumentation over the island to monitor the surface water requirements. Henceforth Remote sensing is an essential tool for contiguous spatial and temporal monitoring. Missions such as Landsat 8 & Landsat 9 provides thermal band, which can be used for Actual Evapotranspiration (ETa) estimation using Surface Energy Balance (SEB) models, however, the temporal and spatial resolution can be a restrictive limit for an adequate monitoring in areas with high cloud cover. To mitigate the lack of data, we used MOD16, Landsat SSEBop and Sentinel-2 coupled with the Evapotranspiration model Penman-Monteith-Leuning V2 (PML-V2), a model that does not require the thermal channel to calculate ETa. The model was applied on Pudeto Basin, where Evapotranspiration measurements based on MOD16 and SSEBop provide error from 1.13 and 1.14 mm day<sup>-1</sup>, respectively. The PML-V2 showed a well performance with an R<sup>2</sup> of 0.89 and RMSE of 1.46 mm day, however, shows a clearly bias (1.32 mm day<sup>-1</sup>). This model was implemented on an interactive Google Earth Engine Python API & Shiny web-based application and readily available for Chile's National Geology and Mining Service (SERNAGEOMIN). Thus, this platform helps stakeholders for take decisions on Pudeto Basin.

### 1 INTRODUCTION

The Evapotranspiration (ET) is a key parameter for estimate the water consumption of basin to determinate the amount of irrigation or calculate precisely the water balance (Wanniarachchi & Surakkalige, 2022). The relevance of calculate the water consumption lies to adapt the water management of temperate ecosystems on the phenological state and avoid climatic variation associated to the precipitation amount (Garreaud et al., 2020).

Remote sensing is an economic and efficient technique for spatially contiguous and frequent information of actual evapotranspiration (ETa) retrievals, based on surface energy balance models (SEB). These models can be categorized as single layer, two-layer, two-patch, dual-source, multi-patch and

multi-layer models (Zhang et al., 2016). Single layers models have been widely used to estimate ETa at regional scale, such as SEBAL, METRIC, SEBS and SSEBop (Bastiaanssen et al., 1998, Allen et al., 2007, Su, 2002, Senay et al., 2013). However, exists also biophysical models based on the water and carbon coupling models, which models the stomatal conductance and the soil fluxes for retrieve the transpiration, the gross primary productivity and the gross primary productivity such as PML-V2 (Zhang et al., 2016).

These models mentioned were evaluated in this area in the study from Moletto-Lobos et al. 2020, where aimed the importance of the usage of these models for irrigation scheduling or water balance modelling. The results shown that PML-V2 at 500m from MODIS and SSEBop from Landsat 7-8 (100m)

provided a good performance for evaluation. Landsat 8 is useful for provide an operational modelling, however, the PML-V2 from MODIS does not update periodically this dataset and the coarse resolution difficult the evapotranspiration retrieval at field scale. However, the actual evapotranspiration from MOD16 (Running et al., 2019) product is already operational and has not been evaluated over the study area. In another hand, PML-V2 is based on calculation based on Leaf Area Index (LAI) and Surface emissivity, the first variable can be obtained from medium resolution satellite such as Sentinel-2 (Pasqualotto et al., 2019) and the surface emissivity for this area, ASTER GED (Hulley et al., 2015) has been proved to be a suitable auxiliary parameter (Moletto-Lobos et al., 2017). For this reason, our aim is developing an operational multi-resolution web-platform for monitoring the evapotranspiration of Pudeto Basin from Chiloé Island for water balance modelling and evaluate with data in situ.

## 2 AREA AND METHODS

### 2.1 Study Area

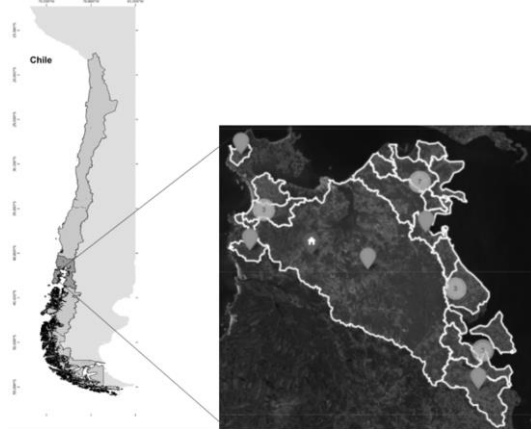


Figure 1. Study Area. The “home” point corresponds to the Matilda Validation Site and the tags are the Pudeto sub-basins.

The study region the Pudeto Basin on Chiloé Island (Figure 1). This region includes the north part along the large island of Chiloé. According to the Koppen–Geiger classification system, the regional climate corresponds to marine west coast (Cfb), with an average annual temperature of 10 °C and annual rainfall of 2100 mm (Sarricolea et al., 2017). The wet season extends from March to November but most precipitation falls in winter (44%) when the mid-latitude austral storm tracks move northward into the region. A dry season develops during the austral summer due to a southward expansion of the Mediterranean-like regional

circulation system prevailing year-round to the north, with minimum seasonal soil moisture levels and frequent drought conditions occurring during February and early March. In the point is shown the Matilda Validation Site, which is on a rainfed grassland cover.

### 2.2 Methods

The methods is three ET source product based on low, medium and high spatial resolution dataset.

1. Low Resolution 500m (MOD16A2) (Running et al., 2019)
2. Medium Resolution – Landsat 8 and Landsat 9 S5EBop (100m)
3. High Resolution – PML\_V2 LAI SeLi based (20m)

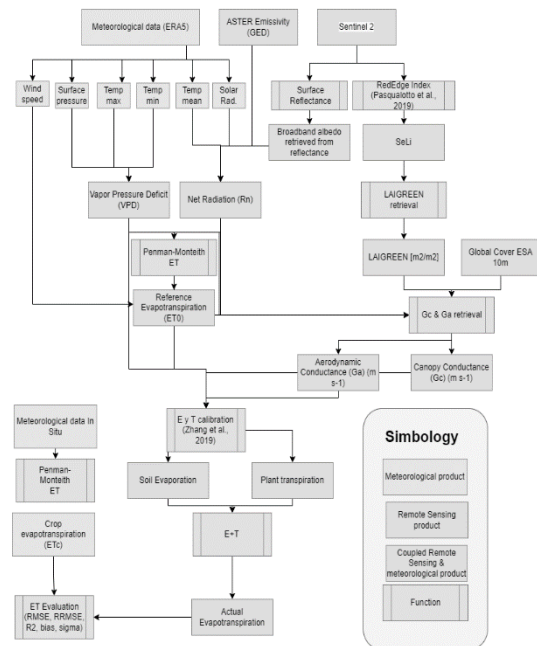


Figure 2. Flowchart of PML\_V2 processing

The MOD16 product is retrieved from Google Earth Engine (Gorelick et al., 2017). S5EBop (Senay et al., 2013) is based on the simplification of Evaporative fraction using the Land Surface Temperature (LST) from the single channel method (Jimenez-Muñoz et al., 2014) and applied to the calculation of ETa (Eq 1 & 2). The validation of LST product is detailed in Moletto-Lobos et al., (2020). The model used on Sentinel 2 is the PML\_V2 (Zhang et al., 2019) which is based in the separation of transpiration (T) and evaporation (E). T component is coupled with carbon cycles, through a conductance model to estimate T and GPP (Gan et al., 2018). Thus, E is derived indirectly with the GPP. water-carbon coupled canopy (Figure 2, Eq 3). Those

datasets were evaluated with ET0 in situ for period 2021-2022 using coefficient of determination ( $R^2$ ), the bias, the standard deviation of residual (sigma), the root mean squared error (RMSE), the relative root mean squared error (RRMSE) and mean absolute error (MAE) in comparison with Matilda Validation Site, and automatic weather station which contains the same sensors provided as OCS from Mattar et al., 2016.

### 2.3 Software used

The software used is based on Python GEE API platform, R-Shiny, PostgreSQL and Google Cloud console modules.

The PML\_V2 is based on the source code of PML ([https://github.com/gee-hydro/gee\\_PML](https://github.com/gee-hydro/gee_PML)) and applied to Sentinel-2 parameters.

The platform is mounted on <https://app.agrospacel.cl>

### 2.4 Equations

$$ET_a = \Lambda k ET_0 \quad (1)$$

Where,

ET0 is the standardized reference evapotranspiration (Allen et al., 2005)

k is the parameter that scales the reference grass vegetation experiencing maximum ET by an aerodynamically rougher crop

$\Lambda$  is the evaporative fraction

$$\Lambda = \frac{T_{hot} - T_s}{dT} = \frac{T_{hot} - T_s}{T_{hot} - T_{cold}} \quad (2)$$

$$ET = E + T = \frac{\varepsilon Q_{A,s}}{\varepsilon + 1} + \frac{\varepsilon Q_A + \frac{\rho C_p}{\gamma} D_a G_a}{\varepsilon + 1 + \frac{G_a}{G_c}} \quad (3)$$

Where,

Qa is the Net Radiation or total available energy (Qa,s in soil, Qa in canopy) [W/m<sup>2</sup>].

Cp corresponds to the specific heat of the air [J/kg °C].

Ga corresponds to aerodynamic conductance [m/s].

Gc corresponds to the exchange interface between leaf stomata and environmental variables [m/s].

Da corresponds to the water vapor deficit [kPa].

$\varepsilon$  corresponds to the slope of water saturation at air temperature [kPa/°C].

$\gamma$  corresponds to the psychrometric constant [kPa/°C].

$\rho$  corresponds to the air density [kg/m<sup>3</sup>].

## 3 RESULTS

The performance of every ET model is shown in Figure 3 and Table 1. Sentinel 2 ET showed the best similarity to the in-situ with  $R^2$  of 0.89 and sigma of 0.63, however there is a bias over the ET of 1.32 mm day<sup>-1</sup>, derived mainly during winter period which does not represent well the radiative limitation for that period.

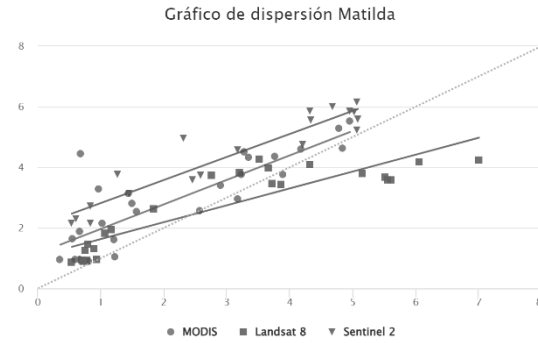


Figure 3. Scatterplot of Evaluation of ET products. X and Y axis correspond to mm/day.

Table 1. Summary of statistics over sites

Stat	Landsat 8	Sentinel 2	MOD16
Bias	-0.22	1.32	0.74
Sigma	1.12	0.63	0.86
RMSE	1.14	1.46	1.13
RRMSE	38.89	47.05	51.95
MAE	0.85	1.32	0.8
$R^2$	0.79	0.89	0.7
Linear fit	$y = 0.56x + 1.07$	$y = 0.76x + 2.06$	$y = 0.81x + 1.16$

The SSEBop model and MOD16 showed a well performance with a bias under of -0.22 mm day<sup>-1</sup> and 0.74 mm day<sup>-1</sup>, respectively. MOD16, a LAI based model present a RMSE of 1.13, similar to SSEBop (SEBS-thermal based model) does not present an strong bias over the dataset. We can hypothesize that the LAI retrieval of Sentinel-2 should it be assessed and be evaluated using in situ parameters for validate the intermediate parameter for provided an adjusted unbiased model. Besides, for the time series all models (Figure 3) showed an expected phenological behaviour in similarity within situ data. The constellation of Landsat 8-9 provided a good frequency of data and assessed a good performance with the lowest absolute and relative error in comparison of another method and expected that LST showed as a key component for perform the evapotranspiration retrieval (Hook et al., 2019), however, in contrast of Sentinel-2 or MOD16A2 dataset does not have the same frequency of parameter, which provide the challenge of perform a good computation at yearly scale, in contrast of MOD16A2 which provide a good performance besides the spatial resolution and almost 8-day value for the whole basin and pixel evaluation.

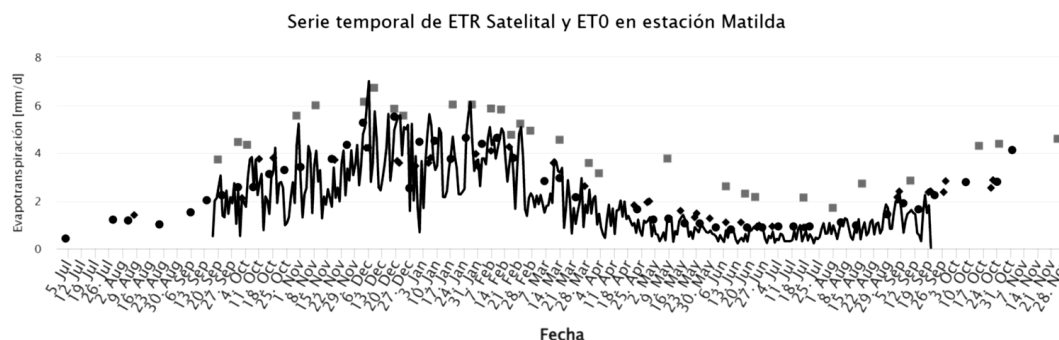


Figure 4. Time series over Matilda site.

The web-based platform (Figure 5) provides the performance of all the time series data available for all missions (MODIS since 2002, Landsat 8 – 9 from 2013 and Sentinel-2A/B from 2019). Also, has the capabilities to calculate the daily, accumulated and mean evapotranspiration over the basin and sub-basin required for SERNAGEOMIN stakeholders. All data can be downloaded in .csv format from time series or .TIFF data for technical assessment. The Matilda Validation Site is connected operative, so the Figure 3, 4 and table 1 is in constantly updating processing when the station and satellite data connects for update the dataset.

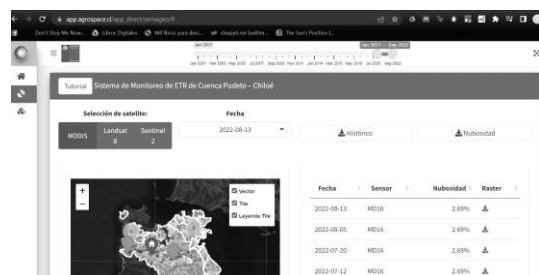


Figure 5. Example of the web platform.

#### 4 CONCLUSIONS

In this work, we applied three Evapotranspiration models with different methods and resolutions for provide data to an operational GIS-based portal. This dataset where calibrated and evaluated with in situ data. Low ( $R^2$  0.7, RMSE: 1.13 mm day<sup>-1</sup>) a medium resolution ( $R^2$  0.79, RMSE: 1.14 mm day<sup>-1</sup>) performed an adequate performance for water balance modelling. The Sentinel 2 based product provide a novelty product of evapotranspiration with a very good linear relationship ( $R^2$  0.89). Also, it can be seen from low variability induced in error (sigma: 0.63 mm day<sup>-1</sup>). However, show an important bias which impact into the RMSE up to 1.42 mm day<sup>-1</sup> and giving an absolute error

of 1.32 mm day<sup>-1</sup>. The model can be adjusted correcting the LAI retrieval in the product, which can be improved collecting LAI in situ and used more biophysical LAI models based on artificial intelligence mixed with radiative transfer model for inversion such as ARTMO (Verrelst et al., 2011). All those parameters are ready to analysis and use for SERNAGEOMIN users for processing and get Ready-to-analysis datasets in a operational context.

#### 5 REFERENCES

- Allen, R.; Walter, I.; Elliott, R.; Howell, T.; Itenfisu, D.; Jensen, M.E. the ASCE standardized reference evapotranspiration equation: ASCE-EWRI Standardization of Reference Evapotranspiration Task Committee Report. 2005.
- Bastiaanssen, W.; Pelgrum, H.; Wang, J.; Ma, Y.; Moreno, J.; Roerink, G.; Van Der Wal, T. A remote sensing surface energy balance algorithm for land (SEBAL). J. Hydrol. 1998, 212–213, 213–229.
- Jiménez-Muñoz, J. C., Sobrino, J. A., Skoković, D., Mattar, C., & Cristóbal, J. (2014). Land surface temperature retrieval methods from Landsat-8 thermal infrared sensor data. Geoscience and Remote Sensing Letters, IEEE, 11(10), 1840–1843. <https://doi.org/10.1109/LGRS.2014.2312032>
- Gao, Jiaqi, et al. "Estimation of actual evapotranspiration distribution in the Huaihe River upstream basin based on the generalized complementary principle." Advances in Meteorology 2018 (2018).
- Garreaud, René D., et al. "The central Chile mega drought (2010–2018): a climate dynamics perspective." International Journal of Climatology 40.1 (2020): 421–439.

- Gorelick, Noel, et al. "Google Earth Engine: Planetary-scale geospatial analysis for everyone." *Remote sensing of Environment* 202 (2017): 18-27.
- Hulley, Glynn C., et al. "The ASTER Global Emissivity Dataset (ASTER GED): Mapping Earth's emissivity at 100 meter spatial scale." *Geophysical Research Letters* 42.19 (2015): 7966-7976.
- Mattar, C.; Santamaria-Artigas, A.E.; Durán-Alarcón, C.; Olivera-Guerra, L.; Fuster, R.; Borvarán, D. The LAB-Net Soil Moisture Network: Application to Thermal Remote Sensing and Surface Energy Balance. *Data* 2016, 1, 6.
- Moletto-Lobos, I.; Mattar, C.; Jiménez-Muñoz, J.C.; Pérez, T. Impact of Atmosphere and emissivity data base in the validation of Land Surface Temperature over pastures. In *Proceedings of the 5th International Symposium on Recent Advances in Quantitative Remote Sensing: RAQRS'V*, Valencia, Spain, 18–22 September 2017.
- Moletto-Lobos, I.; Mattar, C.; Barichivich, J. Performance of Satellite-Based Evapotranspiration Models in Temperate Pastures of Southern Chile. *Water* 2020, 12, 3587. <https://doi.org/10.3390/w12123587>
- Sarricolea, P.; Herrera-Ossandon, M. Meseguer-Ruiz, Óliver Climatic regionalisation of continental Chile. *J. Maps* 2017, 13, 66–73
- Senay, G.B.; Bohms, S.; Singh, R.K.; Gowda, P.H.; Velpuri, N.M.; Alemu, H.; Verdin, J.P. Operational Evapotranspiration Mapping Using Remote Sensing and Weather Datasets: A New Parameterization for the SSEB Approach. *JAWRA J. Am. Water Resour. Assoc.* 2013, 49, 577–591.
- Pasqualotto, N.; Delegido, J.; Van Wittenberghe, S.; Rinaldi, M.; Moreno, J. Multi-Crop Green LAI Estimation with a New Simple Sentinel-2 LAI Index (SeLI). *Sensors* 2019, 19, 904. <https://doi.org/10.3390/s19040904>
- Running, Steven W., et al. "MODIS global terrestrial evapotranspiration (ET) product (MOD16A2/A3 and year-end gap-filled MOD16A2GF/A3GF) NASA Earth Observing System MODIS Land Algorithm (for collection 6)." National Aeronautics and Space Administration, Washington, DC, USA [data set], [https://doi.org/10.5067/MODIS/MOD16A2\\_6](https://doi.org/10.5067/MODIS/MOD16A2_6) (2019).
- Singh, R.K.; Senay, G.B. Comparison of Four Different Energy Balance Models for Estimating Evapotranspiration in the Midwestern United States. *Water* 2015, 8, 9.
- Su, Z. The Surface Energy Balance System (SEBS) for estimation of turbulent heat fluxes. *Hydrol. Earth Syst. Sci.* 2002, 6, 85–100.
- Verrelst, J., et al. "ARTMO: An Automated Radiative Transfer Models Operator toolbox for automated retrieval of biophysical parameters through model inversion." *Proc. EARSeL 7th SIG-Imag. Spectrosc. Workshop*. 2011.
- Wanniarachchi, S.; Sarukkalgige, R. A Review on Evapotranspiration Estimation in Agricultural Water Management: Past, Present, and Future. *Hydrology* 2022, 9, 123. <https://doi.org/10.3390/hydrology9070123>
- Zhang, K.; Kimball, J.S.; Running, S.W. A review of remote sensing based actual evapotranspiration estimation. *Wiley Interdiscip. Rev. Water* 2016, 3, 834–853.
- Zhang, Y.; Kong, D.; Gan, R.; Chiew, F.H.; McVicar, T.R.; Zhang, Q.; Yang, Y. Coupled estimation of 500 m and 8-day resolution global evapotranspiration and gross primary production in 2002–2017. *Remote. Sens. Environ.* 2019, 222, 165–182.



# Building and validating NOAA-AVHRR orbital drift correction methods by using MSG-SEVIRI temperature data

Y. Julien, J. A. Sobrino

Global Change Unit, Image Processing Laboratory, Parque Científico, Universidad de Valencia, C/ Catedrático Jose Beltran n°2, 46980 Paterna, Spain.

yves.julien@uv.es

**ABSTRACT** - The temperature data acquired by the AVHRR (Advanced Very High-Resolution Radiometer) sensors since the early 80s cannot be used for a better knowledge of climate warming, due to the orbital drift of the NOAA (National Oceanic and Atmospheric Administration) satellite series carrying them. Even though various methods have been presented in the literature to correct this orbital drift effect, the lack of validation data has prevented their practical application. However, basing us on alternative satellite data, namely MSG-SEVIRI (Meteosat Second Generation - Spinning Enhanced Visible and InfraRed Imager), we can design and validate orbital drift correction methods. Indeed, this sensor spatial resolution is similar to the footprint of available AVHRR datasets, while its temporal resolution is fifteen minutes, allowing for the simulation of both drifted and reference time series for most land covers. In this work we simulated such time series for 177 land and 500 sea pixels and for all NOAA afternoon satellites (NOAA-7, 9, 11, 14, 16, 18 and 19). Pixels of all land covers show an effect of the orbital drift on surface temperature, although this effect is stronger for arid areas and the Southern Hemisphere. Such effect is characterized by the values of the bias and trend of the difference between reference and drifted time series, above 1K and around -1.5K per year respectively for the first four NOAA platforms. The correction we also present decreases difference trend values towards zero on land, except for the first two NOAA platforms (7 and 9), with absolute values around 0.1K per year. As for bias absolute values, these are around 0.3 K. Such correction improves on existing methods, although work is still needed for a complete removal of the orbital drift effect on NOAA-AVHRR derived surface temperatures, for example by including the effect of the daily temperature cycle in the statistical correction.

## 1 INTRODUCTION

Even though NOAA-AVHRR (National Oceanic and Atmospheric Administration – Advanced Very High-Resolution Radiometer) satellites have been retrieving observations of our planet since the 80s, these data have been seldom used to analyze the evolution of the Surface Temperature (ST). The main reason for this resides in the orbital drift of NOAA platforms, which effect consists in a progressive decrease of the observed temperature through each satellite life span, due to a delay in the local overpass time (Price, 1990). The scientific literature includes various methods for this orbital drift effect correction (for a review, see Julien and Sobrino, 2021). However, validating these corrections is difficult, since no continuous measurements are available since the 80s at a spatial scale of the AVHRR sensor footprint. Although there is no access to *in situ* data to validate these corrections, we can use independent data to simulate the effect of the orbital drift on surface temperatures. The SEVIRI (Spinning Enhanced Visible and InfraRed Imager) sensor, onboard the MSG (Meteosat Second Generation) satellites, with a spatial resolution similar to the AVHRR data in the publicly available databases (see for example Pedelty

et al., 2007), with a temporal resolution of 15 minutes, is fit for this task.

In this work, we present the methodology we use to simulate the orbital drift effect for the different NOAA platforms, which allows us to analyze and correct the effect of this orbital drift on ST.

## 2 DATA

The Global Change Unit of the University of Valencia operates an MSG-SEVIRI receiving station since 2007, although in this work, we have used the data corresponding to years 2013-2019 (inclusive). The SEVIRI sensor has a spatial resolution of 3km at nadir, with new data every 15 minutes. These data spread over 11 bands, 2 in the visible and near infrared spectrum (Vis06, Vis08), 2 in the middle infrared (Ir016, Ir039), and 7 in the thermal infrared (Wv062, Wv073, Ir087, Ir097, Ir108, Ir120, and Ir134). The detailed description of the reception systems, the pre-processing, as well as the algorithms used to estimate surface temperatures can be found in Julien et al. (2015), Sobrino et al. (2020) and Sobrino and Julien (2021). Additionally, cloud masks for the 2013-2019 period have been downloaded through EUMETSAT portal.



### 3 METHODS

From the MSG-SEVIRI 15-minutes ST data between 2013 and 2019, and by setting each satellite activity period as it appears in LTDR-V4 (Long Term Data Record – Version 4, Pedelty et al., 2007) dataset, we simulate orbital drifted ST time series for each of the following NOAA platforms: 7, 9, 11, 14, 16, 18, and 19. To that end, we remove the observations labelled as cloudy, and we use the equations developed by Ignatov et al. (2004) to determine NOAA's Equator crossing times, which allow for the estimation of local overpass time for any location. With these overpass times, we interpolate ST data from the two neighboring (in time) observations, in order to build the orbital drifted ST time series for the above-mentioned NOAA platforms. We also build reference ST time series for each platform for analysis and validation purposes, using as reference overpass time 14:30, 14:30, 13:30, 13:30, 14:00, 14:00 and 14:00 for NOAA-7, 9, 11, 14, 16, 18 and 19 platforms respectively. Details of the methodology can be found in Julien and Sobrino (2021).

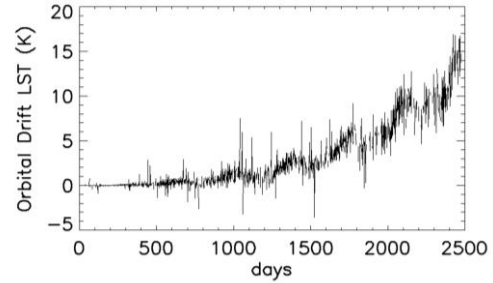
For our study, we have selected as study sites 500 random pixels over sea, and the 177 BELMANIP (Baret et al., 2006) pixels over land which are located within the observation disk of MSG-SEVIRI. For each of these pixels, we use two statistical indicators to evaluate orbital drift impact, as well as the validity of its correction. These indicators are the *bias*, and the linear trend of the difference between the reference time series and the one which validity we want to assess.

As for the orbital drift correction, we use once again the equations developed by Ignatov et al. (2004), in this case as a fit of the difference between the orbital drifted ST time series and a reference estimated from the first year of the activity period of the corresponding NOAA platform.

### 4 RESULTS

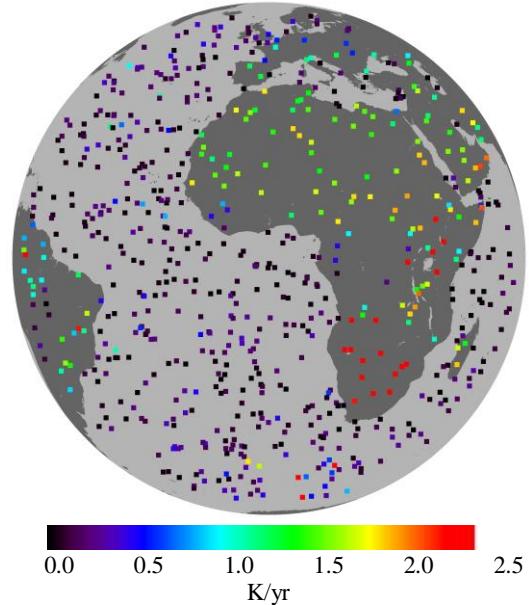
#### 4.1 Orbital drift effect

Figure 1 presents the orbital drift effect for NOAA-11 platform for site 208, corresponding to a desert pixel, located at (25,159°; 22,71°) latitude and longitude. This effect is obtained by estimating the difference between the orbital drifted and the reference ST time series for this pixel and this platform. We see that the orbital drift impact for this pixel increases progressively with time, reaching 15K at the end of NOAA-11 satellite lifetime. We can also observe the presence of a seasonal component within this orbital drift, which amplitude increases with time. To this date, this seasonal component had not been identified in the literature.



**Figure 1.** Orbital drift effect on Surface Temperature (in Kelvin degrees) for NOAA-11 platform for site 208 (25,159°; 22,71°).

In Figure 2, we display the value of the linear trend between the orbital drifted and reference ST time series, also for NOAA-11 platform, for each of the selected pixels, both over land and sea. We see that over land, pixels located in arid areas of the Southern Hemisphere are the ones suffering the strongest orbital drift effect. Mainly, arid and semi-arid areas are the ones showing the highest orbital drift effect, although most of the selected pixels over land show an effect higher than 0.5K per year.



**Figure 2.** Orbital drift effect for NOAA-11 satellite on surface temperature (in K per year).

On average, this effect is  $1,5 \pm 0,7$  K per year over land. Over sea, the orbital drift effect is lower, around  $0,04 \pm 0,17$  K per year on average. In this latter case, pixels with extreme values are located in areas with persistent cloud cover. Although orbital drift effect over sea is lower than over land, this effect, when cumulated over several years, is of a similar

magnitude as the expected error on surface temperature estimation (0.5K), and therefore needs to be corrected.

#### 4.2 Correction validation

Table 1 presents the trend values for the difference between the reference and orbital drifted ST time series for each NOAA platform (left), averaged over the 177 selected land pixels. We observe that the older platforms (NOAA-7, 9, 11 and 14) are the ones with the strongest orbital drift effect, with *bias* absolute values over 1K, and difference trend above 1K per year. As a matter of fact, following platforms orbits were designed to minimize its orbital drift during their first years on orbit.

If we compare these values with the ones at the right of Table 1, referred to the same statistical parameters, this time obtained from the orbital drift corrected ST time series, we see that values of both statistical parameters have been reduced, although *bias* values remain relatively high. Numerically, absolute values of the difference trend after correction are almost null, except for NOAA-7 and 9 platforms, with values close to 0.1 K per year. As for bias absolute values, they are always below 0.3K. However, this remaining *bias* can be corrected *a posteriori*, by intercalibrating the simultaneous activity periods for different platforms, allowing the obtention of orbital drift corrected ST time series.

**Table 1.** Analysis of the orbital drift effect for NOAA satellites over land (standard deviation between parentheses) on the left, and after correction on the right.

Platform	Before correction		After correction	
	<i>bias</i> (K)	trend (K/yr)	<i>bias</i> (K)	trend (K/yr)
NOAA-7	-1,30 (0,76)	-1,44 (0,82)	-0,19 (0,62)	0,12 (0,54)
NOAA-9	-1,53 (0,90)	-1,52 (0,86)	0,00 (0,69)	-0,08 (0,47)
NOAA-11	-1,99 (1,27)	-1,36 (0,79)	-0,24 (0,88)	0,02 (0,27)
NOAA-14	-2,36 (1,43)	-1,43 (0,79)	-0,09 (0,95)	0,01 (0,22)
NOAA-16	-0,59 (0,41)	-0,49 (0,33)	-0,22 (0,89)	-0,04 (0,30)
NOAA-18	0,04 (0,09)	-0,03 (0,04)	-0,29 (0,81)	-0,02 (0,10)
NOAA-19	0,05 (0,10)	-0,02 (0,04)	-0,29 (0,83)	-0,02 (0,08)

This remaining *bias* is due to the complex task of retrieving a reference time series in practical cases – here the first year of activity of each platform – since we do not have access to orbital drift free time series.

Additionally, uncertainties due to atmosphere and cloud influence, for example, can introduce considerable variability in such reference time series.

#### 5 CONCLUSIONS AND PERSPECTIVES

In this work, we have analyzed NOAA orbital drift effect on surface temperature. To this end, we have used MSG-SEVIRI data to simulate temperature time series, both over land and sea, with and without orbital drift. Thanks to these simulated data, we have evidenced the orbital drift effect of NOAA satellites for most of the analyzed pixels, and not only in arid, semi-arid and cultivated areas as mentioned in the literature. We have also presented a methodology for the correction of this orbital drift, with good results. However, corrected surface temperature time series present a remaining *bias* which needs for a posterior correction.

To improve on the presented correction, a correct estimation of the reference time series is needed. To this end, we will analyze the orbital drift effect on the surface temperature annual amplitude. In a near future, we will also study the representativity of the simulated time series with MSG-SEVIRI data in regards to the time series observed with NOAA-AVHRR.

#### ACKNOWLEDGEMENT

The authors are grateful to all the members of the Global Change Unit of the University of Valencia for their dedication in keeping the MSG receiving station running over the years. The authors also thank EUMETSAT for providing Cloud Mask data. This work was supported by the Spanish Agencia Estatal de Investigación and the Spanish Ministerio de Ciencia e Innovación (IPL-LSTM, project PID2020-112494RB-I00).

#### REFERENCES

- Baret, F., Morisette, J., Fernandes, R., Champeaux, J. L., Myneni, R., Chen, J., Plummer, S., Weiss, M., Bacour, C., Garrigues, S. et al. 2006. Evaluation of the representativeness of networks of sites for the validation and inter-comparison of land biophysical products proposition of the CEOS-BELMANIP. IEEE Transactions on Geoscience and Remote Sensing, 44, 1794–1803.
- Ignatov, A., Laszlo, I., Harrod, E. D., Kidwell, K. B. and Goodrum, G. P. 2004. Equator crossing times for NOAA, ERS and EOS sun-synchronous satellites. International Journal of Remote Sensing, 25, 5255–5266, <https://doi.org/10.1080/01431160410001712981>.

- Julien, Y. and Sobrino, J. A. 2021. NOAA-AVHRR Orbital Drift Correction: Validating Methods Using MSG-SEVIRI Data as a Benchmark Dataset. *Remote Sensing*, 13(5):925. <https://doi.org/10.3390/rs13050925>.
- Julien, Y., Sobrino, J. A. and Sòria, G. 2015. Retrieving and broadcasting near-real time biophysical parameters from MODIS and SEVIRI receiving stations at the Global Change Unit of the University of Valencia, *International Journal of Remote Sensing*, <https://doi.org/10.1080/01431161.2015.1040134>.
- Pedety, J., Devadiga, S., Masuoka, E., Brown, M., Pinzon, J., Tucker, C., Vermote, E., Prince, S., Nagol, J., Justice, C. et al. 2007. Generating a long-term land data record from the AVHRR and MODIS Instruments. In *Proceedings of the 2007 IEEE International Geoscience and Remote Sensing Symposium*, Barcelona, Spain, pp. 1021–1025, <https://doi.org/10.1109/igarss.2007.4422974>.
- Price, J. 1990. Using spatial context in satellite data to infer regional scale evapotranspiration. *IEEE Transactions on Geoscience and Remote Sensing*, 28, 940–948, <https://doi.org/10.1109/36.58983>.
- Sobrino, J. A., Julien, Y., Muñoz, J.-C., Skokovic, D. and Sòria, G. 2020. Near real-time estimation of Sea and Land surface temperature for MSG SEVIRI sensors. *International Journal of Applied Earth Observation and Geoinformation*, 89, 2096, <https://doi.org/10.1016/j.jag.2020.102096>.
- Sobrino, J. A., Julien Y. 2021. Near Real-Time Processing Chain for MSG SEVIRI Data for Free and Immediate Earth Monitoring Capabilities. *Frontiers in Remote Sensing*, 2, 2021, <https://doi.org/10.3389/frsen.2021.666516>.

# ECOSTRESS products for drought monitoring over different land covers

J. C. Jimenez<sup>1</sup>, G. Cotlier<sup>2</sup>, J. A. Sobrino<sup>1</sup>, D. Skokovic<sup>1</sup>, G. Sòria<sup>1</sup>, Y. Julien<sup>1</sup>, B. Franch<sup>1</sup>, S. García<sup>1</sup>, R. Llorens<sup>1</sup>

<sup>1</sup>GCU/IPL, University of Valencia, Spain

<sup>2</sup>HCTPA/DSRC, University of Haifa, Israel

[icjm@uv.es](mailto:icjm@uv.es)

**ABSTRACT-** Droughts are one of the most complex natural hazards having large negative impacts on society, economy, and the environment. In the face of global climate change, the drought situation in many regions has already become more severe, with predicted increases in drought frequencies. Thermal infrared remote sensing data acquired from Earth Observation sensors allows the retrieval of information about the energy exchange between the surface and the atmosphere, and therefore it provides a valuable tool for drought monitoring. In this work, we show the results extracted from ECOSTRESS level 2 and level 4 products of Land Surface Temperature (LST) and Evaporative Stress Index (ESI), respectively. We selected sites with different land covers, including tropical forests, croplands, and semi-arid areas. Temporal series (period 2019-2022) of the different parameters were analyzed, and the LST product was validated over a tropical forest area in the Peruvian Amazon. Scatter plots of ESI vs. LST showed a negative linear correlation over all the sites, but these correlations were stronger over the tropical and semi-arid areas, and weaker over the agricultural areas. LST validation provided high accuracy, but precision exceeded 5 K.

## 1 INTRODUCTION

Droughts have become one of the major hazards under the current climate change scenario (IPCC, 2021). Satellite data allows the characterization of both spatial and temporal patterns of droughts and its impacts over different landscapes characterized by different spatial extents (Jiao et al. 2021).

Characterization of droughts through evaporative indicators require the availability of Thermal InfraRed (TIR) data to quantify the energy exchange between the surface and the atmosphere. The ECOSystem Spaceborne Thermal Radiometer Experiment on Space Station (ECOSTRESS) provides multispectral TIR data with 38-m in-track by 69-m cross-track spatial resolution. Its primary mission is to assess water use by plants and improve the accuracy of drought estimates which requires measuring surface land/water temperature. Data is available since 2018, and the TIR instrument has five bands in the 8-13  $\mu\text{m}$  spectral range, although only three of them are currently available (Anderson et al., 2021; Gorokhovich et al., 2022; Hulley et al., 2021; Hook et al., 2019).

In this work we used ECOSTRESS level 2 and level 4 products to analyse the temporal evolution of Land Surface Temperature (LST) and Evaporative Stress Index (ESI) over different sites, including also a validation of LSTs against in situ measurements over a tropical forest.

## 2 METHODS

### 2.1 ECOSTRESS products

In this work we used ECOSTRESS ECO2LST and ECO4ESIPTJPL products. ECO2LST provides LST values retrieved from multispectral TIR data using the Temperature and Emissivity Separation (TES) algorithm (Gillespie et al., 1998).

ECO4ESIPTJPL provides estimations of the ESI using the PT-JPL model (Fisher et al., 2008). ESI is a normalized remote sensing-based agricultural drought index, and it does not require information about the soil moisture status or rainfall, but rather diagnoses vegetation stress via impacts of elevated canopy temperature on the ET retrieval (Anderson et al., 2011). ESI has been demonstrated to be a valuable early warning indicator of stress at different spatial scales (e.g., Anderson et al. 2013; Yang et al. 2021).

ECOSTRESS data were freely extracted through the tool Application for Extracting and Exploring Analysis Ready Samples (AppEEARS).

### 2.2 Test sites

We randomly selected three sites with different land covers to analyse the temporal variations of LST and ESI. These test sites include Bourdeaux (agricultural area), Barrax (agricultural area), and Somalia (arid

area). We added an additional test site located in Tambopata, in the Peruvian Amazon, where in situ measurements are available (Figure 1).



Figure 1. Views of the test sites extracted from Google Earth ©.

### 2.3 Validation data

The test site located in Tambopata includes an instrumented tower where in situ measurements are continuously recorded. Among the different set of measurements, surface temperatures over the top of the canopy are measured using thermal radiometers Apogee SI-111 and Campbell IR-120. Shortwave and longwave components are also measured using Kipp & Zonen net radiometers (Figure 2).

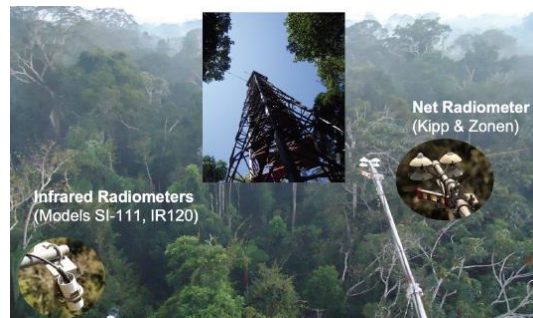


Figure 2. Tambopata validation site in the Peruvian Amazon.

## 3 RESULTS

### 3.1 Temporal series

Temporal series of LST and ESI (2019-2022) were extracted from ECOSTRESS products over the sites presented in Section 2.2. Results are provided in Figure 3. Mean values over the entire period are also presented in Figure 4. The tropical forest site (Tambopata) shows the lowest variation (standard deviation) in LST and ESI, with values of  $301 \pm 5$  K and  $0.84 \pm 0.07$ , respectively. It also shows the highest values of ESI. In contrast, the agricultural and semi-arid sites show higher variations of LST and ESI, and agricultural areas show the lowest mean values of ESI.

Figure 5 includes scatter plots of ESI *versus* LST. These plots show a clear negative linear correlation between these two parameters, which indicates that drought conditions (low ESI values) are favoured by high temperatures. The highest correlation coefficients were obtained for Tambopata and Somalia sites. In any case, not all the relationships are statistically significant, and LST is not the only factor controlling the evapotranspiration regime.

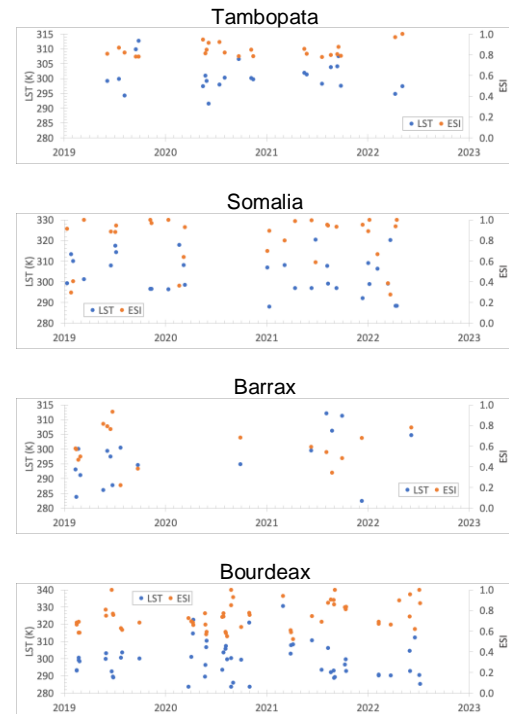


Figure 3. Temporal series of Land Surface Temperature (LST) and Evaporative Stress Index (ESI) over different sites (see Figure 1).



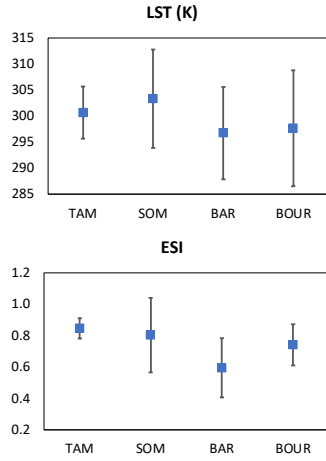


Figure 4. Mean values of Land Surface Temperature (LST) and Evaporative Stress Index (ESI) over the period 2019-2022 for the different sites (Tambopata – TAM, Somalia – SOM, Barrax – BAR, Bourdeaxu – BOUR).

over the whole period, with values higher than 0.98. Temporal series of emissivities show these expected variations in most cases, but also anomalous low values over particular dates (especially for band 12.09  $\mu\text{m}$ ). However, removal of these anomalous values did not improve the LST validation statistics.

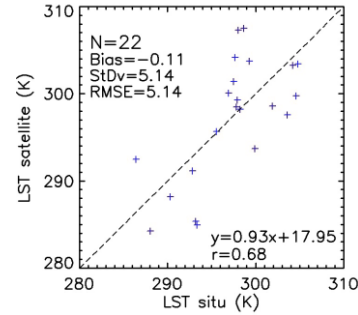


Figure 6. Validation of Land Surface Temperature (K) extracted from the ECOSTRESS product over the Tambopata site.

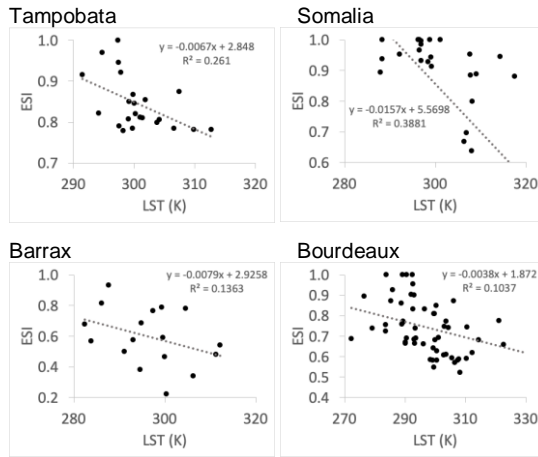


Figure 5. Scatter plots of Evaporative Stress Index (ESI) and Land Surface Temperature (LST) for the period 2019-2022 over the different sites.

### 3.2 Validation over the Tambopata site

LSTs extracted from ECO2LSTE product were compared against in situ measurements collected over the tower located in the Tambopata site. Results show a high accuracy of the product, with a bias near to 0 K, but low precision, with a standard deviation value exceeding 5 K (Figure 6).

We also analyzed band emissivities extracted from the ECO2LSTE product (Figure 7). Because the site is characterized by an evergreen broadleaf forest, it is expected that emissivities remain more or less constant

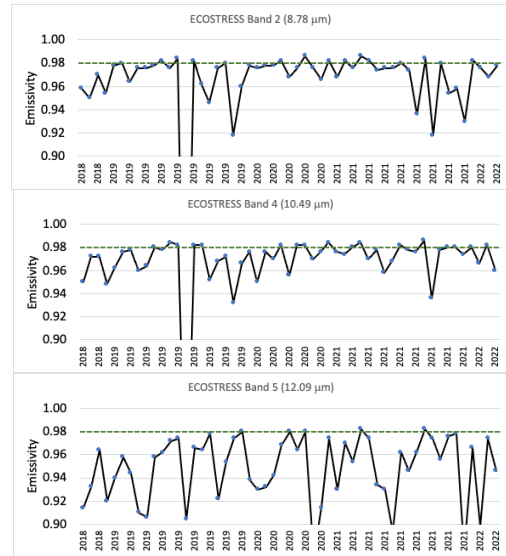


Figure 7. Temporal series of band emissivities (ECO2LSTE product) over the Tambopata site.

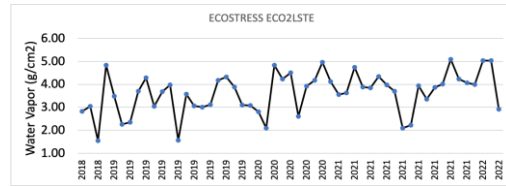


Figure 8. Temporal series of atmospheric water vapor content over the Tambopata site.

The low precision obtained in the validation may be also attributed to strong atmospheric absorption over this tropical site (Figure 8), with total atmospheric water vapor values ranging between 2 and 5 g/cm<sup>2</sup> (mean value of 3.6±0.9 g/cm<sup>2</sup>).

#### 4 CONCLUSIONS

ECOSTRESS is one of the scarce Earth Observation sensors providing multispectral TIR data at high spatial resolution. These data are useful for a number of applications, especially those related to the monitoring of evapotranspiration and detection of drought conditions.

In this work we showed results extracted from ECO2LST and ECO4ESIPTJPL products, which include LST (and emissivities) and ESI values, respectively, over different land covers. ESI is indicative of stress conditions, and its sensitive to different sites and land covers. It also shows a negative linear relationship with LST, although ESI also depends on other factors. Validation of ECO2LSTE product over one tropical forest site provides high accuracy (-0.1 K) and low precision (>5K), may be due to the high atmospheric absorption of the validation site.

#### 5 ACKNOWLEDGEMENTS

This work was partly supported by projects EIN2020-112420 and PID2020-112494RB-I00 (Ministerio de Ciencia e Innovación).

#### 6 REFERENCES

- Anderson MC, Hain C, Wardlow B, Pimstein A, Mecikalski JR, Kustas WP (2011) Evaluation of drought indices based on thermal remote sensing of evapotranspiration over the continental United States. *J Clim* 24:2025–2044.
- Anderson MC, Hain C, Otkin J, Zhan X, Mo K, Svoboda M, Wardlow B, Pimstein A (2013) An intercomparison of drought indicators based on thermal remote sensing and NLDAS-2 simulations with US Drought Monitor classifications. *J Hydrometeorol* 14:1035–1056.
- Anderson, M. C., Yang, Y., Xue, J., Knipper, K. R., Yang, Y., Gao, F., . . . Rey-Sanchez, C. (2021). Interoperability of ECOSTRESS and landsat for mapping evapotranspiration time series at sub-field scales. *Remote Sensing of Environment*, 252, 112189. doi:10.1016/j.rse.2020.112189.
- Fisher, J. B., Tu, K. P., & Baldocchi, D. D. (2008). Global estimates of the land-atmosphere water flux based on monthly AVHRR and ISLSCP-II data, validated at 16 FLUXNET sites. *Remote Sensing of Environment*, 112(3), 901-919.
- Gillespie, A.R., Rokugawa, S., Matsunaga, T., Cothorn, J.S., Hook, S.J. and Kahle, A.B. (1998) A Temperature and Emissivity Separation Algorithm for Advanced Spaceborne Thermal Emission and Reflection Radiometer (ASTER) Images. *IEEE Transactions on Geoscience and Remote Sensing*, 36, 1113-1126. <http://dx.doi.org/10.1109/36.700995>
- Gorokhovich, Y., Cawse-Nicholson, K., Papadopoulos, N., & Oikonomou, D. (2022). Use of ECOSTRESS data for measurements of the surface water temperature: Significance of data filtering in accuracy assessment. *Remote Sensing Applications: Society and Environment*, 26, 100739. doi:10.1016/j.rsase.2022.100739
- Hook, S. J., Cawse-Nicholson, K., Barsi, J., Radocinski, R., Hulley, G. C., Johnson, W. R., ... & Markham, B. (2019). In-flight validation of the ECOSTRESS, Landsats 7 and 8 thermal infrared spectral channels using the Lake Tahoe CA/NV and Salton Sea CA automated validation sites. *IEEE Transactions on Geoscience and Remote Sensing*, 58(2), 1294-1302.
- Hulley, G. C., *et al.*, "Validation and Quality Assessment of the ECOSTRESS Level-2 Land Surface Temperature and Emissivity Product," in *IEEE Transactions on Geoscience and Remote Sensing*, vol. 60, pp. 1-23, 2022, Art no. 5000523, doi: 10.1109/TGRS.2021.3079879.
- IPCC, 2021, Climate change, in *The Physical Science Basis. Contribution of Working Group I to the Sixth Assessment Report of the Intergovernmental Panel on Climate Change*, eds V. Masson-Delmotte, P. Zhai, A. Pirani, S.L. Connors, C. Péan, S. Berger, et al. (Cambridge: Cambridge University Press).
- Jiao, W., Wang, L., & McCabe, M. F. (2021). Multi-sensor remote sensing for drought characterization: Current status, opportunities and a roadmap for the future. *Remote Sensing of Environment*, 256, 112313. doi:10.1016/j.rse.2021.112313.
- Yang Y, Anderson MC, Gao F, Johnson DM, Yang Y, Sun L, Dulaney W, Hain CR, Otkin JA, Prueger J (2021) Phenological corrections to a field-scale, ET-based crop stress indicator: an application to yield forecasting across the US Corn Belt. *Remote Sens Environ* 257:112337.

# Mediterranean Climate Zones, Time Series Analysis from 2010 to 2022: 100 Biophysical Indices, 300 Algorithms and 6 Satellites

F-E. Ezzaher<sup>1,2</sup>, N. Ben Achhab<sup>1,2</sup>, H. Naciri<sup>1,2</sup>, J. A. Sobrino<sup>3</sup>, N. Raissouni<sup>1,4</sup>

<sup>1</sup> Remote Sensing & Geographic Information System Unit (RS&GIS), University of Abdelmalek Essaadi, Morocco.

<sup>2</sup> Mathematics and Intelligent Systems (MASI), University of Abdelmalek Essaadi, Morocco.

<sup>3</sup> Goba Change Unit (GCU)- Imaging Processing Lab. (IPL), University of Valencia, Spain.

<sup>4</sup> Remote Sensing, Systems and Telecommunications (TST), University of Abdelmalek Essaadi, Morocco.

Email-1: nbenachhab@uae.ac.ma, Email-2: nraissouni@uae.ac.ma. Tel: +212671703704

**ABSTRACT** - Due to its impact on our ecosystem (e.g., vegetation, soil, water, etc.), global change has become more significant over time. Therefore, several biophysical indices (i.e., Normalized Difference Vegetation Index, Modified Soil-Adjusted Vegetation Index, Normalized Difference Water Index, etc.) have been developed to quantify, assess, and monitor the ecosystem's reaction to these changes. Numerous and various satellite imagery might be integrated into multiple mathematical models to carry out this monitoring. One of the efficient models in this field is Time Series Analysis (TSA), which allows the decomposition of data into tree components (i.e., seasonality, irregularity, and trend). In this review paper, we considered more than 300 remote sensing algorithms of different satellites sensors (i.e., AVHRR [2010-2019], SPOT [2010-2014], ASTER [2010-2021], MODIS [2010-2022], Landsat 8 [2013-2022], and Sentinel-2 [2015-2022]). Definitively, 100 biophysical indices have been classified into four different categories (i.e., vegetation algorithms, soil algorithms, water algorithms, and other algorithms). Consequently, more than 300 algorithms were computed in order to conduct a comparative study of their quarterly time series trends from 2010 to 2022. Thus, more than 1800 hyperspectral remotely sensed images retrieved from six different satellites were used to monitor four Mediterranean climate zones (BWh: hot arid, BSk: cold arid, Csa: warm temperate hot summer, Cfa: warm temperate warm summer), as well as the whole Mediterranean region. The Mediterranean climate zones were selected based on Köppen Geiger classification. Accordingly, more than 34000 images have been computed, resulting in huge number of time series charts where many biophysical indices have taken specific forms. Finally, times series trend component was extracted using the Centered Moving Average [CMA] method.

## 1 INTRODUCTION

As the number of years increases, so does global change and its impact on our ecosystem (i.e., Storms, a lack of rain, heat waves, increasing sea levels, etc.), which poses a threat to human future on earth (Kim et al., 2018). Therefore, researchers studying this disaster, intensified their efforts to confront the growth of pests resulting from it, by jargonizing certain concepts (i.e., Energy efficiency, Recycling, Renewable Energy, etc.) and gradually integrating them into our daily lives. (Wang et al., 2011). However, quantifying and monitoring a problem's growth is thought to be the first step in finding a solution; in our case, this involves monitoring the damage caused by global change on vital sectors (i.e., vegetation, water, soil, burn), and that by developing biophysical indices for various categories (i.e., Normalized Difference Vegetation Index [NDVI] (Rouse et al., 1974), Soil Adjusted Vegetation Index

[SAVI] (Huete, 1988), Normalized Difference Water Index [NDWI] (McFEETERS, 1996), etc.), these indices have been evolving over time, to keep up with the appearance of new remote sensing technologies and to expand its use on many global change studies.

The output of computing these indices might be integrated into multiple mathematical models, and one of the most popular methods for analysing multitemporal data in general and remotely sensed data, in particular, is Time Series Analysis (Ezzaher et al., 2022; Naciri et al., 2022; Vogelmann et al., 2012), which quantify the changes occurring on a specific area of our earth over a certain time period, and also predict the future, with the potential to extract the four components (i.e., trend, seasonality, cycle, and irregularity). In this review paper, we present a versatile database containing more than 300 algorithms of 100 biophysical indices on 6 different satellites (i.e., AVHRR, MODIS, SPOT VGT5, SENTINEL 2, ASTER, and LANDSAT 8), which are



characterized by different resolutions (temporal, spatial, and spectral), in addition to the application of these algorithms on more than 1800 images of the 6 different satellites from 2010 to 2022 of the entire Mediterranean region and the 4 Mediterranean climate zones (BWh: hot arid, BSk: cold arid, Csa: warm temperate hot summer, Cfa: warm temperate warm summer) selected based on Köppen Geiger Classification (Beck et al., 2018), in order to conduct a time series study emphasizing these indices' trend components and their reaction to different parameters.

### 3 MATERIALS AND METHODS

#### 3.1 Study area

The study areas for this research are 4 Mediterranean climatic regions selected based on Köppen Geiger classification (i.e., warm temperate hot summer (Csa): Morocco-Tangier, cold arid (BSk): Spain-Murcia, warm temperate warm summer (Cfa): Italy-San Severo, hot arid (BWh): Libya-Tobruk) for high resolution satellite images, as well as the entire Mediterranean region for 1Km resolution satellite images (See figure 1).

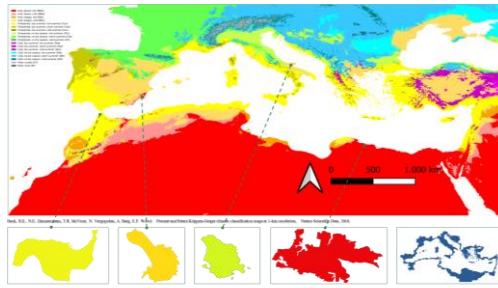


Figure 1. Study area

Partitioning the study areas was based on the administrative zoning provided by OpenStreetMap database using OSM Server Side Scripting.

#### 3.2 Satellite data

Satellite data used in this research are the study areas

seasonal images from 2010 to 2022 of 6 different satellites products (i.e., AVHRR-AVH09C1, SPOT VGT 5-VGTS10, MODIS-MOD09GA, ASTER-ASTLIT, SENTINEL 2-L1C, and LANDSAT 8-L2SP Collection 2), acquired from different platforms, respectively (LAADS DAAC, Terrascope, LPDAAC, and USGS) (Ben Achhab et al., 2018) (See table 1).

The pre-processing of these images consisted of generating monthly composite images for AVHRR data, Cloud masking, and calibration. The later one was carried out for Sentinel 2, Landsat 8, and ASTER using the Semi-Automatic classification plugin (Congedo, 2021), As for SPOT data it was calibrated manually following the SPOT-VGT collection 3 products user manual V1.2.

#### 3.3 Methods

##### a) Biophysical indices computing

100 biophysical indices and their algorithms on 6 satellites (i.e., AVHRR, SPOT VGT5, MODIS, ASTER, SENTINEL 2, and LANDSAT 8) were assembled and sorted by year ascendingly, and by category (i.e., Vegetation, Water, Soil, Others), forming a significant and multipurpose database (see Table 2) (Bannari et al., 1995; Heiskanen, 2006; Yan et al., 2021). Then, using a self-developed software, we computed these algorithms and their means to generate seasonally time series for the 5 study areas from 2010 to 2022 (Ben Achhab et al., 2010).

##### b) Time series analysis

In Time Series Analysis (TSA), imputing missing values is crucial and it can be done using multiple methods (e.g, backward filling, forward filling, average filling, and interpolation). As our seasonal time series follow a yearly cycle, the average filling method was the most suitable. This method consists of filling in the missing quarter of year 'X' by averaging the value of the same quarter in year 'X-1' and 'X+1'.

Table 1. Satellite data.

		2010		2011		2012		2013		2014		2015		2016		2017		2018		2019		2020		2021		2022		Total Size (GB)	Spatial resolution	Temporal resolution
AVHRR	Mediterranean	X	X	X	X	X	X	X	X	X	X	X	X	X	X	X	X	X	X	X	X	X	X	X	X	X	X	493	1 Km	daily
SPOT	Mediterranean	X	X	X	X	X	X	X	X	X	X	X	X	X	X	X	X	X	X	X	X	X	X	X	X	X	X	26	1 Km	composite
MODIS	Tangier	X	X	X	X	X	X	X	X	X	X	X	X	X	X	X	X	X	X	X	X	X	X	X	X	X	X	14	250 m	1-2 days
	Murcia	X	X	X	X	X	X	X	X	X	X	X	X	X	X	X	X	X	X	X	X	X	X	X	X	X	X			
	San Severo	X	X	X	X	X	X	X	X	X	X	X	X	X	X	X	X	X	X	X	X	X	X	X	X	X	X			
	Tobruk	X	X	X	X	X	X	X	X	X	X	X	X	X	X	X	X	X	X	X	X	X	X	X	X	X	X			
ASTER	Tangier				X				X		X		X				X		X		X	X						6.82	15-90 m	-
	Murcia								X			X					X		X		X		X	X	X					
	San Severo												X					X				X		X						
	Tobruk		X									X							X				X							
SENTINEL	Tangier												X	X	X	X	X	X	X	X	X	X	X	X	X	X	X	76	10-60 m	10 days
	Murcia												X	X	X	X	X	X	X	X	X	X	X	X	X	X	X			
	San Severo													X	X	X	X	X	X	X	X	X	X	X	X	X	X			
	Tobruk													X	X	X	X	X	X	X	X	X	X	X	X	X	X			
LANDSAT	Tangier								X	X	X	X	X	X	X	X	X	X	X	X	X	X	X	X	X	X	X	122	15-30 m	16 days
	Murcia								X	X	X	X	X	X	X	X	X	X	X	X	X	X	X	X	X	X	X			
	San Severo									X	X	X	X	X	X	X	X	X	X	X	X	X	X	X	X	X	X			
	Tobruk									X	X	X	X	X	X	X	X	X	X	X	X	X	X	X	X	X	X			



In this study, TSA consists of visualizing the data and decomposing its three main components (i.e., Trend, Seasonality, and Irregularity), wherefore, the multiplicative model was used to represent data (see equation 1):

$$Y_t = S_t \times I_t \times T_t \quad (1)$$

where  $Y_t$  is the time series,  $S_t$  and  $T_t$  are respectively Seasonality and Trend.

Besides, the Centered Moving Average (CMA) method was used to extract the trend component (Liu et al., 2020; Masselot et al., 2018). As a first step, a Moving Average (MA) was calculated with a width window of 4 (i.e., averaging the value of the window at time  $t$  and then moving it). Since the width window is an even number, its CMA was calculated to get smoothed data. The next step was to deseasonalize the time series (i.e., eliminate the seasonal and the irregular components), to finally extract the trend by employing linear regression method providing the slope and intercept of the trend's equation (see equation 2):

$$T = at + b \quad (2)$$

Where  $T$  is the trend,  $a$  and  $b$  respectively the slope and the intercept, and  $t$  the time code.

#### 4 RESULTS

In this paper, computing indices yielded more than 34000 output images and 1138 time series [(37 SPOT's algorithms + 21 AVHRR's algorithms) x All Mediterranean region + (88 SENTINEL's algorithms + 48 ASTER's algorithms + 75 LANDSAT's algorithms + 59 MODIS's algorithms (see figure 2)) x 4 Climate zones = 1138], where their seasonality component are clearly apparent, especially for the warm temperate regions.

Each time series trend was extracted using the CMA method, which resulted in a wealth of data that can be branched to many major studies in different fields (ASTER was excluded from this step as its data is insufficient to use this method). Resulting trends were represented by index, see figure below for an example of 30 indices trends. Trends graphs were framed by category (Vegetation, Water, Soil, and Others) as specified in table 2, and their time axis was represented seasonally from 2010 to 2021 (1: Winter, 2: Spring, 3: Summer, and 4: Autumn), as for the Y axis it shows the indices values, with ranges adjusted for each index.

In trends graphs, the clustering of each zones trends with an order that varies depending on the relevance of

each index is obvious, which makes the area impact quite clear in the trend figures of most indices.

It is also noticeable that in many instances, the trend of an index in the same zone measured by different satellites changes, and this may be because of a variety of factors, including the study time period of each satellite, since adding the value of one date would change the trend's equation and thus the line. This is in addition to the variation of satellites characteristics, as each one has different temporal, spatial, and spectral resolutions, as mentioned in table 1, and this point has a significant impact on the response of the index as monitoring a zone with a spatial resolution of 10m is not the same as 500m and 1Km the same applies to the other types of resolutions.

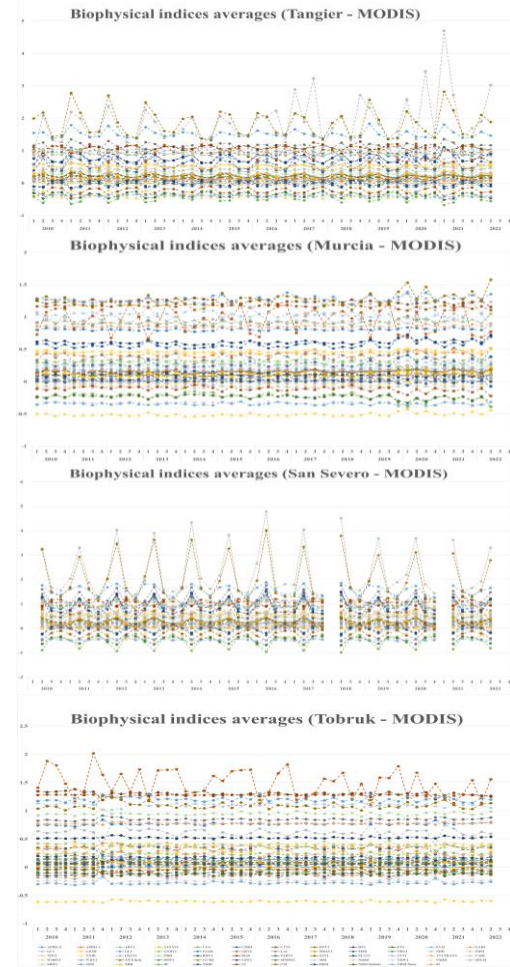


Figure 2. Biophysical indices Averages (MODIS images), 1: Winter, 2: Spring, 3: Summer, and 4: Autumn

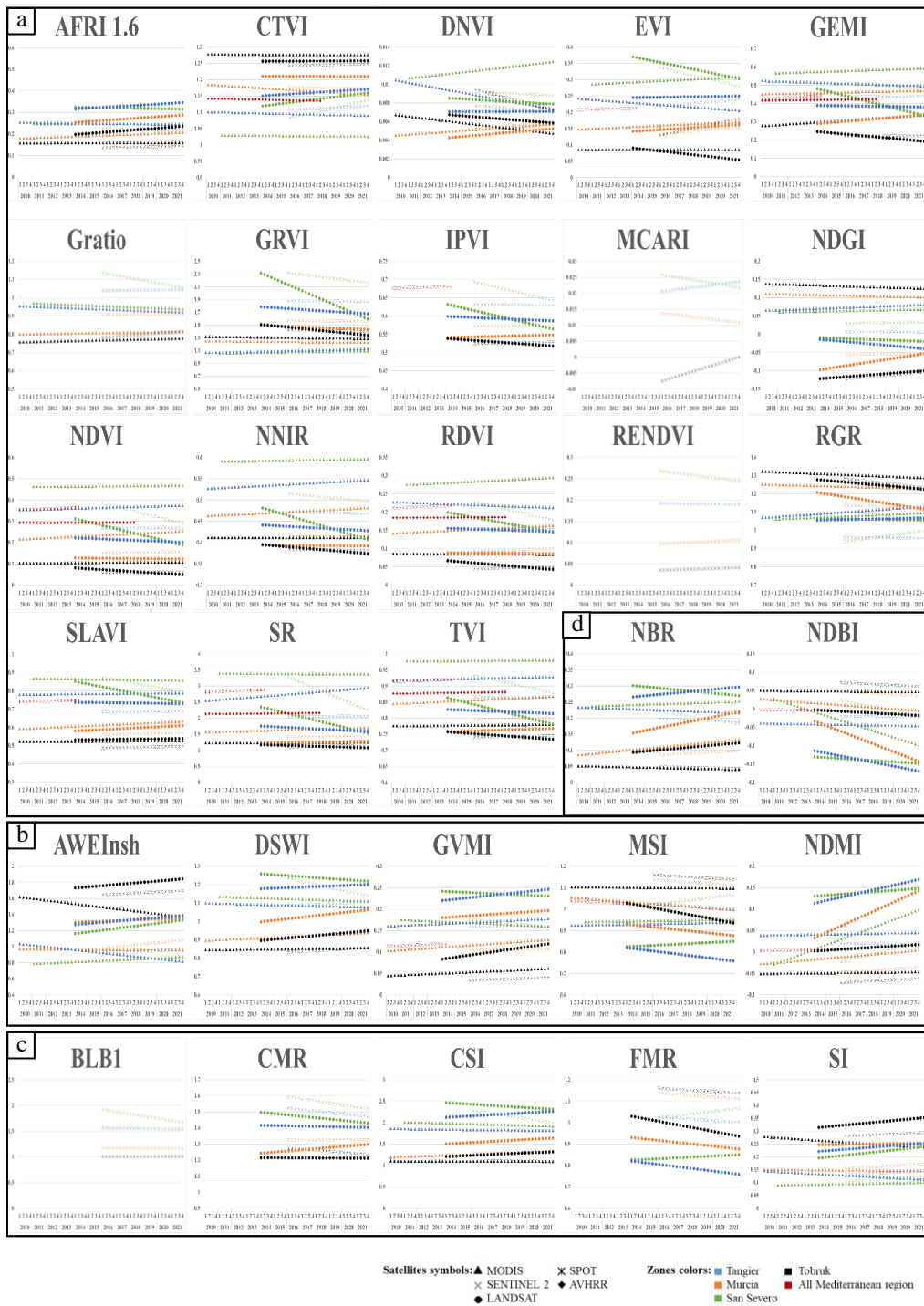


Figure 3. Biophysical indices trends, a: vegetation indices, b: water indices, c: soil indices, d: others indices

## 5 CONCLUSION

In this research, a database assembling more than 300 biophysical indices algorithms of 6 satellites (i.e., AVHRR, SPOT VGT5, MODIS, ASTER, SENTINEL 2, and LANDSAT 8), sorted by category (i.e., Vegetation, Water, Soil, and Others) and by year was presented. Then, the database algorithms were used on 1700 satellites images of 5 zones (Tangier, Murcia, San Severo, Tobruk, and all Mediterranean region) from 2010 to 2022, yielding more than 34000 output images and 1138 time series. Applying the CMA method on time series permitted the extraction of their trend component. Trends results demonstrated the impact of various factor such as climate zone, satellite resolutions, and time period, on indices responses.

## 6 ACKNOWLEDGEMENT

This work is supported in part by the University Abdelmalek Essaâdi Thematic project, 2019 – 2022, Monitoring land cover dynamics of the TTA region in the context of global warming: Contribution of Earth's observation satellites and high-performance computing

## 7 REFERENCES

- Bannari, A., Morin, D., Bonn, F., Huete, A.R., 1995. A review of vegetation indices. *Remote Sens. Rev.* 13, 95–120.
- Beck, H.E., Zimmermann, N.E., McVicar, T.R., Vergopolan, N., Berg, A., Wood, E.F., 2018. Present and future Köppen-Geiger climate classification maps at 1-km resolution. *Sci. Data* 5, 180214.
- Ben Achhab, N., Raissouni, N., NAOUFAL, ABDELILAH, A., Asaad, C., Lahraoua, M., 2010. High performance computing software package for multitemporal Remote-Sensing computations. *Int. J. Eng. Technol.* 2.
- Ben Achhab, N., Raissouni, N., Sobrino, J.A., Chahboun, A., Azyat, A., Lahraoua, M., El Adib, S., 2018. A high performance GPU implementation for multitemporal analysis of huge satellite remote sensing databases. *Fifth Recent Adv. Quant. Remote Sens.* 356.
- Congedo, L., 2021. Semi-Automatic Classification Plugin: A Python tool for the download and processing of remote sensing images in QGIS. *J. Open Source Softw.* 6, 3172.
- Ezzaher, F.E., Ben Achhab, N., Naciri, H., Raissouni, N., 2022. PROBA-V MEP monitoring NDVI variations in Mediterranean countries from 2014 to 2020. pp. 206–218.
- Heiskanen, J., 2006. Estimating aboveground tree biomass and leaf area index in a mountain birch forest using ASTER satellite data. *Int. J. Remote Sens. - INT J REMOTE SENS* 27.
- Huete, A.R., 1988. A soil-adjusted vegetation index (SAVI). *Remote Sens. Environ.* 25, 295–309.
- Kim, Y., Kong, I., Park, H., Kim, H.J., Kim, I.J., Um, M.-J., Green, P.A., Vörösmarty, C.J., 2018. Assessment of regional threats to human water security adopting the global framework: A case study in South Korea. *Sci. Total Environ.* 637–638, 1413–1422.
- Liu, X., Schnelle-Kreis, J., Zhang, X., Bendl, J., Khedr, M., Jakobi, G., Schlöter-Hai, B., Hovorka, J., Zimmermann, R., 2020. Integration of air pollution data collected by mobile measurement to derive a preliminary spatiotemporal air pollution profile from two neighboring German-Czech border villages. *Sci. Total Environ.* 722, 137632.
- Masselot, P., Chebana, F., Bélanger, D., St-Hilaire, A., Abdous, B., Gosselin, P., Ouarda, T.B.M.J., 2018. Aggregating the response in time series regression models, applied to weather-related cardiovascular mortality. *Sci. Total Environ.* 628–629, 217–225.
- McFEETERS, S.K., 1996. The use of the Normalized Difference Water Index (NDWI) in the delineation of open water features. *Int. J. Remote Sens.* 17, 1425–1432.
- Naciri, H., Ben Achhab, N., Ezzaher, F.E., Raissouni, N., 2022. Global change impact on Sub-Saharan Africa regions: vegetation evolution based PROBA-V TOC NDVI. pp. 219–233.
- Rouse, J.W., Jr., Haas, R.H., Schell, J.A., Deering, D.W., 1974. Monitoring Vegetation Systems in the Great Plains with ERTS. *NASA Spec. Publ.* 351, 309.
- Vogelmann, J.E., Xian, G., Homer, C., Tolk, B., 2012. Monitoring gradual ecosystem change using Landsat time series analyses: Case studies in selected forest and rangeland ecosystems. *Remote Sens. Environ., Landsat Legacy Special Issue* 122, 92–105.
- Wang, J., Botterud, A., Bessa, R., Keko, H., Carvalho, L., Issicaba, D., Sumaili, J., Miranda, V., 2011. Wind power forecasting uncertainty and unit commitment. *Appl. Energy* 88, 4014–4023.
- Yan, S., Yao, X., Zhu, D., Liu, D., Zhang, L., Yu, G., Gao, B., Yang, J., Yun, W., 2021. Large-scale crop mapping from multi-source optical satellite imageries using machine learning with discrete grids. *Int. J. Appl. Earth Obs. Geoinformation* 103, 102485.

# Mediterranean Basin Vegetation Forecasting Approaches: Accuracy Analysis & Climate-Land Cover-Sensor nexus Impacts

H. Naciri<sup>1,2</sup>, N. Ben Achhab<sup>1,2</sup>, F-E. Ezzaher<sup>1,2</sup>, J. A. Sobrino<sup>3</sup>, N. Raissouni<sup>1,4</sup>,

<sup>1</sup> Remote Sensing & Geographic Information System Unit (RS&GIS), University of Abdelmalek Essaadi, Morocco.

<sup>2</sup> Mathematics and Intelligent Systems (MASI), University of Abdelmalek Essaadi, Morocco.

<sup>3</sup> Goba Change Unit (GCU)- Imaging Processing Lab. (IPL), University of Valencia, Spain.

<sup>4</sup> Remote Sensing, Systems and Telecommunications (TST), University of Abdelmalek Essaadi, Morocco.

Email addresses : nbenachhab@uae.ac.ma, [nraissouni@uae.ac.ma](mailto:nraissouni@uae.ac.ma)

**ABSTRACT** - From land degradation and desertification to cyclones and tropical storms, and so on, the repercussions of global change have become increasingly severe in recent years. Consequently, land cover forecasting is now required in order to assess and monitor such environmental impacts, although it remains a challenging task. Indeed, to study and analyse these impacts, several time series forecasting models have been widely developed. In this study, accuracy of the most used forecasting approaches has been quantified taking into consideration three impacts (i.e., climate regions, land cover, and satellite sensor). Firstly, three different forecasting approaches (i.e., Long Short Term Memory Network (LSTM), convolutional LSTM, and moving average) were used for predicting vegetation biophysical indices (i.e., Normalized Difference Vegetation Index (NDVI), Enhanced Vegetation Index (EVI), Chlorophyll Vegetation Index (CVI), etc.). Secondly, eight Mediterranean regions (north and south) were selected (i.e., 2 regions hot arid, 2 regions cold arid, 2 regions warm temperate hot summer, 2 regions warm temperate warm summer) based on Köppen climate classification. Using 993 hyperspectral images retrieved from USGS satellite images database (i.e., MODIS, Landsat 8 OLI/TIRS, and Sentinel 2) from 2015 to 2022. Accordingly, more than 20000 images were computed resulting in 720 time series forecasted using the aforementioned approaches. Finally, 2160 forecasted time series has been determined and compared, and the computed approaches' corresponding accuracies are showing interesting and promising results.

**Keywords:** Mediterranean basin, vegetation forecasting, LSTM, moving average, time series.

## 1 INTRODUCTION

One of the foundational elements of the terrestrial ecosystem is vegetation which is considered as a significant environmental indicator. Indeed, vegetation can both influence and be influenced by various factor majorly relating to climatic changes. As well, forecasting studies in land use and land cover are extremely useful for analysing vegetation time series and predicting directions of future patterns and trends in a specific period of time. This, has been a challenging or impossible task until a few years ago. However, with the emergence of machine learning (Liu et al., 2017) methods based on artificial neural networks, complicated and deep features has become more accessible.

Within this context, Mediterranean basin is considered in this study because it is one of the world's biodiversity hot-spots due to it profound environmental heterogeneities and its complex historical biogeography (Mittermeier et al., 2011). So,

using very high resolution satellite images of eight different climate regions (Köppen, 1900) selected from the Mediterranean zone and derived from three different satellites (i.e., Sentinel-2, Landsat-8 and MODIS), we conducted a multitude of vegetation analysis based time series from 2015 to 2022, by computing 30 biophysical indices. Then, we quantified the accuracy of two types of forecasting approaches: i) statistical (i.e., Moving Average (MA)) and ii) machine learning (ML) approach (i.e., Long Short Term Memory Network (LSTM) (Hochreiter and Schmidhuber, 1997), Convolutional LSTM (ConvLSTM) (SHI et al., 2015)).

The paper is organized as follows: first we present the materials including study areas and satellite data, then we explain both approaches in the context of time series forecasting then we present the results as we compare the accuracy of both approaches in order to analyse climate, land cover and sensor nexus impacts in the Mediterranean region.



## 2 MATERIALS

### 2.1 Study areas

In this work we used the Köppen-Geiger climate classification maps to select 8 study areas in the Mediterranean regions, four regions located in north and the other four in the south, with four different climate zones. The first four regions main climate is arid with hot and cold temperature (i.e. BWh: Libya-Tobruk, Egypt-Matrouh; BSk: Spain-Valencia, Spain-Murcia), while the main climate for the other four regions is warm temperate (i.e. Cfa: Italy-Padova, Italy-San Severo ; Csa: Morocco-Tangier, Algeria-Oran).

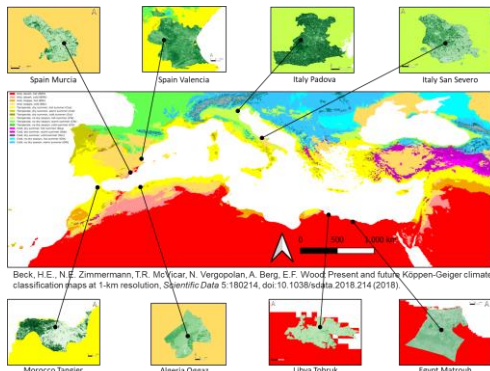


Figure 1. Mediterranean regions

### 2.2 Satellite data

In this study, 7 years (from 2015 to 2022) of Landsat-8 Operational Land Imager (OLI) surface reflectance data at 30m spatial resolution were used over the eight study areas, providing 331 hyper-spectral images with a total size of 255GB. In addition, Sentinel-2A data were derived between 2016 and 2022 over the eight study areas providing information in 13 bands in the visible, near infra-red and short wave infra-red spectrum at a 10, 20, and 60m spatial resolution depending on the band. Sentinel data size is 228GB with 302 images. MODIS Terra Surface Reflectance Daily products were used as well in this study, with 7

bands at 500m and 1km with a total size 32GB.

For each year, four images were selected representing the four seasons (see Table 1): Winter, Spring, Summer, and Autumn to monitor vegetation variation in studies regions. Both Landsat-8 and Sentinel-2A were downloaded through the United States Geological Survey (USGS) Earth Resources Observation and Science (EROS) Center Science Processing Architecture (ESPA), while MODIS images were downloaded from NASA's Earth Observing System Data and Information System (EOSDIS).

## 3 METHODOLOGY

Time series analysis and forecasting can be obtained by several methods of which there are statistical models such as AutoRegressive (AR), univariate Moving Average (MA), and Autoregressive Integrated Moving Average (ARIMA), etc. On the other hand, with the recent outbreak of more advanced machine learning algorithms and approaches, namely in deep learning (DL), new algorithms are developed to analyse and forecast time series data such as Recurrent Neural Networks (RNN), Convolutional Neural Networks (CNN), and latterly the Long Short Term Memory Network (LSTM). In our case, we have studied the accuracy of time series forecasting by adopting the Moving Average (MA) as statistical approach, and Long Short Term Memory Network (LSTM) (Ngoc Hai et al., 2020; Patterson and Gibson, 2017) as well as the convolutional LSTM (Conv-LSTM) as machine learning approaches.

### 3.1 Computed biophysical indices

In order to evaluate and analyse both statistical and ML models accuracy relating to land cover forecasting, 30 different vegetation indices were assembled and sorted by year ascendingly. Then, 15 of them were computed using a self-developed software with a focus on producing their time series that will be applied in forecasting approaches. The Table 2 reorganizes 30 biophysical vegetation algorithms by year and satellite.

Table 1. Satellite data

Year	Season	Tanger				Oran				Tobruk				Matrouh				Murcia				Valencia				Padova				San Severo			
		LANDSAT	MODIS	SENTINEL	DATE	LANDSAT	MODIS	SENTINEL	DATE	LANDSAT	MODIS	SENTINEL	DATE	LANDSAT	MODIS	SENTINEL	DATE	LANDSAT	MODIS	SENTINEL	DATE	LANDSAT	MODIS	SENTINEL	DATE	LANDSAT	MODIS	SENTINEL	DATE	LANDSAT	MODIS	SENTINEL	DATE
2015	Winter	03-jan	01-jan	08-feb	01-jan	23-jan	23-jan	02-jan	23-jan	29-dec	01-jan	14-jan	01-jan	13-jan	12-jan	13-jan	13-jan	29-dec	01-jan	14-jan	01-jan	13-jan	12-jan	13-jan	13-jan	29-dec	01-jan	14-jan	01-jan	13-jan	12-jan	13-jan	13-jan
	Spring	30-avr	29-avr	30-avr	13-avr	18-avr	18-avr	02-jan	23-jan	24-avr	18-avr	02-jan	23-jan	24-avr	18-avr	02-jan	23-jan	24-avr	18-avr	02-jan	23-jan	24-avr	18-avr	02-jan	23-jan	24-avr	18-avr	02-jan	23-jan	24-avr	18-avr	02-jan	23-jan
	Summer	07-jul	05-jul	18-jul	05-jul	18-jul	05-jul	02-jul	13-jul	02-jul	02-jul	02-jul	02-jul	13-jul	02-jul	02-jul	02-jul	13-jul	02-jul	02-jul	02-jul	13-jul	02-jul	02-jul	13-jul	02-jul	02-jul	02-jul	02-jul	02-jul	02-jul	02-jul	
	Autumn	09-sep	22-sep	19-sep	22-sep	02-sep	02-sep	02-sep	02-sep	02-sep	02-sep	02-sep	02-sep	02-sep	02-sep	02-sep	02-sep	02-sep	02-sep	02-sep	02-sep	02-sep	02-sep	02-sep	02-sep	02-sep	02-sep	02-sep	02-sep	02-sep	02-sep	02-sep	
2016	Winter	16-jan	16-jan	10-jan	16-jan	02-jan	02-jan	05-jan	09-jan	05-jan	05-jan	05-jan	06-jan	17-jan	16-jan	12-jan	02-feb	16-jan	12-jan	16-jan	17-jan	20-jan	13-jan	13-jan	16-jan	12-jan	16-jan	17-jan	20-jan	13-jan	13-jan	13-jan	
	Spring	09-avr	07-avr	14-mai	09-avr	18-avr	15-avr	19-avr	21-avr	10-avr	19-avr	09-avr	09-avr	09-avr	09-avr	09-avr	09-avr	09-avr	09-avr	09-avr	09-avr	09-avr	09-avr	09-avr	09-avr	09-avr	09-avr	09-avr	09-avr	09-avr	09-avr	09-avr	
	Summer	02-jul	20-jul	05-aout	02-jul	17-jul	13-jul	04-jul	20-jul	15-jul	04-jul	14-jul	11-jul	02-jul	30-jul	11-jul	02-jul	20-jul	11-jul	02-jul	20-jul	11-jul	02-jul	20-jul	11-jul	02-jul	20-jul	11-jul	02-jul	20-jul	11-jul	02-jul	
	Autumn	30-sep	24-sep	19-sep	11-oct	24-sep	20-sep	09-sep	09-sep	10-sep	06-oct	09-sep	17-sep	24-sep	13-sep	19-sep	24-sep	13-sep	30-aout	21-sep	12-oct	15-sep	15-sep	15-sep	15-sep	15-sep	15-sep	15-sep	15-sep	15-sep	15-sep	15-sep	
2017	Winter	11-jan	02-jan	17-jan	16-feb	02-jan	16-jan	08-jan	13-jan	08-jan	27-feb	13-jan	20-jan	22-jan	02-jan	16-jan	22-jan	02-jan	16-jan	22-jan	02-jan	16-jan	22-jan	02-jan	16-jan	22-jan	02-jan	16-jan	22-jan	02-jan	16-jan	22-jan	
	Spring	17-avr	17-avr	17-avr	05-avr	17-avr	01-avr	05-avr	01-avr	23-avr	31-mai	01-avr	01-avr	28-avr	17-avr	16-avr	27-mai	17-avr	27-mai	26-mai	20-avr	19-avr	22-avr	26-avr	13-avr	02-jul	02-jul	02-jul	02-jul	02-jul	02-jul		
	Summer	06-jul	16-jul	16-jul	24-jul	16-jul	05-jul	03-jul	03-jul	03-jul	03-jul	03-jul	04-jul	17-jul	16-jul	10-jul	17-jul	16-jul	10-jul	17-jul	16-jul	10-jul	17-jul	16-jul	10-jul	17-jul	16-jul	10-jul	17-jul	16-jul	10-jul	17-jul	
	Autumn	24-sep	24-sep	19-sep	30-sep	24-sep	28-sep	28-sep	18-sep	18-sep	23-sep	18-sep	02-oct	19-sep	24-sep	19-sep	24-sep	19-sep	24-sep	19-sep	24-sep	19-sep	24-sep	19-sep	24-sep	19-sep	24-sep	19-sep	24-sep	19-sep	24-sep	19-sep	
2018	Winter	07-jan	13-jan	17-jan	02-jan	13-jan	01-jan	11-jan	22-jan	18-jan	14-fev	22-jan	19-jan	05-jan	13-jan	05-jan	13-jan	05-jan	13-jan	05-jan	13-jan	05-jan	13-jan	05-jan	13-jan	05-jan	13-jan	05-jan	13-jan	05-jan	13-jan	05-jan	
	Spring	13-avr	27-avr	17-avr	10-mai	27-avr	16-avr	08-avr	27-avr	11-avr	27-avr	25-avr	15-avr	27-avr	26-avr	01-mai	27-avr	27-avr	27-avr	27-avr	27-avr	27-avr	27-avr	27-avr	27-avr	27-avr	27-avr	27-avr	27-avr	27-avr	27-avr	27-avr	
	Summer	18-jul	04-jul	16-jul	29-jul	09-jul	15-jul	22-jul	29-jul	22-jul	08-jul	29-jul	09-jul	20-jul	09-jul	20-jul	09-jul	20-jul	09-jul	20-jul	09-jul	20-jul	09-jul	20-jul	09-jul	20-jul	09-jul	20-jul	09-jul	20-jul	09-jul	20-jul	
	Autumn	27-sep	24-sep	09-sep	17-oct	24-sep	30-sep	24-sep	03-oct	10-oct	02-sep	12-sep	22-sep	12-sep	22-sep	12-sep	22-sep	12-sep	22-sep	12-sep	22-sep	12-sep	22-sep	12-sep	22-sep	12-sep	22-sep	12-sep	22-sep	12-sep	22-sep	12-sep	
2019	Winter	01-jan	12-jan	07-jan	05-jan	12-jan	08-jan	05-jan	13-jan	13-jan	04-mai	13-jan	30-jan	12-jan	12-jan	11-jan	12-jan	11-jan	12-jan	11-jan	12-jan	11-jan	12-jan	11-jan	12-jan	11-jan	12-jan	11-jan	12-jan	11-jan	12-jan	11-jan	
	Spring	01-mai	29-avr	21-mai	29-avr	27-avr	19-avr	13-avr	03-mai	21-avr	13-avr	14-avr	03-mai	29-avr	30-avr	03-mai	29-avr	30-avr	03-mai	29-avr	30-avr	03-mai	29-avr	30-avr	03-mai	29-avr	30-avr	03-mai	29-avr	30-avr	03-mai	29-avr	
	Summer	20-jul	06-jul	15-jul	29-jul	06-jul	15-jul	01-jul	16-jul	26-jul	01-jul	03-jul	06-jul	06-jul	06-jul	06-jul	06-jul	06-jul	06-jul	06-jul	06-jul	06-jul	06-jul	06-jul	06-jul	06-jul	06-jul	06-jul	06-jul	06-jul	06-jul	06-jul	
	Autumn	29-sep	28-sep	28-sep	01-oct	28-sep	27-sep	26-sep	05-oct	24-sep	28-sep	05-sep	26-sep	28-sep	22-sep	13-oct	28-sep	22-sep	13-oct	28-sep	22-sep	13-oct	28-sep	22-sep	13-oct	28-sep	22-sep	13-oct	28-sep	22-sep	13-oct	28-sep	
2020	Winter	12-jan	03-jan	28-sep	12-oct	03-jan	12-jan	17-jan	31-jan	30-jan	18-jan	31-jan	09-jan	14-jan	09-jan	15-jan	14-jan	09-jan	15-jan	14-jan	09-jan	15-jan	14-jan	09-jan	15-jan	14-jan	09-jan	15-jan	14-jan	09-jan	15-jan	14-jan	
	Spring	18-avr	18-avr	06-avr	12-mai	18-avr	20-avr	22-avr	22-avr	12-avr	08-avr	22-avr	04-avr	06-mai	18-avr	05-mai	06-mai	18-avr	05-mai	06-mai	18-avr	05-mai	06-mai	18-avr	05-mai	06-mai	18-avr	05-mai	06-mai	18-avr	05-mai		
	Summer	07-jul	21-jul	20-jul	02-aout	21-jul	24-jul	11-jul	13-jul	06-jul	13-jul	13-jul	03-jul	21-jul	19-jul	14-jul	22-jul	06-jul	14-jul	22-jul	06-jul	14-jul	22-jul	06-jul	14-jul	22-jul	06-jul	14-jul	22-jul	06-jul	14-jul		
	Autumn	04-sep	18-sep	04-sep	04-sep	12-sep	20-sep	21-sep	22-sep	30-aout	21-sep	21-sep	13-sep	04-sep	17-sep	27-sep	04-sep	17-sep	27-sep	04-sep	17-sep	27-sep	04-sep	17-sep	27-sep	04-sep	17-sep	27-sep	04-sep	17-sep	27-sep	04-sep	
2022	Winter	07-jan	16-jan	06-jan	10-jan	16-jan	10-jan	03-jan	07-jan	07-jan	06-fev	07-jan	04-jan	17-jan	16-jan	20-jan	17-jan	16-jan	15-jan	16-jan	18-avr	08-jan	19-jan	11-avr	17-jan	16-jan	15-jan	16-jan	18-avr	08-jan	19-jan	11-avr	
	Summer	07-mai	16-avr	16-avr	08-avr	10-avr	16-avr	10-avr	03-avr	07-avr	27-avr	14-avr	09-avr	07-avr	16-avr	25-avr	20-jul	15-jul	14-jul	03-jul	17-jul	18-avr	11-mai	20-jul	12-avr	16-jan	24-sep	16-jan	24-sep	16-jan	24-sep		

Table 2. Sentinel, Landsat, and MODIS vegetation biophysical indices algorithms

Biophysical index		Sentinel 2	Landsat 8	MODIS
SR	1969	band8/band4	band5/band4	band2/band1
NDVI	1973	(Band8 - Band4)/(Band8 + Band4)	(Band5 - Band4)/(Band5 + Band4)	(Band2 - Band1)/(Band2 + Band1)
TVI	1975	sqrt(0.5 + NDVI)	sqrt(0.5 + NDVI)	sqrt(0.5 + NDVI)
DVI	1979	Band8 - Band4	Band5 - Band4	Band2 - Band1
CTVI	1984	(NDVI+0.5)/ (Abs(NDVI+0.5))*sqrt(Abs(NDVI+0.5))	(NDVI+0.5)/ (Abs(NDVI+0.5))*sqrt(Abs(NDVI+0.5))	(NDVI+0.5)/ (Abs(NDVI+0.5))*sqrt(Abs(NDVI+0.5))
WDVI	1989	band8 - $\gamma$ band4, $\gamma=0.5$	band5 - $\gamma$ band4, $\gamma=1.06$	band2 - $\gamma$ band1, $\gamma=1.06$
NDGI	1991	(band3-band4)/(band3+band4)	(band3-band4)/(band3+band4)	(band1-band4)/(band1+band4)
GEMI	1992	eta*(1-0.25*eta)-((band4-0.125)/(1-band4)), eta= (2*(band8^2-band4^2)+1.5*band8+ 0.5*band4)/(band8+band4+0.5)	eta*(1-0.25*eta)-((band4-0.125)/(1-band4)), eta= (2*(band5^2-band4^2)+1.5*band5+ 0.5*band4)/(band5+band4+0.5)	eta*(1-0.25*eta)-((band1-0.125)/(1-band1)), eta= (2*(band2^2-band1^2)+1.5*band2+ 0.5*band1)/(band2+band1+0.5)
ARVI	1992	(band8 - band4 - $\gamma$ *(band4 - band2))/ (band8 + band4 - $\gamma$ *(band4 - band2)), $\gamma=1$	(band5 - band4 - $\gamma$ *(band4 - band2))/ (band5 + band4 - $\gamma$ *(band4 - band2)), $\gamma=1$	(band2 - band1 - $\gamma$ *(band1 - band3))/ (band2 + band1 - $\gamma$ *(band1 - band3)), $\gamma=1$
GRVI	1993	band8/band3	band5/band3	band1/band4
EVI	1995	G*(Band8 - Band4)/(Band8 + C1*Band4 - C2*Band2 + L), G= 2.5 C1=6 C2=7.5 L=1	G*(Band5 - Band4)/(Band5 + C1*Band4 - C2*Band2 + L), G= 2.5 C1=6 C2=7.5 L=1	G*(Band2 - Band1)/(Band2 + C1*Band1 - C2*Band3 + L), G= 2.5 C1=6 C2=7.5 L=1
RDVI	1995	(band8 - band4)/sqrt(band8 + band4)	(band5 - band4)/sqrt(band5 + band4)	(band2 - band1)/sqrt(band2 + band1)
GNDVI	1996	(Band8 - Band3)/(Band8 + Band3)	(Band5 - Band3)/(Band5 + Band3)	(Band2 - Band4)/(Band2 + Band4)
GARI	1996	(band8-(band3- $\gamma$ (band2 - band4)))/ (band8+(band3- $\gamma$ (band2 - band4))), $\gamma=1.7$	(band5-(band3- $\gamma$ (band2-band4)))/ (band5+(band3- $\gamma$ (band2-band4))), $\gamma=1.7$	(band2-(band4- $\gamma$ (band3-band1)))/ (band2+(band4- $\gamma$ (band3-band1))), $\gamma=1.7$
MSR	1996	((band8/band4) - 1)/(sqrt(band8/band4) + 1)	((band5/band4) - 1)/(sqrt(band5/band4) + 1)	((band2/band1) - 1)/(sqrt(band2/band1) + 1)
PSRI	1999	(band4-Band2)/Band8	(band4-band2)/band5	(band1-band3)/band2
RGR	1999	band4/band3	band4/band3	band1/band4
SLAVI	2000	band8/(band4+band11)	band5/(band4+band6)	band2/(band1+band6)
AFRIL6	2001	(Band8 - 0.66*band11)/(Band8 + 0.66*band11)	(band5 - 0.66*band6)/(band5 + 0.66*band6)	(band2 - 0.66*band6)/(band2 + 0.66*band6)
AFRI 2.1	2001	(band8 - 0.5*band12)/(band8 + 0.5*band12)	(band5 - 0.5*band7)/(band5 + 0.5*band7)	(band2 - 0.5*band7)/(band2 + 0.5*band7)
GLI	2001	(2*band3 - band4 - band2)/ (2*band3 + band4 + band2)	(2*band3 - band4 - band2)/ (2*band3 + band4 + band2)	(2*band4 - band1 - band3)/ (2*band4 + band1 + band3)
VARI	2002	(band3 - band4)/(band3 + band4 - band2)	(band3 - band4)/(band3 + band4 - band2)	(band4 - band1)/(band4 + band1 - band3)
GCI	2003	(band8/band3)-1	(Band5/Band3)-1	(Band2/Band4)-1
LAI	2003	3.16 EVI - 0.118	3.16 EVI - 0.118	3.16 EVI - 0.118
WDRVI	2004	(0.2*band8-band4)/(0.2*band8+band4)	(0.2*band5-band4)/(0.2*band5+band4)	(0.2*band2-band1)/(0.2*band2+band1)
NNIR	2006	band8/(band8+ band4 + band3)	band5/(band5+ band4 + band3)	band2/(band2+ band1 + band4)
CVI	2007	(band8*band4)/(band3^2)	(Band5*Band4)/(Band3^2)	(Band2*Band1)/(Band4^2)
EVI2	2008	2.5 * [(band8 - band4)/(band8 + 2.4 band4 + 1)]	2.5 * [(band5 - band4)/(band5 + 2.4 band4 + 1)]	2.5 * [(band2 - band1)/(band2 + 2.4 band1 + 1)]
CMRI	2018	[(band8-band4)/(band8+band4)] - [(band3-band8)/(band3+band8)]	[(band5-band4)/(band5+band4)] - [(band3-band5)/(band3+band5)]	[(band2-band1)/(band2+band1)] - [(band4-band2)/(band4+band2)]
DNVI	2018	(band11-band12)^2/sqrt(band11+band12)	(band6-band7)^2/sqrt(band6+band7)	(band6-band7)^2/sqrt(band6+band7)

### 3.2 Classical statistic approach

Based on the statistical concept, MA is used to forecast vegetation time series. It takes into accounts dependency between observations and residual error terms when a moving average model is used to the lagged observations ( $q$ ). An MA model of order  $q$  MA( $q$ ), can be written in the form (see equation 1):

$$x_t = \mu + \sum_{i=0}^q \theta_i \varepsilon_{t-i} \quad (1)$$

Where  $\mu$  is the expectation of  $x_t$  (usually assumed equal to zero), the  $\theta_i$  terms are the weights applied to the current and prior values of a stochastic term in the time series, and  $\theta_0=1$ . We assume that  $\varepsilon_t$  is a Gaussian white noise series with mean zero and variance  $\sigma_\varepsilon^2$ .

### 3.3 Machine learning approach

Many different types of machine learning algorithms have been designed to conduct time series forecasting. In this part, one of the most used approaches in machine learning, namely LSTM is introduced.

#### 3.3.1 Long Short Term Memory Network (LSTM)

Long Short Term Memory Network (LSTM) is a type of Recurrent Neural Network (RNN) with the purpose to architect temporal sequences that may solve prediction problems.

Before implementing data into our LSTM model, it must follow a specific procedure that begins with data normalization because LSTM uses sigmoid and tanh that are sensitive to magnitude. After that the data is split into train and test sets which will be reshaped as X and y samples. Next step is to define our model with 64 LSTM units in the hidden layer and an output layer that predicts a single numerical value (see figure 2).

The mean squared error, or "mse" loss function is used to optimize the model after it has been fitted using the effective Adam form of stochastic gradient descent. Finally, the model is called to predict data.



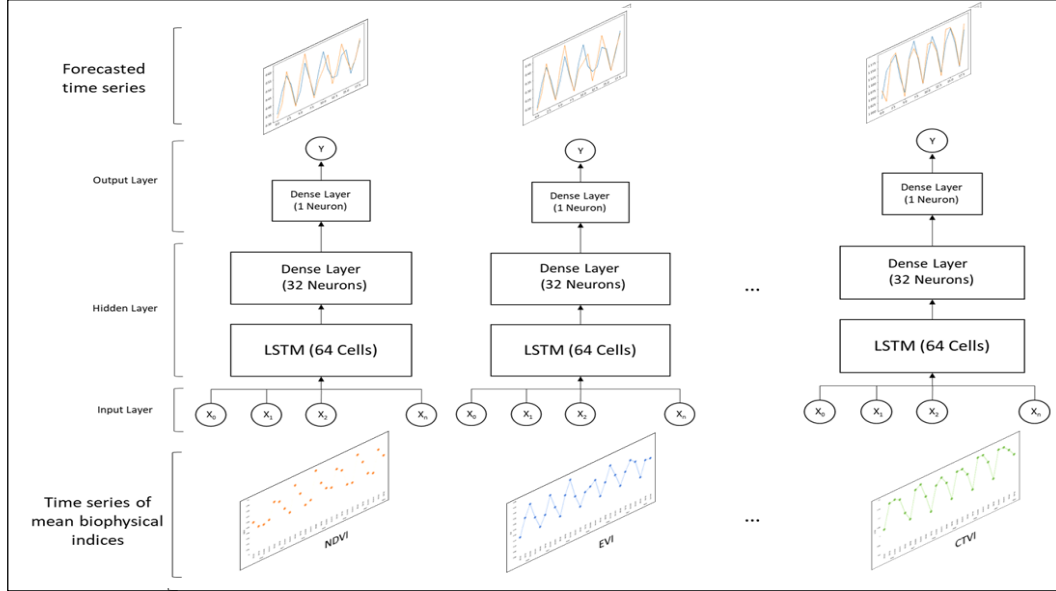


Figure 2. LSTM architecture

### 3.3.2 Conv-LSTM

This model is considered a fusion of two methods (i.e., convolutional neural network and LSTM) where each LSTM unit has the convolutional reading of the input embedded right in. This method's pre-processing phase differ from the LSTM one, specifically in reshape step as subsequence parameter is introduced before building our model. This last contains a single layer with 64 filters and a two-dimensional kernel size (rows, columns). Since we are dealing with a one-dimensional series, the kernel's fixed-row number is always 1. The output of the model must then be flattened before prediction.

## 4. RESULTS

In this part, prediction accuracy of each method is presented and assessed using coefficient of determination ( $R^2$ ).

### 4.1 Moving Average approach accuracies

In comparison to Landsat, moving average approach generally demonstrates great accuracy for Sentinel and MODIS satellites. Regarding the regions, high accuracies are always observed in Italy Padova and San Severo regions. On the other hand, Spain Murcia has high accuracy in Sentinel only. The remaining region's accuracy fluctuates differently from one index to another (see Figure 3).

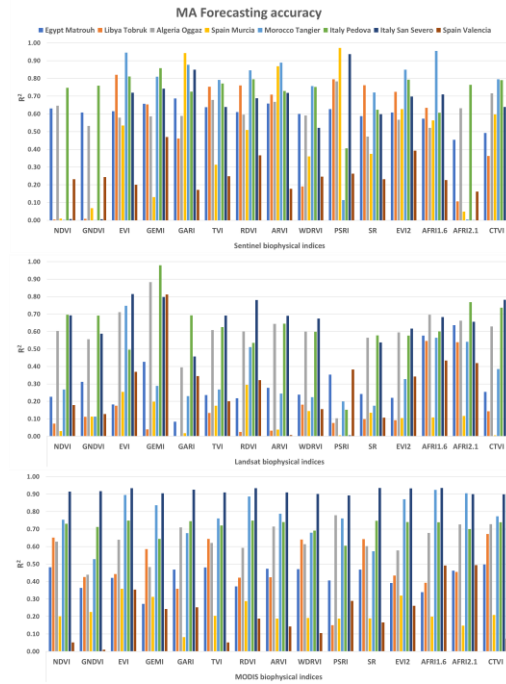


Figure 3. Moving Average (MA) model accuracy

### 4.2 LSTM accuracies

Globally, Sentinel satellite present the highest  $R^2$  values compared to MODIS and Landsat. High accuracy is consistently seen in the regions of Padova and San Severo. The accuracy of the remaining region varies from one index to another (see Figure 4).

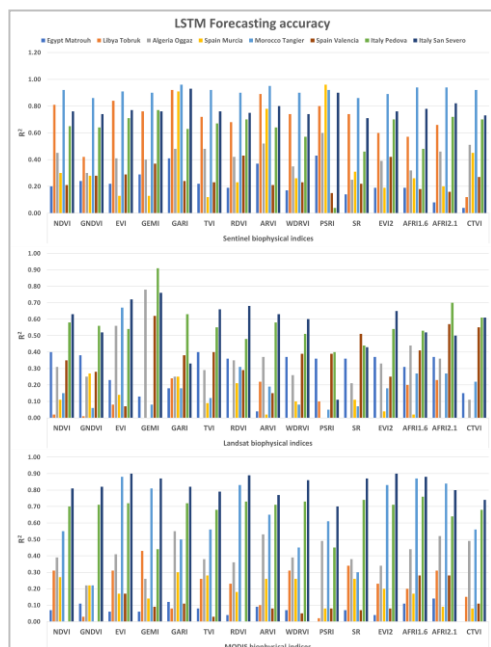


Figure 4. LSTM model accuracy

#### 4.3 Conv-LSTM model accuracy

Given the high accuracy of Sentinel and MODIS, this technique has strong similarities to the MA model.

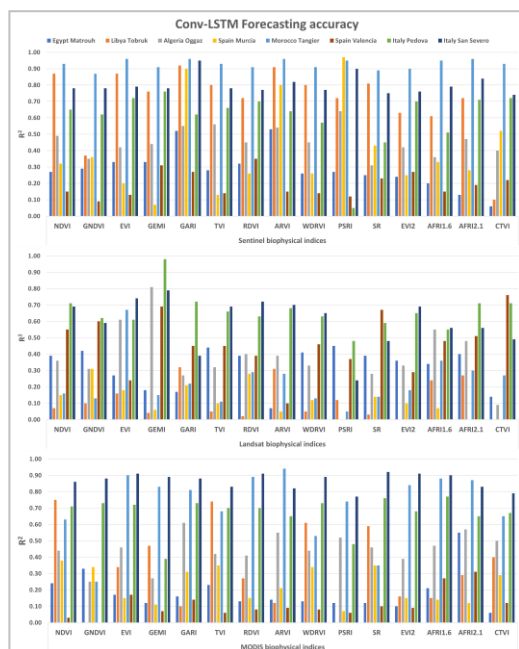


Figure 5. Conv-LSTM model accuracy

## 5 CONCLUSION

In this research, we presented a versatile database containing more than 90 algorithms of 30 biophysical indices of three different satellites (i.e., MODIS, Landsat 8, and Sentinel 2), and then we applied 15 of these algorithms using a self-developed software on very high resolution satellite images of Tangier-Morocco, Murcia-Spain, San Severo-Italy, Tobruk-Libya, Oggaz-Algeria, Matrouh-Egypt, and Padova-Italy in order to conduct an accuracy forecasting study, from 2015 to 2022 using three different forecasting approaches (i.e. ConvLSTM, Long Short Term Memory Network, and Moving Average).

## 6 ACKNOWLEDGEMENT

This work is supported in part by the University Abdelmalek Essaâdi Thematic project, 2019 – 2022, Monitoring land cover dynamics of the TTA region in the context of global warming: Contribution of Earth's observation satellites and high performance computing.

## 7 REFERENCES

- Hochreiter, S., Schmidhuber, J., 1997. Long Short-Term Memory. *Neural Computation* 9, 1735–1780. <https://doi.org/10.1162/neco.1997.9.8.1735>
- Köppen, W., 1900. Versuch einer Klassifikation der Klimate, vorzugsweise nach ihren Beziehungen zur Pflanzenwelt. (Schluss). *Geographische Zeitschrift* 6, 657–679.
- Liu, P., Zhang, H., Eom, K.B., 2017. Active Deep Learning for Classification of Hyperspectral Images. *IEEE Journal of Selected Topics in Applied Earth Observations and Remote Sensing* 10, 712–724. <https://doi.org/10.1109/JSTARS.2016.2598859>
- Mittermeier, R.A., Turner, W.R., Larsen, F.W., Brooks, T.M., Gascon, C., 2011. Global Biodiversity Conservation: The Critical Role of Hotspots. *Biodiversity Hotspots* 3.
- Ngoc Hai, P., Manh Tien, N., Trung Hieu, H., Quoc Chung, P., Thanh Son, N., Ngoc Ha, P., Tung Son, N., 2020. An Empirical Research on the Effectiveness of Different LSTM Architectures on Vietnamese Stock Market, in: 2020 International Conference on Control, Robotics and Intelligent System. Presented at the CCRIS 2020: 2020 International Conference on Control, Robotics and Intelligent System, ACM, Xiamen China, pp. 144–149. <https://doi.org/10.1145/3437802.3437827>
- Patterson, J., Gibson, A., 2017. *Deep Learning: A Practitioner's Approach*. O'Reilly Media, Inc.
- SHI, X., Chen, Z., Wang, H., Yeung, D.-Y., Wong, W., WOO, W., 2015. Convolutional LSTM Network: A Machine Learning Approach for Precipitation Nowcasting, in: *Advances in Neural Information Processing Systems*. Curran Associates, Inc.

# Estimation of fire severity using Sentinel-2 spectral indices in the 2020 Galicia forest fires

Rafael Llorens <sup>1</sup>, José Antonio Sobrino <sup>1</sup>, Cristina Fernández <sup>2</sup>, José M. Fernández-Alonso <sup>2</sup>, José A. Vega <sup>2</sup>

<sup>1</sup> *Global Change Unit, Image Processing Laboratory, University of Valencia, Paterna E-46980, Spain.*

<sup>2</sup> *Centro de Investigación Forestal de Lourizán, Xunta de Galicia, Pontevedra, E-36156, Spain.*

[jose.sobrino@uv.es](mailto:jose.sobrino@uv.es)

**ABSTRACT** - Galicia forest areas suffer forest fire events at differing frequencies, intensities, and fire severities. Fire severity is directly related to the amount of biomass consumed, the rate of vegetation recovery and the risk of erosion. Consequently, a correct assessment of fire severity involves selecting the appropriate treatment and minimizing the restoration time of the affected area. In this sense, the objective of this article is to develop a methodology for the fire severity assessment, in forest fires occurred in Galicia in 2020. As input data, this study is based on the use of Sentinel-2 spectral indices, which are characterized by having spectral bands in the near-infrared (NIR) and short-wave infrared (SWIR) spectral regions, allowing a high distinction between different fire severity degrees. All possible combinations between Sentinel-2 bands applied to a spectral normalized difference index (SPI) were analysed, along with one of the most commonly used burn spectral indices in remote sensing: the relative differential Normalized Burn Ratio (RdNBR). In addition, in order to delete confusions between burned area and the presence of other land cover areas, the temporal differences between pre-fire and post-fire dates were obtained for each spectral index (dSPI). The results obtained were compared by field points classified as in Ruiz-Gallardo et al. (2004) study (null, low, moderate and high severity). Previously, the influence of pre-fire vegetation density on fire severity values was analysed. The separability index (SI) was also applied, based on averages and standard deviations, to select the most suitable band combinations. The final statistic results obtained, show that the combination of the Normalized Difference Vegetation Index (NDVI) and the modified Normalized Burn Ratio (NBR2), used in areas with mixed and full vegetation respectively, provides the best results in fire severity assessment (kappa statistic equal to 0.81). This work is carried out in the context of the project "Joint Strategy for the Protection and Recovery of ecosystems affected by wildfires" (EPyRIS).

## 1 INTRODUCTION

Forest fires, together with climate change, are considered one of the main disturbances causing, among other impacts, the destruction of vegetation in the Iberian Peninsula (Sousa, 1984). Specifically, fire severity (defined as how fire intensity affects ecosystems) is high correlated with vegetation recovery after fire and erosion risks (Keeley, 2009).

Nowadays, satellite data play an important role in the knowledge about fire severity, as they provide information that allows mapping fire-damaged areas, which is essential to support fire control, assess environmental losses, define planning strategies and monitor vegetation restoration (Filipponi, 2019). Remote sensing tools have proven to be useful to accurately estimate fire-affected areas and their severity, to assist in the prevention, assessment and monitoring forest fires at global, regional and local scales (Chuvieco, 2009). However, remote sensing also has limitations such as the decrease in accuracy in

areas with very heterogeneous vegetation surfaces, the solution to which is conditioned by fieldwork validations (Arellano et al., 2017; Soverel et al., 2010).

In the context of the multiple remote sensing data that can be used, the multispectral instrument (MSI) on board the Sentinel-2 satellite constellation offers the possibility to obtain information at medium and high spatial resolution (10-20m) (ESA, 2015). In addition, the MSI sensor provides spectral information in several bands, with the near infrared (NIR) and shortwave infrared (SWIR) being the regions where there is the greatest difference between the different fire severity degrees (Fernández-Manso et al., 2016). MSI sensor also allows the possibility to obtain several spectral indices as a combination of the NIR, SWIR and red-edge spectral region, which is considered as a great descriptor of chlorophyll content (Korets et al., 2010; Curran et al., 1990; Fernández-Manso et al., 2016; Navarro et al., 2017). On the basis of the variations between the NIR and SWIR regions,

all possible combinations between Sentinel-2 bands applied to a spectral normalized difference index (SPI) were analysed, along with one of the most remarkable spectral index specifically designed to analyse fire severity: the relative differential Normalized Burn Ratio (RdNBR) proposed by Miller & Thode (2007). Furthermore, in order to delete confusions between burned area and the presence of other land cover areas, it is recommended to use the temporal differences between pre-fire and post-fire dates for each spectral index (dSPI).

Inside the project "Joint Strategy for the Protection and Restoration of Ecosystems affected by Forest Fires" (EPyRIS - SOE2/P5/E0811), the objective of this study is developing a methodology for the fire severity assessment, using Sentinel-2 spectral indices in forest fires occurred in Galicia in 2020.

## 2 METHODOLOGY

### 2.1 Study Area

The work that is described was carried out in 9 forest fires occurred in Galicia (Spain) in 2020, being all of them large fires (> 500 Ha). Those fires burned over 8000 Ha, classified mainly as *Pinus pinaster* Ait. (maritime pine) and *Eucalyptus globulus* Labill. (blue gum) stands. The understory vegetation was dominated by *Pteridium aquilinum* (L.) Kuhn and *Ulex europaeus* L. Figure 1 shows the map of all the forest fires occurred in Galicia 2020 and used in this study.

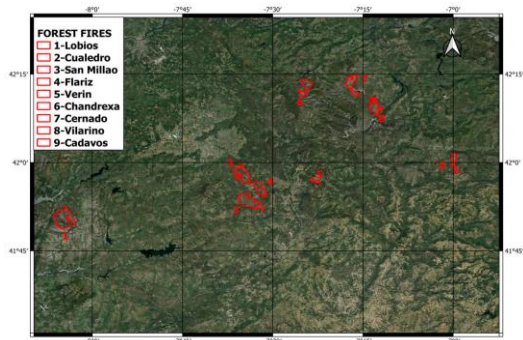


Figure 1. Map of all the forest fires occurred in Galicia 2020 and used in this study. The reference coordinate system is WGS84 (EPSG: 4326).

### 2.2 Sentinel-2 data

Atmospherically corrected Sentinel-2 images (Kaufman & Sendra, 1988) were used, considering the date closest (cloud-free) to the extinction of the fire. Two images per fire (pre- and post-fire) were downloaded and pre-processed: cropping (fire area), resampling (highest spatial resolution, 10 m) and

cloud correction (using the Scene Classification map (SCL) mask, implicit in the download folder) (Gascón et al., 2017). All areas not corresponding to forest land (agricultural land, water areas, rocks...) were also removed, using the Land Cover S2GLC, obtained from Sentinel-2 images of 2017 (more than 15000 images and an overall accuracy of 86% using 52000 validation samples distributed all over Europe) and whose spatial resolution is 10 m (Malinowski et al., 2020).

Majority of the most commonly used spectral indices in forest fires, employs a normalized difference algorithm (i.e. the subtraction of two bands reflectivity divided by the sum of those same bands reflectivity), being the only difference, the combination of bands used (Chuvieco et al., 2006; Fernández-Manso et al., 2016). For this reason, all possible combinations of normalized difference spectral indices (SPI) were calculated from the Sentinel-2 bands in order to obtain the combination that best assess fire severity (Delegido et al., 2018). In addition, for each SPI and considering forest fires as a change detection case, the temporal differences between pre-fire and post-fire dates were obtained (Equation 1).

$$SPI = \frac{B_x - B_y}{B_x + B_y} \quad (1)$$

$$dSPI = SPI_{PRE-FIRE} - SPI_{POST-FIRE}$$

Were  $B_x$  and  $B_y$  are all the different pair of Sentinel-2 bands used in this study. Furthermore, one of the most widely used spectral index in forest fires field, the Relative difference Normalized Burn Ratio (RdNBR) proposed by Miller & Thode (2007), was obtained in order to exclude the amount of pre-fire vegetation (Equation 2).

$$NBR = \frac{(B8 - B12)}{(B8 + B12)} \quad (2)$$

$$dNBR = NBR_{PRE-FIRE} - NBR_{POST-FIRE}$$

$$RdNBR = \frac{dNBR}{\sqrt{|NBR_{PRE-FIRE}|}}$$

Were B8 and B12 are the NIR and SWIR2 Sentinel-2 bands, respectively; NBR is the Normalized Burn Ratio and dNBR is the differenced Normalized Burn Ratio.

### 2.3 Field data

Fire severity validation was realized by visual analysis based on Ruiz-Gallardo et al., 2004 study, which assess the fire severity on the basis of burned vegetation percentages. Table 1 shows the percentage of burned vegetation for each field fire severity degree. A total of 158 field plots were measured, corresponding 25 to null, 8 to low, 46 to moderate and 87 to high severity, respectively.

Table 1. Ruiz-Gallardo et al. (2004) fire severity classification.

Fire severity degree	Percentage of burn vegetation
Null severity	Global vegetation $\approx 0\%$
Low	$0\% \leq \text{Global vegetation} \leq 50\%$ $0\% \leq \text{Tree canopy} \leq 30\%$
Moderate	$50\% \leq \text{Global vegetation} \leq 90\%$ $30\% \leq \text{Tree canopy} \leq 75\%$
High	Global vegetation $\geq 90\%$

#### 2.4 Statistical analysis

Fire severity assessment to obtain the most suitable dSPI index is based on a modification of the Separability Index ( $SI_w$ ) algorithm (Equation 3) adding different weights depending on the fire severity degree (the higher fire severity, the higher weight) (Tran et al., 2018).

$$SI_w = (SI_{UB-L} * 0.1) + (SI_{L-M} * 0.3) + (SI_{M-H} * 0.6) \quad (3)$$

$SI_{UB-L}$ ,  $SI_{L-M}$  and  $SI_{M-H}$  are the separability index between unburned and low severity, low and moderate severity and moderate and high severity, respectively. Due to all  $SI_w$  values obtained were, in all the cases, very low (less than one) and since there are studies that relate fire severity to vegetation type (Fornacca et al., 2018), forest fire was divided according to pre-fire vegetation. This division was carried out based on Normalized Difference Vegetation Index (NDVI, Equation 4) (Rouse et al., 1973) and using the classification proposed by Sobrino et al., 2008 study.

$$NDVI = \frac{(B8 - B4)}{(B8 + B4)} \quad (4)$$

B4 band correspond to Red Sentinel-2 band. NDVI pixels above 0.5 were classified as full vegetation and pixels below 0.5 as mixed vegetation. Despite the existence of a third class corresponding to bare soil, it was not considered.

In this context, several spectral indices obtained from the combination of post-fire bands reached  $SI_w$  values higher than 1. On the one hand, the combination of B4 and B8 post-fire bands, which is equal to NDVI algorithm (Equation 4), was selected as the best predictor in mixed vegetation areas ( $SI_w = 1.62$ ). On the other hand, the combination of the post-fire bands B8A and B12 shown in Equation 5, which is similar than NBR algorithm but using the B8A red-edge band, was selected as the best predictor in full vegetation areas ( $SI_w = 1.12$ ).

$$NBR2 = \frac{(B8A - B12)}{(B8A + B12)} \quad (4)$$

Once the spectral indices were selected as the best predictors, approximately 40% of the field plots were used to extract the mean and standard deviation statistics. The remaining 60% of field points were used for validation (using the confusion matrix and the kappa statistic) (Congalton, 1991). Table 2, shows the thresholds (low, moderate and high severity) as a combination of  $\mu$  and  $\sigma$ . The null severity is validated according to if the field plots are inside or outside the forest fire.

Table 2. Thresholds of low, moderate and high severity as a combination of  $\mu$  and  $\sigma$ .

	Low	Moderate	High
<b>RdNBR</b>	$X < 0.60$	$0.60 \leq X < 0.95$	$X \geq 0.95$
<b>NDVI</b>	$X > 0.45$	$0.45 \geq X > 0.15$	$X \leq 0.15$
<b>NBR2</b>	$X > -0.15$	$-0.15 \geq X > -0.30$	$X \leq -0.30$

### 3 RESULTS AND DISCUSSION

Figure 2a, 2b and 2c show the fire severity results obtained using, on the one hand, the RdNBR index and, on the other hand, the combination of NDVI and NBR2 spectral indices. Figure 3a and 3b, show the final maps of fire severity classified using thresholds obtained in Table 2 using RdNBR index and the combination of NDVI and NBR2 spectral indices. The forest fire represented is Lobios forest fire (2062 Ha), the largest analysed in this study.

NDVI and NBR2 spectral indices combination, represents the most accurate results (accuracy = 0.85 and kappa = 0.80) against RdNBR index (accuracy = 0.82 and kappa = 0.72). The value of kappa obtained (0.84) is considered such as an almost perfect agreement by Landis & Koch (1977) classification, and it is similar to Quintano et al. (2018) study (kappa equal to 0.80).



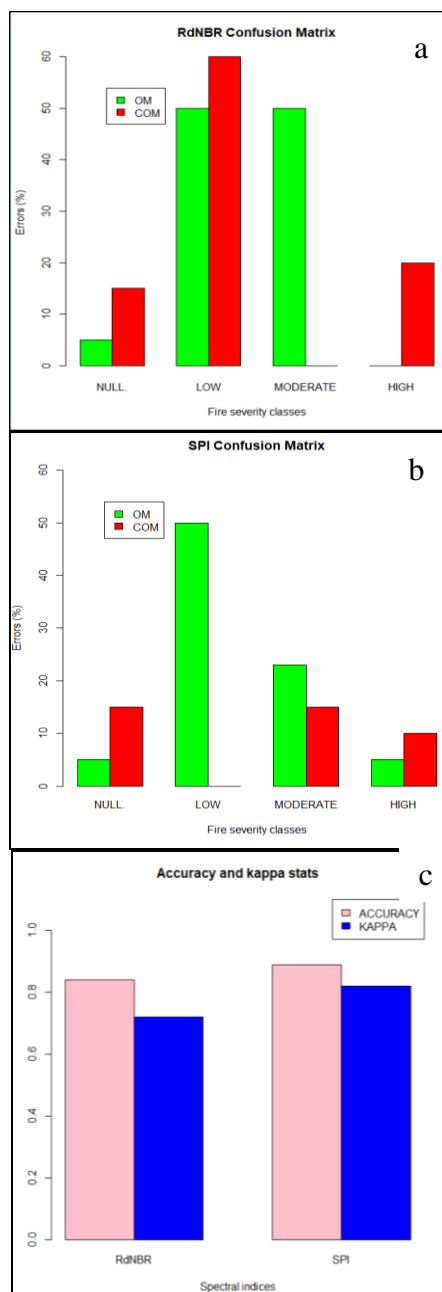


Figure 2. (a) Fire severity results obtained using the RdNBR index based on omission errors and commission errors. (b) Fire severity results obtained using the combination of NDVI and NBR2 spectral indices and based on omission errors and commission errors. (c) Comparative of RdNBR and the combination of NDVI and NBR2 spectral indices, based on accuracy kappa index.

In terms of omission and commission errors, NDVI and NBR2 combination improves the RdNBR result, except in null and low severity degrees, which value is equal (5 and 50 %, respectively). The fire severity omission errors results obtained are higher than Arellano et al. (2017) study in low and moderate severity (omission = 20% and 13,5%, commission = 20% and 10,3%, respectively) and lower in high severity (omission = 8%, commission = 23,3%, respectively). In this sense, it is important to note that this study assigns more importance to high severity, as it considers the strong relationship between high severity and erosion risks (forest structure completely damaged leads to high risk of erosion).

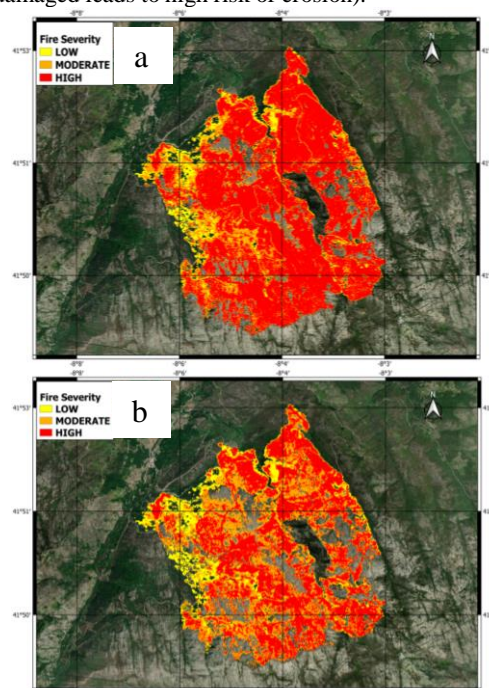


Figure 3. (a) Fire severity map obtained using the RdNBR index and classified using thresholds obtained in Table 2. (b) Fire severity map obtained using the combination of NDVI and NBR2 spectral indices and classified using thresholds obtained in Table 2. The forest fire represented is Lobios forest fire (2062 Ha), the largest analysed in this study. The reference coordinate system is WGS84 (EPSG: 4326).

#### 4 CONCLUSIONS

This study presents a methodology for the estimation of fire severity. Statistical tests were performed using one of the most commonly used burn spectral indices in remote sensing: the relative differential Normalized Burn Ratio (RdNBR) and all possible combinations of normalized differential spectral indices from Sentinel-2 bands.

The combination of the NDVI and NBR2 indices (SPI) provides more accurate results than the RdNBR index. Low severity was the worst classified class (50% omission error). It is demonstrated that the combinations between red, near infrared (NIR) and short-wave infrared (SWIR) bands are suitable for differentiating between fire severity degrees.

## 5 ACKNOWLEDGMENTS

This study was made possible thanks to the Interreg SUDOE programme of the EPyRIS SOE2/P5/E0811 project. In addition, the authors would like to acknowledge the support offered by the Centro de Investigación Forestal de Lourizán (CIF), for allowing the field campaigns.

## 6 REFERENCES

- Arellano Pérez, S., Vega, J. A., Rodríguez y Silva, F., Fernández, C., Vega Nieva, D. J., Álvarez González, J. G., & Ruiz González, A. D. Validación de los índices de teledetección dNBR y RdNBR para determinar la severidad del fuego en el incendio forestal de Oia-O Rosal (Pontevedra) en 2013.
- Chuvieco, E. (Ed.). (2009). *Earth observation of wildland fires in Mediterranean ecosystems* (p. 257). Berlin/Heidelberg, Germany: Springer.
- Chuvieco, E., Riaño, D., Danson, F. M., & Martin, P. (2006). Use of a radiative transfer model to simulate the postfire spectral response to burn severity. *Journal of Geophysical Research: Biogeosciences*, 111(G4).
- Congalton, R. G. (1991). A review of assessing the accuracy of classifications of remotely sensed data. *Remote sensing of environment*, 37(1), 35-46.
- Curran, P.J., Dungan, J.L., Gholz, G.H., 1990. Exploring the relationship between reflectance red edge and chlorophyll content in slash pine. *Tree Physiol.* 7, 33–48.
- Delegido, J., Pezzola, A., Casella, A., Winschel, C., Urrego, E. P., Jimenez, J. C., ... & Moreno, J. (2018). Estimación del grado de severidad de incendios en el sur de la provincia de Buenos Aires, Argentina, usando Sentinel-2 y su comparación con Landsat-8. *Revista de Teledetección*, (51), 47-60.
- Fernández-Manso, A., Fernández-Manso, O., & Quintano, C. (2016). SENTINEL-2A red-edge spectral indices suitability for discriminating burn severity. *International journal of applied earth observation and geoinformation*, 50, 170-175.
- Filipponi, F. (2019). Exploitation of sentinel-2 time series to map burned areas at the national level: A case study on the 2017 Italy wildfires. *Remote Sensing*, 11(6), 622.
- Fornacca, D., Ren, G., & Xiao, W. (2018). Evaluating the best spectral indices for the detection of burn scars at several post-fire dates in a mountainous region of Northwest Yunnan, China. *Remote Sensing*, 10(8), 1196.
- Gascon, F., Bouzinac, C., Thépaut, O., Jung, M., Francesconi, B., Louis, J., ... & Fernandez, V. (2017). Copernicus Sentinel-2A calibration and products validation status. *Remote Sensing*, 9(6), 584.
- Kaufman, Y. J., & Remer, L. A. (1994). Detection of forests using mid-IR reflectance: an application for aerosol studies. *IEEE transactions on geoscience and remote sensing*, 32(3), 672-683.
- Keeley, J. E. (2009). Fire intensity, fire severity and burn severity: a brief review and suggested usage. *International journal of wildland fire*, 18(1), 116-126.
- Korets, M.A., Ryzhkova, V.A., Danilova, I.V., Sukhinin, A.I., Bartalev, S.A., 2010. Forest disturbance assessment using satellite data for moderate and low resolution. In: Balzter, H. (Ed.), *Environment Change in Siberia: Earth Observation, Field Studies and Modeling*. Springer.
- Landis, J. R., & Koch, G. G. (1977). The measurement of observer agreement for categorical data. *biometrics*, 159-174.
- Malinowski, R., Lewiński, S., Rybicki, M., Gromny, E., Jenerowicz, M., Krupiński, M., ... & Schauer, P. (2020). Automated production of a land cover/use map of Europe based on Sentinel-2 imagery. *Remote Sensing*, 12(21), 3523.
- Miller, J. D., & Thode, A. E. (2007). Quantifying burn severity in a heterogeneous landscape with a relative version of the delta Normalized Burn Ratio (dNBR). *Remote Sensing of Environment*, 109(1), 66-80.
- Navarro, G., Caballero, I., Silva, G., Parra, P. C., Vázquez, Á., & Caldeira, R. (2017). Evaluation of forest fire on Madeira Island using Sentinel-2A MSI imagery. *International Journal of Applied Earth Observation and Geoinformation*, 58, 97-106.

- Quintano, C., Fernández-Manso, A., & Fernández-Manso, O. (2018). Combination of Landsat and Sentinel-2 MSI data for initial assessing of burn severity. *International journal of applied earth observation and geoinformation*, 64, 221-225.
- Rouse Jr, J. W., Haas, R. H., Schell, J. A., & Deering, D. W. (1973, December). Paper a 20. In *Third Earth Resources Technology Satellite-1 Symposium: The Proceedings of a Symposium Held by Goddard Space Flight Center at Washington, DC on* (Vol. 351, p. 309).
- Ruiz-Gallardo, J. R., Castaño, S., & Calera, A. (2004). Application of remote sensing and GIS to locate priority intervention areas after wildland fires in Mediterranean systems: a case study from south-eastern Spain. *International Journal of Wildland Fire*, 13(3), 241-252.
- Sentinel, E. S. A. (2). User Handbook. *ESA Standard Document*, 64.
- Sobrino, J. A., Jiménez-Muñoz, J. C., Sòria, G., Romaguera, M., Guanter, L., Moreno, J., ... & Martínez, P. (2008). Land surface emissivity retrieval from different VNIR and TIR sensors. *IEEE transactions on geoscience and remote sensing*, 46(2), 316-327.
- Sousa, W. P. (1984). The role of disturbance in natural communities. *Annual review of ecology and systematics*, 15, 353-391.
- Soverel, N. O., Perrakis, D. D., & Coops, N. C. (2010). Estimating burn severity from Landsat dNBR and RdNBR indices across western Canada. *Remote Sensing of Environment*, 114(9), 1896-1909.
- Tran, B. N., Tanase, M. A., Bennett, L. T., & Aponte, C. (2018). Evaluation of spectral indices for assessing fire severity in Australian temperate forests. *Remote Sensing*, 10(11), 1680.



# Monitoring winter barley within-field yield using PolSAR, backscatter coefficients and surface reflectance data

B. Mollà-Bononad <sup>1</sup>, B. Franch <sup>1</sup>, I. Moletto-Lobos <sup>1</sup>, J. M. López-Sánchez <sup>2</sup>, J. Cintas <sup>1</sup>, M. J. Sánchez-Torres <sup>1</sup>, A. San Bautista <sup>3</sup>, C. Rubio <sup>4</sup>

<sup>1</sup>Global Change Unit, Image Processing Laboratory, Parc Científic, Universitat de València (Paterna), 46980, Spain.

<sup>2</sup>Departamento de Física, Ingeniería de Sistemas y Teoría de la Señal, Universitat d'Alacant (Sant Vicent del Raspeig), 03690, Spain

<sup>3</sup>Departamento de Producción Vegetal, Universitat Politècnica de València (València), 46022, Spain

<sup>4</sup>Departamento de Física Aplicada, Universitat Politècnica de València (València), 46022, Spain

[bertran.molla@uv.es](mailto:bertran.molla@uv.es), [belen.franch@uv.es](mailto:belen.franch@uv.es)

**ABSTRACT** - In this work we monitor within-field barley yield based on Earth Observation (EO) data from Sentinel-2 and Sentinel-1. Both satellites' data has been preprocessed granting Sentinel-2 surface reflectance and Sentinel-1  $\gamma_0$  backscatter coefficients and noise free H-A- $\alpha$  decomposition. Yield data has been measured by harvest machines during 2020 and 2021 seasons, providing dry yield roughly every 7m, over irregular polygons. Thus, field data has also been preprocessed to achieve spatial consistency and reduce measuring software errors. Training and validation has followed a structure of k-fold cross validation. The main objective of this work is exploring the integration of C-band SAR data to monitor barley yield. On one hand, Sentinel-1 data can increase Sentinel-2 temporal resolution and assure that even in cloudy conditions information on crop development can be retrieved. But on the other side, in cloud free conditions each spectral band and polarization is analyzed to define the combination that is best correlated with the final yield maps. Therefore, linear regression and machine learning algorithms were tested using different spectral bands and polarizations from both Sentinel satellites. An optimal date for the final model has been selected attending to performance metrics such as  $R^2$  and RMSE; creating predicted within-field yield maps and tracking their uncertainties.

## 1 INTRODUCTION

According to United Nations' Department of Economic and Social Affairs, by the end of this decade, global population will have risen to 8 plus thousands of million people. This manifests the necessity of increasing food production in order to feed our rising population. The previous, in the context of a changing climate and energy vector scarcity, highlights the importance of ensuring and monitoring essential resources such as crops (and specifically winter cereals) to maintain and improve food production.

The price of barley, as with any other food, can fluctuate significantly depending on production. Consequently, proper crop management and monitoring are required to predict crop production in order to make decisions to avoid market speculation and guarantee fair prices.

For all these reasons, and in line with similar studies (Becker-Reshef et al., 2019; Skakun et al., 2021), this paper addresses the development of

empirical models for barley yield prediction based on *in situ* data from collected in different fields in the province of Valladolid, Spain.

## 2 DATA

The data used for training and validating the models is, on the Earth Observation (EO) part, surface reflectance measured by Sentinel-2 at 10 m and 20 m spatial resolution, Sentinel-1  $\gamma_0$  backscatter coefficients and noise free H-A- $\alpha$  decomposition at 10 m spatial resolution and ERA5/ECMWF daily precipitation; and on the *in situ* data part, the within-field yield maps of the 2020 and 2021 seasons.

The data available from Sentinel-2 is limited and corresponds mostly to the months of May and June due to the high cloud cover from January to April in the study area. The raw yield maps obtained by the harvester (figure 1a) are made up of irregular rectangles of approximately 7 x 3 m<sup>2</sup> that show extreme yield values, i.e. within an irrigation pivot, contiguous irrigation pixels that differ by several

tonnes of yield or yields that are far in excess of those expected for a crop of this class, due to faults in the measurement software. In order to be able to work with these products we require a pre-processing, which consists of spatial regularization of the data to a regular grid of 10 x 10 m<sup>2</sup> squares (figure 1b), the application of an average filter to smooth out the anomalies in yield values discussed above (figure 1c) and finally an erosion of the pixels at the edge of the map in order to remove non-representative values that may be affected by the contribution of bare soil (figure 1d)

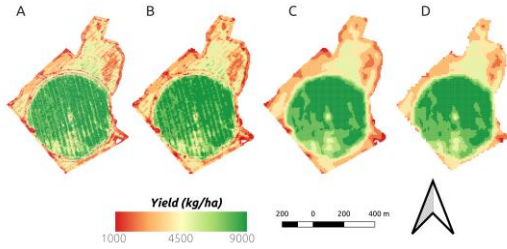


**Figure 1.** Example of yield map processing pipeline.

The fields of study are located in the surroundings of Medina del Campo, a small village in the province of Valladolid, and their main properties are shown in the following table.

**Table 1.** Distribution and area of the in situ data across the 2020 and 2021 seasons.

Season	Number of Fields	Area (ha)
2020	9	167.43
2021	24	174.89

### 3 THEORETICAL BACKGROUND

Two types of algorithms have been selected to build the empirical models for predicting performance: regularised Ridge regressions and random forest regressions. It is important to emphasise that the models created by random forest are intended to narrow down the best metrics to be achieved, since, due to their low interpretability, it is more complex to carry out an analysis of the influence of the different bands. The training and validation of the models will follow a leave-one-out stratified cross-validation structure where each iteration, the model will be trained with all the fields except one, which will be used to validate the model. In order to choose the optimal model features, Pearson's correlation coefficient  $r^2$  of the features with the final yield will be analysed.

The optimal model will be the one that has the highest  $R^2$  coefficient of determination (equation 1) and the smallest root mean square error (equation 2):

$$R^2 = 1 - \frac{\sum_{i=1}^n (y_{est}^i - y_{ref}^i)^2}{\sum_{i=1}^n (y_{est}^i - \bar{y}_{ref})^2} \quad (1)$$

$$RMSE = \sqrt{\frac{1}{n} \sum_{i=1}^n (y_{est}^i - y_{ref}^i)^2} \quad (2)$$

### 4 METHODOLOGY

First, the EO data has been preprocessed. For the case of Sentinel-2 Bottom-Of-Atmosphere (BOA) corrected reflectance products have been obtained and clipped to our area of interest using LaSRC (Vermote et al., 2016). For Sentinel-1, both SLC and GRD products have been processed performing different corrections such as orthorectification, radiometric calibration, thermal noise removal, etc. (Filipponi et al., 2019; Mascolo et al., 2021). Additionally, rainy dates where daily precipitation is above 10 mm have been left outside of the study (Tamm et al., 2016).

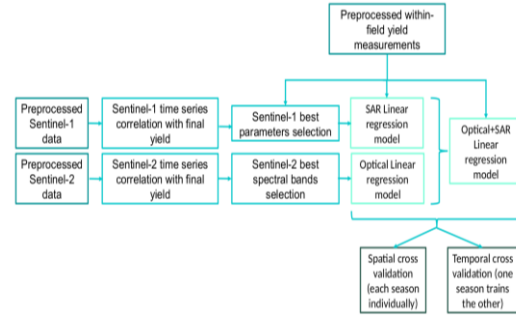


**Figure 2.** Methodology overview.

The yield maps have been processed to obtain a regularised grid at 10 m without extreme yield values. The correlation coefficient of the different spectral bands along the time series has been calculated, revealing the most relevant features for the model. With the optimal parameters, the models have been trained and validated with both spatial cross validation (each season individually) and temporal cross validation (one season trains the model and it is validated in the other) for each date of the time series using optical, SAR and optical-SAR features.

Finally, the  $R^2$  and the  $RMSE$  have been analysed to discern which date has the highest prediction accuracy. General overview of the methodology can be seen in the figure below:

## 5 RESULTS

By plotting the  $r^2$  time series of all the different optical and SAR parameters, it has been found that from all features, the bands associated with the SWIR, red and red-edge show the greatest correlation of all Sentinel-2 features. In the case of Sentinel-1, the maximum correlation corresponds to VV and VH polarizations and to Anisotropy as well. With this information, we have created two models labelled initial and trimmed as can be seen in the figures below. For Sentinel-2, the initial model is formed by bands 4, 5, 8A, 11 and 12; the trimmed model reduces the number of bands to three, being 4, 8A and 11. As can be seen in both figure 3 and 4, almost halving the number of bands for the Sentinel-2 model only affects correlation by a negligible factor. For Sentinel-1, the initial model was formed with all the available features and then the trimmed model has been elaborated using only VV, VH and Anisotropy. In the same way as in the previous optical case, the correlation between the initial and trimmed SAR models does not show any significant variation (figures 5 and 6).

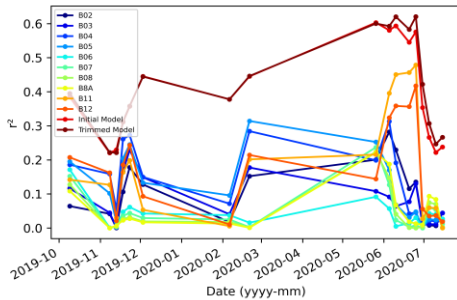


**Figure 3.** Optical parameters correlation with yield for the 2020 season.

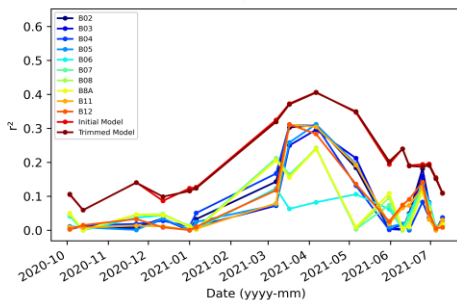


**Figure 4.** Optical parameters correlation with yield for the 2021 season.

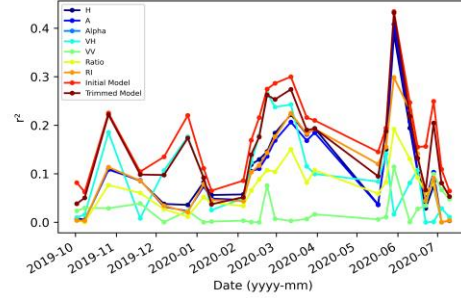


**Figure 5.** SAR parameters correlation with yield for the 2020 season.

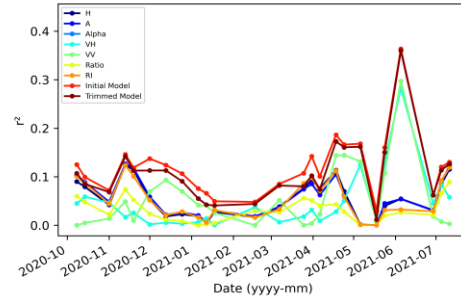


**Figure 6.** SAR parameters correlation with yield for the 2021 season.

With the optimal spectral features selected, three models have been trained and validating using only optical features, only SAR features and mixing optical and SAR features in a 10 day window. Analysing the time series for the  $RMSE$  of the spatial cross validation it can be seen that mixing optical and SAR features consistently yields a lower  $RMSE$  throughout both seasons (figures 7 and 8), reaching the minimum value in 25<sup>th</sup> of June for 2020 and 6<sup>th</sup> of April for 2021. As may be seen in figures 9 and 10, mixing optimal optical and SAR features when available can increase the coefficient of determination of the model thus making it more robust.

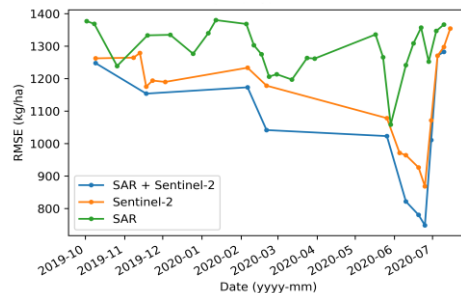


**Figure 7.**  $RMSE$  time series with spatial cross validation for the 2020 season.

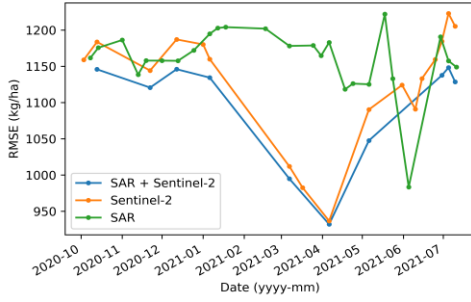


**Figure 8.** RMSE time series with spatial cross validation for the 2021 season.

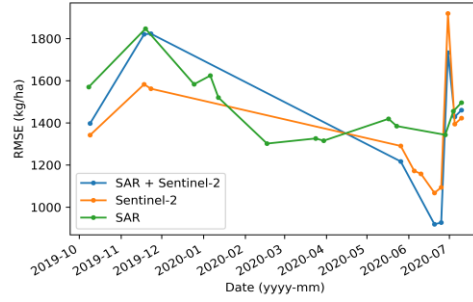


**Figure 11.** RMSE time series with temporal cross validation for the 2020 season.

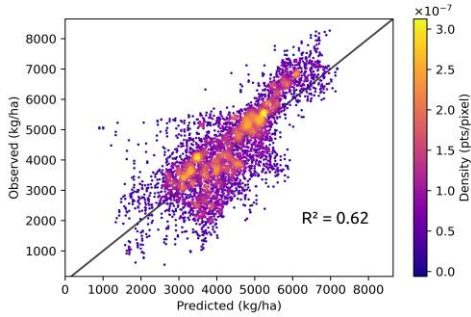


**Figure 9.** Observed yield vs predicted yield using only optical data for the 06-25-2020.

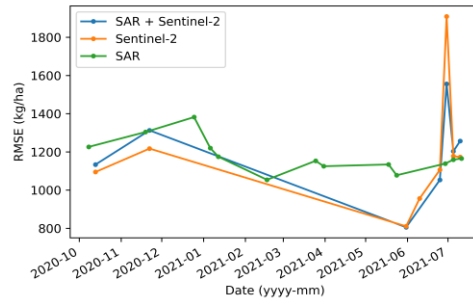


**Figure 12.** RMSE time series with temporal cross validation for the 2021 season.

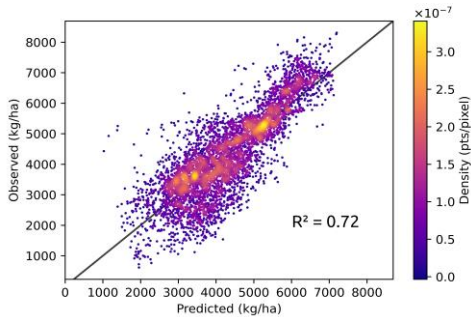


**Figure 10.** Observed yield vs predicted yield using optical and SAR data for the 06-25-2020.

When performing the temporal cross validation, metrics are not conclusive (figures 11 and 12). The main reason for this is the lack of cloud-free Sentinel-2 data from February to May in 2021. The lack of overlap between seasons makes impossible performing a temporal cross validation in a crucial period of time for the crop development and growth. In this case, although Sentinel-1 may not provide information as accurate as its optical counterpart, it can fill the gaps in these crucial dates and still provide some kind of insight about the crop state.

## 6 DISCUSSION AND CONCLUSIONS

Normally yield models are based on the analysis of NDVI or DVI indices. In this work, a more basic approach has been chosen, relating spectral information directly to yield. SWIR, and in particular band 11 of Sentinel-2, is particularly useful for monitoring leaf water content. Due to the heterogeneous nature of the agricultural practices in the fields of study, the highest correlation of the SWIR could be indicative of the importance of the presence of water and irrigation in yield improvement. As stated previously for the SAR parameters, VV, VH and Anisotropy but the interpretation of the correlation of the SAR features is not as straightforward and consequently more work needs to be done in this particular field of study. Despite the limited dataset, this simple approach has provided information about which optical and SAR features best correlate with within-field yield and it has also shown the potential that SAR data has to complement optical features, reaching *RMSEs* below 1000 kg/ha when this synergy is exploited. The immediate application and extrapolation of this model to other fields in other seasons is not trivial. Due to the amount of data available at the moment as well as the location of the data i.e. the fields on which the model has been trained

are in the same town; the model is potentially sensitive to longitudinal and latitudinal variation. It is expected to be able to obtain data from future campaigns at different locations in order to develop a more robust model applicable to fields with no yield information.

## 7 REFERENCES

- Becker-Reshef, I., Justice, C., Sullivan, M., Vermote, E., Tucker, C., Anyamba, A., Small, J., Pak, E., Masuoka, E., Schmaltz, J., Hansen, M., Pittman, K., Birkett, C., Williams, D., Reynolds, C., & Doorn, B. (2010). Monitoring Global Croplands with Coarse Resolution Earth Observations: The Global Agriculture Monitoring (GLAM) Project. In *Remote Sensing* (Vol. 2, Issue 6, pp. 1589–1609). MDPI AG. <https://doi.org/10.3390/rs2061589>
- Filipponi, F. (2019). Sentinel-1 GRD Preprocessing Workflow. In 3rd International Electronic Conference on Remote Sensing. International Electronic Conference on Remote Sensing. MDPI. <https://doi.org/10.3390/ecrs-3-06201>
- Mascolo, L., Lopez-Sanchez, J. M., & Cloude, S. R. (2022). Thermal Noise Removal From Polarimetric Sentinel-1 Data. In *IEEE Geoscience and Remote Sensing Letters* (Vol. 19, pp. 1–5). Institute of Electrical and Electronics Engineers (IEEE). <https://doi.org/10.1109/lgrs.2021.3050921>
- Skakun, S., Kalecinski, N. I., Brown, M. G. L., Johnson, D. M., Vermote, E. F., Roger, J.-C., & Franch, B. (2021). Assessing within-Field Corn and Soybean Yield Variability from WorldView-3, Planet, Sentinel-2, and Landsat 8 Satellite Imagery. In *Remote Sensing* (Vol. 13, Issue 5, p. 872). MDPI AG. <https://doi.org/10.3390/rs13050872>
- Tamm, T., Zalite, K., Voormansik, K., & Talgre, L. (2016). Relating Sentinel-1 Interferometric Coherence to Mowing Events on Grasslands. In *Remote Sensing* (Vol. 8, Issue 10, p. 802). MDPI AG. <https://doi.org/10.3390/rs8100802>
- Vermote, E., Justice, C., Claverie, M., & Franch, B. (2016). Preliminary analysis of the performance of the Landsat 8/OLI land surface reflectance product. In *Remote Sensing of Environment* (Vol. 185, pp. 46–56). Elsevier BV. <https://doi.org/10.1016/j.rse.2016.04.008>

## Yield forecast models and nitrogen content management in rice crops in Valencia.

M.J. Sánchez-Torres<sup>(1)</sup>, B. Franch<sup>(1,2)</sup>, A. San Bautista<sup>(3)</sup>, C. Rubio<sup>(3)</sup>, C. Domingo<sup>(4)</sup>

<sup>(1)</sup> *Global Change Unit, Image Processing Laboratory, Universitat de València, Paterna (Valencia) 46980, Spain*

<sup>(2)</sup> *Department of Geographical Sciences, University of Maryland, College Park MD 20742, USA*

<sup>(3)</sup> *Departamento de Producción Vegetal, Universitat Politècnica de València (Valencia), 46022, Spain*

<sup>(4)</sup> *Instituto Valenciano de Investigaciones Agrarias (IVIA), Moncada (Valencia) 46113, Spain*

maria.jose.sanchez-torres@uv.es; belen.franch@uv.es; asanbau@prv.upv.es;  
crubiom@fis.upv.es; domingo\_concar@gva.es

**ABSTRACT** - Rice is one of the major commodities traded in the international food market and basic food in the diet of more than half of the world's population, especially in developing countries. Rice-producing systems are critical for ensuring food security, reducing poverty and improving livelihoods. Accurate and timely crop yield forecasts are necessary for making viable agricultural investments, developing proper agricultural planning, increasing market efficiency and stability, as well as managing food shortages. On the other hand, fertilizers and pesticides are routinely used in rice cultivation to maintain optimal yield and to protect plants from diseases. However, the overuse of them, has adverse effects on the environment and human health, that has led to the regulation of the use on nitrogen in agriculture to minimize its impact. The main objective is to obtain prediction models based on linear regression and machine-learning that correlate the spectral bands of Sentinel-2 with the final yield data. In this work, rice yield at field scale from 2017 to 2020 have been used, covering an area of 78 ha/year around the Albufera de Valencia. Results show that linear regression models provide a RMSE of 0.29 t/ha (6.4%) in Bomba and 0.47 t/ha (5.2%) in JSendra about three months before harvest. The second objective is to analyse rice crops with different nitrogen level treatments using Sentinel-2 and drone data. This is conducted over an experimental field close to the Albufera. Preliminary results show that NIR band can monitor the rice development over different nitrogen management.

**Keywords:** remote sensing, Sentinel-2, rice, yield, fertilization

### 1. INTRODUCTION

Globally, the harvested area of rice is second only to wheat. Considering its caloric contribution, rice is the cereal that provides the most calories per hectare and is the most consumed cereal globally. Rice production is the main source of income for some 100 million households in Asia and Africa. All this leads to the need for rice yield and production forecasting, as it plays a key role in world markets, impacting policy and decision making, and allowing more efficient and sustainable crop. Precision agriculture is defined as the management of crops based on the knowledge of the spatial and temporal variability in an agricultural holding, to improve the economic return and minimize the environmental impact. Remote sensing data provides timely, objective and accurate information that is critical for precision agriculture applications. Many methods have been developed to estimate crop

yields using remotely sensed data (Weiss et al., 2020). The most used are those based on empirical relationships between field yields and spectral data during a given phenological period (Becker-Reshef et al., 2018). In rice crop, there are many studies that relate spectral information to the field yield (Franch et al., 2021) or to its nutritional status (Zhang et al., 2020). However, so far, high spatial resolution satellite data have not been used to forecast rice yield. First, we develop a rice yield model at field scale based on yield measurements over 78 ha/year around the Albufera in Valencia (Spain) from 2017 to 2020 seasons. The dataset covers the two main varieties, that is JSendra and Bomba, and provides average yields at field scale. Training and validation follow a structure of k-folds cross validation. The main objective is to obtain prediction models based on linear regression and machine-learning that correlate the spectral bands of Sentinel-2 with the final yield data.



Fertilizers are routinely used in rice cultivation to maintain optimal yield. The overuse of fertilizers has adverse effects on the environment and human health. According to the Sustainable Development Goals approved by the United Nations Conference on environmental, political and economic challenges for the coming years, agricultural crop production must evolve towards efficient, profitable and sustainable systems. Fertilization management in modern agriculture aims to supply just the fertilizer needed to maximize yields while avoiding their excesses to ensure environmental sustainability. Previous works have shown that the growth of the rice crops as well as the nitrogen content can be inferred based on the spectral reflectance from EO sensors. For instance, Cai et al. (2019) showed that the Normalized Difference Vegetation Index (NDVI) or the Green NDVI (GDVI) can be used to monitor the nitrogen content of rice crops. In fact, other studies show how remote sensing data can be used to monitor the nitrogen deficit in rice (Bacenetti et al., 2020; Moreno-García et al., 2018). The second objective of this work is to analyse rice crops with different nitrogen level treatments using Sentinel-2 and drone data. This is conducted over an experimental field close to the Albufera that was split into three different areas characterized by different nitrogen treatments.

The implementation of remote sensing technologies in rice farming has evident advantages in monitoring rice growth, soil fertility evaluation and yield estimation, among others.

## 2. MATERIAL

The study is developed over rice plots located around the Albufera Natural Park in Valencia, eastern Spain (Figure 1). We selected the two main rice varieties in the region, JSendra and Bomba, and a yield database is available for the years 2017-2020. Table 1 collects the number of plots, total area and average yield of the studied plots for each year. On the other hand, we use Sentinel-2 images (tile 31SBD) from January 2017 to December 2020 every 5 days. Spectral bands with 10 m and 20 m spatial resolution (B02, B03, B04, B05, B05, B06, B07, B08, B11 and B12) are considered for this study.

To develop the nitrogen study, we have an experimental JSendra rice field close to the Albufera with three different nitrogen treatments that are 130.9 kgN/ha, 176.2 kgN/ha and 243.1 kgN/ha. Field data on the within-field yield was collected by harvesting machines (Figure 2A). Finally, we use Sentinel-2 images (tile 31SBD) for the year 2021, and a multispectral drone with RGB-NIR bands (Figure 2B).

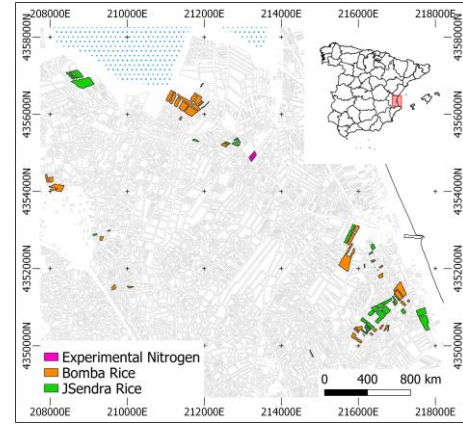


Figure 1. Location of the studied rice plots.

Table 1. Rice plots database.

		2017	2018	2019	2020
JSendra	Plots	16	17	17	28
	Area (ha)	33.84	38.94	42.81	48.57
	Yield (t/ha)	8.0±0.7	8.4±0.8	8.8±1.4	8.6±0.9
Bomba	Plots	15	16	27	17
	Area (ha)	24.71	32.77	50.62	38.46
	Yield (t/ha)	4.9±1.2	4.1±0.4	4.7±0.5	3.8±0.7

The Sentinel-2 satellite images have been previously downloaded from SciHub Copernicus and processed to perform the atmospheric correction using the Land Surface Reflectance Code (LaSRC) algorithm (Vermote et al., 2016) obtaining the surface reflectance values.

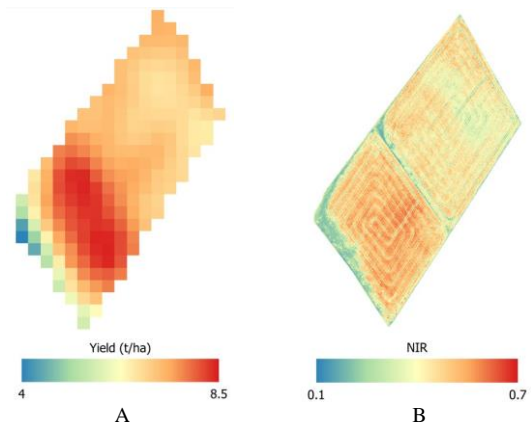


Figure 2. (A) Experimental JSendra rice within-field yield. (B) Drone image, NIR band.

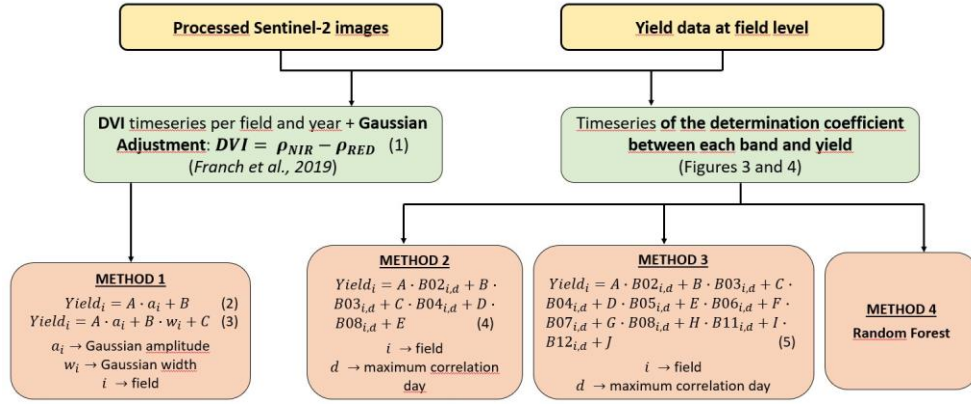


Figure 3. Rice yield study methodology flowchart.

### 3. METHODOLOGY

#### 3.1. Rice yield study

From the data collected in Table 1 and the satellite images, the mean surface reflectance (and standard deviation) per plot for each spectral band is obtained. Seventy percent of the plots for each variety are randomly selected for the model training dataset and the remaining 30% for validation, applying three iterations in the random selection. This iterative process is applied to the four forecasting models developed. Figure 3 shows a flowchart of the methodology used to develop the rice yield study.

##### 3.1.1. Method 1

This method studies the evolution of the DVI (Difference Vegetation Index, equation 1) for each plot by fitting it to a Gaussian curve. With this analysis, the yield is directly correlated with the amplitude of the curve. This method 1 uses a regression model that expresses yield per plot ( $i$ ) as a function of two parameters of the curve: Gaussian amplitude ( $a$ ) (equation 2) and Gaussian amplitude and width ( $w$ ) together (equation 3).

$$DVI = \rho_{NIR} - \rho_{RED} \quad (1)$$

$$Yield_i = A \cdot a_i + B \quad (2)$$

$$Yield_i = A \cdot a_i + B \cdot w_i + C \quad (3)$$

##### 3.1.2. Methods 2, 3 and 4

To develop the following three yield forecasting models, we first perform an analysis of the temporal evolution by date of the correlation coefficient obtained by directly correlating the surface reflectance values of each band on each date of data acquisition

with the yield considering all the years together. As we do not have the images at the same dates in each year and to minimize the possible variation in the phenological evolution of each year, we averaged the images every 10 days from the day of the year 150 to 280. Figures 4 and 5 show the evolution of the coefficient of determination of JSendra and Bomba rice fields. In the case of JSendra rice (Figure 4), two times can be distinguished, separated by a minimum correlation. The first one presents a relative maximum on July 9, then the correlation decreases until reaching a minimum on August 18 and finally increases again until reaching the absolute maximum correlation on September 7. Similarly, for Bomba rice (Figure 5), two phases are observed. A relative maximum is observed on July 9 (it should be noted that it coincides with the same date as JSendra), the correlation minimum occurs on July 29 and the absolute maximum is reached on August 8. In both cases, the dates of maximum correlation correspond to different phenological stages, which will allow us to know the stage in which the prediction is more accurate.

The second forecasting method consists of a linear regression model as a combination of the spectral bands with 10 m spatial resolution for the two selected days with maximum correlation ( $doy$ ) in both rice varieties (equation 4), the third method is a regression model as a linear combination of all the bands in the two dates of maximum correlation for both rice varieties (equation 5), and finally we applied the machine-learning technique Random Forest, which consists of generating multiple subsets of data from the training set, building multiple models using multiple decision trees where each one of them is trained with a subset of data and finally combining by averaging the predictions of each tree. Thus, this algorithm builds a prediction model based on the relative importance of each spectral band to the independent variable (yield).



$$Yield_{i,doy} = A \cdot B02_{i,doy} + B \cdot B03_{i,doy} + C \cdot B04_{i,doy} + D \cdot B08_{i,doy} + E \quad (4)$$

$$Yield_{i,doy} = A \cdot B02_{i,doy} + B \cdot B03_{i,doy} + C \cdot B04_{i,doy} + D \cdot B05_{i,doy} + E \cdot B06_{i,doy} + F \cdot B07_{i,doy} + G \cdot B08_{i,doy} + H \cdot B11_{i,doy} + I \cdot B12_{i,doy} + J \quad (5)$$

### 3.2. Rice nitrogen content study

First, we analyse surface reflectance average values for each Sentinel-2 spectral band every day, comparing the three regions with different nitrogen

treatment. Figure 6A shows the spectral curve of the three regions for July 9.

In addition, we analyse for each Sentinel-2 band and each day the correlation between the pixel-level spectral band and final yield for the three different nitrogen treatment regions (Figure 6B).

### 3.3. Evaluation

We evaluate the yield forecasting models with a standard set of metrics which are the coefficient of determination  $r^2$  (equation 6), the Root Mean Square Error RMSE (equation 7) and the Relative Root Mean Square Error RRMSE (equation 8).

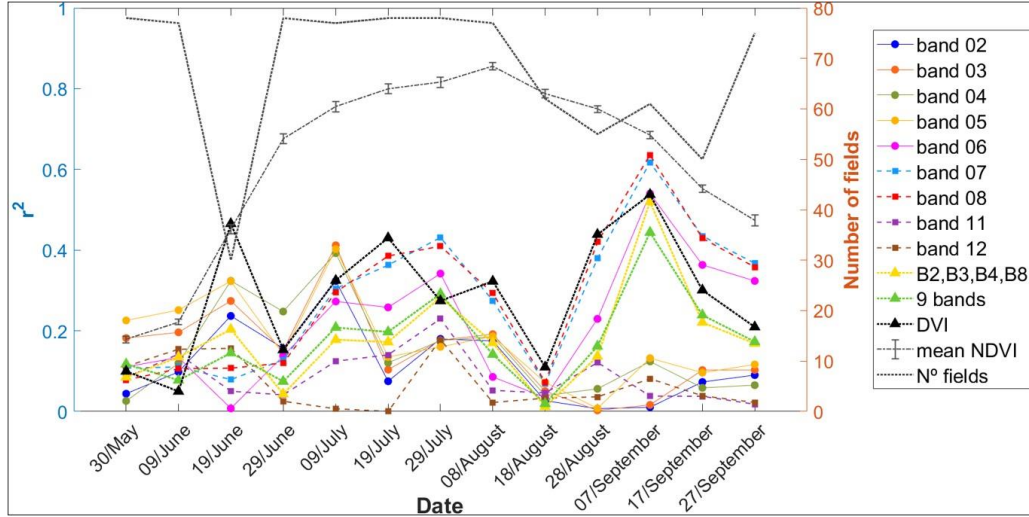


Figure 4. Timeseries of the determination coefficient (yield-band) for JSendra rice.

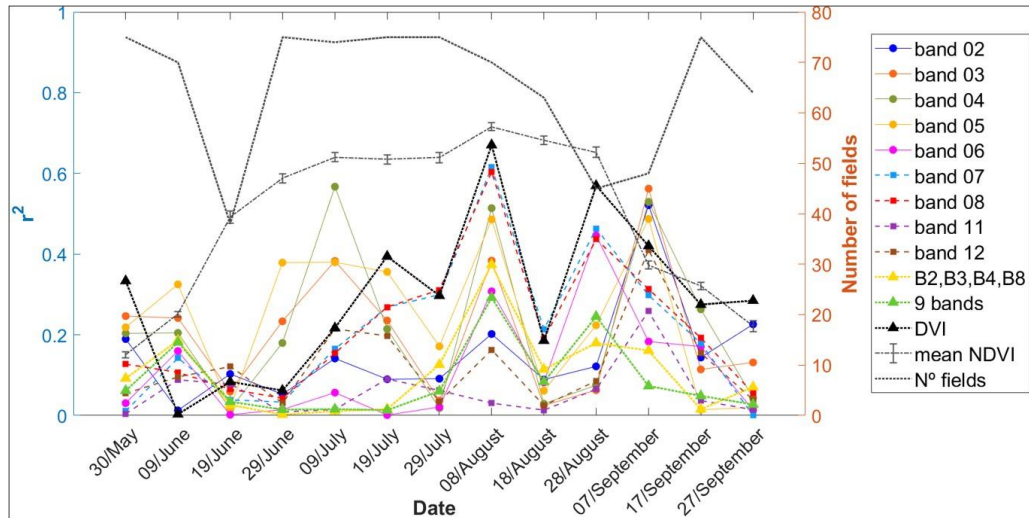


Figure 5. Timeseries of the determination coefficient (yield-band) for Bomba rice.

$$r^2 = 1 - \frac{\sum_{i=1}^N (\text{REND}_{\text{est}} - \text{REND}_{\text{real}})^2}{\sum_{i=1}^N (\overline{\text{REND}}_{\text{real}} - \text{REND}_{\text{real}})^2} \quad (6)$$

$$\text{RMSE} = \sqrt{\frac{1}{N} \sum_{i=1}^N (\text{REND}_{\text{est}} - \text{REND}_{\text{real}})^2} \quad (7)$$

$$\text{Error} = \text{RRMSE} = \frac{\text{RMSE}}{\overline{\text{REND}}_{\text{real}}} \times 100 \% \quad (8)$$

#### 4. RESULTS

Each prediction model is developed with 70% of the data reserved for training, obtaining different yield estimation equations (one for each model). Table 2 shows the evaluation metrics (equations 6, 7 and 8), resulting from the application of the yield estimation equation of each model to 30% of the data reserved for validation (test data).

From Table 2, we can see that for the two rice varieties analysed, the estimation model based on amplitude and Gaussian width slightly improves the model that only uses amplitude; however, it does not reach 1% in the improvement of the relative RMSE, so it is not particularly interesting.

**Table 2.** Performance metrics for each forecasting model for JSendra and Bomba rice.

		BOMBA			JSENDRA			
		$r^2$ (Eq.6)	RMSE (t/ha) (Eq.7)	RRMSE (%) (Eq.8)	$r^2$ (Eq.6)	RMSE (t/ha) (Eq.7)	RRMSE (%) (Eq.8)	
MÉTODO 1	Eq.2	0,68	0,35	7,74	0,64	0,45	5,24	Eq.2
	Eq.3	0,64	0,34	7,44	0,67	0,38	4,40	Eq.3
MÉTODO 2	Eq.4, Jul 9	0,84	0,32	7,11	0,46	0,44	5,19	Eq.4, Jul 9
	Eq.4, Aug 8	0,75	0,27	6,19	0,54	0,43	5,11	Eq.4, Sep 7
MÉTODO 3	Eq.5, Jul 9	0,77	0,29	6,39	0,51	0,47	5,52	Eq.5, Jul 9
	Eq.5, Aug 8	0,79	0,27	6,27	0,56	0,58	6,68	Eq.5, Sep 7
MÉTODO 4	Jul 9	0,52	0,34	7,71	0,55	0,49	5,86	Jul 9
	Aug 8	0,80	0,28	6,28	0,79	0,39	4,56	Sep 7

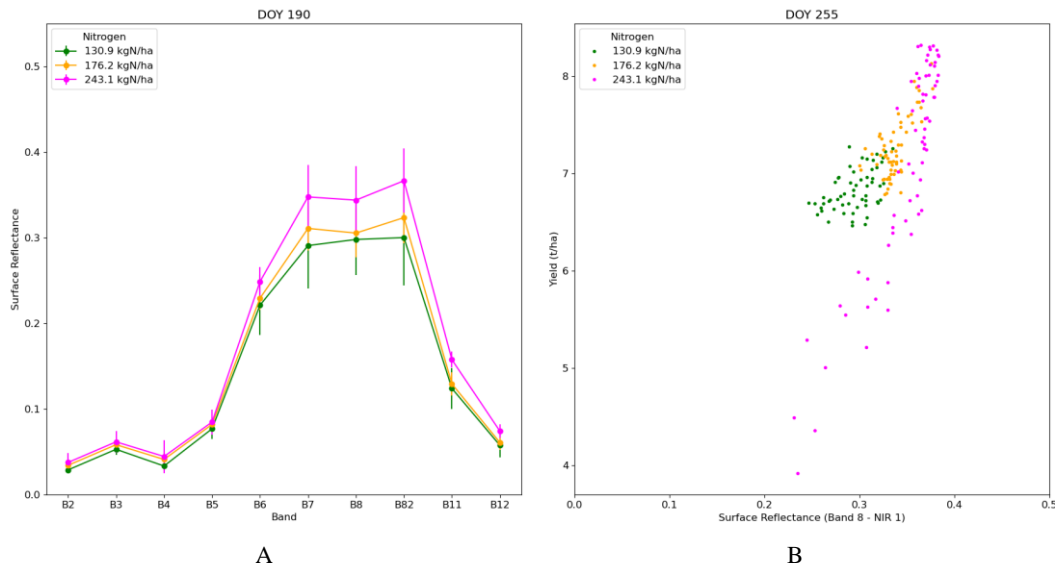


**Figure 6.** (A) Surface reflectance average values for each Sentinel-2 band for day 190. (B) Correlation of the pixel-level NIR band and final yield for day 255.

As for methods 2 and 3, the errors are very similar for both days and both methods, obtaining a difference in error around 1%, so the models on July 9 allow us to make early predictions with good accuracy. Finally, we see that the Random Forest models do not improve the previous methods and are not very useful.

Figure 6A shows that NIR band can monitor the rice development over different nitrogen management and therefore the more nitrogen we have, the surface reflectance in the near infrared band will be higher. Finally, Figure 6B shows that when applying a really high nitrogen soil content, the final yield is comparable to the medium nitrogen content, which indicates that we should avoid overfertilization.

## 5. CONCLUSIONS

In this work, four rice crop yield forecasting models of JSendra and Bomba rice varieties have been developed and evaluated using high spatial resolution Sentinel-2 data. The results show that it is possible to provide field-level rice yield estimations with an RMSE of 0.47 t/ha (5.2% error) for the JSendra rice variety and with an RMSE of 0.29 t/ha (6.4% error) for Bomba on July 9, about three months before harvest, thus satisfying the important premise of precision agriculture about providing early estimations that allow farmers to improve crop interventions. These results show us that the management of rice fields in the first weeks is determinant in the final yield. On the other hand, the study of nitrogen in rice has shown that overfertilization does not help to increase yields and should be avoided.

As a possible extension, it would be interesting to perform a relationship analysis between spectral data and the nitrogen content of rice fertilizers, study how it influences final yield and develop prediction models that include both variables (Huang et al., 2015), and finally incorporate meteorological data to improve the accuracy of prediction models (Sarma et al., 2008). All this will allow for more efficient, profitable and environmentally sustainable rice management practices.

## REFERENCES

- Bacenetti, J., Paleari, L., Tartarini, S., Vesely, F. M., Foi, M., Movedi, E., Ravasi, R. A., Bellopede, V., Durello, S., Ceravolo, C., and others, 2020, May smart technologies reduce the environmental impact of nitrogen fertilization? A case study for paddy rice. *Science of The Total Environment*, 715, 136956.
- Becker-Reshef, I., Franch, B., Barker, B., Murphy, M., Santamaria-Artigas, A., Humber, M., Skakun, S. and Vermote, E., 2018, Prior Season Crop Type Masks for Winter Wheat Yield Forecasting: A US Case Study. *Remote Sensing*, 10(10), 1659.
- Cai, Y., Guan, K., Nafziger, E., Chowdhary, G., Peng, B., Jin, Z., Wang, S. and Wang, S., 2019, Detecting in-season crop nitrogen stress of corn for field trials using UAV- and CubeSat-based multispectral sensing. *IEEE Journal of Selected Topics in Applied Earth Observations and Remote Sensing*, 12(12), 5153-5166.
- Franch, B., San Bautista, A., Fita, D., Rubio, C., Tarrazó-Serrano, D., Sánchez, A., Skakun, S., Vermote E., Becker-Reshef, I. and Uris, A., 2021, Within-Field Rice Yield Estimation Based on Sentinel-2 Satellite Data. *Remote Sensing*, 13, 4095.
- Huang, S., Miao, Y., Zhao, G., Yuan, F., Ma, X., Tan, C., Yu, W., Gnyp, M.L., Lenz-Wiedemann, V.I.S., Rascher, U. and Bareth, G., 2015, Satellite Remote Sensing-Based In-Season Diagnosis of Rice Nitrogen Status in Northeast China. *Remote Sensing*, 7, 10646-10667.
- Moreno-García, B., Casterad M.A., Guillén, M. and Quílez, D., 2018, Agronomic and Economic Potential of Vegetation Indices for Rice N Recommendations under Organic and Mineral Fertilization in Mediterranean Regions. *Remote Sensing*, 10(12), 1908.
- Sarma, A.A.L.N., Lakshmi Kumar, T.V. and Koteswararao, K., 2008, Development of an agro-climatic model for the estimation of rice yield. *J. Ind. Geophys. Union*, 12, 89-96.
- Vermote, E., Justice, C., Claverie, M. and Franch, B., 2016, Preliminary analysis of the performance of the Landsat 8/OLI land surface reflectance product. *Remote Sensing of Environment*, 185, 46-56.
- Weiss, M., Jacob, F. and Duveiller, G., 2020, Remote sensing for agricultural applications: A meta-review. *Remote Sensing of Environment*, 236, 111402.
- Zhang, G., Xu, T., Tian, Y., Xu, H., Song, J. and Lan, Y., 2020, Assessment of rice leaf blast severity using hyperspectral imaging during late vegetative growth. *Australasian Plant Pathology*, 49(5), 571-5.

# Analysis of Surface Urban Heat Island effect during 2021 using automatic classification of Spanish cities with Deep Learning algorithms

Salinas-González, Daniel, Skoković, Drazen, Sobrino, José A.  
Global Change Unit (GCU), Imaging Processing Laboratory (IPL).  
[daniel.salinas@uv.es](mailto:daniel.salinas@uv.es), [drazen.skokovic@uv.es](mailto:drazen.skokovic@uv.es), [jose.sobrino@uv.es](mailto:jose.sobrino@uv.es)

**ABSTRACT** - This work aims to perform an analysis of the surface urban heat island effect (SUHI) during the year 2021 in all major cities in Spain, in order to obtain an estimate of the increase in the surface temperature of each city, with respect to its surrounding green areas. Land Surface Temperature (LST) was used to measure the temperature difference, which is retrieved from the MYD21 and MOD21 products of the Aqua and Terra satellite of MODIS, respectively. This product was chosen for its daily temporal resolution for the areas under study and for using the Temperature Emissivity Separation (TES) algorithm for LST estimation.

It is known that the spatial resolution of 1 km per pixel is quite low for the study being pursued, but the proposed approach aims to apply more complex statistical methods based on Deep Learning algorithms to classify and differentiate urban areas from their surrounding green areas. State-of-the-art models based on natural language processing (NLP), more specifically the 'Transformers' model will be used for classification. This model uses attention mechanisms to search for contextual relationships between image pixels, decreasing the computational and temporal cost and achieving accuracies in the range of 90% to 95% in classification or segmentation of satellite images.

## 1 INTRODUCTION

The use of predictive analysis algorithms on remotely sensed imagery is a field of exploration that has made great advances either in the field of pixel-based image classification or image segmentation for soil classification (He, 2021). This work is carried out using Deep Learning and NLP (Natural Language Processing) algorithms based on "attention" (Vaswani, 2017) in order to obtain an approximation of a global predictive model to classify urban areas and their surrounding rural areas to automatically determine the urban heat island effect (SUHI).

According to (Sobrino, 2013) and (Sobrino 2012) the calculation of the SUHI is determined by the temperature difference between urban areas and their surrounding rural areas, since this task becomes complex when trying to classify such areas in a large number of cities or globally, due to the different characteristics of the cities, it is more than necessary to find a methodology that automates this process.

Therefore, this work focuses on finding an approach to a global model that is capable of automatically classifying urban areas from the surrounding rural areas, in order to determine and analyse the urban heat island effect not only locally

but also globally. The first phase focuses on obtaining data based on geophysical variables from the MODIS (moderate resolution imaging spectroradiometer) remote sensor, which are used as input data sets and predictive characteristics. For this work we use the LST (Land Surface Temperature) and LSE (Land Surface Emissivity) bands 29, 31, 32 obtained by using the TES algorithm (Gillespie, 1998) (see figure 1). with a daily temporal resolution and a spatial resolution of 1km/pixel.

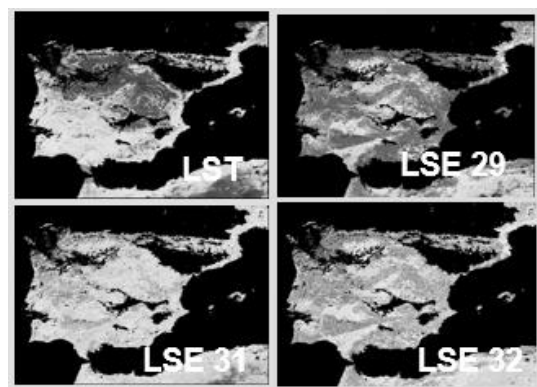


Figure 1. LST&LSE MODIS Product.

Once the training dataset is generated, a supervised classification based on Deep Learning algorithms is performed taking as validation data the MODIS land cover product (MCD12Q1) 1km/pixel to validate the classified areas, so that the algorithm is able to automatically classify urban and rural areas. Once this is done, the LST of each area is extracted to determine the urban heat island effect (SUHI) in different cities in Spain during the summer (June-August) of 2021.

## 2 METHODOLOGY

As mentioned above, the present work is divided into several phases: a first phase focuses on obtaining data based on geophysical variables, a second phase is based on the creation of a predictive model for the classification of urban areas and surrounding rural areas, and a final phase focuses on the analysis of the heat island effect in three cities in Spain during the summer of 2021.

### 2.1 Process chain in the creation of the dataset

To differentiate urban areas from their surrounding rural areas in a city, one can take the centroid or (latitude/longitude) point located in the city centre and a (latitude/longitude) point located in the surrounding rural areas of the city. This methodology is more than valid for determining the urban heat island effect, but this process becomes complex when one wants to analyse this effect in a larger number of cities, due to the different characteristics of each city, such as climate, geographical location, altitude or proximity to the coast (Sobrino, 2012).

All these characteristics make this task difficult to carry out. Therefore, the aim is to create a methodology capable of tackling this problem, based on the use of Deep Learning algorithms to classify urban areas and their rural areas. This requires a supervised classification based on segmentation and manual labelling of pixels. First of all, a selection of cities is made, which are different cities in Spain with different characteristics, such as geographical extension, number of inhabitants, proximity to the coast, altitude, etc. For this work, cities with a surface area greater than 5 km and cities with more than 25,000 inhabitants were chosen.

Once the study cities have been chosen, the pixels within the city are labelled as "urban areas" and the pixels of the surrounding rural areas as "rural areas", the interior areas or areas with a higher density of vegetation as "forest areas" and the rest of the pixels are labelled as "Others". A total of 12,485 points are taken for urban areas, 821,236 points for rural areas and 263,807 points for forest areas (see table 1).

The MODIS land classification product (MCD12Q1) at 1 km/pixel and the Sentinel-2 Land Cover product at 10 m/pixel are used as a reference base.

*Table 1. Points labelled by segmentation*

	Urban	Rural	Forest	Other
Points	12.485	821.236	263.807	100.000

Once the points have been obtained, the geophysical variables are obtained using the MODIS products (MYD21/MOD21). From these products we obtain LST (Land Surface Temperature) and LSE (Land Surface Emissivity) for bands 29, 31, 32 from the MODIS satellite (Terra/Aqua). To finalise the construction of the training dataset, it is necessary to carry out an interpolation of the labelled points on the MOD21 and MYD21 products, an example of the training dataset can be seen in table 2.

*Table 2 Training dataset points.*

Points	E29	E31	E32	LST
Urban	12.485	12.485	12.485	12.485
Rural	821.236	821.236	821.236	821.236
Forest	236.807	236.807	236.807	236.807
Other	100.000	100.000	100.000	100.000

Once the training dataset has been created, the next step is to create the predictive model.

### 2.2 Process chain in the creation of the training network and automatic classification results

#### 2.2.1 Baseline

To have a first approximation we have to establish a baseline on which to validate the final predictive model, for this we propose a classification based on Machine Learning algorithms such as the random forest (Breiman, 2001) and decision trees (Kingsford, 2008). Before starting with the creation of the baseline we have to divide the dataset into training, validation and test samples, using our training dataset in proportion 80% for training, 15% for validation and 5% for test. We then train our data with the baseline models. Once the training is finished, we obtain a classification accuracy of around 65~70% (see in table 3). This first approximation leads us to use more complex algorithms based on "attention".

Table 3. Metrics for baseline evaluations

Model	RMSE Trainig	RMSE Prediction	Training	Prediction
<b>Decision Trees</b>	0.0492	0.0563	0.671	0.664
<b>Random Forest</b>	0.0487	0.0524	0.693	0.682

### 2.2.2 Attention Based Algorithm

Following the above data partitioning we went on to build the attention-based training model (Vaswani, 2017) (see figure 2).

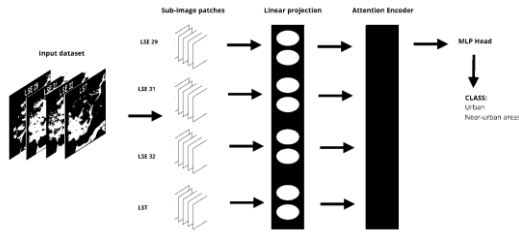


Figure2.Training network and automatic classification

Once the model is trained, an accuracy of about 85~90% is achieved (see table 4). To validate the robustness of the model, it is tested with the land cover product MCD12Q1 (MODIS LC\_TYPE1). As it is a classification based on four labels, urban land, rural land, forest and other, the model is able to separate the pixels associated with these labels, so this first approximation to a global model achieves good accuracies in training and prediction of pixels associated with urban and rural areas, which is fundamental for the analysis of the urban heat island effect.

Table 4. Metrics for model evaluations.

Model	RMSE Trainig	RMSE Prediction	Training	Prediction
<b>Attention</b>	0.0263	0.0342	0.892	0.884

## 3 RESULTS

### 3.1 Results of the automatic classification process

This approach to a global model based on attention has achieved accuracies of around 90%. In figure 3 we can

see the result of the classification, in this figure the classification of the urban areas and the surrounding rural areas of the city of Valencia as a result of the automatic classification is presented as an example. We can see that the model is able to differentiate the two zones, so this first approximation to a global model achieves good results for the study zones.

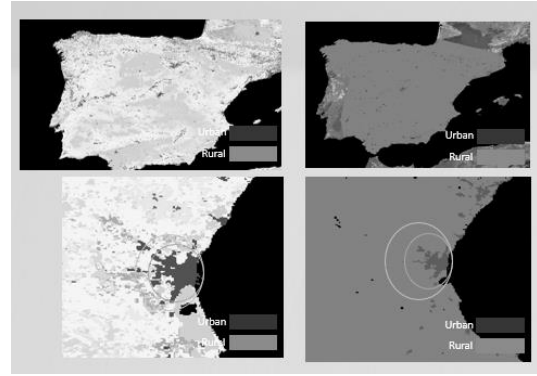


Figure 3. Left image, MCD12Q1 land cover classification, right image, automatic classification of urban areas (black), rural areas (grey) Valencia (Spain)

### 3.1 Analysis of the urban heat island effect

Once the images resulting from the automatic classification have been obtained, the LST is extracted from the pixels classified as urban and rural areas. From the classification we selected three cities (Alicante, Valencia, and Tarragona) (see figures 4, 5, 6) to carry out the analysis. With the difference between the LST(Urban) and the LST(Rural), the SUHI effect is determined, for this analysis the night temperatures are used.

It can be seen that for the three cities the effect remains constant during the summer period, reaching temperature differences from 1k to 5k. On the other hand, it can be seen that for the city of Tarragona, which has a lower infrastructure density than Alicante and Valencia, there is a smaller difference between the urban temperature and the temperature of the surrounding areas, so the SUHI effect is lower for the same summer period. The opposite case is the city of Valencia, whose infrastructure density is higher, so that of the three cities it is the one with the highest urban heat island effect for the same period.

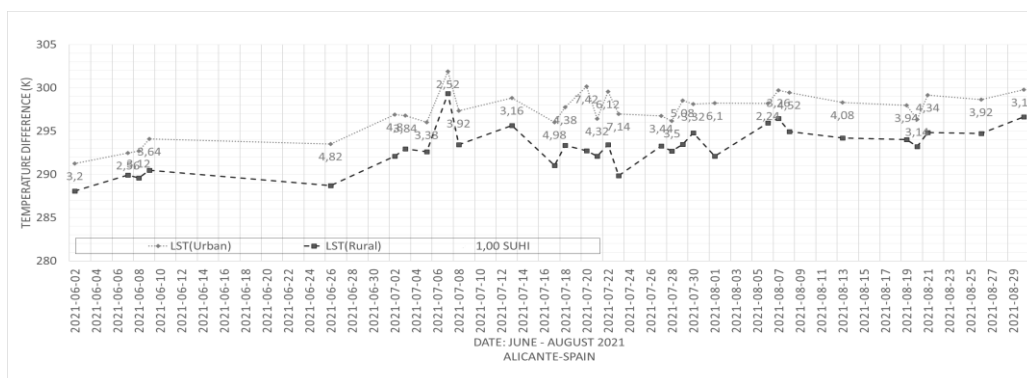


Figure 4. SUHI effect obtained from the LST (urban) and LST (rural) values resulting from the automatic classification, Alicante (Spain).

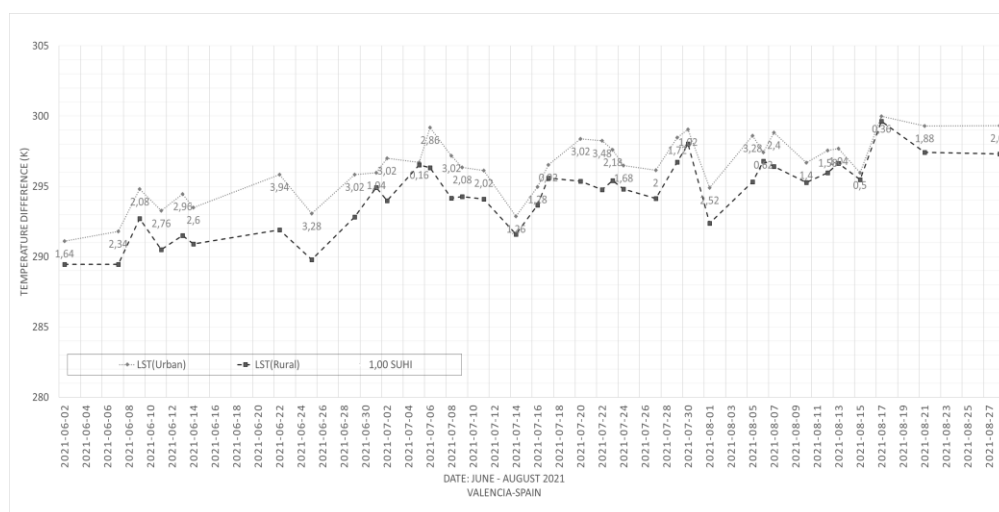


Figure 5. SUHI effect obtained from the LST (urban) and LST (rural) values resulting from the automatic classification, Valencia (Spain).

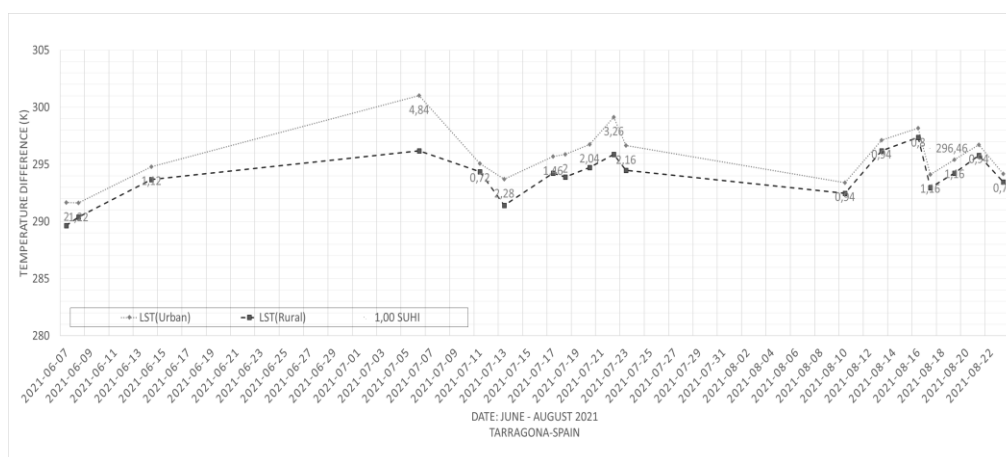


Figure 6. SUHI effect obtained from the LST (urban) and LST (rural) values resulting from the automatic classification, Tarragona (Spain).



#### 4 CONCLUSIONS

The use of automatic classification algorithms is of great help in determining the different SUHI, UHI, etc. effects. It has been seen that this approach to a global model gives good results in the classification of cities and rural areas as they reach a fairly high accuracy and manage to differentiate these areas. This makes it possible to automate the calculation of the urban heat island effect and to generate warning maps of this effect more quickly and with a daily update of data. As future work, the use of different geophysical variables is proposed, as well as the use of different products obtained by remote sensors that help to improve the spatial resolution of the image and, in turn, the classification.

#### 5 REFERENCES

- Breiman, L. (2001). "Random Forests. Machine Learning" 45, 5–32
- Gillespie, A. R., Rokugawa, S., Hook, S., Matsunaga, T., and Kahle, A. B. (1998) "A temperature and emissivity separation algorithm for Advanced Spaceborne Thermal Emission and Reflection Radiometer (ASTER) images" IEEE Transactions on Geoscience and Remote Sensing, vol. 36, pp. 1113–1126.
- He, Xin, Yushi Chen, and Zhouhan Lin. 2021. "Spatial-Spectral Transformer for Hyperspectral Image Classification" Remote Sensing 13, no. 3: 498.
- J.A. Sobrino, R. Oltra-Carrió, G. Sòria, R. Bianchi, M. Paganini. (2012) "Impact of spatial resolution and satellite overpass time on evaluation of the surface urban heat island effects" Remote Sensing of Environment, vol. 117, pp. 50-56.
- Kingsford, C., Salzberg, S. (2008) "What are decision trees?". Nat Biotechnol 26, 1011–1013
- Seemann, S.W., Borbas, E.E., Li, J., Menzel, W.P. and Gumley, L.E. (2006) "MODIS atmospheric profile retrieval Algorithm Theoretical Basis Document (version 6)."
- Sobrino, Jose & Oltra-Carrió, Rosa & Sòria Barres, Guillem & Jimenez-Munoz, Juan-Carlos & Franch, Belén & Hidalgo, Victoria & Mattar, Cristian & Julien, Yves & Cuenca, Juan & Romaguera, Mireia & Gómez, Jose. & Miguel, Eduardo & Bianchi, Remo & Paganini, Marc. (2013). "Evaluation of the surface urban heat island effect in the city of Madrid by thermal remote sensing. International Journal of Remote Sensing". 34. 3177. 10.1080/01431161.2012.716548.
- Vaswani, Ashish and Shazeer, Noam and Parmar, Niki and Uszkoreit, Jakob and Jones, Llion and Gomez, Aidan N. and Kaiser, Lukasz and Polosukhin, Illia. (2017) "Attention Is All You Need", Curran Associates Inc., pp. 6000–6010.

## Inter-annual trends of FAPAR and FVC SEVIRI/MSG climate data records along the period 2005-2020

B. Martínez, S. Sánchez-Ruiz, M. Campos-Taberner, F.J. García-Haro, M.A. Gilabert  
*Environmental Remote Sensing Group (UV-ERS), Departament de Física de la Terra i Termodinàmica, Facultat de Física, Universitat de València, 46100 Burjassot, Spain.*  
e-mail: beatriz.martinez@uv.es

**ABSTRACT-** *Inter-annual trends of land surface vegetation over the geostationary Meteosat disk (covering Europe, Africa, the Middle East and parts of South America) are analyzed. For this purpose, the Climate Data Record (CDR) time series for fraction of absorbed photosynthetically active radiation (FAPAR) and fractional vegetation cover (FVC) are considered. These CDRs offer consistent, homogeneous and continuous 10-day data for the period 2005-2020 derived from the best version of their equivalent near real time FAPAR and FVC products. The multi-resolution analysis (MRA) based on the wavelet transform (WT) was applied to derive the inter-annual trends of FAPAR and FVC time series. The MRA provides a temporal decomposition of the original series, where different components of the signal can be derived removing the contribution of specific temporal resolutions. The MRA-WT has demonstrated its potential to trace the inter-annual variability to detect trends using FAPAR and FVC climate data records from MSG/SEVIRI data. The results have shown a general greening in the central and eastern Sahel region, eastern Africa (Horn of Africa), eastern Spain and Turkey, which is associated with an increase in precipitation along the period. Some local negative changes have been observed in Senegal region and Southern parts of Africa, mainly attributed to variations of precipitation during the same period.*

### 1 INTRODUCTION

The scientific community requires consistent long-term data records with well-characterized uncertainty and suitable for modelling terrestrial ecosystems and energy cycles at regional and global scales. A climate data record (CDR) of different variables for the characterization of terrestrial ecosystems is freely available within the EUMESAT Satellite Application Facility for Land Surface Analysis (LSA SAF) from SEVIRI sensor on board MSG 1-4 geostationary satellites. These CDRs offer more than fifteen years (2005-present) of homogeneous time series required for climate and environmental applications and are freely available from the LSA SAF web site (<http://lsa-saf.eumetsat.int>).

The development of effective methodologies for the analysis of time series (TS) is one of the most important challenging issues for the remote sensing community due to the dynamic nature of terrestrial ecosystems. In this study, the multiresolution analysis based on the wavelet transform (MRA-WT) is used because of its results during the last decades as a time-frequency analysis tool for complex non-stationary signals in several study areas (Martínez and Gilabert, 2009). Particularly, it was useful in the study of non-stationary TS for the inter-annual variability of

vegetation dynamics. The correspondence of vegetation inter-annual variability and climatic factors, particularly air temperature and precipitation, have been studied in other regions (Martínez *et al.*, 2022).

The main goal of this work is to analyze inter-annual trends of land surface vegetation over the geostationary Meteosat disk. For this purpose, CDRs time series for fraction of absorbed photosynthetically active radiation (FAPAR) and fractional vegetation cover (FVC) are considered. These CDRs offer consistent, homogeneous and continuous 10-day data for the period 2005-2020 derived from the best version of their equivalent near real time FAPAR and FVC products. The MRA based on the wavelet transform is applied to derive the inter-annual trends of FAPAR and FVC time series. A local assessment over selected sites is performed enhanced with a regional analysis mainly focused in the African continent. Precipitation data is also considered in order to identify and understand the vegetation changes.

### 2 METHODS

The MRA-WT provides a temporal decomposition of the original series by removing from the original signal the contribution of specific temporal resolutions. The MRA-WT allows a fast decomposition by means of the implementation of the

discrete wavelet transform into timescales based on powers of two,  $2^j$  ( $j = 1, \dots, m$ ), where  $j$  refers to the different levels of decomposition and  $m$  to the highest level considered (Martínez and Gilabert, 2009). As a result of the MRA-WT, the original signal can be reconstructed as,

$$g(t) = A_m(t) + \sum_{j=1}^m D_j(t) \quad (1)$$

where  $A$  is the approximation component and  $D$  the detail component. The temporal resolution of each level depends on the center frequency of the selected wavelet and the temporal resolution of the TS. In our case, the Meyer wavelet (with central frequency  $\nu_c = 0.672$  Hz) is chosen due to its potential for vegetation dynamic analysis shown in previous studies (Rhif *et al.*, 2022). The MRA-WT is applied until level 6 since it gives us the approximation component ( $A_6$ ) to assess the inter-annual changes. Once the inter-annual component is derived, the Mann-Kendall non-parametric test and the Theil-Sen slope estimator (Martínez and Gilabert, 2009) are applied to statistically detect the FAPAR and FVC slope along the considered period.

### 3 MATERIALS

#### 3.1 FAPAR

FAPAR is the fraction of PAR that is absorbed by leaves and provides a link between the canopy function, i.e. its energy absorption capacity, and its structure and condition. The FAPAR CDR is compounded of the 10-day MSG FAPAR product (MTFAPAR, LSA-426) delivered by the LSA SAF network. The MTFAPAR product is a composition of the daily MSG FAPAR product (MDFAPAR), which is based on a linear relationship between the Renormalized Difference Vegetation Index (RDVI), computed from clear-sky top of the canopy reflectances in the red and near infrared bands for an optimal angular geometry in the solar principal plane. Observed deviations between MSG FAPAR and other FAPAR products are about 0.1 (García-Haro *et al.*, 2019).

#### 3.2 FVC

FVC represents the fraction of green vegetation covering a unit area of horizontal soil, corresponding to the gap fraction in the nadir direction. The FVC CDR is a composition of the 10-day MSG FVC product (MTFVC, LSA-422). The FVC MSG product is derived from a stochastic spectral mixture model that addresses the variability of soils and vegetation types using statistical distributions (García-Haro *et al.*,

2019). The MTFVC retrieval error has shown to be within the range of the typical differences found between satellite products, typically between 0.05 and 0.10.

#### 3.3 Precipitation data

The GPM data (GPM3IMERG product at monthly and  $0.1^\circ \times 0.1^\circ$  temporal and spatial resolutions) is also included for each site in order to qualitatively assess the precipitation-vegetation correspondence. The standardized precipitation index (SPI) at inter-annual scale is also computed since it quantifies precipitation anomalies by transforming observed precipitation into a gamma distribution for a specific time period.

#### 3.4 GLC2000

Last, the 1-km Global Land Cover 2000 (GLC2000) is considered to perform a local analysis (see the 13 selected sites in Figure 1). The global map is obtained from regional products modified to the local conditions offering an overall accuracy of 68.6%, similar to other land cover maps, such as the International Geosphere Biosphere Programme (66.9%) or Globe Cover 2009 (67.5%).

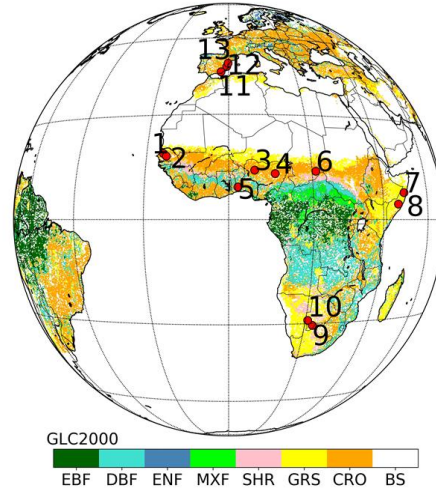


Figure 1. Location of different selected sites over the GLC2000 image.

### 4 RESULTS

#### 4.1 Local assessment

The Theil-Sen slope of the inter-annual component ( $A_6$ ) for the FAPAR and FVC CDRs is computed for 13 selected sites. Figure 2 shows two examples of the obtained results for sites #6 and #8 located in the Sahel and Somalia regions, respectively. Both original and  $A_6$ FAPAR time series are plotted.

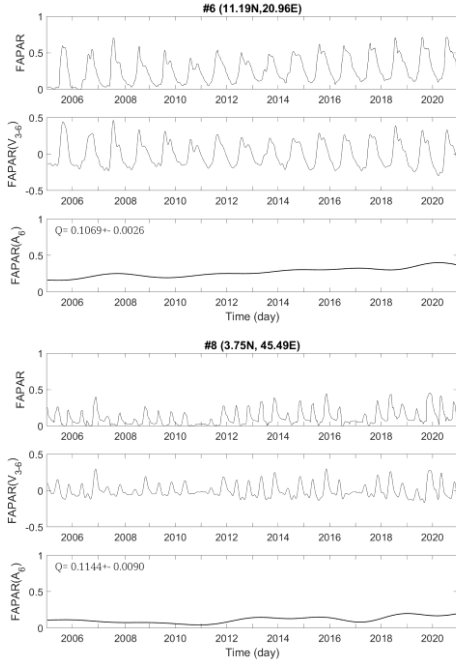


Figure 2. Example of original (top) and  $A_6$  FAPAR (bottom) time series for site #6 and #8. The  $V_{3-6}$  component is displayed in the center plot.

The  $V_{3-6}$  component is a measured of the intra-annual variability, defined as the contribution of the detail components from level 3 to 6. Figure 3 shows SPI-12 over the period 2005-2020. We can observe a clear recovery of site #6 from 2010 mainly associated to precipitation (Figure 3). For site #8, several drought events occurred during 2008-2012 and 2017, which had a direct impact in FAPAR. Nevertheless and in spite of those events, vegetation managed to partly recover and reach FAPAR levels higher than those before the drought of 2017.

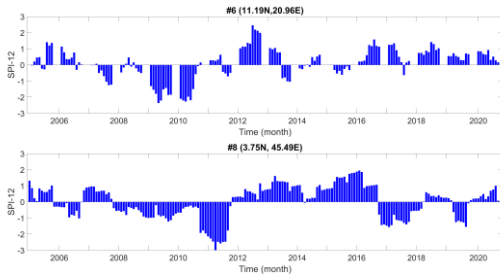


Figure 3. SPI-12 from GPM data for site #8 located in Somalia region.

Table 1 shows the slope derived from the FAPAR and FVC inter-annual component for all selected sites. Negative changes are smaller in magnitude than the positive ones (e.g., sites #1 and

#2). Some local negative changes are observed in Senegal region and southern Africa. These changes are mainly attributed to variations of precipitation during the same period as exception of local areas, which can be affected by human activity or hazards events, such as forest fires (site #13 in Valencia region, Spain).

Table 1. Local analysis over selected sites is performed. The Theil-Sen slope of the inter-annual component ( $A_6$ ) for the FAPAR and FVC CDRs is computed.

Site ID	Land cover GLC2000	FAPAR slope	FVC slope
#1	Grassland	$0.063 \pm 0.004$	$0.074 \pm 0.009$
#2	Grassland	$-0.016 \pm 0.005$	$-0.04 \pm 0.01$
#3	Cropland	$-0.034 \pm 0.003$	$-0.026 \pm 0.003$
#4	Cropland	$-0.053 \pm 0.002$	$-0.061 \pm 0.003$
#5	Forest	$0.104 \pm 0.006$	$0.025 \pm 0.001$
#6	Cropland	$0.107 \pm 0.003$	$0.048 \pm 0.003$
#7	Grassland	$0.188 \pm 0.015$	-
#8	Grassland	$0.114 \pm 0.009$	$0.063 \pm 0.005$
#9	Grassland	$-0.037 \pm 0.005$	$-0.099 \pm 0.009$
#10	Forest	$-0.038 \pm 0.003$	$-0.056 \pm 0.004$
#11	Grassland	$-0.026 \pm 0.009$	$-0.044 \pm 0.006$
#12	Grassland	$-0.022 \pm 0.002$	$-0.026 \pm 0.002$
#13	Open dec. & shrubland	$0.060 \pm 0.004$	$0.033 \pm 0.004$

#### 4.2 Regional assessment

The inter-annual trend images for FAPAR and FVC CDRs along the period 2005-2020 are shown in Figure 4. The results suggest a *greenness* concentrated on  $10^\circ$  N and  $16^\circ$  N, particularly in the central and eastern Sahel region (see Figure 2, site #6) and east part of Africa (Horn of Africa), which has been affected by severe drought periods in 2011 and 2016-2017 (see Figure 2, site #8). Previous studies reported a *re-greening* and a vegetation growth after the drought and advancing desert in the 80s (Fensholt *et al.*, 2012, Wu *et al.*, 2022). This increase can be partly explained by precipitation.

Regarding negative changes, southern Africa contains the major part of those changes. This is a particularly high risk area affected by drought events (Meza *et al.*, 2020). Global assessments focused on how drought risk impacts on agriculture have recognized South Africa as a drought-prone country (Baudoin *et al.*, 2017) that has experienced several “severe” drought events, as those occurred during the period 2014–16 (Baudoin *et al.*, 2017), and the recent ongoing drought since 2018 (Mahlalela *et al.*, 2020).

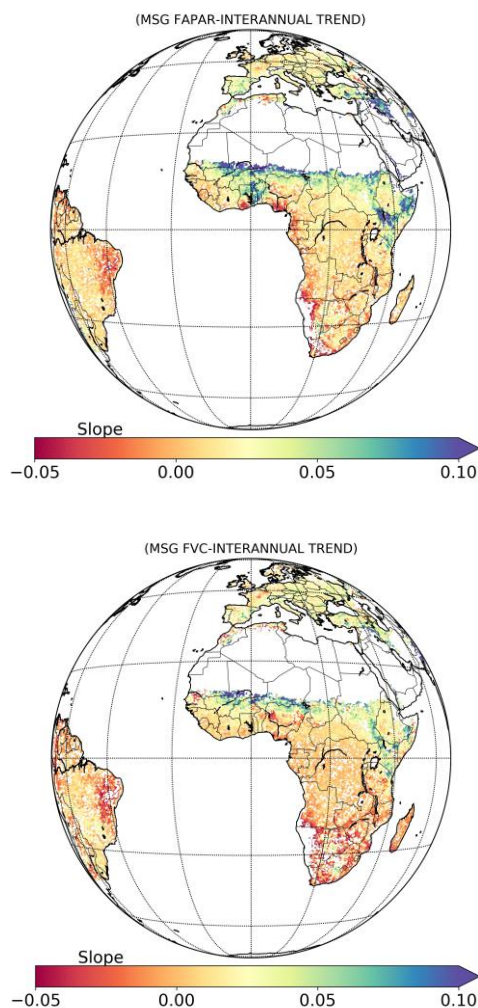


Figure 4. Inter-annual trend images for FAPAR and FVC CDRs along the period 2005-2020.

## 5 CONCLUSIONS

The MRA-WT has demonstrated its potential to trace the inter-annual variability for detecting trends using FAPAR and FVC CDRs from MSG/SEVIRI data with low uncertainties. Results have shown a general *greening* in the central and eastern Sahel region, east part of Africa (Horn of Africa), eastern part of Spain and Turkey, which is mainly associated with an increase in precipitation along the period. Some local negative changes are observed in Senegal region and southern parts of Africa. These changes are mainly attributed to variations of precipitation as exception of small areas, which may be affected by human activity or hazard events, such as forest fires.

## 6 ACKNOWLEDGMENTS

This research was supported by the LSA SAF (EUMETSAT) and ECCE EO project (Grant PID2020-118036RB-I00 funded by MCIN/AEI/10.13039/501100011033 and by “ERDF A way of making Europe”).

## 7 REFERENCES

- Baudoin, M.-A., Vogel, C., Nortje, K., Naik, M., 2017. Living with drought in South Africa: lessons learnt from the recent El Niño drought period. *Int. J. Disaster Risk Reduct.* 23, 128–137.
- Fensholt, R. *et al.* 2012. Greenness in semi-arid areas across the globe 1981–2007 - an Earth Observing Satellite based analysis of trends and drivers. *Rem. Sens. Env.* 121, 144–158.
- García-Haro, F.J., Camacho, F., Martínez, B., Campos-Taberner, M., Fuster, B., Sánchez-Zapero, J., Gilabert, M.A. 2019. Climate Data Records of Vegetation Variables from Geostationary SEVIRI/MSG Data: Products, Algorithms and Applications. *Remote Sens.* 11, 21.03.
- Mahlalela, P.T., Blamey, R.C., Hart, N.C.G., Reason, C.J.C., 2020. Drought in the eastern cape region of South Africa and trends in rainfall characteristics. *Clim. Dyn.* 55, 2743–2759.
- Martínez, B., and Gilabert, M.A. 2009. Vegetation dynamics from NDVI time series analysis using the wavelet transform. *Rem. Sens. Env.* 113, 1823–1842.
- Martínez, B. Sánchez-Ruiz, S. Campos-Taberner, M., García-Haro, F.J., Gilabert, M.A. 2022. Exploring Ecosystem Functioning in Spain with Gross and Net Primary Production Time Series. *Remote Sens.* 14, 1310.
- Meza, I., *et al.*, 2020. Global-scale drought risk assessment for agricultural systems. *Nat. Hazards Earth Syst. Sci.* 20, 695–712.
- Rhif, M., Ben Abbes, A., Martínez, B., de Jong, R., Sang, Y., Riadh Farah, I. 2022. Detection of trend and seasonal changes in non-stationary remote sensing data: Case study of Tunisia vegetation dynamics, *Ecol. Inform.* 69, 101596.
- Wu, S., Gao, X., Lei, J., Zhou, N., Guo, Z., Shang, B. 2022. Ecological environment quality evaluation of the Sahel region in Africa based on remote sensing ecological index. *J. Arid Land* 14, 14–33.

# Spatiotemporal evolution of the land cover over Deception Island, Antarctica, its impact on albedo and its relationship with meteorological variables

Javier F. Calleja<sup>1</sup>, Susana Fernández<sup>2</sup>, Rubén Muñoz<sup>3</sup>, Jaime Otero<sup>4</sup>, Francisco Navarro<sup>4</sup>, Alejandro Corbea-Pérez<sup>5</sup>, Carleen Reijmer<sup>6</sup>, Miguel Ángel de Pablo<sup>7</sup>

<sup>1</sup> Departamento de Física, Universidad de Oviedo, Spain.

<sup>2</sup> Departamento de Geología, Universidad de Oviedo, Spain.

<sup>3</sup> Departamento de Informática, Universidad de Oviedo, Spain.

<sup>4</sup> Departamento de Matemática Aplicada a las TIC, Universidad Politécnica de Madrid, Spain

<sup>5</sup> Departamento de Explotación y Prospección de Minas, Universidad de Oviedo, Spain.

<sup>6</sup> Faculty of Science, Utrecht University, The Netherlands.

<sup>7</sup> Departamento de Geología, Geografía y Medio Ambiente, Universidad de Alcalá, Spain. jfcalleja@uniovi.es

**ABSTRACT-** *In this work we use shortwave broadband albedo from satellite sensors and from in-situ surveys to calculate the monthly relative abundances of land cover types over Deception Island, Antarctica. In-situ distributed shortwave albedo data were collected using a portable albedometer over seven types of covers: continuous clean fresh snow (S1); continuous clean old snow (S2); continuous dirty snow (S3); mixture of clean snow; dirty snow and lapilli (S4); mixture of snow and bare soil patches (S5); shallow snow with small bare soil holes (S6); continuous bare soil (S7). MODIS MCD43A3 daily albedo product was downloaded using the Google Earth Engine API from 2000-2001 to 2019-2020 seasons. Each season extends from September to March of two consecutive years. Mean summer air temperature was calculated from data collected by an Automatic Weather Station. From the in-situ albedo data, each land cover type was characterized by a shortwave albedo normal distribution. From the satellite data, the monthly mean shortwave albedo histogram was calculated. The monthly relative abundance of each cover type was calculated by fitting for each month a linear combination of the normal distributions to the histogram of the satellite data. We calculated the seasonal mean albedo over the whole island and the seasonal relative abundance of each cover type. The results provide an accurate picture of the land cover change and its driving mechanisms. The mean albedo of the island is determined by the competition between land covers S4 and S6, the summer air temperature being the driving mechanism.*

## 1 INTRODUCTION

The relative amount of snow and ice cover in Antarctica plays a crucial role in the surface energy budget. A precise description of the spatiotemporal evolution of the snow and ice cover is mandatory to understand the impact of climate change and to predict the future evolution of the ice cover. Although high- and mid-resolution satellite sensors may provide an accurate instantaneous picture of the land cover, their low temporal resolution is a serious drawback to obtain long time series. The reflectance of the surface in areas covered totally or partially by snow and ice depends on the properties of the snow and ice cover and on the relative amount of snow, ice and bare soil. Snow reflectance evolves over time at different time scales: it can change abruptly in few hours, and it also exhibits daily, monthly, and seasonal variations, along with

long-term variations (trend) (Calleja et al. 2019). Moreover, in areas where snow melt is ubiquitous, the albedo of the surface varies along summer with the exposition of bare soil. The sole estimation of a mean albedo in such cases provides a poor description of the real picture. For example, a decrease in albedo can be due to the metamorphization of the snow or to an increase of the abundance of bare soil. On the other hand, albedo can increase as a consequence of new fresh snow or to an increase of the area covered by snow. It is our aim to show that the combined use of satellite and in-situ shortwave broadband albedo (albedo integrated in the range 300-3000 nm) can provide an accurate description of the land cover over an Antarctic site. The advantage of the method presented lies in the fact that in-situ measurements are easy to carry out, the equipment being rough, light and easy to transport over snowed and iced areas.



## 2 DATA AND METHODS

### 2.1 Study area

The study site is Deception Island, located in the South Shetland Islands Archipelago, in the NW coast of the Antarctic Peninsula (Fig. 1). Deception Island is an active volcano with recent eruptions and unrest episodes. It has areas of dark soil with varying size along summer as well as large areas of snow contaminated with volcanic ash. The changing mixture of bare soil and snow/ice makes it a suitable location for detecting changes in the land cover. The Spanish Antarctic station Gabriel de Castilla is on the island.

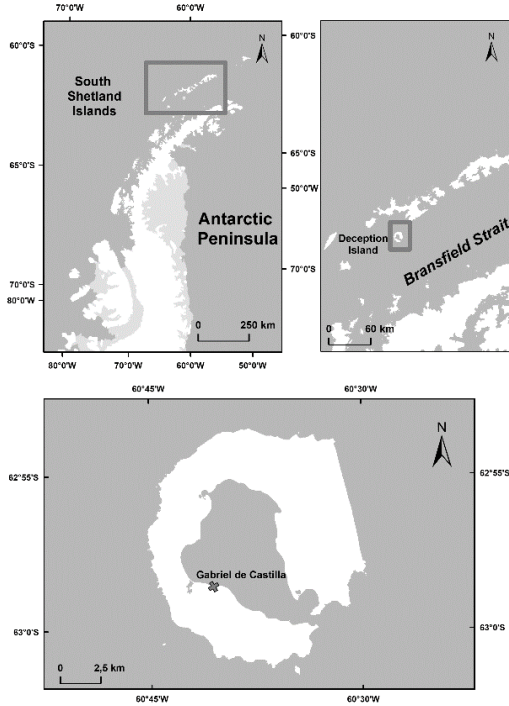


Figure 1. Location of Deception Island.

### 2.2 In-situ data

We used data from an Automatic Weather Station (AWS) on Deception Island and distributed albedo data collected in January 2019. Data from the AWS include hourly air temperature, as well as mean daily air temperature (AEMET 2022). Distributed albedo measurements were carried out using a homemade portable albedometer consisting of two pyranometers, one facing the sky and another facing the surface, and two synchronized dataloggers. The ratio of the signal from the pyranometer facing the surface to the signal of the pyranometer facing the sky provides the albedo of the surface. One measurement was collected every 5 seconds while walking over a given sampling plot. The

pyranometers were all the time placed parallel to the surface, and the chosen sampling plots were flat. Six landscape units were chosen as representative of the landscape following the expert criteria (Fig. 2): continuous clean fresh snow (S1); continuous clean old snow (S2); continuous dirty snow (S3); mixture of clean snow, dirty snow and lapilli (S4); mixture of snow and bare soil patches (S5); shallow snow with small bare soil holes (S6); continuous bare soil (S7).

### 2.3 Satellite data

MODIS daily albedo product MCD43A3 (C6) was used in this work (Schaaf and Wang 2015). The time span is from 2000-2001 season to 2019-2020. Only data with  $SZA < 75^\circ$  are considered, this means from September 1 to April 1. Data were downloaded using the Google Earth Engine API (Gorelick et al. 2017). MCD43A3 includes one band of shortwave Black Sky Albedo (BSA), and one band of shortwave White Sky Albedo (WSA). In this work we present the results obtained using the shortwave BSA band.

### 2.4 Data processing

In situ data were processed as follows. Regarding the data from the AWS monthly and season means of meteorological variables were calculated only if data were available for at least 80% of the days (Bañón and Vasallo 2016). Mean summer temperatures were also calculated for seasons 2004-2005 to 2013-2014. Regarding albedo distributed measurements, we have to be sure that variations in the data correspond to variations in the surface, and we have to eliminate data fluctuations due to changes in illumination conditions. To achieve this, data were firstly filtered eliminating outliers in incident irradiance, reflected irradiance and albedo. Because snow albedo is very sensitive to the relative amount of direct and diffuse radiation, only datasets for which the coefficient of variation ( $CV = \text{standard deviation} / \text{mean}$ ) of the incident radiation was below 6% were considered. We then checked that there was no correlation between the incident radiation and the albedo. We applied then a correction for cloudiness (Greuell and Konzelmann 1994). The method consists in calculating the albedo under clear sky from the actually measured albedo as:

$$\alpha_{clear} = \alpha_{cloud} + 0.05(n - 0.5) \quad (1)$$

Where  $\alpha_{clear}$  and  $\alpha_{cloud}$  are the broadband albedos measured under clear and cloudy sky (the actually measured one) respectively, and  $n$  is the cloud index ( $n=1$  means a completely overcast sky,  $n=0$  means a completely clear sky). The cloud index can be calculated from the cloud transmittance ( $T$ ) and the height of the observation site ( $h$ ) using the relation:



$$T = 1 - An^2e^{-Bh} \quad (2)$$

with  $A = 0.78$  and  $B = 0.00085$ .  
The value of  $T$  is calculated assuming that

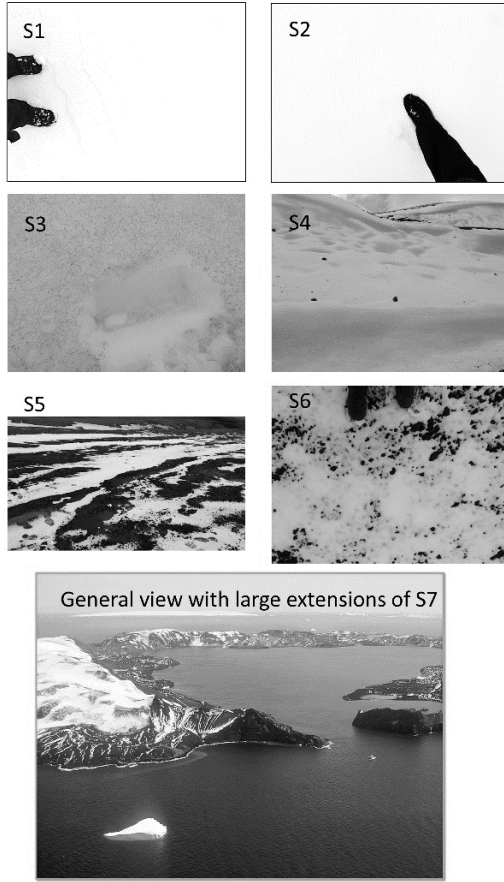


Figure 2. Landscape units and a typical general view of Deception Island in summer with large extensions of bare soil.

$$T = \frac{E(\text{cloud})}{E(\text{clear})} \quad (3)$$

where  $E(\text{cloud})$  is the measured irradiance and  $E(\text{clear})$  is the irradiance that would have been measured under clear sky conditions.  $E(\text{clear})$  depends on the SZA. To calculate  $E(\text{clear})$  at the time of the acquired  $E(\text{cloud})$  we used the measured irradiance on the closest date along a day with clear sky during all day. In our case, this happened on February 16, 2019.  $E(\text{clear})$  at any time of the day was obtained by fitting hourly irradiance to the SZA:

$$E(\text{clear}) = a(\cos SZA)^b \quad (4)$$

From the fit we obtained  $a = 1088 \text{ W/m}^2$  and  $b = 1.7$ , with a coefficient of determination  $R^2 = 0.97$ .

With the resulting data sets we built a histogram for each of the landscape units. The histograms were fitted to a normal distribution. The mean albedo value and the standard deviation of each landscape unit is given in Table 1.

Table 1. Mean albedo and standard deviation of the normal distribution of each landscape unit.

Landscape unit	Mean	$\sigma$
S1	0.830	0.016
S2	0.736	0.013
S3	0.457	0.018
S4	0.599	0.040
S5	0.313	0.080
S6	0.166	0.053
S7	0.041	0.009

Satellite data were filtered to assure that the variations in the land cover were appropriately tracked. We must take into account that snow albedo changes in the span of a few days due to snow metamorphism and that due to the special characteristics of Deception Island, the snow cover can disappear in hours or days due to melting. Because of this, only pixels for which the mean difference between two consecutive albedo data along a month was below 8 days were considered in the analysis. With those pixels we calculated the monthly mean albedo and the seasonal mean albedo and the corresponding histograms (albedo range versus number of pixels).

Each MCD43A3 pixel is the statistical mixture of the landscape units. The histograms on MCD43A3 monthly means were fitted to a linear combination of the normal distributions of the landscape units. The coefficients of the linear combination were interpreted as the relative amount of each landscape unit. We calculated the relative abundance of each landscape unit per month and the seasonal mean.

### 3 RESULTS

The mean relative abundance of each landscape unit along the period 2000—2020 to 2019—2020 is: S5 (38%), S4 (27%), S6 (12%), S3 (11%), S2 (6%), S7 (4%), and S1 (2%).

Of all the meteorological variables measured at the AWS, the mean summer air temperature (mean air temperature in the period December-January-February) was the one exhibiting the highest correlation with the seasonal mean albedo over the island (Fig. 3).

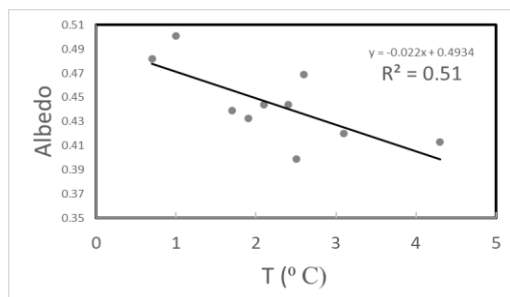


Figure 3. Mean albedo against mean summer air temperature over Deception Island for seasons 2004-2005 to 2013-2014.

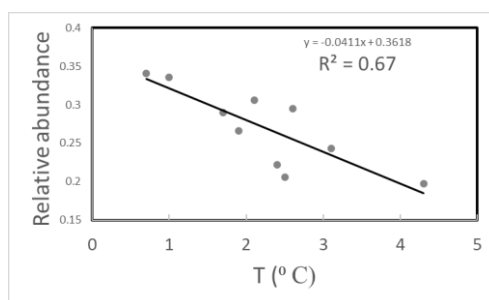


Figure 4. Seasonal relative abundance of landscape unit S4 against mean summer air temperature for seasons 2004-2005 to 2013-2014.

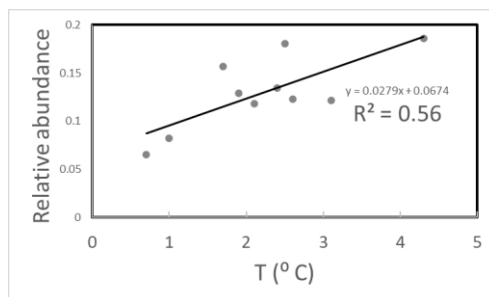


Figure 5. Seasonal relative abundance of landscape unit S6 against mean summer air temperature for seasons 2004-2005 to 2013-2014.

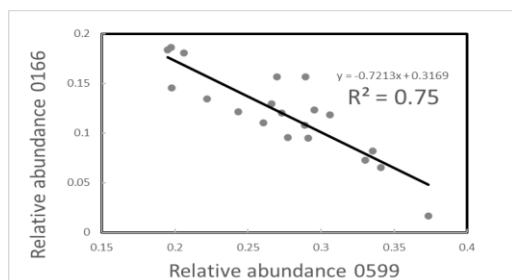


Figure 6. Relative abundance of S4 against relative abundance of S6 for seasons 2000-2001 to 2019-2020.

On the other hand the relative abundance of S4 and S6 exhibit a large correlation with the mean summer air temperature (Figs. 4 and 5) and a large negative correlation between them (Fig. 6). From these results, we can conclude that the evolution over time of the albedo over Deception Island is mainly driven by air temperature, such that the increase of air temperature seems to induce a decrease in albedo. The albedo variation over the island is the result of a competition between landscape units S4 and S6. While the relative abundance of S4 decreases with increasing temperature, the relative abundance of S6 increases with increasing temperature. These results provide a first insight of the processes taking place over the island: it seems that soot, dust and lapilli (present in S4) act as melting centres, giving way to holes of bare soil (those observed in S6). This process seems to be the one determining the decrease of albedo with increasing temperature.

#### 4 ACKNOWLEDGMENTS

This work was supported by the Spanish Ministry of Science and Innovation under grants PID2021-127060OB-IOO, CTM2017-84441-R, and CTM2014-52021-R. The work of Alejandro Corbea-Pérez was supported by the Ph.D. Grant: “Severo Ochoa” from the Government of the Principality of Asturias [BP17-151].

#### REFERENCES

- AEMET (2022) Weather Services.  
[https://www.aemet.es/es/datos\\_abiertos/AEMET\\_OpenData](https://www.aemet.es/es/datos_abiertos/AEMET_OpenData)
- Bañón M, Vasallo F (2016) AEMET en la Antártida
- Calleja JF, Corbea-Pérez A, Fernández S, et al (2019) Snow albedo seasonality and trend from MODIS sensor and ground data at johnsons glacier, livingston island, maritime antarctica. Sensors (Switzerland) 19:.  
<https://doi.org/10.3390/s19163569>
- Gorelick N, Hancher M, Dixon M, et al (2017) Google Earth Engine: Planetary-scale geospatial analysis for everyone. Remote Sens Environ 202:18–27.  
<https://doi.org/https://doi.org/10.1016/j.rse.2017.06.031>
- Greuell W, Konzmann T (1994) Numerical modelling of the energy balance and the englacial temperature of the Greenland Ice Sheet. Calculations for the ETH-Camp location (West Greenland, 1155 m a.s.l.). Glob Planet Change 9:91–114.  
[https://doi.org/https://doi.org/10.1016/0921-8181\(94\)90010-8](https://doi.org/https://doi.org/10.1016/0921-8181(94)90010-8)
- Schaaf C, Wang Z (2015) MCD43A1 MODIS/Terra+Aqua BRDF/Albedo Model Parameters Daily L3 Global - 500m V006 [Data set]. Accessed 2022-10-28 from <https://doi.org/10.5067/MODIS/MCD43A1.006>. In: NASA EOSDIS L. Process. DAAC.  
<https://doi.org/10.5067/MODIS/MCD43A1.006>

# Long-term Dynamics of Land Surface Temperature over Europe: Towards a Daytime normalized AVHRR Land Surface Temperature Product

Philipp Reiners<sup>1,\*</sup>, Stefanie Holzwarth<sup>1</sup>, Sarah Asam<sup>1</sup>, Ursula Gessner<sup>1</sup>, Claudia Kuenzer<sup>1,2</sup>

1 German Aerospace Center (DLR), German Remote Sensing Data Center (DFD), 82234 Wessling, Germany

2 University of Wuerzburg, Institute of Geography and Geology, Chair of Remote Sensing, 97074 Würzburg, Germany

\* Correspondence: philipp.reiners@dlr.de; Tel.: +49-8153-28-4533

**ABSTRACT** - In this study a statistical orbit drift correction method was applied to TIMELINE AVHRR LST from NOAA 7, 9, 11, 14, 16, 18 and 19 afternoon overpasses at 12 sites across Europe. The corrected LST anomalies were validated against Ta anomalies from nearby meteorological stations. The results showed an improvement of the correlation (R) between the LST and Ta anomalies at most sites. A few sites showed a decrease of R, which can be explained by complex land cover (urban) or missing daytime effects of LST (at forest sites). After the orbit drift correction, the long-term trends of the LST anomalies were much closer to the Ta trends. Furthermore, climatological features visible in the Ta time series (like e.g. a warm period in the late 1980s) are more distinct in the LST time series after the correction. However, similar studies reached higher correlations between LST and Ta anomalies. This can be explained by a more uniform generation of the LST and Ta anomalies. Further improvements and validation are necessary to obtain a reliable and continent-wide orbit drift correction for AVHRR. It is also planned to extend the analysis to further orbit drift correction methods and also to other validation data, e.g. Landsat LST.

## 1 INTRODUCTION

LST is an important quantity for tracing the impact of changing climatic conditions on our environment from local to global scale. Changes in LST represent on the one side climate change processes like global warming and on the other side land surfaces processes like urbanization and deforestation. LST is recognized as one of the Essential Climate Variables (ECVs) by the World Meteorological Organization and has a strong link to near surface air temperature.

For monitoring conditions repeatedly over large areas, satellite derived LST has become an indispensable tool. However, to make climate relevant statements and quantify the impact of land surface variables over long time, we need sensors that are, unlike e.g. the Moderate Resolution Imaging Spectroradiometer (MODIS), available for more than 30 years. The Advanced Very High Resolution Radiometer (AVHRR) is the only sensor providing spatially and temporally continuous, daily measurements for 40 years. The TIMELINE project (“Time Series Processing of Medium Resolution Earth Observation Data Assessing Long-Term Dynamics in our Natural Environment”, [www.timeline.dlr.de](http://www.timeline.dlr.de)) of the Earth Observation Center (EOC) of the German Aerospace Center (DLR) aims at the generation of a

homogeneous multi-decadal time series from AVHRR data over Europe and North Africa (Dech et al. 2021). The resulting collection of remote sensing products contains land and sea surface parameters, a.o. LST (Reiners et al. 2021). It is planned to offer these products online to a wider community using a free and open data policy.

However, the different overpass times and the orbital drift effect hide actual trends and anomalies in LST. Several methods exist to account for this effect of varying acquisition times on LST time series, which can be classified into physical and statistical methods. While physical models, as e.g. proposed by Liu et al. 2019 try to reconstruct the diurnal LST cycle, statistical models try to delineate the orbit drift signal from the time series itself.

In this study, the statistical daytime correction model by Julien and Sobrino 2021 is applied to the TIMELINE LST data and its performance is analyzed at different sites with different land cover across Europe. The model uses the regression between the LST anomalies and the corresponding SZA anomalies for each day of the year throughout the time series. This allows to remove the orbit drift effect for each sensor. An additional offset is used to adjust the observation times of the sensors.

An important requirement for these methods is that they preserve the actual trends in LST. However, especially for the period before the year 2000 no independent LST datasets exist to validate these methods. As an approximation, historical measurements of near surface air temperature ( $T_a$ ) at various stations across Europe can be used. Despite the known differences between LST and  $T_a$  at short time scales, it is expected, that long term trends correspond in these two variables. In this study the performance of the model is validated through the correlation of the monthly anomalies of LST and  $T_a$  and through the comparison of their long-term trends.

## 2 DATA AND METHODS

### 2.1 Study sites

For the evaluation of the orbit drift correction 12 sites across Europe have been selected from the

Benchmark Land Multisite Analysis and Intercomparison of Products (BELMANIP) network (Baret et al. 2006). These sites are characterized by a homogenous and stable land cover on the AVHRR sensor scale. This is important to reduce the influence of land cover change on the LST climatology at the respective site.

For the comparison with  $T_a$ , the nearest measuring station to the respective BELMANIP site with the same land cover was selected from the EU Surface Temperature for All Corners of Earth (EUSTACE) network (Rayner et al. 2020). The map on Figure 1 shows the location of the BELMANIP sites and the corresponding EUSTACE stations. The smallest distance is between the cropland site 251 and the station Szeget (19 km), the hugest distance is between the Urban site 269 and the station Krasnaja Gra (369 km).

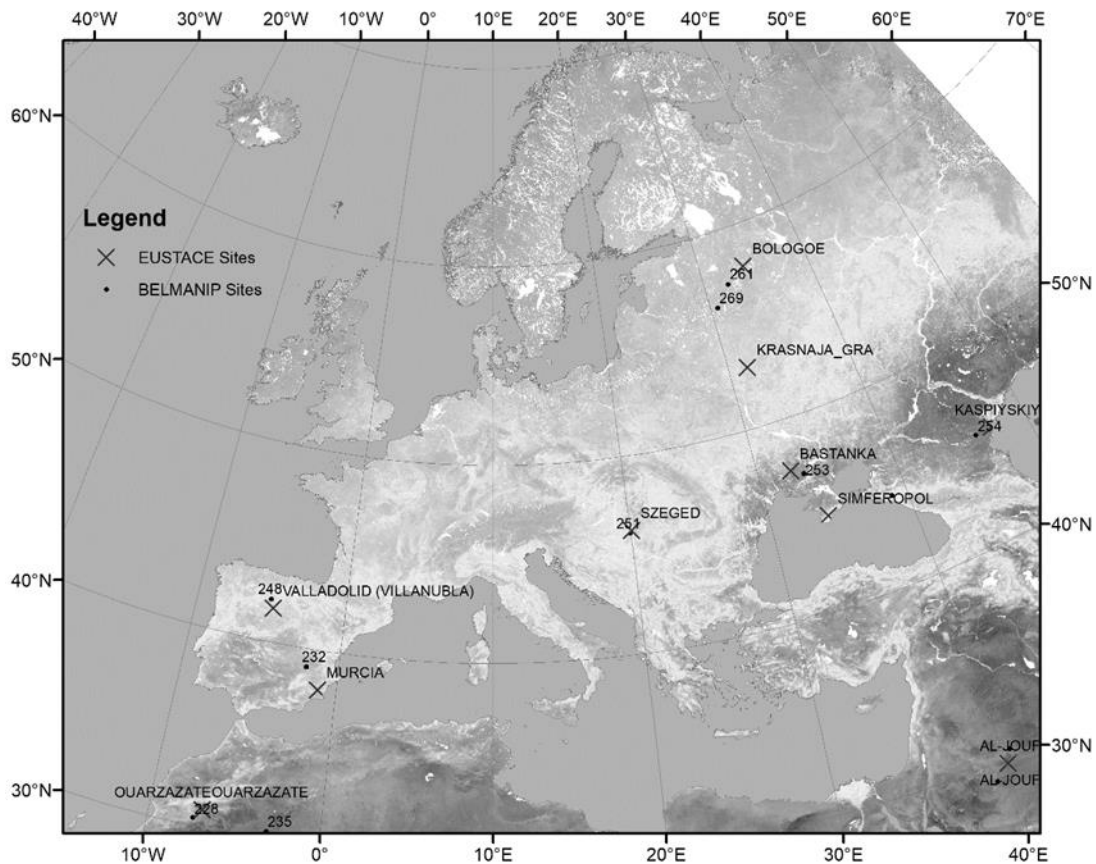


Figure 1: Map of the Study Sites from BELMANIP and EUSTACE network

## 2.2 TIMELINE LST

The TIMELINE LST product was derived from the brightness temperatures of AVHRR channels 4 and 5. Atmospheric correction was performed with an extension of the Split Window Algorithm by Becker and Li 2007 for AVHRR 2 and 3 and an extension of the Mono Window Algorithm by Qin, Karnieli and Berliner 2001 for AVHRR 1. Frey, Kuenzer and Dech 2017 extended these algorithms with a different set of coefficients for daytime and nighttime, each AVHRR sensor, sensor view angle class, Total Columnar Water Vapor (TCWV) class and LST class. The Level 3 products consist of daily, 10-days and monthly composites of LST. While the daily composites contain the best LST observation of the day (lowest sensor zenith angle), the 10-daily and monthly composites contain maximum, minimum, median and mean LST for the respective period.

Daily LST and monthly maximum LST was extracted at the nearest pixel to the respective BELMANIP site. Only data from afternoon overpasses (12.00-16.00h true solar time) from NOAA-7, 9, 11, 14, 16, 18, and 19 was taken.

## 2.3 Air Temperature Data

Ta data were taken from the (EUSTACE) project (Rayner et al. 2020), which offers daily homogenized measurements from meteorological stations. From the dataset the daily maximum Ta was selected (Tmax) and aggregated to monthly maximum Ta.

## 2.4 Methodology

The statistical orbit drift correction method by Julien and Sobrino 2021 is referred to as 'C0' in their publication. It uses a linear regression between the LST anomalies and a second degree fit of the sun zenith anomalies for each sensor. For the calculation the daily LSTs were aggregated for each day of the year through the complete time series of the respective sensor. The anomaly is the deviation of each observation to the mean of the respective day. The same procedure was carried out to calculate the sun zenith anomalies. A second-degree fit was applied to the sun zenith anomaly time series to reduce noise.

The orbit drift contribution (ODC) to LST can then be described with the formula:

$$ODC = a_i * SZA\_anom\_fit_i \quad (1)$$

where  $SZA\_anom\_fit_i$  is the second degree fit of the sun zenith angle anomalies and  $a_i$  is the regression coefficient. The regression coefficients were fitted to the LST anomaly time series via least square fitting. To correct the LST time series the ODC was subtracted from the LST values.

For the validation the monthly maximum LST anomalies and the monthly maximum Ta anomalies were correlated before and after the correction. Also, the long-term trends of both variables were compared before and after the correction.

		R between monthly Ta anomalies and monthly LST anomalies			Trend [K/yr]		
BELMANIP site	Landcover	Original	Corrected	Change [%]	Original LST	Ta	Corrected LST
210	Desert	0.26	0.269	3.5	0.22	0.05	0.07
228	Desert	0.321	0.37	15.3	0.11	0.07	0.07
232	Croplands	0.263	0.277	5.3	0.12	0.04	0.04
235	Desert	0.29	0.299	3.1	0.2	0.05	0.13
239	Desert	0.358	0.404	12.8	0.2	0.04	0.07
243	BroadDec	0.407	0.423	3.9	-0.03	0.04	-0.04
248	OpenShrub	0.435	0.462	6.2	0.06	0.02	0.01
251	Croplands	0.518	0.518	0.0	0.13	0.04	0.06
253	Croplands	0.357	0.395	10.6	0.14	0.12	0.02
254	Grassland	0.374	0.332	-11.2	0.13	0.06	0.01
261	MixedForest	0.477	0.463	-2.9	-0.04	0.02	-0.06
269	Urban	0.38	0.362	-4.7	0.11	0.04	0.01

Figure 2: Results of the Orbit Drift Correction for all sites: Correlation coefficients (R) between LST and Ta anomalies (left) and long-term trends of uncorrected LST, Ta and corrected LST (right)

### 3 RESULTS

#### 3.1 Correlation between LST and Ta anomalies

Figure 2 shows an overview for all sites of the correlation coefficient ( $R$ ) between monthly LST anomalies and Ta anomalies, as well as the trends before and after the correction. Looking at the left side of the Figure it becomes visible that  $R$  increases for 8 of 13 sites. For three sites (228-Desert, 239-Desert, 253-Croplands) the increase is over 10 %. Two sites show a small decrease of  $R$  (261-Mixed Forest, 269-Urban), one site shows a decrease over 10% (254-Grassland). For 251-Cropland the  $R$  stays the same before and after the correction.

#### 3.1 Comparison of the long-term trends

Looking at the right side of Figure 2 it becomes visible, that before the correction the long term LST trends are one magnitude higher than the Ta trends at almost all sites. After the correction the LST trends are in a similar range as the Ta trends except for the site 253-Croplands. Similar trends of corrected LST and Ta can be observed at 228-Desert and 232-Croplands. Nearly similar trends are observed at 210-Desert, 251-Croplands and 248-Open Shrub. For the sites 243-Broadleafed/Deciduous Forest, 254-Grassland, 261-Mixed Forest and 269-Urban the LST trend almost vanished or even was turned into negative through the correction.

#### 3.2 The results at the site 239-Desert as an example

An alternative interpretation of the LST or Ta climatology is the observation of climatological features in the time series. For example, the Ta time series at site 239 at Figure 3 shows warm periods in the late 1980s and 1990s. These warm periods can be related to climate modes like El Nino/Nina and can represent heatwaves and droughts. Looking at the time series of uncorrected LST anomalies at Figure 4 these warm periods are hidden by the orbit drift effect. However, after the correction the one year moving mean of the LST anomalies shows a similar progress as the moving mean of the Ta anomalies, as visible in Figure 5.

### 4 DISCUSSION

The purpose of this study was to apply the statistical orbit drift correction method by Julien and Sobrino 2021 on the TIMELINE LST data and to validate the results against historical Ta measurements. Julien and Sobrino 2021 validated their method against geostationary SEVIRI measurements from 2009-2015 with bias absolute values under 1 K. However, their validation method provides no information, if the orbit drift correction is preserving the actual changes of LST over time.

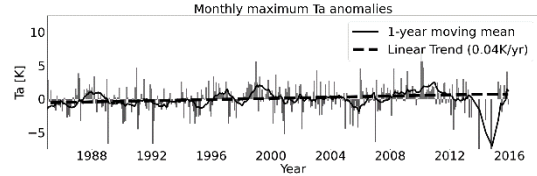


Figure 1: Monthly anomalies of maximum Ta at 239-Desert

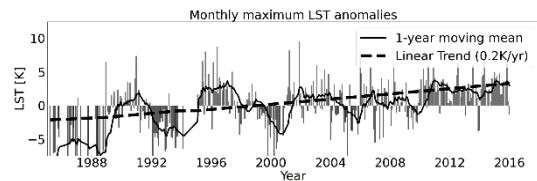


Figure 2: Monthly anomalies of maximum uncorrected LST at 239-Desert

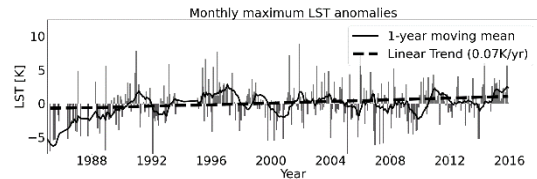


Figure 3: Monthly anomalies of maximum corrected LST at 239-Desert

Our validation showed that the orbit drift correction improved the  $R$  between the monthly LST anomalies and Ta anomalies at most sites. At four sites the correction did not increase or even decrease the  $R$ , which could be explained by several reasons: One site (261) is a forest site, where the influence of the daytime on LST is not strong. Site 251 already has a comparatively high  $R$ , which was not improved through the correction. Site 269 has urban land cover, where the complex structure of the surface at the AVHRR scale could influence the performance of the model. The strong decrease of  $R$  at the grassland site (254) has still to be investigated.

Already Gutman 2010 applied a similar orbit drift correction method AVHRR data from NOAA-9, 11 and 14 over the Sahel area. A visual comparison of the corrected LST anomalies with Ta anomalies at Niamey Niger showed a good accordance. Ta anomalies were also used in a recent study by Good et al. 2022 to assess the stability of the LST\_cci datasets derived from MODIS and AATSR. The correlation between LST anomalies and Ta anomalies in their study reached correlation coefficients between 0.77 and 0.94. However, the generation of their monthly Ta anomalies were based on the same coordinates and day as the LST anomalies, opposed to our study.

Further improvements are possible to enhance the significance for subsequent studies: First, the generation of the Ta anomalies and the LST anomalies should follow the strategy by Good et al. 2022 to get higher correlations between the Ta and LST anomalies. Second, it is possible to enhance the model describing the relationship between the LST anomalies and the sun zenith angle anomalies. For example, Julien and Sobrino 2022 introduced a seasonal component to the model, which could improve the results. Third, also physical models using the diurnal cycle of LST should be tested within this framework. And at last, there is Landsat remote sensing LST dating back to the 1980s, which also could be an independent source to validate orbit drift correction methods for AVHRR.

## 5 CONCLUSIONS

A statistical orbit drift correction method was applied to TIMELINE LST at 12 sites across Europe. The corrected LST anomalies were validated against Ta anomalies from nearby meteorological stations. Following results were obtained:

The orbit drift correction method...

- ...improved R between the monthly anomalies of LST and Ta at most of the study sites.
- ...leads to more realistic long-term trends of LST at most study sites.
- ...mostly preserves climatological events in the LST time series at most study sites.

Further improvements and validation are necessary to obtain a reliable and continent-wide orbit drift correction for AVHRR.

## 6 REFERENCES

- Baret, F., J. T. Morisette, R. A. Fernandes, J. L. Champeaux, R. B. Myneni, J. Chen, S. Plummer, M. Weiss, C. Bacour, S. Garrigues & J. E. Nickeso (2006) Evaluation of the representativeness of networks of sites for the global validation and intercomparison of land biophysical products: proposition of the CEOS-BELMANIP. *IEEE Transactions on Geoscience and Remote Sensing*, 44, 1794-1803.
- Becker, F. & Z.-L. Li (2007) Towards a local split window method over land surfaces. *International Journal of Remote Sensing*, 11, 369-393.
- Dech, S., S. Holzwarth, S. Asam, T. Andresen, M. Bachmann, M. Boettcher, A. Dietz, C. Eisfelder, C. Frey, G. Gesell, U. Gessner, A. Hirner, M. Hofmann, G. Kirches, D. Klein, I. Klein, T. Kraus, D. Krause, S. Plank, T. Popp, S. Reinermann, P. Reiners, S. Roessler, T. Ruppert, A. Scherbachenko, R. Vignesh, M. Wolfmueller, H. Zwenzner & C. Kuenzer (2021) Potential and Challenges of Harmonizing 40 Years of AVHRR Data: The TIMELINE Experience. *Remote Sensing*, 13.
- Frey, C., C. Kuenzer & S. Dech (2017) Assessment of Mono- and Split-Window Approaches for Time Series Processing of LST from AVHRR—A TIMELINE Round Robin. *Remote Sensing*, 9.
- Good, E. J., F. M. Aldred, D. J. Ghent, K. L. Veal & C. Jimenez (2022) An Analysis of the Stability and Trends in the LST\_cci Land Surface Temperature Datasets Over Europe. *Earth and Space Science*, 9.
- Gutman, G. G. (2010) On the monitoring of land surface temperatures with the NOAA/AVHRR: Removing the effect of satellite orbit drift. *International Journal of Remote Sensing*, 20, 3407-3413.
- Julien, Y. & J. A. Sobrino (2021) NOAA-AVHRR Orbital Drift Correction: Validating Methods Using MSG-SEVIRI Data as a Benchmark Dataset. *Remote Sensing*, 13. --- (2022) Toward a Reliable Correction of NOAA AVHRR Orbital Drift. *Frontiers in Remote Sensing*, 3.
- Liu, Tang, Yan, Li & Liang (2019) Retrieval of Global Orbit Drift Corrected Land Surface Temperature from Long-term AVHRR Data. *Remote Sensing*, 11.
- Qin, Z., A. Karnieli & P. Berliner (2001) A mono-window algorithm for retrieving land surface temperature from Landsat TM data and its application to the Israel-Egypt border region. *International Journal of Remote Sensing*, 22, 3719-3746.
- Rayner, N. A., R. Auchmann, J. Bessembinder, S. Brönnimann, Y. Brugnara, F. Capponi, L. Carrea, E. M. A. Dodd, D. Ghent, E. Good, J. L. Høyer, J. J. Kennedy, E. C. Kent, R. E. Killick, P. van der Linden, F. Lindgren, K. S. Madsen, C. J. Merchant, J. R. Mitchelson, C. P. Morice, P. Nielsen-Englyst, P. F. Ortiz, J. J. Remedios, G. van der Schrier, A. A. Suintu, A. Stephens, P. W. Thorne, R. T. Tonboe, T. Trent, K. L. Veal, A. M. Waterfall, K. Winfield, J. Winn & R. I. Woolway (2020) The EUSTACE Project: Delivering Global, Daily Information on Surface Air Temperature. *Bulletin of the American Meteorological Society*, 101, E1924-E1947.
- Reiners, P., S. Asam, C. Frey, S. Holzwarth, M. Bachmann, J. Sobrino, F.-M. Götsche, J. Bendix & C. Kuenzer (2021) Validation of AVHRR Land Surface Temperature with MODIS and In Situ LST—A TIMELINE Thematic Processor. *Remote Sensing*, 13.



# Evaluation of repeat-pass interferometric coherence from Sentinel-1 as a vegetation index for crop monitoring

Arturo Villarroya-Carpio<sup>1</sup>, Juan M. Lopez-Sanchez<sup>1</sup>, Marcus Engdahl<sup>2</sup>

<sup>1</sup> Institute for Computer Research, University of Alicante, Alicante, Spain

<sup>2</sup> European Space Research Institute, European Space Agency, Frascati, Italy

[arturo.villarroya@ua.es](mailto:arturo.villarroya@ua.es), [juanma.lopez@ua.es](mailto:juanma.lopez@ua.es), [marcus.engdahl@esa.int](mailto:marcus.engdahl@esa.int)

**ABSTRACT** - Optical and radar data are extensively used for vegetation and crop monitoring, particularly using vegetation indices. In the case of Synthetic Aperture Radar (SAR), these indices are mostly based on the backscattered intensity or descriptors extracted from polarimetry. The interferometric coherence, an observable obtained from radar interferometry, has sensitivity to the properties of crops in a scene (presence and growth of vegetation). Therefore, it could potentially be used as a vegetation index. The use of Sentinel-1 interferometric coherence data as a tool for crop monitoring has been explored in this work. For this purpose, time series of images acquired by Sentinel-1 and 2, spanning 2017, were analysed. The study site is an agricultural area in Sevilla, Spain, covered by a variety of different crop species. The time series of 6-day repeat pass coherence for each polarimetric channel (VV and VH), as well as their difference and ratio, were compared to the NDVI and the backscattering ratio (VH/VV). The contribution of different decorrelation sources, the use of different orbits and the effect of the bias from the space-averaged sample coherence magnitude estimation were evaluated. The results support using coherence (particularly the VV channel) as a measure for monitoring crop evolution, as it shows good correlations with the NDVI ( $R^2 > 0.7$ ), and its temporal evolution fits well the main phenological stages of the crops. The study was then extended to a bigger set of crop classes and a longer time series (2017-2021), validating all previous results.

## 1. INTRODUCTION

Crop monitoring is an important tool in the context of agricultural production. It can provide useful information for pest prevention and precision farming or help evaluate the effects of drought and other weather events. It serves an important role in crop yield forecasting and can inform decisions about policies regarding food supply and food security.

The use of remote sensing imagery offers a regular and non-destructive way to acquire information about plant growth and development. The use of different techniques and spectral regions can help address problems and limitations: temporal and spatial resolutions, sensitivity to weather conditions (clouds, rain), ability to perceive specific characteristics of the scene, etc.

Vegetation indices (VI) are combinations of different sources of information (bands, parameters, etc.) that provide descriptors of vegetation surfaces, used to highlight vegetation in a scene and for many other purposes, such as land cover classification, detection of crop diseases, retrieval of biophysical parameters, drought monitoring or crop management.

VI for optical data are usually defined as combination of different spectral bands. There are a wide variety of indices, depending on their objectives and limitations. The most used, such as the NDVI

(Bannari et al., 1995), rely on combinations of bands corresponding to the red and near infrared frequencies. This is based on the characteristic rapid change in reflectance of vegetation in the region between 650 nm and 730 nm, known as the red edge.

In the case of SAR imagery, direct estimations of biophysical parameters are not trivial. Radar VI provide a more physically interpretable description of vegetation. They are generally based on the backscattered intensity at different polarimetric channels or descriptors extracted from polarimetry (Mandal et al., 2021). These polarimetric channels represent the polarization of the returned radar signal. In the case of S1, the emitted signal is polarized vertically, and VV and VH represent the components of signal received from the scene with vertical or horizontal polarization respectively.

An alternative to working with the backscattered intensity is exploiting the use of parameters derived from SAR interferometry, or InSAR (Bamler and Hartl, 1998). One particular product of the interferogram between pairs of images (pairs of images corresponding to consecutive dates in the case of this study) is the interferometric coherence. It can be used as a measure of the quality of the interferometric phase. Its estimation is carried out using the sample coherence magnitude (Touzi et al., 1999), which can serve as a measure of change between the pair of images. Low

values generally indicate changes in the scene from one image to the other, and vice versa. Other factors can lead to lower coherence values. For instance, both the change and the presence of vegetation lead to a decrease in coherence.

The sample coherence is a biased estimator, where low values of measured coherences are higher than the actual coherence. This bias depends on the number of independent samples used in the estimation, and decreases when this number grows, as the estimator is asymptotically unbiased (Touzi et al., 1999).

The coherence can be understood as the product of different contributions (Zebker and Villasenor, 1992; Bamler and Hartl, 1998), representing different sources of decorrelation:

$$\gamma = \gamma_{geom} \gamma_{vol} \gamma_{SNR} \gamma_{temp} \quad (1)$$

The first term represents the geometric decorrelation caused by the spatial distance between the orbital positions at the moment of acquisition (baseline). The second refers to the volumetric decorrelation and appears when there is a vertical distribution of scatterers over the same pixel. These two effects can be disregarded in this case due to the small and stable baselines of S1 (typically below 150m).

The remaining terms describe the thermal noise caused by the instrument, dependent on the signal-to-noise ratio (SNR), and the temporal decorrelation. The temporal decorrelation represents the loss of correlation due to changes in the scene, including changes and wind-induced movement in the vegetation, water content (both in the soil and the canopy) or man-made changes, like processes associated with agricultural exploitation (ploughing, sowing and harvesting).

The changes in the time series for the coherence over the cycle of a crop's development reflect the phenological stages of the vegetation. The coherences for each polarimetric channel take high and relatively constant values outside of the growing season, as there is not much variability when the surface is bare soil. When the crop starts to grow the coherence diminishes, as the vegetation grows and changes from one date to the next. Then, the coherence stays low, and very similar for both channels, as the movements in the plants caused by the wind result in an almost complete loss in correlation. The agricultural processes associated with the ploughing, sowing and harvesting of the crop have an impact in the coherence as well, by changing the texture and cover of the surface. The curves for the coherence for each channel, as well as the ones obtained for combinations of them, are shaped by these effects in a way that resemble the NDVI and other commonly used vegetation indices. Some recent studies support this relationship between the interferometric

coherence and the NDVI (Nasirzadehdizaji et al., 2021; Pandit et al., 2022).

The purpose of this work was to explore whether the apparent similarities between the coherence time series and the NDVI could be quantified, as a measure of the potential for the interferometric coherence as a descriptor of crop evolution. Initial results for the time series of 2017 are described in a recently published article (Villarroya-Carpio et al., 2022). The study of the complete time series (2017-2021) used that work as a starting point, as well as serving as validation of the observations.

## 2. MATERIALS AND METHODS

### 2.1 Study area

The test site chosen for the study is an agricultural area near Sevilla, Spain, entitled BXII sector (Figure 1). A wide variety of crops species are planted in this region every year.

Satellite imagery from both Sentinel-1 and 2 covering the test site during the 2017-2021 period were used. Additionally, data regarding the distribution of crops in the scene, as well as information regarding the cycle of the crops, and meteorological data, were used in the process of construction of the time series.

### 2.2 Satellite imagery and reference data

The complete series of products from the Sentinel-1 (S1) constellation covering the period of study were used. This includes images corresponding to orbit 74 from both S1 A and B, with polarisations VV and VH, and a revisit time of 6 days. 60-61 images were available for each year, except for 2021, with 58, due to operation problems with S1 B starting in December from that year. All images from 3 different orbits (74, 147 and 154) were used in the case of 2017, in order to study the effect of the observation geometry and the time of acquisition.

Regarding Sentinel-2 (S2), the images used correspond to the reflectance product, with Level-2A processing. These images present a 10m spatial resolution, and while the revisit time is 5 days, only 33-41 partially or completely cloud-free images were available, depending on the year.

The reference data consisted of:

- 1) Ground truth classification maps, giving information about the distribution of different types of crops over the area. These maps were acquired from the official land parcel identification system.

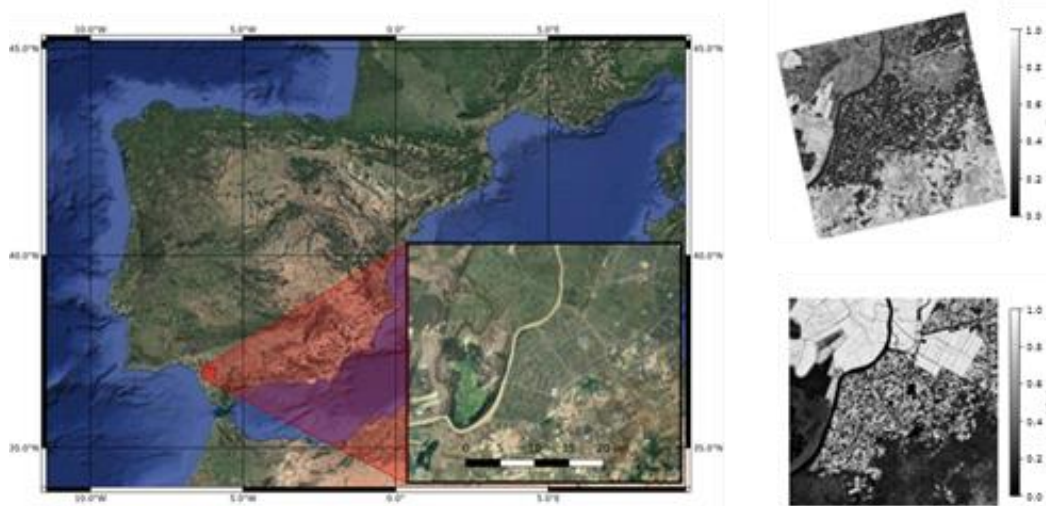


Figure 1. Test site for the study. On the top right, a map of coherence for the VV channel. On the bottom right, the NDVI. Both images correspond to a date at the beginning of August of 2017.

- 2) A crop calendar for the crops cultivated in the region, with approximate starting and ending dates for the periods of sowing, growth and harvesting.
- 3) Daily rainfall and wind speed data, obtained from the *Sistema de Información Agroclimática para el Regado* (SIAR, 2022).

### 2.3 Methodology

The first part of the process was the pre-processing of the Sentinel products. The steps performed for the S1 images were as follows:

- 1) Selection of sub-swath and bursts.
- 2) Refining of the orbit state vectors.
- 3) Radiometric calibration.
- 4) Coregistration.
- 5) Speckle filtering and coherence estimation.
- 6) Geocoding, with an output posting of 10 m.

As a result of this process, series of images for the backscattering coefficient and the coherence amplitude were obtained. In the case of the study covering 2017, additional steps were taken in order to perform the compensation of the bias and removal of the thermal noise (Villarroya-Carpio et al., 2022).

As for S2, the pre-processing included the steps of cloud masking, the mosaicking of the 2 tiles covering the test site and the computation of the NDVI. The resulting images share with the S1 products a spatial resolution of 10 m.

Following the pre-processing, time series for each of these products were generated using the crop type classification data. The results were series of values of NDVI, backscatter and coherence for each of the crops in the scene. Additionally, the time series for different radar VI were computed, including the ratio between the backscattering coefficients (VH/VV), and also the difference and ratio between the coherences for both channels: VH/VV and VH-VV. The series were constructed by extracting the values for all the pixels corresponding to each of the crops. An example of the time series for one of the crops can be seen in Figure 2.

Finally, the crop calendar was used to delimit the period of crop growth in the time series, in order to establish the comparison between different series both for this selected period and for the complete curve. To study this relation, the correlations between the SAR data and the NDVI were calculated.

## 3. RESULTS

### 3.1 Initial study in 2017

The results of the initial analysis for the time series spanning 2017 are comprehensively described in Villarroya-Carpio et al., 2022. Several points of interest were examined. First, the effect of compensating for the systematic bias in the measured coherence. The bias appears for lower coherence values, and therefore has a larger impact on the VH channel, as it generally shows lower coherences. The result of this bias is a reduction in the range of values for the coherence. Its effect on the correlation between the coherence and NDVI time series was evaluated.

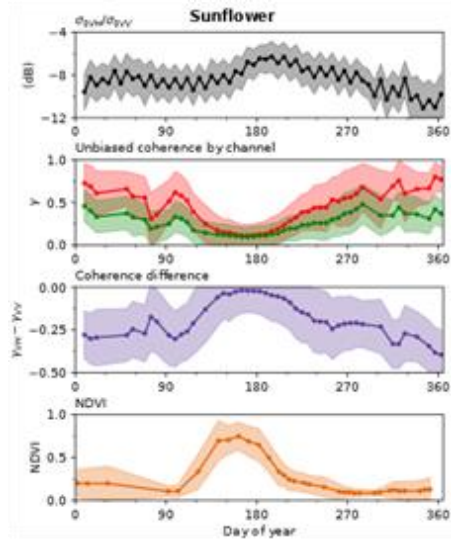


Figure 2. Example of the time series for one of the crops in 2017. From top to bottom: the backscattering ratio, the coherence for both channels (VV in red/light and VH in green/dark), the difference between them, and the NDVI. The average value for all the corresponding pixels is represented in a continuous line, while the shaded area shows the corresponding standard deviation.

Additionally, the comparisons between coherence and NDVI were performed before and after removing the component related to the thermal noise (Equation 1).  $\gamma_{SNR}$  takes very high and constant values for the VV channel, yet it is noticeably lower and more variable for VH. The thermal noise affects mainly areas of low backscatter, and the backscattered intensity is lower for VH. The impact of subtracting this term on the ability for the coherence to describe crop dynamics was studied.

Other analysed sources of variability in the results were explored: the use of 3 orbits, each with some differences in the observation conditions (flight direction, moment of acquisition, observation angle) and different temporal baselines: 6 and 12 days.

In most cases, the coherence was found to be well correlated with the NDVI ( $R^2 > 0.7$ ), with VV providing the best results, and VH performing better in some cases. Additionally, while the coherence was generally more correlated to the NDVI than the backscattering, this was not the case for all crops, for instance in the case of rice.

From all the available orbits, the one with the steepest observation provided the best results. A change in the angle of observation influences the combination of the radar responses from the vegetation and the soil. A more vertical observation angle increases the component received from the ground, and,

consequently, should lead to higher values of coherence, as the ground is less susceptible to temporal decorrelation. Other observation conditions proved to be less impactful.

The processing steps required in order to address and compensate the bias and remove the thermal noise from the coherence did not provide meaningful increases in the correlations with the NDVI and are not critical to obtain good results.

Finally, regarding the use of different temporal baselines, the curves obtained for a 12-day temporal baseline are less correlated with the NDVI, but the correlations are still high in most cases.

### 3.2 Full analysis: 2017-2021

Using these results as a starting point, the study has been extended to a longer time series, from 2017 to 2021. In this case, only the images from the optimal orbit (orbit 74) were used to create the radar time series. Likewise, the steps of bias and thermal noise removal were not performed.

The pre-processing and creation of the time series for each year were analogous to those for 2017. The comparisons between SAR and optical time series were established both for the delimited periods of crop growth and for the complete time series. Figure 3 shows the evolution of the coherences for both VV and VH over the years in the case of a particular crop.

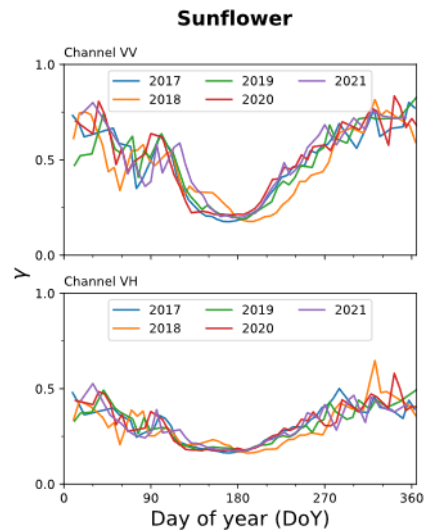


Figure 3. Time series of the biased coherence for both polarimetric channels for one of the studied crops.

The sets of curves in each case qualitatively follow the same trends. VV covers a wider range of values, as well as higher coherences outside the period of maximum growth of the crop. The coherence decreases for both channels as vegetation starts to grow, and stays

at a minimum value (different from zero due to the bias in the measured coherence) while the crops cover the scene. This consistency from one year to the next is observed for all crops, and the series for the different years replicate the results obtained for 2017.

Table 1 contains the coefficients of determination ( $R^2$ ) for some of the correlations between the coherence and NDVI time series.

VV is generally the series correlated the most to the NDVI. The exceptions are some crops that grow earlier in the year and generally consist of more sparse vegetation (carrot, chickpea and onion). In the case of sunflower, the correlations for both channels are equally good.

The correlations are particularly low in 4 cases. In the case of barley and oats this happens because these crops occupy the smallest surface and number of fields. Due to this, the presence of some errors in crop type classification has a big impact in the quality of the curves for the time series. Alfalfa and rice are special cases, where the poor results are due to specific features of the time series. Alfalfa is cultivated differently from other species, with a multi-annual growing cycle and periodic harvests where the crop is partially cut and left to regrow. This results in relatively constant values of coherence and NDVI, and poorly defined curves.

Table 1. Coefficient of determination ( $R^2$ ) for the linear regressions between the measured coherence and the NDVI, for each channel and year. The values in bold correspond to the best result in each case.

	2017		2018		2019		2020		2021	
	VV	VH	VV	VH	VV	VH	VV	VH	VV	VH
Alfalfa	0,01	-0,01	-0,03	-0,02	<b>0,19</b>	0,12	0,04	0,01	<b>0,36</b>	0,14
Barley	-	-	-0,06	-0,07	-0,04	<b>0,18</b>	0,02	-0,14	<b>0,58</b>	0,30
Carrot	0,37	<b>0,65</b>	0,13	<b>0,72</b>	0,30	<b>0,81</b>	0,29	<b>0,56</b>	0,57	<b>0,68</b>
Chickpea	<b>0,68</b>	0,60	<b>0,76</b>	0,66	0,63	<b>0,66</b>	<b>0,84</b>	0,67	0,39	<b>0,47</b>
Cotton	<b>0,93</b>	0,84	<b>0,92</b>	0,84	<b>0,90</b>	0,85	<b>0,92</b>	0,77	<b>0,81</b>	0,41
Fallow	-	-	-	-	-	-	-	-	-	-
Maize	<b>0,88</b>	0,75	<b>0,96</b>	0,68	<b>0,87</b>	0,57	<b>0,94</b>	0,80	<b>0,83</b>	0,59
Oats	-	-	0,10	<b>0,17</b>	<b>0,18</b>	0,02	0,07	<b>0,14</b>	0,60	0,36
Onion	0,66	<b>0,82</b>	<b>0,72</b>	0,70	<b>0,85</b>	0,80	0,67	<b>0,76</b>	<b>0,80</b>	0,76
Pepper	<b>0,89</b>	0,72	<b>0,85</b>	0,78	<b>0,92</b>	0,69	0,87	<b>0,90</b>	<b>0,88</b>	0,71
Potato	<b>0,92</b>	0,74	0,29	<b>0,50</b>	<b>0,68</b>	0,66	<b>0,47</b>	0,35	-	-
Pumpkin	<b>0,80</b>	0,76	0,82	<b>0,87</b>	<b>0,88</b>	0,82	<b>0,96</b>	0,83	<b>0,89</b>	0,85
Quinoa	<b>0,83</b>	0,67	<b>0,75</b>	0,20	<b>0,89</b>	0,79	<b>0,80</b>	0,66	<b>0,88</b>	0,59
Rice	<b>0,18</b>	0,07	<b>0,36</b>	0,25	<b>0,33</b>	0,30	0,08	<b>0,17</b>	0,30	<b>0,35</b>
Sugar beet	<b>0,85</b>	0,78	0,78	<b>0,80</b>	<b>0,82</b>	0,76	<b>0,73</b>	0,67	<b>0,83</b>	0,76
Sunflower	0,72	<b>0,77</b>	<b>0,82</b>	0,72	<b>0,74</b>	0,69	<b>0,72</b>	<b>0,72</b>	0,81	<b>0,94</b>
Sweet potato	<b>0,78</b>	0,72	<b>0,90</b>	0,76	<b>0,95</b>	0,67	<b>0,96</b>	0,75	<b>0,89</b>	0,78
Tomato	<b>0,85</b>	0,81	<b>0,90</b>	0,71	<b>0,79</b>	0,55	<b>0,83</b>	0,62	<b>0,75</b>	0,64
Wheat	<b>0,72</b>	0,51	0,03	-0,06	<b>0,49</b>	0,45	<b>0,28</b>	0,24	<b>0,55</b>	0,26

In the case of rice, the coherence behaves differently with respect to the other crops: the ground is flooded before the sowing, leading to a loss in correlation before the crop begins to grow. This is not the case for the backscattering coefficient and the NDVI, which show the typical increase when plants develop.

The results of considering the complete time series, instead of restricting the dates used to those corresponding to the growing cycle of the crop, show that the correlations remain generally high. This could mean that selecting the right window in the time series for the comparison is not critical. Finally, correlations between coherences and NDVI while working with the difference between channels (VH-VV) or the ratio (VH/VV), were generally lower than for each of the channels on its own.

#### 4. CONCLUSIONS

The main key point to be concluded from the results of this study is that Sentinel-1 interferometric coherence can be used as a vegetation index for crop monitoring, as it appears to describe the evolution of vegetation in a similar way as already used VI. In the cases where the coherence did not offer a good description of the dynamics of the crop, the backscatter can offer complementary information.

The series for the VV channel are generally the most correlated with the NDVI. For some cases of early crops with sparser vegetation cover, VH offers a better performance. Simple combinations of the channels, such as the difference or the ratio between them, do not provide advantages over the use of the channels separately. The processing steps required for the correction of the bias and the separation of sources of decorrelation could be skipped, as they do not provide clear improvements in the results.

Regarding the conditions of observation, using the orbit with the steepest angle of observation guarantees the best correlation with the NDVI. While a 6-day temporal baseline provides the best results, the 12-day temporal resolution should still be useful for monitoring most crops. Finally, the good correlations between the coherence and the NDVI appear not to be restricted to the crop's growing cycle.

#### 5. ACKNOWLEDGEMENTS

This research was supported by the European Space Agency (project SEOM-S14SCI-Land, "SInCohMap") and by the State Agency of Research from the Spanish Ministry of Science and Innovation and the European Funds for Regional Development (project PID2020-117303GB-C22). The crop type classification map used as reference data was provided by the Regional Government of Andalusia.

#### 6. REFERENCES

- Bamler, R., Hartl, P., 1998. Synthetic aperture radar interferometry. *Inverse Problems* 14, R1–54. <http://dx.doi.org/10.1088/0266-5611/14/4/001>
- Bannari, A., Morin, D., Bonn, F., Huete, A.R., 1995. A rev. vegetation indices. *Remote Sensing Reviews* 13 (1–2), 95–120. <http://dx.doi.org/10.1080/02757259509532298>
- Mandal, D., Bhattacharya, A., Rao, Y.S., 2021. Radar Remote Sensing for Crop Biophysical Parameter Estimation. Springer. <http://dx.doi.org/10.1007/978-981-16-4424-5>
- Nasirzadehdizaji, R., Cakir, Z., Balik Sanli, F., Abdikan, S., Pepe, A., Calò, F., 2021. Sentinel-1 interferometric coherence and backscattering analysis for crop monitoring. *Computer and Electronics in Agriculture*. 185, 106118. <http://dx.doi.org/10.1016/j.compag.2021.106118>
- Pandit, A., Sawant, S., Mohite, J., Pappula, S., 2022. Sentinel-1-derived coherence time-series for crop monitoring in Indian agriculture region. *Geocarto International*. 1–21. <http://dx.doi.org/10.1080/10106049.2021.2022008>
- SIAR, 2022. Sistema de Información Agroclimática para el Regado. Gobierno de España. Ministerio de Agricultura, Pesca y Alimentación. Online <https://eportal.mapa.gob.es/websiar/Inicio.aspx>. (Accessed on September 27th, 2022).
- Touzi, R., Lopes, A., Bruniquel, J., Vachon, P., 1999. Coherence estimation for SAR imagery. *IEEE Transactions on Geoscience and Remote Sensing*. 37 (1), 135–149. <http://dx.doi.org/10.1109/36.739146>
- Villarroya-Carpio A, Lopez-Sanchez J, Engdahl M., 2022. Sentinel-1 interferometric coherence as a vegetation index for agriculture. *Remote Sensing of Environment* 2022; 280:113208. <https://doi.org/10.1016/j.rse.2022.113208>
- Zebker, H., Villasenor, J., 1992. Decorrelation in interferometric radar echoes. *IEEE Transactions on Geoscience and Remote Sensing*. 30 (5), 950–959. <http://dx.doi.org/10.1109/36.175330>



# Study of Effects of Different Vegetation Model Parameter Settings on Quantitative CFD Simulation of Urban Spatial Air Temperature and Wind-field

Chen Fei<sup>1</sup>, Hongyuan Huo<sup>1\*</sup>, Jing Tao<sup>1</sup>, Zhaofang Wang<sup>1</sup>, Li Guo<sup>2</sup>, Xiangtian Bai<sup>2</sup>, Zhao-Liang Li<sup>3,4</sup>

<sup>1</sup> Faculty of Architecture, Civil and Transportation Engineering, Beijing University of Technology, Beijing 100124, China; odd\_chen@163.com, taoj@emails.bjut.edu.cn, [2877595997@qq.com](mailto:2877595997@qq.com);

<sup>2</sup> Information Engineering University, Zhengzhou 450052, China; gl\_750312@163.com, 846778060@qq.com;

<sup>3</sup> Key Laboratory of Agricultural Remote Sensing, Ministry of Agriculture/Institute of Agricultural Resources and Regional Planning, Chinese Agricultural Academy of Sciences, Beijing 100081, China; lizl@unistra.fr;

<sup>4</sup> ICube, CNRS, Université de Strasbourg, 300 Boulevard Sébastien Brant, CS10413, 67412 Illkirch, France

Corresponding address: Hongyuan Huo, [huohongyuan@bjut.edu.cn](mailto:huohongyuan@bjut.edu.cn).

**ABSTRACT:** *The rapid acceleration of urbanization has a serious impact on the urban ecological environment. It is of great significance to carry out numerical simulation research on urban spatial thermal environment for improving urban ecological environment, optimizing building energy consumption and promoting sustainable urban development. At present, in the simulation research of vegetation mitigation of urban thermal environment based on computational fluid dynamics, there are few studies on the influence and accuracy evaluation of different vegetation settings in CFD on the simulation results. Aiming at the quantification of the impact of vegetation changes and vegetation model settings on the numerical simulation of urban three-dimensional thermal environment, this study is carried out: 1) Based on the combination of Gaofen-2 remote sensing data and CFD model, the current situation of wind and heat environment at the block scale was simulated and analyzed; 2) The vegetation model is assumed to be three models, including cold source, constant temperature wall, and porous medium. Based on the heat transfer and cooling mechanism of vegetation, these three different vegetation models and their related CFD parameter settings are used to simulate the thermal environment of urban three-dimensional space. Analysis of applicable scenarios and accuracy studies to optimize vegetation setting parameters. The research results show that: 1) The distribution of temperature has a great correlation with the direction of wind. The temperature distribution at different heights at night did not show significant differences. Due to the obvious convective heat transfer between the building surface and the atmosphere, the temperature in the upwind direction is significantly lower than that in the downwind direction. 2) At a height of 2m and below, setting the vegetation as the wall model has the best performance, and at a height above 5m, the results of the wind and heat environment of the three setting methods are basically similar. The wind environment results of the same vegetation setting are different at different heights.*

**Keywords:** CFD, remote sensing, air temperature, vegetation model

## 1. INTRODUCTION

In recent years, with the rapid development of industry and urbanization, various urban ecological environment problems have emerged. Among them, the urban thermal environment closely related to people's health and life is particularly prominent, which has attracted extensive attention of scholars. On the one hand, the urban thermal environment not only

has a significant impact on people's living comfort, urban climate and atmospheric environment; On the other hand, the severe thermal environment has increased energy consumption and greenhouse gas emissions, making the incidence rate and mortality of diseases related to thermal environment rise. A large number of greenhouse gas emissions further aggravate the severe urban thermal environment.



The urban thermal environment is spatially represented by the horizontal and vertical distribution of the surface temperature and atmospheric temperature field. It is a physical environment system in which human activities interact with nature. The urban thermal environment has a significant impact on the urban climate and micro meteorology, with the surface temperature and atmospheric temperature of the urban underlying surface as the core and the underlying surface condition, atmospheric transmission condition and solar radiation as the components after being affected by human activities. It is one of the important indicators to measure the urban ecological environment, and its spatio-temporal evolution process is inseparable from human social and economic activities. Therefore, it is of great significance for urban ecological security and sustainable development to study the urban thermal environment, quantitatively analyze the spatial and temporal change process of the high-resolution thermal environment distribution pattern, and mitigate the urban thermal environment based on modern advanced technology and methods.

Green space and vegetation play an important role in mitigating urban thermal environment and reducing heat island effect. Therefore, the research on urban thermal environment mitigation and improvement based on green space and vegetation has attracted extensive attention of scholars (Gülden 2016). The research focuses on the relationship between urban heat island effect and various factors of vegetation, such as urban heat island intensity and vegetation index (Gallo 1993), vegetation abundance (Weng Q 2004), standardized compactness index (Yangzhou Zhang 2017), etc. The mechanism of green vegetation to mitigate heat island effect is mainly reflected in the following two aspects (Hou C 2018): on the one hand, vegetation absorbs some solar radiation through its own photosynthesis, and then reflects some solar radiation through vegetation leaves (Dimoudi A 2003). The maximum temperature difference caused by trees by shielding solar radiation and absorbing energy can reach 6 °C; On the other hand, transpiration of vegetation absorbs most of the heat and converts it into latent heat flux, thus preventing the rise of temperature. Under the combined effect of tree transpiration and shading, the outdoor thermal comfort has been greatly improved (Lin B R 2008).

However, most scholars use ground observation and satellite remote sensing methods to quantitatively study vegetation mitigation of urban three-dimensional thermal environment. Among them, the urban space thermal environment research based on ground observation can effectively calculate the change rule of station temperature at different time scales, but

there is a problem that discrete point data replaces area data, and the station observation airspace is not representative. In addition, the data obtained from ground observation mostly depends on meteorological stations and manual collection of instruments, which is time-consuming and laborious in obtaining data in a large area and at multiple points; The research on urban space thermal environment based on remote sensing can retrieve the surface temperature field and surface ecological parameters, but at present, limited by the resolution accuracy of remote sensing data, the research on vegetation mitigation of urban thermal environment focuses on large suburban parks, while the parks with small urban center area are difficult to study and analyze by remote sensing.

Based on computational fluid dynamics (CFD) numerical simulation method, this paper simulates the mitigation effect of vegetation on urban thermal environment at the community scale. In addition, explore the different CFD settings of vegetation under fine scale, the heat conduction and heat convection between vegetation and atmosphere and other physical processes through numerical simulation to obtain the distribution of urban three-dimensional space temperature field and wind speed field. The mechanism of thermal environment mitigation of vegetation is analyzed and explored from the microscopic perspective by setting vegetation as wall, cold source and porous medium, and the heat transfer mechanism of vegetation is analyzed and discussed according to the simulation results to simplify the heat transfer process and optimize the parameters. Compare the measured data with the simulation results to evaluate the advantages and disadvantages of the three different vegetation settings, and apply the vegetation settings with the highest accuracy to the simulation study of the thermal environment of vegetation mitigation in a park.

## 2. METHODOLOGY

### 2.1 Study area

In this study, Beijing Yaowa Lake Park was selected as the study area. Beijing Yaowa Lake Park is located in Nanmofang Township, East Fourth Ring Road, Chaoyang District, Beijing (as shown in Figure 1), bordering Daliushu Road in the south, Nanmofang Road in the north, and Chemical Road in the northeast. The whole park is divided into east and west parts by the Fourth Ring Road, with a total area of 545 mu, including 169 mu for the East Park and 376 mu for the West Park.

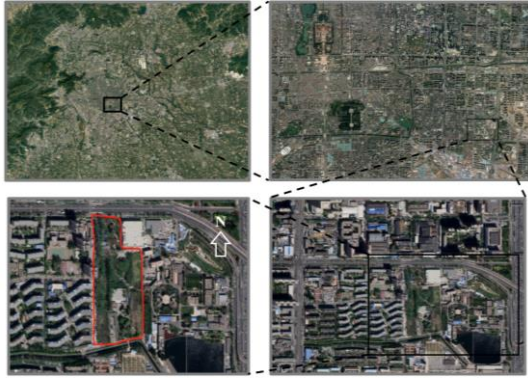


Fig. 1 Satellite remote sensing image of Yao Wahu park in the study area

## 2.2 Physical model establishment

In order to discuss the influence of different settings of vegetation area in CFD on simulation results. Taking Yaowa Lake Park as an example, CFD flow and heat transfer simulation was carried out by establishing a three-dimensional model of the trees in the park. The physical model of Yaowa Lake Park is established according to the obtained high-resolution remote sensing images.

In the model, the tree model is reflected in the physical model, and the tree part is divided into the crown and trunk. Since different shapes of tree crowns will also affect the simulation of convection field, Li Liang et al. compared the effects of different crown shapes on the convection field through wind tunnel experiments. The results show that the rectangular crown shape can get more accurate results, and has the characteristics of simple modeling, fast solution and good convergence. The size of the tree crown model is set as a cylinder with a trunk height of 3m and a diameter of 0.3m, and a cuboid with a crown height of 4m and a length and width of 3m. According to the field survey, the trees in the north of the park are tall, so the crown height of the trees in the north is set at 6m. The tree model is shown in the following figure:



Fig. 2 Physical model and tree model of Yaowahu Park

## 2.3 Three Setting Modes of Vegetation Heat Transfer

The heat exchange that occurs when a fluid flows over a solid surface is called convection heat transfer.

The heat transfer mode between the vegetation and the atmosphere at the block scale is mainly convection heat transfer. The basic formula of convection heat transfer is Newton's cooling formula, which is as follows:

$$q = h(T_s - T_\infty) \quad (1)$$

Where:  $h$  is the convection heat transfer coefficient, which represents the parameter of convection heat transfer capacity,  $W/(m^2 \cdot ^\circ C)$ .

It can be seen from the non slip boundary condition that heat is transferred through heat conduction in the extremely thin fluid layer attached to the wall. The non slip boundary condition is applicable to both laminar and turbulent flows. According to the equality of heat transfer and Fourier's law and Newton's cooling formula theorem, it is obtained that:

$$q = h(T_s - T_\infty) = -k \left( \frac{\partial T}{\partial y} \right)_{y=0} \rightarrow h = -\frac{k}{\Delta t} \frac{\partial T}{\partial y} \quad (2)$$

In this paper, the same meteorological parameters and boundary conditions are used, and different settings of vegetation areas are used as a single variable for simulation comparison. Vegetation is set as wall, cold source and porous medium to participate in CFD simulation. The heat transfer mechanism of three different settings is slightly different:

The way that vegetation is set as wall and porous medium is to consider the heat exchange between vegetation surface and atmosphere as convective heat transfer; The way to set vegetation as cold source is to consider vegetation as a solid heat absorber, and then participate in the heat exchange between the atmosphere. According to Fourier's law and energy conservation equation, the differential equation of heat conduction with internal heat source in rectangular coordinate system is obtained:

$$\frac{\partial t}{\partial \tau} = \frac{\lambda}{\rho c} \left( \frac{\partial^2 t}{\partial x^2} + \frac{\partial^2 t}{\partial y^2} + \frac{\partial^2 t}{\partial z^2} \right) + \frac{\phi}{\rho c} = a \left( \frac{\partial^2 t}{\partial x^2} + \frac{\partial^2 t}{\partial y^2} + \frac{\partial^2 t}{\partial z^2} \right) + \frac{\phi}{\rho c} \quad (3)$$

Where:  $a$  is thermal diffusivity, also known as thermal conductivity,  $m^2/s$ ;  $\phi$  is the heat generated by the internal heat source in unit time and unit volume,  $W/m^3$ .

## 3. RESULT

### 3.1 Simulation results of Temperature field

The results of thermal environment and wind environment simulated by CFD block scale flow and heat transfer model are shown in Table 4-1, which shows the simulation results of temperature distribution and velocity distribution at different heights and with different settings.

Vegetation plays an important role in mitigating heat island effect in summer. From the perspective of botany, the cooling mechanism of vegetation can be divided into direct cooling effect and indirect cooling

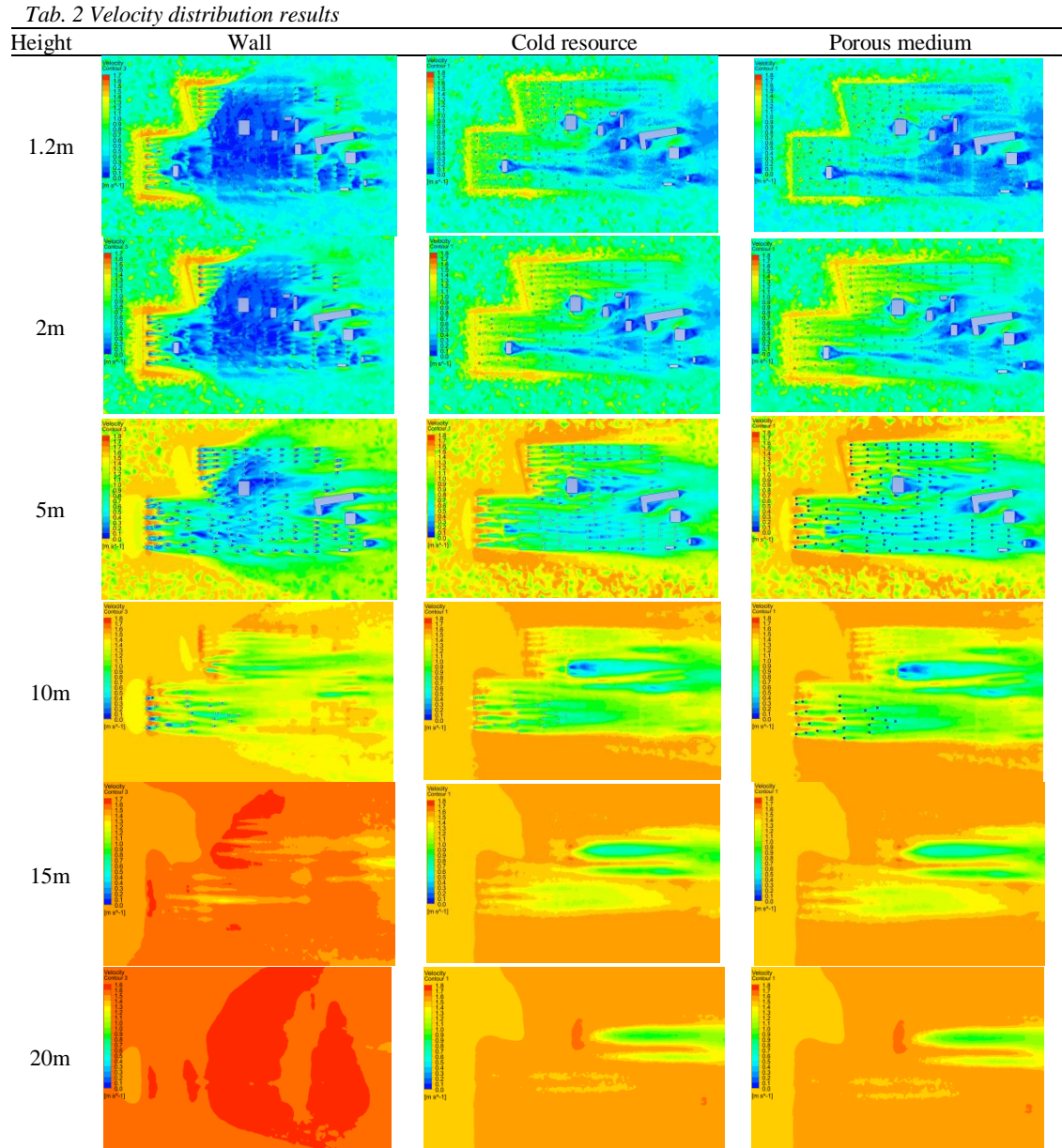
effect. The direct cooling effects include: ① transpiration of plants emits water and converts solar radiation energy into latent heat. ② Photosynthesis of plants absorbs solar radiation, thereby reducing the temperature of the surrounding environment. Indirect cooling effects include: ① shielding and reflection of plant leaves, and the temperature of the environment under the leaves decreases. ② The large area of vegetation cooling makes the temperature difference between this part of the region and the surrounding temperature, which drives the flow of air flow and enables heat transfer and heat exchange, thus improving the surrounding temperature.

### 3.2 Simulation results of wind speed field

The block scale wind environment simulation results of different vegetation settings based on CFD are shown in Table 2. The following table shows the wind environment simulation results at different heights. Different from the temperature distribution results at different heights, due to the high tree planting density and leaf density in the park, the roughness of the underlying surface is high, and the influence of the boundary layer, the air flow at 10m and above is still affected by the vegetation.

Tab. 1 Temperature distribution results

Height	Wall	Cold resource	Porous medium
1.2m			
2m			
5m			
10m			
15m			
20m			



The wind environment results of the same vegetation setting mode are different at different heights. First of all, it is reflected in the height of 2m and below (that is, near the ground). At this height, the speed of the wall is significantly reduced in the park. Vegetation blocks the airflow and forms a wake, which is mainly distributed in the upwind direction. At 5m, the area of low wind speed area decreases, and there is also obvious wake in the downwind direction of trees, and the wake is distributed throughout the park. The speed of the other two settings has little difference and




even distribution in the height of 10m and below. Low wind speed areas are mainly distributed in the downwind direction of buildings. At a height of 5m, the wake generated by vegetation and buildings is more obvious. At the heights of 5m and 10m, the wind environment results of the three settings are similar.

### 3.3 Acquisition of measured data

The instruments used for the measured data are shown in Table 3.



Tab. 3 Introduction to measuring instruments

Instrument category	Instrument parameters	
testo 610 high-precision temperature & humidity	temperature	range: -10.0-50.0 °C; accuracy: $\pm 0.5$
	humidity	range: 0-100%RH; accuracy: $\pm 2.5$ %RH
SW6086 Thermal anemometer	temperature	range: 0.0-45.0 °C; accuracy: $\pm 1.0$ °C
	风速	range: 0.0-30.0m/s; accuracy: $\pm 0.1$ m/s
	humidity	range: 0-99%RH; accuracy: $\pm 4.0$ %RH
Outdoor electronic thermometer and hygrometer	temperature	range: -50.0-70.0 °C; accuracy: $\pm 1.0$ °C
	humidity	range: 0-100%RH; accuracy: $\pm 2.5$ %RH

### 3.4 Collection of experimental data

Sort out the measured data and remove the abnormal values. Then, calculate the average of multiple groups of data measured at the same time as the final temperature data of the point.

Through the collection of field measured temperature data, eight outdoor thermometers were used to record the temperature data at 1.2m in real time. The measuring points of different outdoor thermometers are distributed as shown in Figure 3.

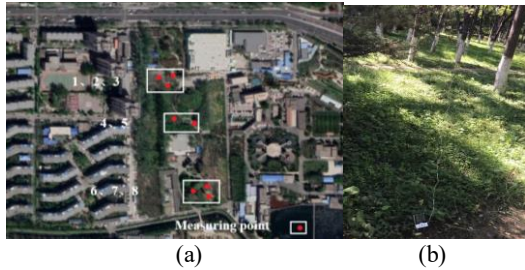


Fig. 3 Measured data, distribution of measuring points (a), measured data of single measuring point (b)

### 4. CONCLUSION

Compare the temperature data of the measured measuring points with the simulation results, and the comparison results are shown in Figure 5.

It can be seen from the comparison chart that the simulation results of the three settings are very close to the measured results, but the differences are reflected

in different measuring points. Compared with other measuring points, the measured data of measuring points 4 and 5 are quite different from the simulated data. It is mainly because measuring points 1-3 and 6-8 are located on the north and south sides near the edge of the park, while measuring points 4 and 5 are located inside the park, surrounded by many dense trees and roads, with complex ventilation and heat distribution, which leads to large differences between the two.

From the perspective of different settings, the temperature simulation results obtained under the cold source setting mode are lower than the measured results. There is no obvious difference between the settings of porous media and wall and the simulation results. The root mean square error between the simulation results of different vegetation settings and the measured data was counted (Figure 6). The error from high to low was wall, porous medium and cold source. Therefore, in the simulation of urban wind and heat environment at the block scale, it is more appropriate to set the vegetation as the wall.

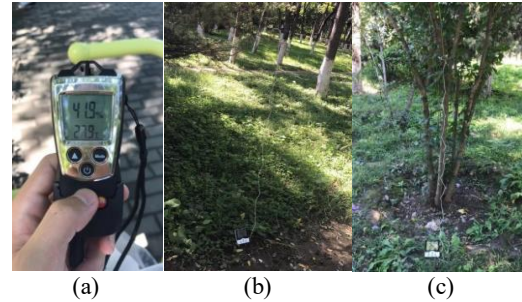


Fig. 4 Field measurement

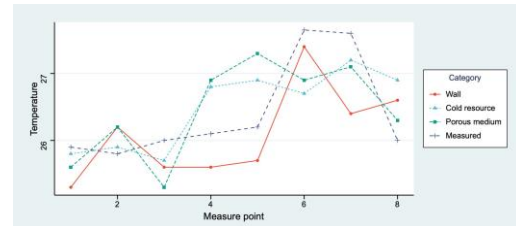


Fig. 5 Comparison chart of results

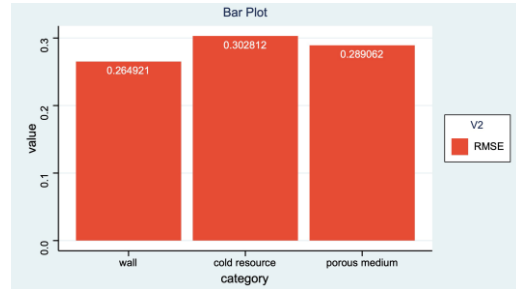


Fig. 6 RMSE comparison chart

## 5.REFERENCE

- Gülten A, Aksoy U T, Öztop H F. Influence of trees on heat island potential in an urban canyon[J]. *Sustainable cities and society*, 2016, 26: 407-418.
- Weng, Q.; Lu, D.; Schubring, J. Estimation of land surface temperature–vegetation abundance relationship for urban heat island studies. *Remote Sens. Environ.* **2004**, *89*, 467–483.
- Gallo, K.P.; Tarpley, J.D. The comparison of vegetation index and surface temperature composites for urban heat-island analysis. *Int. J. Remote. Sens.* **1996**, *17*, 3071–3076, doi:10.1080/01431169608949128.
- Hou, C.; Hou, J.; Kang, Q.; Meng, X.; Wei, D.; Liu, Z.; Zhang, L. Research on urban park design combined with the urban ventilation system. *Energy Procedia* **2018**, *152*, 1133–1138, doi:10.1016/j.egypro.2018.09.139.
- Dimoudi, A.; Zoras, S.; Kantzioura, A.; Stogiannou, X.; Kosmopoulos, P.; Pallas, C. Use of cool materials and other bioclimatic interventions in outdoor places in order to mitigate the urban heat island in a medium size city in Greece. *Sustain. Cities Soc.* **2014**, *13*, 89–96.
- Lin, B.; Li, X.; Zhu, Y.; Qin, Y. Numerical simulation studies of the different vegetation patterns' effects on outdoor pedestrian thermal comfort. *J. Wind. Eng. Ind. Aerodyn.* **2008**, *96*, 1707–1718, doi:10.1016/j.jweia.2008.02.006.

# Simulation of Canopy Urban Heat Island at a Block Scale Based on Local Climate Zones and Urban Weather Generator

Wenzhi Zhang <sup>1</sup>, Hongyuan Huo <sup>2\*</sup>, Xiaowei Geng <sup>2</sup>, Jing Tao <sup>2</sup>, Ping Zhou <sup>1</sup>, Li Guo <sup>3</sup>

<sup>1</sup> School of Earth Sciences and Resources, China University of Geosciences Beijing, Beijing 100083, China; 2001210201@email.cugb.edu.cn, zhoupx@cugb.edu.cn;

<sup>2</sup> Faculty of Architecture, Civil and Transportation Engineering, Beijing University of Technology, Beijing 100124, China;

[huohongyuan@bjut.edu.cn](mailto:huohongyuan@bjut.edu.cn), [gengxw@emails.bjut.edu.cn](mailto:gengxw@emails.bjut.edu.cn), [taoj@emails.bjut.edu.cn](mailto:taoj@emails.bjut.edu.cn);

<sup>3</sup> University of Information Engineering, Zhengzhou 450052, China; [gl\\_750312@163.com](mailto:gl_750312@163.com)

Corresponding address: Hongyuan Huo, [huohongyuan@bjut.edu.cn](mailto:huohongyuan@bjut.edu.cn).

**ABSTRACT:** The current research on urban heat island effect mostly focuses on the analysis of land use type changes, and most of them focus on the surface urban heat island effect. From the perspective of urban microclimate, the canopy heat island effect is a key factor affecting human thermal comfort. Therefore, this study will combine the local climate zone classification system and the UWG (Urban Weather Generator) model to simulate and quantitatively analyze the urban canopy heat island effect in Beijing at the block scale. First, based on Sentinel-2 Multispectral remote sensing images, the ResNet (residual neural network) method was used to obtain the local climate zone in Beijing, and the LCZ was verified based on the google earth engine (GEE) platform; Secondly, according to the classification results of local climate zones, the input parameters of the UWG model are calculated; Finally, the UWG model is used to simulate the canopy temperature in different local climate zones, and the urban canopy temperature is verified based on the meteorological station data. We quantitatively analyze the temperature differences between different types of local climate zones. The results shows that the canopy heat island effect in Beijing gradually weakened outward from the city center. This is mainly due to the relatively dense distribution of compact local climate zones in the center of Beijing, while the surrounding areas of Beijing have lower building density and better natural coverage. From the perspective of local climate zones, the heat island intensity of built-up LCZs is significantly stronger than that of natural-covered LCZs. The variation of the heat island intensity of each built-up type of LCZ shows a certain regularity, that is, the heat island intensity of the compact LCZ is higher than that of the open LCZ with the same building height. However, for LCZs with comparable compactness, the heat island intensity of high-level LCZs is higher than that of low-level LCZs. According to the conclusions drawn from this study, we hope to provide theoretical guidance for the sustainable and healthy development of Beijing and rational planning in the future.

**Keywords:** Local climate zone, canopy urban heat island, urban weather generator, Sentinel-2

## 1 INTRODUCTION

Urbanization can greatly alter the form, fabric, structure and metabolism of the original landscape, thus changing the local climate. The universal urban heat island effect (UHI) has attracted extensive attention. The urban Heat island effect (UHI) refers to the fact that the screen height temperature in an urban area is significantly higher than the screen height temperature in the surrounding rural area. In order to make urban heat island effect studies more objective and standardized, Stewart and Oke proposed the concept of "local climate zones". It is defined as an area that spans hundreds to thousands of meters on a horizontal scale and has the same land cover, urban structure, materials,

and similar human activities (Stewart and Oke, 2012; Stewart and Oke, 2014).

Based on this classification system, the calculation of urban heat island intensity is no longer the ambiguous urban-rural temperature difference, but the temperature difference of different LCZ categories (Stewart and Oke, 2014). The LCZ classification system provides a standard framework for urban heat island research. Therefore, a large number of scholars have studied the urban heat island effect based on the LCZ classification System (Stevan and Dragan et al, 2013). As for temperature data, the Urban Weather Generator (UWG) model generates meteorological information for specific urban areas based on known rural site data and urban morphology. This model has been widely used in



the study of urban spatial thermal environment (Martinez et al, 2021).

Combined with previous studies, this paper will take the central urban area of Beijing as the main research area, and use LCZ classification system and UWG model to study the urban canopy heat island effect. The main contents include: ① the use of Sentinel-2 multispectral remote sensing data and ResNetV2 model to draw the LCZ distribution map of the study area. ② Based on the classification results, a representative site was selected for each LCZ category to calculate various surface parameters required by the UWG model. ③ The representative canopy temperature data of each LCZ category were obtained by running the UWG model using meteorological data and calculated land surface parameters. At the same time, the real meteorological data observed by the adjacent meteorological stations are used to verify. ④ Finally, the urban canopy heat island effect was studied based on the simulated temperature data.

## 2 STUDY AREA AND DATA

### 2.1 study area

The study area of this paper is the central urban area of Beijing, namely Dongcheng District, Xicheng District, Haidian District, Chaoyang District, Shijingshan District and Fengtai District, as shown in Figure 1.



Figure 1. Scope of the study area

### 2.2 Data

#### 2.2.1 Remote sensing data

In this paper, a standard dataset So2Sat LCZ42 in LCZ field is used to train the deep convolution model. The dataset consists of approximately 500,000 Sentinel-1 and Sentinel-2 image patches and their LCZ labels from 42 major urban sites worldwide (plus 10 additional smaller areas), with an overall confidence of 85% (Zhu X X et al, 2019). The specific training process is carried out using Sentinel-2 image patches in So2Sat LCZ42 dataset. Therefore, after the training, the LCZ map of the study area is obtained using the preprocessed Sentinel-2 multispectral data.

#### 2.2.2 Vector data and Meteorological data

Since the UWG model requires many city parameters, which are not consistent with the attribute indicators defined in the LCZ. Therefore, this paper will use the AOI data of the study area to calculate some parameters required by the UWG model that have a great impact on the simulation results, and the setting of other parameters will refer to the practices of other scholars in thermal environment simulation research using the LCZ classification system (Stewart et al, 2014). In addition, this paper uses the meteorological data of Shunyi meteorological station in Beijing in 2019 and Element software to generate the input file of UWG model. Meanwhile, in order to verify the simulation results of the UWG model, the meteorological data of meteorological stations in the central urban area of Beijing in 2019 were collected.

## 3 METHODS AND RESULTS

### 3.1 LCZ classification

#### 3.1.1 Classification network and model training

Recent years, ResNet network and its variants have been used in many LCZ classification studies. The main feature of this network is the residual structure which is composed of identity mapping and shortcut connection (He et al, 2016).

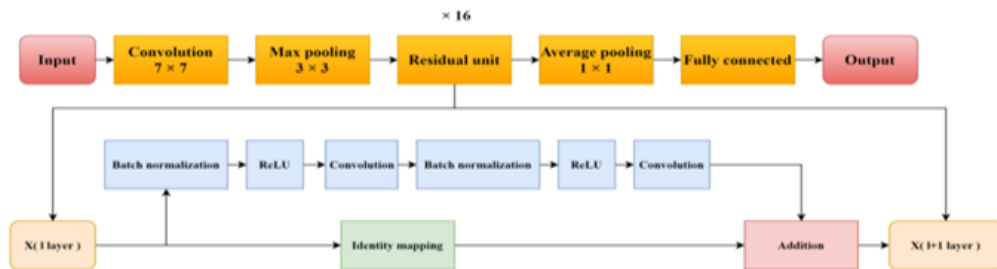


Figure 2. The architecture of the classification network

This paper uses an improved ResNetV2, whose specific network model is shown in Figure 2. When carrying out LCZ classification, the specific network training process refers to Qiu et al.'s experiment (Qiu et al., 2020). The whole training process adopts keras 2.6.0 framework to implement.

### 3.1.2 LCZ classification results

Figure 3 is the confusion matrix of the model adopted in this paper on the test set. The ResNetV2 model adopted in this paper achieves good classification accuracy in LCZ classification task. OA is 89.46%, while Kappa coefficient is 0.88. The classification accuracy of the model is high in the land cover type LCZs(LCZ A-LCZ G), while the classification accuracy is not high in the built type LCZs(LCZ 1-LCZ 10). There was some confusion between LCZ 1 - LCZ 3 and LCZ 4 - LCZ 6. It is mainly because the Sentinel-2 multispectral data used in this paper contains a large amount of spectral information of ground objects, and contains less spatial structure information of ground objects, especially the height information is very lack.

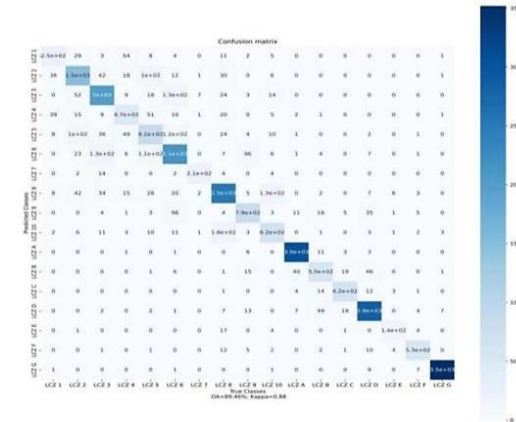


Figure 3. Confusion matrix of the study area

After the model training is completed, this paper uses the sliding window method to draw the LCZ map of the study area according to Qiu et al., and the specific results are shown in figure 4 (Qiu et al., 2020). From the results, the LCZ map shows the overall urban structure characteristics of the central urban area of Beijing, and is consistent with the actual situation on the ground. The central urban area of Beijing presents a compact urban structure. The closer it is to the urban center, the more compact it is. The compactness gradually weakens from the downtown to the surrounding suburbs. The central area represented by the Palace Museum is mainly of the LCZ 3, with a small amount of LCZ G. Tightly surrounding the central area is the LCZ 4. In this range, LCZs of land cover type are relatively rare. Further looking outwards, LCZ 5 and

LCZ 6 are the main LCZ types. At the same time, LCZ blocks with land cover types also gradually increased. LCZ A and LCZ D were the most common types in the suburbs of the study area. In conclusion, the overall urban structure of Beijing is crowded, and there is less green vegetation in the central area, which aggravates the urban heat island effect.

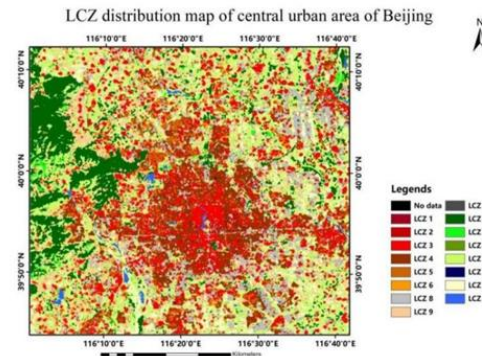


Figure 4. Spatial distribution of LCZ in the central urban area of Beijing

### 3.2 UWG simulation

#### 3.2.1 UWG simulation fundamentals

Bueno developed the UWG model using the Urban Energy Balance Model (TEB) based on Building Energy Model (BEM), which rapidly generates local microclimates based on meteorological information from rural sites and site-specific urban characteristics (Bueno et al., 2013). UWG processes suburban to urban meteorological information through four modules to obtain the wind-thermal environment at a specific block scale. The four main modules are Rural station model (RSM), Vertical Diffusion Model (VDM), Urban Boundary Layer (UBL), Urban Canopy-Building Energy Model (UC-BEM). The whole UWG simulation process is shown in Figure 5.

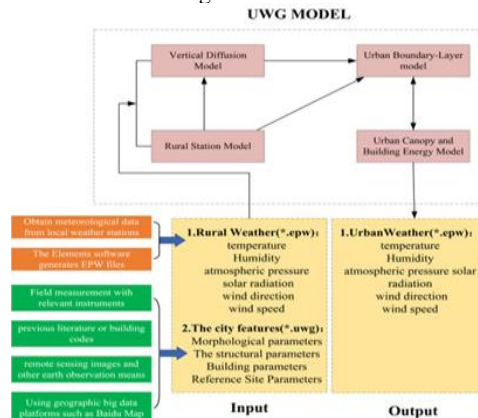


Figure 5. Simulation flow of UWG model

### 3.2.2 UWG simulation results

According to the spatial distribution of LCZ in the study area, representative sites were selected for each LCZ type to obtain the input parameters needed for the UWG simulation. In this paper, the Dragonfly plugin in Grasshopper was used to run the UWG model to obtain the simulated temperature values of each LCZ type for the whole year of 2019. At the same time, the real temperature values observed by the adjacent meteorological stations are selected to verify the accuracy of the UWG simulation. In this paper, two periods, from January 14 to January 15 in the winter of 2019 and from July 14 to July 15 in the summer of 2019, were selected as typical research periods. The prediction accuracy of UWG model is evaluated quantitatively by using  $R^2$  and RMSE.

According to Table 1, the UWG simulation results of each LCZ category achieved satisfactory accuracy on the whole. For most LCZ types, the UWG simulation results in summer were significantly better than those in winter for most LCZ blocks. The reason for the poor simulation results in winter may be related to the more complex meteorological and heating factors in the central urban area of Beijing in winter. Then from the perspective of space, except for LCZ 3, the UWG simulation results of LCZ blocks with built-up types were better than those of LCZ blocks with land cover types. The simulation accuracy of LCZ 3 is not high, because LCZ 3 types are mainly distributed in the center of Beijing, and a small amount of LCZ G is distributed in this area. These blocks differ greatly in urban climatology.

### 3.3 Heat island intensity calculation

A large number of scholars used the UHI magnitude to characterize the heat island effect in the study area. The specific calculation process of the UHI magnitude based on LCZ classification system is shown in equation 1.

$$UHI_{LCZ X} = T_{LCZ X} - T_{LCZ D} \quad \text{Equation 1}$$

Where,  $UHI_{(LCZ X)}$  refers to the magnitude of UHI for LCZ X (LCZ X Denotes any type of LCZ),  $T_{(LCZ X)}$  denotes the temperature of the LCZ X,  $T_{(LCZ D)}$  denotes the temperature of the LCZ X.

After obtaining the UHI magnitude of each LCZ block, Arcgis software and its Python programming interface were used to draw the daytime UHI magnitude map and nighttime UHI magnitude map of the study area, as shown in Figure 6. From the perspective of time, nighttime UHI magnitude is generally stronger than daytime UHI magnitude. From the perspective of space, the distribution of UHI magnitude during the daytime is basically consistent with that at night. The area with the highest UHI magnitude in Beijing is the area between the Second Ring Road and the Third Ring Road. There are many high-rise buildings in these areas, and the flow of people is large. Therefore, the UHI effect is most obvious. However, the UHI magnitude in the central area represented by the Palace Museum has weakened, mainly because there are a small number of LCZ G in these areas, and this LCZ type have a certain cooling effect, which alleviates the UHI effect in the central area. In a word, the UHI magnitude of the outer ring of Beijing is lower than that of the inner ring of Beijing.

Table 1 Accuracy evaluation table of temperature simulation result of LCZ Blocks in Typical Study Period

Built types				Land cover types			
Classes	Seasons	$R^2$	RMSE	Classes	Seasons	$R^2$	RMSE
LCZ 1	winter	0.84	1.50	LCZ A	winter	0.74	3.14
	summer	0.76	2.17		summer	0.76	2.32
LCZ 2	winter	0.86	1.50	LCZ B	winter	0.84	0.84
	summer	0.80	1.92		summer	0.95	0.87
LCZ 3	winter	0.75	1.97	LCZ C	winter	0.69	2.94
	summer	0.65	2.67		summer	0.84	1.75
LCZ 4	winter	0.92	1.31	LCZ D	winter	0.85	1.81
	summer	0.92	1.09		summer	0.91	1.19
LCZ 5	winter	0.80	1.78	LCZ E	winter	0.90	1.32
	summer	0.84	1.53		summer	0.94	0.88
LCZ 6	winter	0.86	1.78	LCZ F	winter	0.74	2.71
	summer	0.93	0.85		summer	0.80	1.91
LCZ 8	winter	0.89	1.38	LCZ G	winter	0.88	1.44
	summer	0.89	1.49		summer	0.70	2.16
LCZ 9	winter	0.92	1.23				
	summer	0.93	0.97				
LCZ 10	winter	0.71	2.55				
	summer	0.80	2.08				

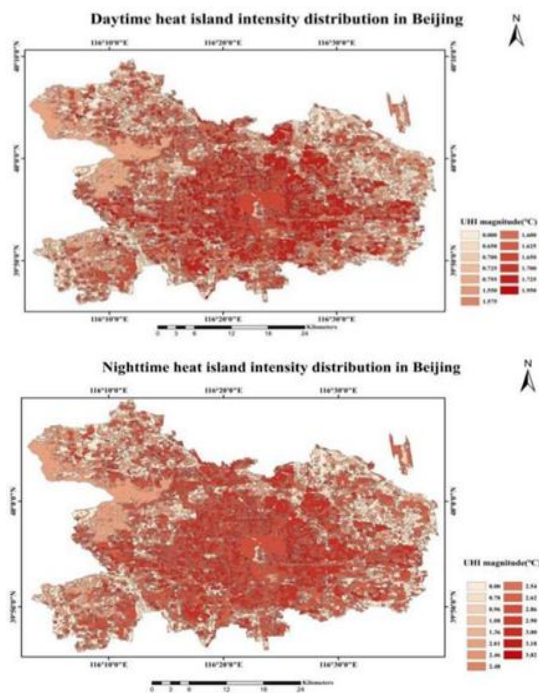


Figure 6. Spatial distribution of daytime heat island intensity(up) and nighttime heat island intensity(down) in the study area

#### 4 CONCLUSIONS

The results of this paper show that: (1) High classification accuracy can be obtained by using CNN network for LCZ classification research. For some built type LCZs, the main difference lies in spatial structure, so adding data that can reflect the features of spatial structure can further improve the classification accuracy. (2) The temperature of the built type LCZs is generally higher than that of the land cover LCZs. The temperature of the inner ring of Beijing, with LCZ 3 and LCZ 4 as the main LCZ types, is generally higher than that of the outer ring of Beijing. (3) The nighttime UHI magnitude of the city is higher than the daytime UHI magnitude of the city. (4) The government should formulate reasonable land use and urban development plans. Land cover type LCZs is beneficial to alleviate UHI effect.

#### 5 REFERENCES

- Stewart, I.D.; Oke, T.R. Local climate zones for urban temperature studies. *Bull. Am. Meteorol. Soc.* 2012, 93, 1879–1900
- Stewart I D, Oke T R, Krayenhoff E S. Evaluation of the 'local climate zone'scheme using temperature observations and model simulations[J]. *International journal of climatology*, 2014, 34(4): 1062-1080.
- Savić S, Milošević D, Lazić L, et al. Classifying urban meteorological stations sites by'local climate zones': Preliminary results for the city of Novi Sad (Serbia)[J]. *Geographica Pannonica*, 2013, 17(3): 60-68.
- Martinez S, Machard A, Pellegrino A, et al. A practical approach to the evaluation of local urban overheating—A coastal city case-study[J]. *Energy and Buildings*, 2021, 253: 111522.
- Zhu X X, Hu J, Qiu C, et al. So2Sat LCZ42: A benchmark dataset for global local climate zones classification[J]. *arXiv preprint arXiv:1912.12171*, 2019.
- He K, Zhang X, Ren S, et al. Deep residual learning for image recognition[C]//*Proceedings of the IEEE conference on computer vision and pattern recognition*. 2016: 770-778.
- Qiu C, Tong X, Schmitt M, et al. Multilevel feature fusion-based CNN for local climate zone classification from sentinel-2 images: Benchmark results on the So2Sat LCZ42 dataset[J]. *IEEE Journal of Selected Topics in Applied Earth Observations and Remote Sensing*, 2020, 13: 2793-2806.
- Bueno B, Norford L, Hidalgo J, et al. The urban weather generator[J]. *Journal of Building Performance Simulation*, 2013, 6(4): 269-281.

# Simulation of UFZ Air Temperature Based on GF-2 Remotely Sensed Data and UWG: A Case Study of Beijing, China

Xiaowei Geng<sup>1</sup>, Hongyuan Huo<sup>1\*</sup>, Yunlong Chen<sup>1</sup>, Wenzhi Zhang<sup>2</sup>, Li Guo<sup>3</sup>, Zhao-Liang Li<sup>4,5</sup>

<sup>1</sup> Faculty of Architecture, Civil and Transportation Engineering, Beijing University of Technology, Beijing 100124, China; gengxw@emails.bjut.edu.cn, 873907011@qq.com;

<sup>2</sup> College of Earth Resources and Environment, China University of Geosciences Beijing, Beijing 100083, China; 2001210201@email.cugb.edu.cn;

<sup>3</sup> University of Information Engineering, Zhengzhou 450052, China; gl\_750312@163.com;

<sup>4</sup> Key Laboratory of Agricultural Remote Sensing, Ministry of Agriculture/Institute of Agricultural Resources and Regional Planning, Chinese Agricultural Academy of Sciences, Beijing 100081, China; lizl@unistra.fr;

<sup>5</sup> ICube, CNRS, Université de Strasbourg, 300 Boulevard Sébastien Brant, CS10413, 67412 Illkirch, France

\* Corresponding address: Hongyuan Huo, huohongyuan@bjut.edu.cn

**ABSTRACT** - Rapid urbanization has led to many urban thermal environment problems, among which the increasing urban heat island effect has been widely concerned by people, and has become one of the most prominent features of climate change in the process of global urbanization. At present, most scholars at home and abroad study and analyze the urban heat island effect from the perspective of land use type, with a large scale, and lack of research from the level of urban microclimate spatial scale. Therefore, from the small-scale perspective of different land-use attributes, it becomes the focus of this paper to study the typical outdoor microclimate of each land-use attribute. Urban functional zone (UFZ) refers to urban planning units with similar spectral characteristics and socio-economic functions, which often have similar energy consumption and outdoor thermal environment. The urban weather generator (UWG) model has good performance in Urban Microclimate Simulation, low computational load and high efficiency. In this paper, the UWG model is used to quantitatively analyze the spatial thermal environment of Beijing. In order to more accurately simulate the urban thermal environment, the underlying surface used in the simulation is replaced by the finely classified underlying surface of the urban functional area. In this paper, we first use POI + OSM data to divide the functional areas of Beijing, then use UWG model to simulate the temperature and humidity differences in different functional areas, and finally use the corresponding urban and rural weather stations to verify. Through UWG simulation and analysis of the thermal environment differences of different functional areas, we can deeply understand the thermal environment characteristics, impact factors and mitigation measures of Beijing, which is of great significance to the sustainable and healthy development of the city and reasonable planning in the future.

**Keywords:** Urban functional zone, Urban air temperature, canopy urban heat island, UWG.

## 1. INTRODUCTION

The continuous advancement of urbanization in the world has resulted in many thermal environmental problems such as reduced urban air quality, increased demand for heating and cooling loads in buildings, and deteriorating health status of urban residents, which seriously affects the sustainable development of cities. Therefore, how to understand the urban thermal environment on a finer scale, and propose thermal environment mitigation measures are the focus and difficulty of current research.

Urban thermal environment refers to the physical environment related to heat that can affect the human

body's perception of cold and warmth, health level, and human survival and development (Oak T R. 1995). At present, there are various research methods for thermal environment. Among them, urban meteorological generator (UWG), as a quantitative method of urban spatial thermal environment, has achieved many research results. It is worth pointing out that this paper uses high-resolution remote sensing data and GIS technology to provide accurate data sources for the initial condition input of the UWG model. At the same time, taking temperature as the optimization target, the 12 uncertain parameters that greatly affect the simulation results are calibrated, and the corrected model error is smaller.



For cities and urban agglomerations with complex land, the thermal environment simulation directly based on UWG considers that the fineness of the underlying surface is not enough, it cannot fully reflect the pattern and intensity of the urban heat island, and the simulation accuracy is not high. Therefore, it is very necessary to finely classify the urban underlying surface and comprehensively obtain the UWG thermal environment simulation results of the city. As the basic unit of the rapid development of modern cities, urban functional areas can help understand the complex interaction between human spatial activities and environmental changes (Zhong et al. 2015, Leichtle et al. 2017), and have important economic, social and ecological implications for cities Impact. In this study, the spatial temperature field under different urban functional areas is simulated by the UWG model, which can deeply understand the interaction mechanism between the underlying surface and the thermal environment, improve the accuracy of the UWG simulation, and deepen the understanding of the urban thermal environment on a finer scale.

This study considers the spatial and temporal distribution of urban thermal environment under different functional areas, and mainly carries out two aspects of work: ①Using POI+OSM data to divide the urban functional areas of the central city of Beijing, which are mainly divided into six single functional areas, including roads and traffic areas, industrial areas, public areas, residential areas, green space and square areas, and commercial areas, as well as a combination functional area; ②Using the dragonfly plug-in of grasshopper modeling software, run the UWG model to simulate the thermal environment, and obtain the thermal environment simulation results under each functional area. According to the distribution pattern of functional areas in the center of Beijing, this paper discusses the temperature field, living environment and heat island situation of the city, and proposes measures and methods to improve the urban thermal environment.

## 2. STUDY AREA AND METHODS

This section mainly carries out the verification analysis of the identification results of urban functional areas and the simulation results of UWG canopy temperature. First, according to the identification results of functional areas, we obtained the spatial distribution characteristics of single functional areas and complex functional areas in Beijing, and used the accuracy rate acc to quantitatively evaluate the identification accuracy of functional areas. Then, running the UWG model for simulation based on the functional area identification, we obtained the canopy temperature and relative humidity of each functional area. The

temperature differences between functional zones of the same type and between different types were compared and analyzed using two typical seasons, summer and winter, and the model accuracy was evaluated by the coefficient of determination  $R^2$  and the RMSE.

### 2.1 Study area

The research areas of this paper are Dongcheng District, Xicheng District, Chaoyang District, Haidian District, Shijingshan District, and Fengtai District in Beijing. As shown in Figure 1.

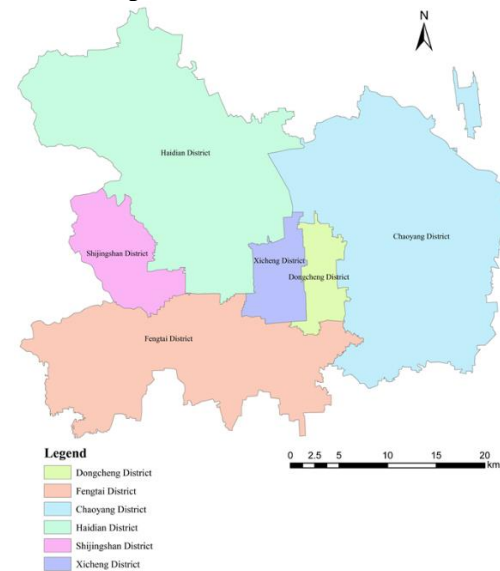


Figure 1. Study area: six urban areas in central Beijing

### 2.2 Identification and Verification of Urban Functional Areas

According to statistics, there are 6 types of single functional areas and 15 types of mixed functional areas in the central urban area of Beijing. Among them, the single functional area is dominated by road traffic land, and residential land accounts for the least. The composite functional area is dominated by public-transportation land, and green space-industrial land is the least. The specific functional area division results are shown in Figure 2.

In order to verify the accuracy of the identification results of urban functional areas, Google Maps was manually visually interpreted and field research was conducted to obtain the true values. The identification results of functional areas were used as predicted values, and 30 block units were randomly selected for comparative analysis. Referring to the research of Kang and Ding (Kang Y et al 2018, Ding Y et al 2020), the overall accuracy rate was 85.6% using the expert

scoring method, indicating that this study can effectively identify single functional areas, mixed functional areas and comprehensive land use Ribbon.

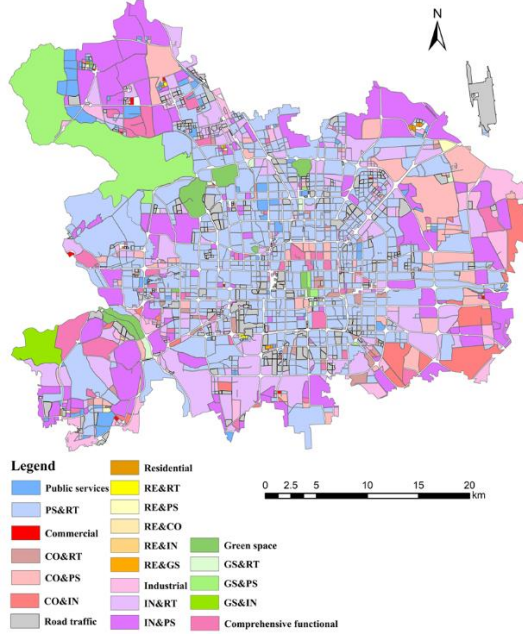


Figure 2. Recognition results of functional areas in the central urban area of Beijing

### 2.3 Verification and Analysis of UWG Temperature and Humidity Simulation Results

According to the obtained UWG simulation parameters, this paper uses the Dragonfly plug-in in Grasshopper to run the UWG model, and obtains the temperature and humidity prediction results of each functional area, selecting July 21-July 22 in summer and January 21-January 22 in winter. Day is a typical study period.

#### 2.3.1 UWG Simulation Fundamentals

The UWG model consists of four coupling modules, through which UWG processes the information from suburban sites to urban sites, thereby obtaining the urban thermal environment of a specific area. The four main modules include the Rural Station Model (RSM), Vertical Diffusion Model (VDM), Urban Boundary Layer Model (UBL), Urban Canopy and Building Energy Model (UC-BEM) (Bueno Unzeta, Bruno, 2012, Bueno, Bruno, et al. 2013). Figure 3 shows the simulation process of the UWG model: the UWG model takes the meteorological data provided by the \*.epw rural weather file as the initial input, and changes the temperature, relative humidity and wind speed according to the urban characteristics described in the \*.uwg file to generate \*.epw simulation City Weather File.

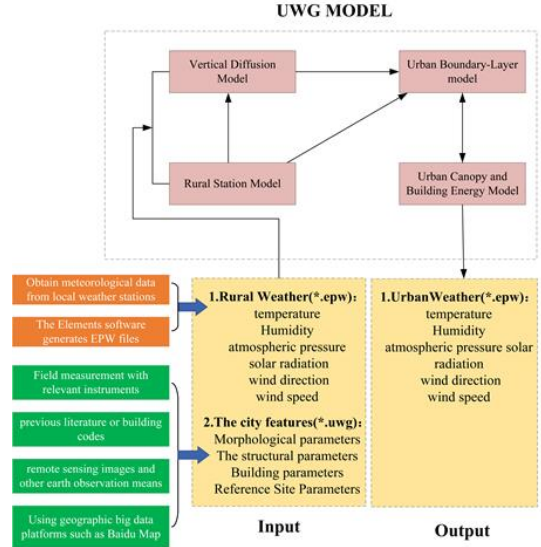


Figure 3. Simulation flow of UWG model

①RSM mainly reads the meteorological data measured hourly at the suburban sites, calculates the sensible heat flux of the suburban sites through the surface energy balance, and provides it to VDM and UBL. The model represents the heat transfer process by dividing the soil into discrete layers and solving a finite difference system of equations :

$$d_1(\rho c)_1 \frac{\partial T_1}{\partial t} = C_{1,2}(T_2 - T_1) + Q_{surf}$$

For the first layer i:

$$d_i(\rho c)_i \frac{\partial T_i}{\partial t} = C_{i,i+1}(T_{i+1} - T_i) + C_{i,i-1}(T_{i-1} - T_i)$$

For any intermediate layer n:

$$d_{n-1}(\rho c)_{n-1} \frac{\partial T_{n-1}}{\partial t} = C_{n-1,n}(T_{deep} - T_{n-1})$$

②The VDM reads the temperature, humidity, and sensible heat flux provided by the RSM, calculates the air temperature at different heights above the rural site through the heat diffusion equation, and provides it to the UBL. The heat diffusion equation is as follows:

$$\frac{\partial \theta(z)}{\partial t} = -\frac{1}{\rho(z)} \frac{\partial}{\partial z} (\rho(z) K_a(z) \frac{\partial \theta(z)}{\partial z})$$

③According to the temperature at different heights provided by VDM and the sensible heat flux provided by RSM, the UBL model calculates the air temperature above the urban canopy to UC-BEM through energy balance. The energy balance is expressed as:

$$V_{cv} \rho c_v \frac{d\theta_{urb}}{dt} = H_{urb} + \int u_{ref} \rho c_p (\theta_{ref} - \theta_{urb}) dA_f$$



④UC-BEM calculates air temperature and humidity in urban canyons through town energy balance and building energy models, while providing urban sensible heat flux and urban canyon air temperature and humidity for UBL. The urban canyon energy balance is as follows:

$$V_{can}\rho c_v \frac{dT_{urb}}{dt} = A_w h_w (T_w - T_{urb}) + A_r h_r (T_r - T_{urb}) + A_r h_{rd,skr} (T_{skr} - T_{urb}) + A_{win} U_{win} (T_{in} - T_{urb}) + V_{inf/vent} \rho c_p (T_{in} - T_{urb}) + u_{ex} \rho c_p (T_{ubl} - T_{urb}) + H_{waste} + H_{traffic}$$

### 2.3.2 Analysis of UWG Simulation Results of Different Types of Functional Areas

Different types of functional areas have different building morphological parameters, vegetation coverage parameters, and anthropogenic thermal parameters. Using the UWG model to explore the thermal environment differences in different urban functional areas can improve the simulation accuracy of the UWG model. Figure 4 shows the temperature prediction results of different functional areas in winter, and Figure 5 shows the temperature prediction results of different functional areas in summer. Figure 6 shows the difference in heat island intensity between functional areas during the day and night in summer. Table 1 quantitatively evaluates the prediction accuracy of the UWG model with  $R^2$  and RMSE.

From the measured values of meteorological stations in the study area, it can be found that the temperature in the outer ring of Beijing is generally lower than that in the inner ring, and the heat island effect in the city center is serious. The daily variation of the average temperature is about 10°C, and the temperature variation of the measured meteorological stations in different functional areas is not very different. Judging from the UWG simulation results, the simulation data has good simulation results in the trend of temperature change, the individual high temperature and low temperature simulation results are not ideal, and the temperature changes between functional areas are not very different.

Table 1. Evaluation table of temperature simulation accuracy of each functional area

Urban functional area category		R <sup>2</sup>	RMSE
Public services land	Summer	0.77	1.87
	Winter	0.72	2.29
Commercial land	Summer	0.88	1.44
	Winter	0.70	2.35
Residential land	Summer	0.90	1.32
	Winter	0.68	2.66
Industrial land	Summer	0.66	2.79
	Winter	0.60	2.54
Green spaces land	Summer	0.78	1.87
	Winter	0.72	2.07
Roads traffic land	Summer	0.77	1.84
	Winter	0.61	2.23

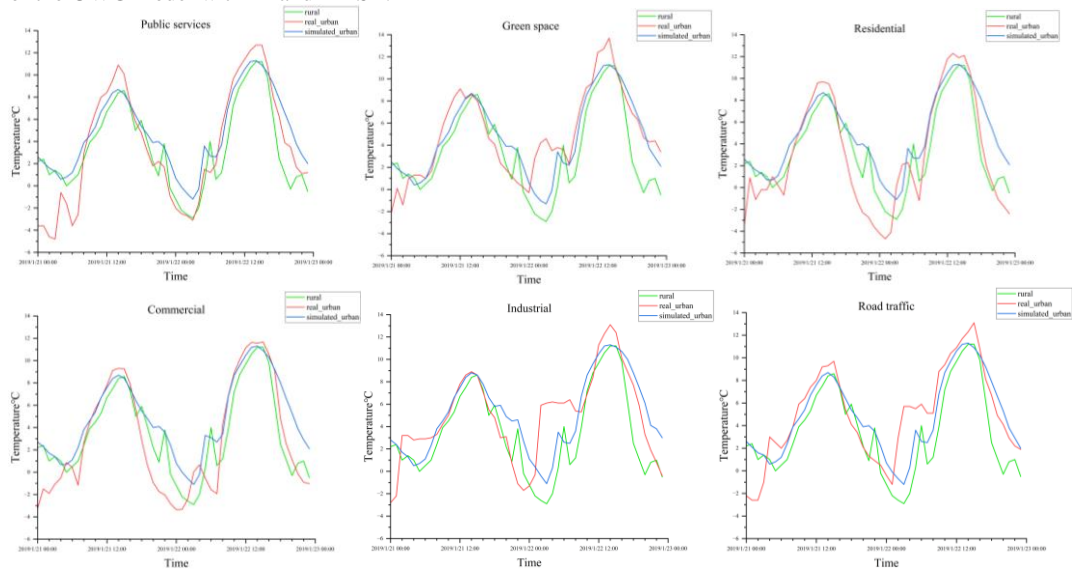


Figure 4. The temperature of each functional area from January 21st to January 22nd in winter

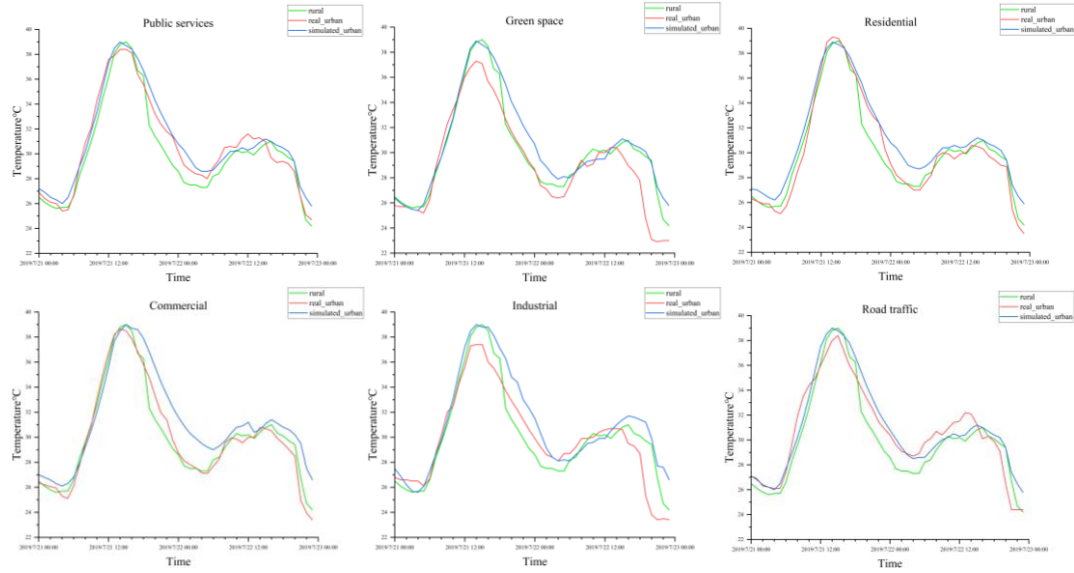


Figure 5. The temperature of each functional area from July 21st to July 22nd in summer

From the temperature simulation accuracy evaluation table, it can be seen that the order of  $R^2$  from high to low is: residential land > commercial land > green space and square > public land > road and traffic > industrial land. It shows that the UWG model has a good fitting effect on the temperature prediction of residential land and commercial land, but has a poor fitting effect on the temperature prediction of industrial land. The order of RMSE from low to high is: commercial land > residential land > green space and square > road and traffic > public land > industrial land, indicating that the UWG model has high temperature prediction accuracy for residential land and commercial land, but low prediction accuracy for industrial land. The  $R^2$  in summer is significantly higher than that in winter, and the RMSE in summer is significantly lower than that in winter, indicating that the temperature prediction performance of the UWG model in summer is better than that in winter, and the poor prediction effect in winter may be related to meteorological factors and heating. The reason for the poor prediction effect on industrial land may be that industrial production consumes a lot of energy to release heat energy, while UWG considers the relationship between buildings and thermal environment more. At the same time, the verified meteorological station has a certain distance from the industrial land, which cannot represent the thermal environment of the specific industrial park, and will also have a certain impact on the simulation results. From the perspective of land use attributes, UWG simulation obtains that the temperature of the functional area from high to low is: industrial area > commercial area > residential area > public area > road and traffic

area > green space and square area. Industrial production releases a lot of heat energy, and the existence of industrial areas will increase the heat island effect in the area; Vegetation and water bodies have a cooling effect, and the existence of green space square area will alleviate the heat island effect in this area.

### 2.3.3 Analysis of UWG simulation results of the same type of functional area

From the UWG thermal environment simulation results of different types of functional areas, it can be seen that the model has the best prediction effect on residential land in summer. In order to explore the thermal environment differences between the same type of functional areas, this paper takes residential blocks as an example, and simulates and analyzes the temperature and humidity of the residential land single functional area and the residential land composite functional area with similar urban geometry. Figure 7 shows the summer temperature prediction results for residential single-functional zone plots and multi-functional zone plots located in different locations.

For an urban area, UWG describes it by three key geometric parameters: average building height, site building density, and the façade-horizontal ratio. These parameters transform the complex, heterogeneous urban structure into a homogeneous description defined by the town energy balance (TEB) (Bueno et al. 2013). It can be seen from the simulation results in Fig. 7 that the thermal environment simulation results of residential areas located in different locations are basically the same, and there are slight differences at

the high and low temperature peaks; The temperature simulation results of the single functional area and the composite functional area of residential land are not significantly different, and the residential-transportation land is slightly higher than that of other functional areas, because the residential-transportation land generates more anthropogenic heat rise during the commute time. Therefore, for plots with similar urban geometry, underlying surface type and anthropogenic heat, the UWG model obtains similar thermal environment simulation results.

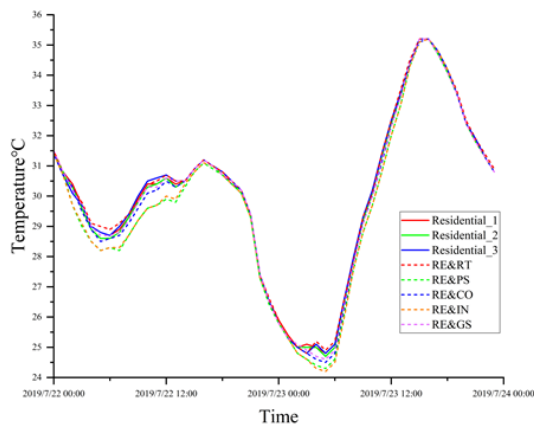


Figure 7. Temperature prediction results for single-functional and multi-functional plots in residential areas

### 3. CONCLUSIONS

This paper divides the functional areas of Beijing based on the POI+OSM method, uses the UWG model to simulate the temperature and humidity differences in different functional areas, and finally uses the corresponding urban and rural meteorological stations to verify the temperature and humidity. The simulation results show that: (1) The canopy temperature of different urban functional areas from high to low are: industrial area > commercial area > residential area > public area > road and traffic area > green space and square area; (2) The temperature of high and dense building land is generally higher, the existence of industrial areas and commercial areas will increase the heat island effect in this area, and the existence of green space square area will alleviate the heat island effect in this area; (3) The UWG model is more suitable for summer thermal environment simulation, and has higher prediction accuracy for commercial land and residential land, and is not suitable for industrial land simulation.

In the future, high albedo (reflectivity) roofs and pavements, porous/permeable pavements, open mesh pavements, etc., can be used to replace existing building materials. The lack of urban vegetation will further exacerbate the UHI effect. Increasing the green space through landscape design is an effective way to improve the microclimate and outdoor thermal comfort. The anthropogenic heat emission of vehicles is an additional source of urban energy balance and contributes to the UHI effect. In the future, mixed functional areas should be reasonably developed according to needs, reducing single land use types and further improving land use efficiency.

### REFERENCES:

- Oke, T. R. "The heat island of the urban boundary layer: characteristics, causes and effects." Wind climate in cities. Springer, Dordrecht, 1995. 81-107.
- ZHONG Y, ZHU Q, ZHANG L. Scene Classification Based on the Multifeature Fusion Probabilistic Topic Model for High Spatial Resolution Remote Sensing Imagery[J]. IEEE Transactions on Geoscience and Remote Sensing, 2015, 53(11): 6207-6222.
- LEICHTLE T, GEIß C, WURM M, et al. Unsupervised change detection in VHR remote sensing imagery – an object-based clustering approach in a dynamic urban environment[J]. International Journal of Applied Earth Observation and Geoinformation, 2017, 54: 15-27.
- Kang Y, Wang Y, Xia Z. Division and identification of urban functional areas in Wuhan Based on POI data. J Geoma. 2018; 43: 81–85. <https://doi.org/10.14188/j.2095-6045.2016352>
- Ding Y, Xu H, Wang C. Urban functional area identification based on OSM road network and POI data. Geo Gis. 2020; 36: 57–63. <https://doi.org/10.3969/j.issn.1672-0504.2020.04.009>
- Bueno Unzeta, Bruno. Study and prediction of the energy interactions between buildings and the urban climate. Diss. Massachusetts Institute of Technology, 2012.
- Bande, Lindita, et al. "Validation of UWG and ENVI-met models in an Abu Dhabi District, based on site measurements." Sustainability 11.16 (2019): 4378.

# 3D Spatial wind and thermal environment simulation of modern gardens in North and South China and its comparative analysis based on CFD and High remote sensing data

Jing Tao<sup>1</sup>, Hongyuan Huo<sup>1\*</sup>, Xiaowei Geng<sup>1</sup>, Wenzhi Zhang<sup>2</sup>, Li Guo<sup>3</sup>, Zhao-Liang Li<sup>4</sup>

<sup>1</sup> Faculty of Architecture, Civil and Transportation Engineering, Beijing University of Technology, Beijing 100124, China;

<sup>2</sup> College of Earth Resources and Environment, China University of Geosciences Beijing, Beijing 100083, China;

<sup>3</sup> University of Information Engineering, Zhengzhou 450052, China;

<sup>4</sup> ICube, CNRS, Université de Strasbourg, 300 Boulevard Sébastien Brant, CS10413, 67412 Illkirch, France;

\* Corresponding address: Hongyuan Huo , [huohongyuan@bjut.edu.cn](mailto:huohongyuan@bjut.edu.cn).

**ABSTRACT** - Chinese modern gardens combine the main design concepts of classical gardens, and integrate people's aesthetics and the sustainable development of the city into the design scheme, which has a good effect on improving the local microclimate of the city. Therefore, it is of great significance to study the wind and heat environment layout of Chinese modern gardens to quantify the impact of local microclimate in cities. To this end, based on high-resolution remote sensing data and computational fluid dynamics, this study simulates the wind-thermal environment of modern gardens in northern and southern China. Firstly, based on high-resolution remote sensing data, combined with 3D modeling software to create a garden geometric model; Secondly, the created geometric model is gridded, the boundary conditions are set according to the collected meteorological data and the measured underlying surface data, and the SST turbulence model and the Couple algorithm are used for numerical calculation; Finally, the accuracy of the simulation results is verified by the results of field measurements. It mainly simulates Jingsi Garden, a modern garden in southern China, and Taoranting Park, a modern garden in the north, to analyze the impact of modern gardens in different locations and their layout and shape on the urban space wind and heat environment. The simulation results show that the cooling effect of Taoranting Park with large green space, large water body and meandering boundary of the park is better than that of Jingsi Garden with a relatively small boundary aspect ratio, and can provide a comfortable wind-heat environment in and around the garden.

## 1 INTRODUCTION

With the continuous acceleration of urbanization, the natural surface of the city is replaced by a large number of artificial surfaces with poor water permeability, which deteriorates the wind-heat environment inside the city and leads to serious wind-heat environment problems (Huo et al.2021; Du et al. 2022; Huo et al. 2022). Urban landscape architecture can effectively alleviate the wind and heat environment in local areas and provide residents with a comfortable outdoor environment (Fallahpour et al.2022). Due to the differences between the northern and southern climates and the spatial layout of modern gardens, studying the mitigation effects of different modern gardens in the north and the south on the local wind-heat environment can effectively solve the deteriorating wind-heat environment.

Landscape gardens in cities have a large number of "cold sources" such as water bodies and green plants (Gromke et al.2014; Tominage et al.2015). Among them, the evaporative cooling effect of the water body can reduce the surrounding air temperature and increase the wind speed very well, especially the cooling effect along the wind direction downstream of the water body is outstanding. As a natural surface, the temperature of green plants is lower than that of artificial surfaces, and the biological effect of vegetation can well reduce the surrounding temperature and provide a comfortable wind-heat environment for local areas. For the study of wind-heat environment, on-site measurement, physical experiment and numerical simulation methods can generally be used. Traditional on-site measurement and physical experiment methods require a lot of manpower, The periodicity is long, and the continuous temperature field and wind speed field in the study area cannot be obtained, so the numerical simulation method

has become the main method to study the wind and heat environment in the local area of the city (Zeng et al.2020; Antoniou et al.2019; Li et al.2008).

This paper mainly uses computational fluid dynamics (CFD) to simulate the mitigation effect of gardens in different regions and layouts in northern and southern China on the surrounding air temperature. The geometric model of the study area is established based on the high-resolution remote sensing images, and the field measured data and meteorological data are used as the boundary conditions and verification methods of the simulation experiments. This study is divided into four parts, the second part, the CFD numerical experiment, the third part, the analysis and discussion of the simulation results, and finally the paper is summarized.

## 2 CFD NUMERICAL EXPERIMENT

### 2.1 Study area and computational domain

Taoranting Park in the north and Jingsi Garden in the south were selected as study areas, located in Xicheng District, Beijing, China, and Wujiang District, Suzhou City, Jiangsu Province, China, with a range of  $116^{\circ}22'05''-116^{\circ}22'54''E$ ,  $39^{\circ}52'10''-39^{\circ}53'17''N$  and  $120^{\circ}41'15''-120^{\circ}41'55''E$ ,  $31^{\circ}09'37''-31^{\circ}09'57''N$ . Beijing has a typical temperate semi-humid continental monsoon climate, with an average annual temperature of  $19^{\circ}C$  and an average annual precipitation of 644mm. Suzhou is located in the northern subtropical humid monsoon climate zone. The average temperature in August 2020 is  $22^{\circ}C$  and the average annual precipitation is 1094mm. On the basis of high-resolution remote sensing satellite images, a certain reasonable simplification is used to establish a geometric model containing various real underlying surfaces such as trees and water bodies, and a computational domain is created according to regulations. The study area and computational domain are shown in Figures 1a and 1b.

### 2.2 Research methods

CFD was used to simulate the impact of urban landscape architecture on the surrounding wind and heat environment. By establishing a three-dimensional geometric model of the urban research area, setting up the computational domain of the numerical experiment according to the specific research area, numerically discretizing the computational domain, selecting the SST turbulence model, using the Couple algorithm to couple the flow equation and the energy equation, and solving the numerical solution. This paper simulates the wind and heat environment around Taoranting Park in Beijing at 2:00 p.m. on September 18, 2022, and uses the measured data to verify it to ensure the reliability of the simulation results; And simulate the wind and heat

environment around Jingsi Garden in Suzhou at 2:00 p.m. on August 2, 2020. The specific technical route of this study is shown in Figure 2.

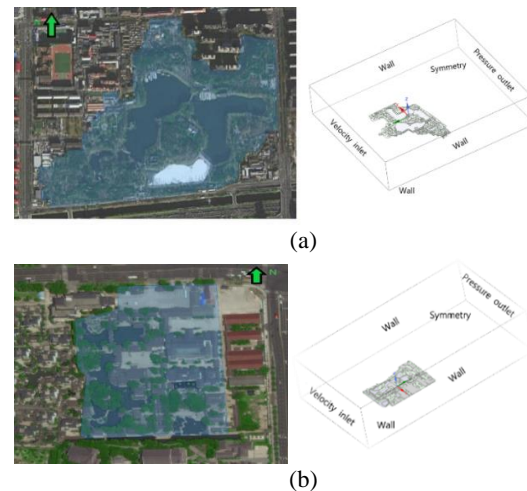


Figure 1 (a) The left image is a high-resolution remote sensing satellite image of Taoranting Park, and the right image is the calculation area of Taoranting Park. (b) The left picture is the high-resolution remote sensing satellite image of Jingsi Garden, and the right picture is the calculation area of Jingsi Garden.

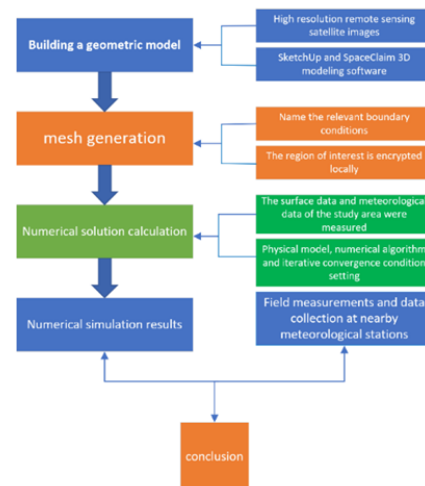


Figure 2. Research Technology Roadmap

### 2.3 Basic principles of CFD simulation

Using CFD to simulate the local area wind and heat environment is generally to solve the Navier-Stokes equation of the incompressible and viscous fluid in three-dimensional space, while coupling the energy equation of the heat transfer effect. The relevant control equations are as follows:

Continuous equation:



$$\frac{\partial u_i}{\partial x_i} = 0$$

Momentum conservation equation:

$$\frac{\partial(\rho u_i)}{\partial t} + \frac{\partial}{\partial x_i}(\rho u_i u_j) = \frac{\partial}{\partial x_j}(\mu \frac{\partial u_i}{\partial x_j}) - \frac{\partial p}{\partial x_i} + F_i$$

Energy conservation equation:

$$\frac{\partial(\rho T)}{\partial t} + \frac{\partial(\rho u_j T)}{\partial x_j} = - \frac{\partial}{\partial x_j}(\frac{\kappa}{c_p} \frac{\partial T}{\partial x_j}) + S_T$$

$\rho$  is the fluid density, The unit is  $\text{kg/m}^3$ ;

$t$  is time, the unit is s;

$u_i$  and  $u_j$  are velocity components, The unit is m/s ;

$x_i$  and  $x_j$  are the coordinate components, The unit is m;

$p$  is the pressure on the fluid micro-body, The unit is Pa;

$F_i$  is the volume force on the micro-element body, The unit is N

$\mu$  is the dynamic viscosity, The unit is  $(\text{N}\cdot\text{s})/\text{m}^2$  ;

$T$  is the temperature, The unit is  $^{\circ}\text{C}$ ;

$\kappa$  is the heat transfer coefficient of the fluid, The unit is  $\text{W}/(\text{m}\cdot\text{K})$  ;

$c_p$  is the specific heat capacity, The unit is  $(\text{kJ}\cdot\text{Kg})/^{\circ}\text{C}$ ;

$S_T$  is the energy source term;

### 3 NUMERICAL EXPERIMENT RESULTS ANALYSIS AND VERIFICATION

#### 3.1 Analysis of Numerical Experiment Results

CFD simulation method was used to study the mitigation effect of urban gardens on the surrounding wind and heat environment. The influence intensity and cooling mechanism of landscape gardens in the city are related to the basic constituent factors inside the garden, such as the size of the "cold source" such as water and vegetation, the complexity of the shape, the size of the garden and the spatial layout and other factors. This paper mainly studies the influence of modern gardens in the north and south on the surrounding wind and heat environment, such as Taoranting Park in the north and Jingsi Garden in the south. The area of Beijing Taoranting Park is larger than that of Suzhou Jingsi Garden, and the water area is larger. We mainly analyze the temperature and wind speed at a distance of 1.5m from the ground, because this affects the outdoor comfort and physical and mental health of residents.

The simulation results of Taoranting Park show that Figure 3a shows that due to the low wind speed on the day, the large water area and green space coverage of Taoranting Park, and the complex boundary shape of the park, it has a mitigation effect on the temperature within about 200m, wide and spread to all boundaries of the park. Figure 3b shows that four temperature lines in the downwind direction within 200m from the park

boundary are randomly selected from the overall park temperature field, the distance from the park boundary is the abscissa and the temperature is the ordinate, it is used to quantitatively analyze the mitigation effect of Taoranting Park on the surrounding temperature. Figure 3b shows that when the distance from the park exceeds 200m, the mitigation effect of temperature gradually decreases until it disappears; with the distance from the boundary, the cooling effect gradually slows down, and the maximum temperature can be reduced by more than  $4^{\circ}\text{C}$ . Figure 4 shows the simulated wind speed field in Taoranting Park. Because of the lower trees and fewer houses in the park, the obstruction to the wind speed is small, and the overall wind speed in the park does not decrease significantly.

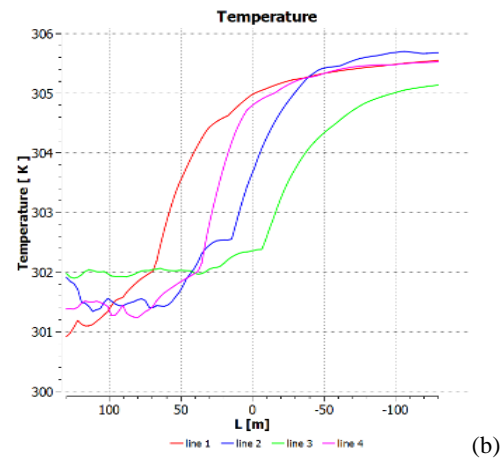
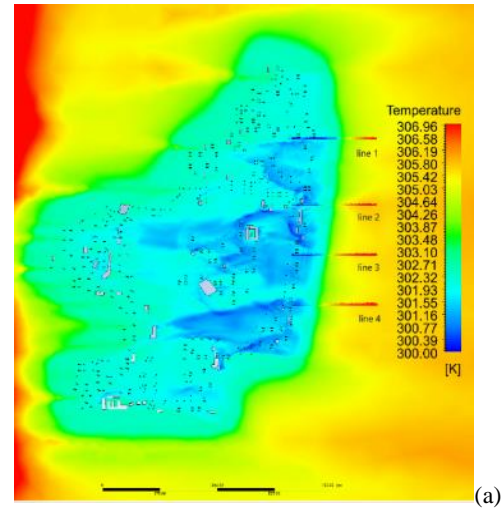


Figure 3 (a) Temperature field at 1.5m in Taoranting Park (b) Temperature variation downwind from the park boundary



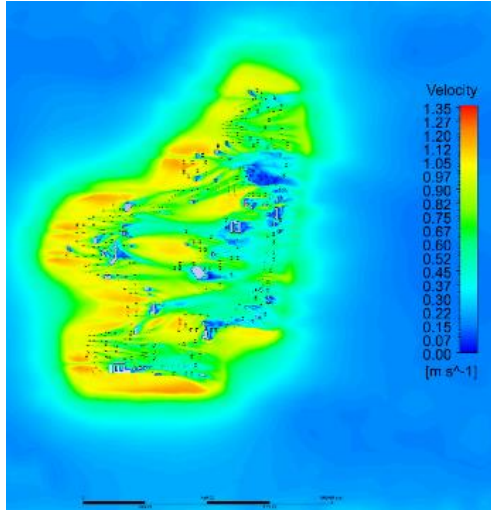


Figure 4 Velocity field at 1.5m in Taoranting Park

The simulation results of the Jingsi Garden show that Figure 5a shows that the wind speed of the simulated Jingsi Garden was relatively large on that day, and the wind speed had a certain influence on the distribution of the temperature field. Therefore, two regions with large temperature difference in the overall temperature field were selected for quantitative analysis. Figure 5b shows that in the downwind direction with large green space coverage and few buildings, the temperature reduction range is wide and the effect is obvious; On the contrary, in the downwind direction with dense buildings, the temperature has increased, and the influence range is about 200m. On the whole, the temperature changes by about 1°C in the downwind direction, and there is no obvious cooling effect around other boundaries. This result may be due to factors such as the small area of Jingsi Garden, the relatively small area of water and green space, and the large number of buildings. Figure 6 shows the wind speed field of Jingsi Garden. Due to the relatively dense buildings, the wind speed in the whole garden is seriously reduced, especially at the wake of the building.

From the simulation results of wind and heat fields of Taoranting and Jingsi Garden, it can be concluded that Taoranting Park, which has a large area and a relatively large area of green space and water body, has a good temperature mitigation effect at a height of 1.5m, and the mitigation range is wide. Compared with the Jingsi Garden, which covers a relatively small area of water and green space, its effect on the surrounding temperature is poor, and the scope is also limited to the downward direction of the garden. Therefore, the cooling effect of Taoranting Park in the north is better than that of Jingsi Garden in the south, and it creates a

more comfortable outdoor environment for nearby residents.

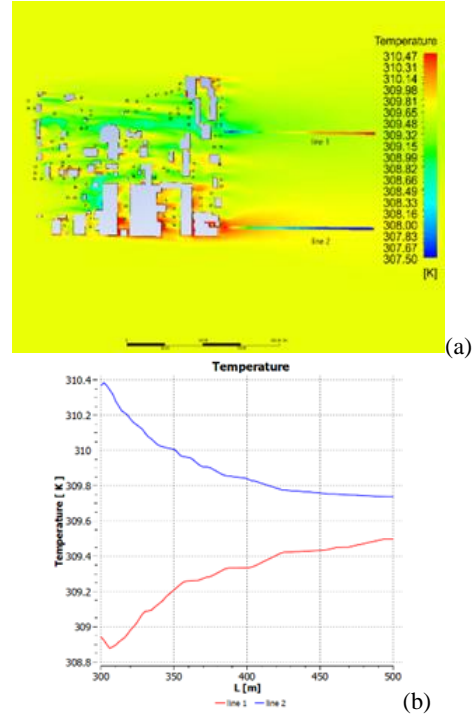


Figure 5 (a) Temperature field at 1.5m from Jingsi Garden (b) Temperature variation downwind from the park boundary

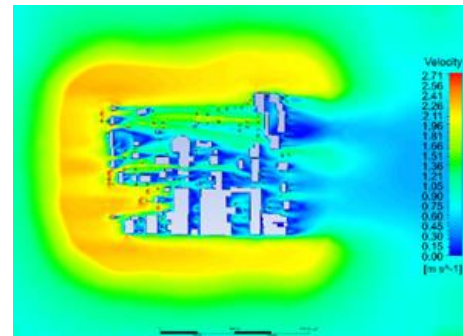


Figure 6 Velocity field at 1.5m from Jingsi Garden

### 3.2 Verification of Numerical Experiment Results

On September 18, 2022, Taoranting Park will be measured on the spot. The selection of measurement points is shown in Figure 7. The temperature measured in the field at 1.5m was compared with the results of the CFD simulation. Figure 8 shows that the temperature difference between the measurement points 2, 3 and 4 is not much different. The temperature difference between the measurement points 1, 5 and 6 is relatively

large, but the temperature difference does not exceed 1 °C. The root mean square error (RMSE) analysis was carried out with the measured data and simulated data, and the root mean square error was 0.48377, indicating that the CFD simulation results have high accuracy and can be used to analyze the mitigation effect of urban gardens on the surrounding wind and heat environment.

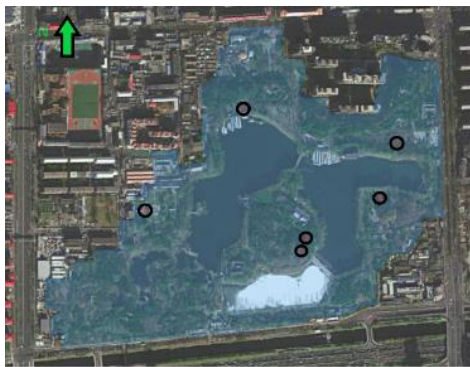


Fig. 7 Marking map of measured points

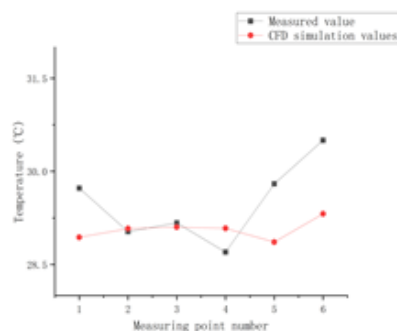


Fig.8 Verification of air temperature at 1.5m

#### 4 CONCLUSION

This study mainly uses the CFD method to simulate the wind and heat environment of different garden layouts in the north and south of China, and the mitigation effect of the urban interior landscape gardens with different spatial layouts on the surrounding wind and heat environment. High-resolution remote sensing data and measured data are used as boundary conditions and verification methods for CFD numerical experiments. Taoranting Park in the north has a better effect on the degree and scope of the surrounding temperature reduction than the Jingsi Garden in the south. Among them, the surrounding temperature of each boundary of Taoranting Park has been relieved, and the mitigation range involves more than 200m, and the maximum temperature can be lowered by more than 4°C. Therefore, the thermal comfort of residents around

Taoranting Park in the north is better than that of Jingsi Garden in the south.

#### 5 REFERENCES

- Huo, H.; Chen, F.; Geng, X.; Tao, J.; Liu, Z.; Zhang, W.; Leng, P. Simulation of the Urban Space Thermal Environment Based on Computational Fluid Dynamics: A Comprehensive Review. *Sensors* 2021, 21, 6898. <https://doi.org/10.3390/s21206898>.
- Du, S.; Zhang, X.; Jin, X.; Zhou, X.; Shi, X. A review of multi-scale modelling, assessment, and improvement methods of the urban thermal and wind environment. *Building and Environment* 213 (2022) 108860. <https://doi.org/10.1016/j.buildenv.2022.108860>
- Huo, H.; Chen, F. A Study of Simulation of the Urban Space 3D Temperature Field at a Community Scale Based on High-Resolution Remote Sensing and CFD. *remote sensing* 2022, 14, 3174. <https://doi.org/10.3390/rs14133174>.
- Fallahpour, M.; Aghamolaei, R.; Zhang, R.; Mirzaei, P. Outdoor thermal comfort in urban neighbourhoods by coupling of building energy simulation and computational fluid dynamics. *Building and Environment* 2022, 10, 9599. <https://doi.org/10.1016/j.buildenv.2022.109599>
- Gromke, C.; Blocken, B.; Janssen, W.; Merema, B.; van Hooff, T.; Timmermans, H. CFD analysis of transpirational cooling by vegetation: Case study for specific meteorological conditions during a heat wave in Arnhem, Netherlands. *Build. Environ.* 2015, 83, 11–26. <https://doi.org/10.1016/j.buildenv.2014.04.022>.
- Tominaga, Y.; Sato, Y.; Sadohara, S. CFD simulations of the effect of evaporative cooling from water bodies in a micro-scale urban environment: Validation and application studies. *Sustain. Cities Soc.* 2015, 19, 259–270. <https://doi.org/10.1016/j.scs.2015.03.011>.
- Zeng, F.; Lei, C.; Liu J., Niu, J.; Gao, N. CFD simulation of the drag effect of urban trees: Source term modification method revisited at the tree scale. *Sustain. Cities Soc.* 2020, 56, 102079. <https://doi.org/10.1016/j.scs.2020.102079>.
- Antoniou, N.; Montazeri, H.; Neophytou, M.; Blocken, B. CFD simulation of urban microclimate: Validation using high-resolution field measurements. *Sci. Total Environ.* 2019, 695, 133743.
- Li, K.; Yu, Z. Comparative and Combinative Study of Urban Heat island in Wuhan City with Remote Sensing and CFD Simulation. *Sensors* 2008, 8, 6692–6703. <https://doi.org/10.3390/s8106692>



# Ensemble Learning methods for Soil Moisture Retrieval from Radar Images

Liguo Wang<sup>a,b</sup>, Ya Gao<sup>a</sup>, Geji Zhong<sup>c</sup>, Yitong Wang<sup>a</sup>

*a. Harbin Engineering University, Harbin, Heilongjiang, China, 150000,*

*b. College of Information and Communications Engineering, Dalian Minzu University, Dalian, 116600, China*

*c. School of Ethnology and Sociology, Minzu University of China, 27 Zhongguancun South Street, Haidian District, Beijing, China*

wangliguo@hrbeu.edu.cn, [gaoya0001@hrbeu.edu.cn](mailto:gaoya0001@hrbeu.edu.cn), 18101356515@163.com,

yitongveton@163.com

\* Corresponding author: Ya Gao, [gaoya0001@hrbeu.edu.cn](mailto:gaoya0001@hrbeu.edu.cn)

**ABSTRACT:** Soil moisture is one of the extremely important parameters on the land surface. Efficient and accurate monitoring of the spatial and temporal distribution of soil water content is of great practical significance and scientific value for crop yield estimation, drought monitoring, water resource allocation and ecological protection. Synthetic Aperture Radar (SAR) has the ability to observe the ground surface all day long and in all weather, independent of clouds and rain, and has a high interest in the study of soil moisture inversion. The Sentinel-1 SAR data has high resolution and accuracy and is freely available to the public, which greatly reduces the development cost, so the inversion study of soil moisture based on Sentry data has great practical significance. In this study, we developed a soil moisture retrieval method using ensemble learning by Sentinel-1 and Sentinel-2 with multi-source datasets. We used Sentinel-1 IW GRD product, synchronous observation data set of soil moisture from TPDC, and ASTER GDEM. The spatial resolution of all remote sensing data is 30m. Techniques like Boosting are iterable, sequential and adaptive because each predictor is corrected for the errors of the previous model. And Categorical boosting (CatBoost) performed slightly better than the Gradient Boosting Decision Tree (GBDT). Better results were obtained using CatBoost for soil moisture prediction, while the best inversion results were obtained when both VV and VH polarizations of the radar signal were used as input data. The MAE is 2.386 vol%, and the RMSE is 4.108 vol%. Ensemble learning, in order to obtain better prediction performance, combines the prediction results of multiple models (weak learners). CatBoost's base model uses a symmetric tree to prevent model overfitting. CatBoost also uses combined category features that can exploit the connections between features, which greatly enriches the feature dimension.

**Key-words:** soil moisture, CatBoost, GBDT, Sentinel-1, remote sensing

## 1 INTRODUCTION

Soil moisture is an important parameter in research in the field of atmospheric science as well as agricultural science. The traditional method of measuring soil moisture is suitable for collecting soil moisture information from small area sample points, which requires a lot of manpower for sampling and laboratory measurements, and is difficult to realize the measurement of soil moisture in large areas (Jiang et al. 2021). The advent of remote sensing technology has solved the shortcomings of traditional methods and allows for large-scale, high-resolution soil moisture monitoring. Microwave remote sensing has now been applied to high-precision soil moisture monitoring (Zhang et al. 2022; Abowarda et al. 2021; Karthikeyan and Mishra 2021; Wei et al. 2019).

With the development of microwave remote sensing in recent years, soil moisture inversion methods based on non-parametric methods on the basis of theoretical models have developed rapidly. El Hajj, M. et al. used a neural network algorithm to estimate SM. they estimated the applicability of C- and L-band radar signals for soil moisture inversion (El Hajj et al. 2019). LIU et al. used generalized regression neural network, support vector regression, random forest, regression (RFR) and deep neural network (DNN) algorithms combined with Sentinel-1A and Sentinel-2A images to estimate SM (Liu et al. 2021). In their study, Nguyen, T. T. et al. used a new approach using advanced machine learning (ML) models and multi-sensor data fusion to make accurate predictions of soil moisture (Nguyen et al. 2022).

In this study, we used sentinel-1 and sentinel-2 and other related data to build a dataset for local soil moisture inversion of vegetation cover areas using an ensemble learning approach.

## 2 MATERIALS AND METHODS

### 2.1 Study area

The ground synchronized sampling samples were distributed in the upstream areas of the Luan River (Shandian River Basin and Little Luan River Basin). The dataset contains surface and soil moisture data measured simultaneously on the ground during the 2018 Soil Moisture Remote Sensing Experiment (SMELR) aerial flight test in the Luan River Basin, which was used to verify the "true value" of the remote sensing inversion (Zhao et al. 2020).

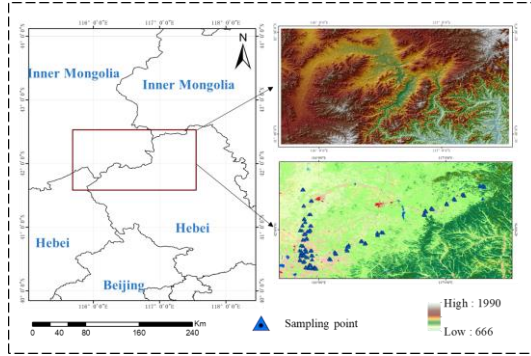


Figure 1. The geographical location of the study area, topographic map and sampling points

### 2.2 Methodology

#### 2.2.1 The water cloud model

Water Cloud Model (WCM) is a kind of semi-empirical model. In 1978, Ulaby et al. proposed it based on the study of regional scattering of crops. The only relevant parameters in the model are vegetation parameters and soil moisture (Attema and Ulaby 1978).

$$\sigma_{can}^0 = \sigma_{veg}^0 + \tau^2 \sigma_{soil}^0 \quad (1)$$

$$\sigma_{veg}^0 = AV \cos \theta (1 - \tau^2) \quad (2)$$

$$\tau^2 = \exp(-2BV_2 / \cos \theta) \quad (3)$$

where  $\sigma_{can}^0$  is the total backscattering coefficient received by the radar.  $\sigma_{veg}^0$  is the signal directly reflected by the vegetation.  $\sigma_{soil}^0$  is the scattered signal of the soil.  $\tau^2$  is the attenuation coefficient of the signal attenuated twice by the vegetation.  $\theta$  is the signal incident angle.  $V$  is vegetation related parameters, NDWI, NDVI and EVI are described as vegetation in this study.  $A$  and  $B$  are empirical coefficients for the model, related to the type of vegetation and radar parameters.

#### 2.2.2. Categorical Boosting (Catboost)

Catboost is a decision tree model based on gradient boosting. The main problem addressed is to handle categorical features efficiently and rationally, which can be seen from its name. CatBoost is composed of Categorical and Boosting. In addition, CatBoost solves the problem of gradient bias and prediction bias, thus reducing the occurrence of overfitting and thus improving the accuracy and generalization of the algorithm. The pseudo-code of CatBoost is expressed as follows (Dorogush A V et al. 2018):

---

**Algorithm:** Updating the models and calculating model values for gradient estimation

---

**input :**  $\{(X_k, Y_k)\}_{k=1}^n$  ordered according to  $\sigma$ , the number of trees  $I$ ;  
 $M_i \leftarrow 0$  for  $i = 1..n$ ;  
**for**  $iter \leftarrow 1$  **to**  $I$  **do**  
  **for**  $i \leftarrow 1$  **to**  $n$  **do**  
    **for**  $j \leftarrow 1$  **to**  $i - 1$  **do**  
       $g_j \leftarrow \frac{d}{da} Loss(y_j, a) \Big|_{a=M_i(X_j)}$ ;  
       $M \leftarrow LearnOneTree((X_j, g_j) \text{ for } j = 1..i-1)$ ;  
       $M_i \leftarrow M_i + M$ ;  
**return**  $M_1 \dots M_n; M_1(X_1), M_2(X_2) \dots M_n(X_n)$

---

#### 2.2.3 Gradient Boosting Decision Tree (GBDT)

A Gradient Boosting Decision Tree (GBDT) is a gradient boosting decision tree, where the output of a GBDT model is the sum of several decision trees, each of which is a fit to the residuals of the previous combination of decision trees, a "correction" to the previous model. ". Gradient boosting trees can be used for both regression problems (in this case known as CART regression trees) and classification problems (in this case known as classification trees) (Guolin Ke et al. 2017; Zhang et al. 2017). The pseudo-code of GBDT is expressed as follows:

---

**Algorithm: Gradient Tree Boosting Algorithm.**


---

**Initialize**  $f_0(x) = \arg \min_{\gamma} \sum_{i=1}^N L(y_i, \gamma)$

**For m = 1 to M:**

**For i = 1, 2, ..., N compute**

$$r_{im} = - \left[ \frac{\partial L(y_i, f(x_i))}{\partial f(x_i)} \right]_{f=f_{m-1}}$$

**Fit a regression tree to the targets  $r_{im}$  giving terminal regions**

**$R_{jm}$ ,  $j = 1, 2, \dots, J_m$ .**

**For  $j = 1, 2, \dots, J_m$  compute**

$$\gamma_{jm} = \arg \min_{\gamma} \sum_{x_i \in R_{jm}} L(y_i, f_{m-1}(x_i) + \gamma)$$

**Update**

$$f_m(x) = f_{m-1}(x) + \sum_{j=1}^{J_m} I(x \in R_{jm})$$

**Output**  $\hat{f}(x) = f_M(x)$

---

### 3 RESULT

Based on ensemble learning algorithm, the SM is estimated with sentinel-1 and other multi-source datasets.

Since SENTINEL-1 is divided into VV and VH polarization methods, we have chosen three data sets as input in this paper. In the input set, the radar signal is divided into three ways VV, VH and VV\_VH. Two algorithms, GBDT and CatBoost, are also used to compare which combination can get better soil moisture results. The estimated SM results with two methods were shown in Figure 2 and 3.

Figure 2 represents Observed soil moisture and predicted soil moisture dispersion point diagram of GBDT. Figure 2(a1) is displayed VV polarization as input, and the MAE is 3.508, Bais is 0.00, RMSE is 5.323. The MAE, Bais, RMSE are 3.157, 0.00, 4.345 respectively with VH as the input (see Figure 2(a2)). When VV\_VH is used as input, the MAE is 3.374, Bais is 0.00, and RMSE is 4.768. From these three input methods, the best results are obtained when the radar signal input is VH polarized, which is better than the VV and VV\_VH polarization methods.

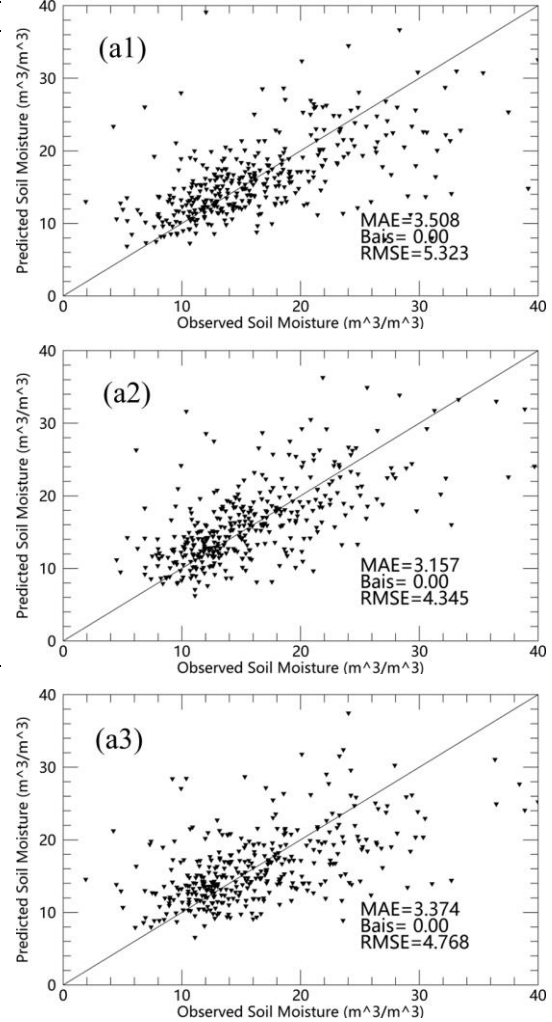


Figure. 2 Observed soil moisture and predicted soil moisture dispersion point diagram of GBDT ((a1)VV, (a2)VH, (a3)VV\_VH)

The results of the CatBoost-based soil moisture inversion method are shown by Figure 3. Similarly, we divided the radar input into three parts. The inputs with VV and VH results are, MAE of 2.433 and 2.474, both Bais of 0.00, RMSE of 4.126 and 4.123, respectively (Figure(b1) and (b2)). Moreover, we can found that the result of VV\_VH input is greater than VV and VH, with MAE of 2.386, Bais of -0.00, RMSE of 4.108, severally (Figure(b3)).



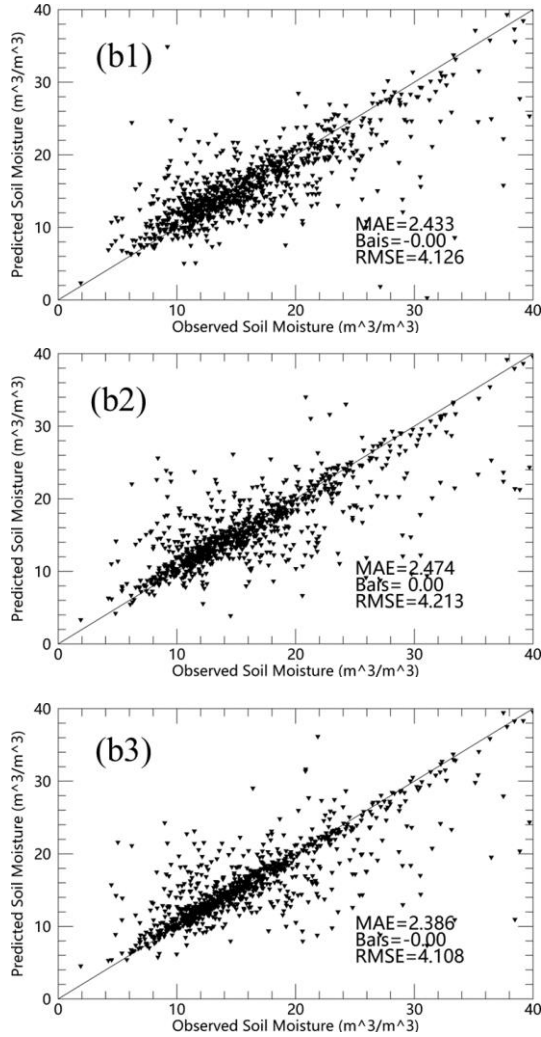


Figure. 3 Observed soil moisture and predicted soil moisture dispersion point diagram of CatBoost ((b1)VV, (b2)VH, (b3)VV\_VH)

CatBoost employs an effective strategy to reduce overfitting while ensuring that the entire dataset is available for learning. That is, the dataset is randomly ranked and the average label values of samples with the same category values are calculated by simply including the label values of the samples before this sample. CatBoost combines all the combined, category-based features of the current tree with all the category-based features in the dataset. We also calculated the MSE comparison curves of different parameters of CatBoost (Figure 4\_c1, c2 c3). We can clearly see that the MSE comparison curves of different parameters of CatBoost values obtained for the three inputs are in the range of 0-0.3.

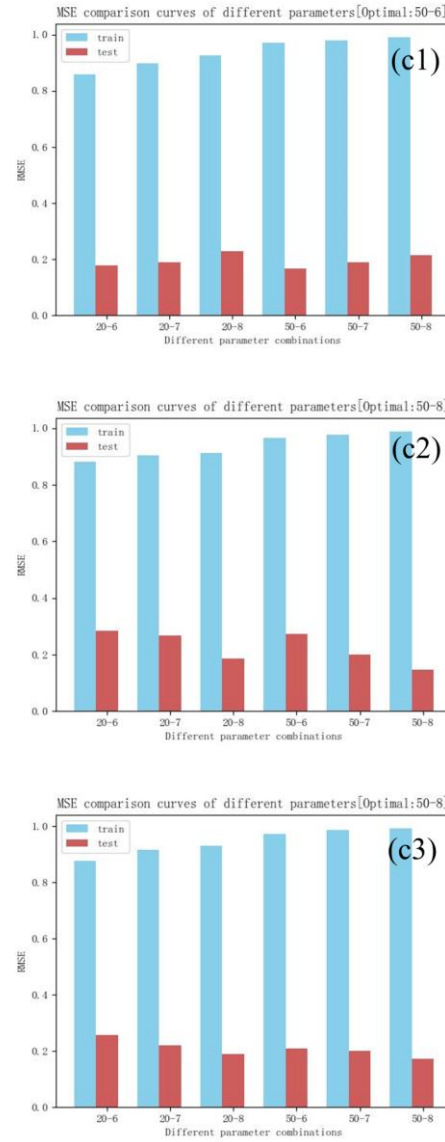


Figure. 4 MSE comparison curves of different parameters of CatBoost (VV, VH, VV\_VH)

#### 4 DISCUSSION

We successfully obtained the predicted soil moisture by both methods GBDT and CatBoost. We can find that both methods can get better results, but the CatBoost algorithm is better than GBDT. The optimal inversion results are obtained when the input set of the algorithm, the radar signal, is VV\_VH polarized. MAE is 2.386, Bias is -0.00, and RMSE is 4.108, respectively.

CatBoost reduces the need for extensive hyperparameter tuning and reduces the chance of overfitting, which also leads to a more general model. Although, CatBoost has several parameters to tune, it contains parameters such as number of trees, learning rate, regularization, tree depth, fold size, bagging temperature, etc.

## 5 CONCLUSION

Three SAR inversion configurations were developed (single VV, single VH, and VV and VH) as the input of ensemble learning algorithm. The results show that inversion results using both VV and VH as inputs due to VV alone and VH alone.

CatBoost employs an effective strategy to reduce overfitting while ensuring that the entire dataset is available for learning. That is, when the data set is randomly arranged and the average label value of samples with the same category value is calculated, the label value of previous samples of this sample is only included in the calculation. It reduces the need for many hyperparameter tuning and reduces the chance of overfitting, which also makes the model more versatile. CatBoost is more effective for soil moisture retrieval.

## 6 ACKNOWLEDGEMENTS

This research was funded by the National Natural Science Foundation of China (grant number 61675051). Leading Talents Project of the State Ethnic Affairs Commission. The data set is provided by National Tibetan Plateau Data Center (<http://data.tpdc.ac.cn>).

## REFERENCES

- Gierloff-Emden, H. G., 1985, Analysis of the Metric Camera MC-BW for land use classification and land use hazard management (thematic mapping of Metric Camera Spacelab black and white photographs). European Remote Sensing Opportunities: Systems, Sensors and Applications, Proceedings of the EARSeL/ESA Symposium held in Strasbourg, France, on 31 March-3 April 1985, SP-233 (Paris: European Space Agency), pp. 79-84.
- Attema, E.P.W., & Ulaby, F.T. 1978. Vegetation modeled as a water cloud. *Radio Science*.
- Dorogush A V, Ershov V, & A, G. 2018. CatBoost: gradient boosting with categorical features support.
- Guolin Ke, Qi Meng, Thomas Finley, Taifeng Wang, Wei Chen, Weidong Ma, Qiwei Ye, & Liu, T. 2017. LightGBM: A Highly Efficient Gradient Boosting Decision Tree.
- Zhang, C., Liu, C., Zhang, X., & Almpandis, G. 2017. An up-to-date comparison of state-of-the-art classification algorithms.
- Zhao, T., Shi, J., Lv, L., Xu, H., Chen, D., Cui, Q., Jackson, T.J., Yan, G., Jia, L., Chen, L., Zhao, K., Zheng, X., Zhao, L., Zheng, C., Ji, D., Xiong, C., Wang, T., Li, R., Pan, J., Wen, J., Yu, C., Zheng, Y., Jiang, L., Chai, L., Lu, H., Yao, P., Ma, J., Lv, H., Wu, J., Zhao, W., Yang, N., Guo, P., Li, Y., Hu, L., Geng, D., & Zhang, Z. (2020). Soil moisture experiment in the Luan River supporting new satellite mission opportunities. *REMOTE SENSING OF ENVIRONMENT*, 240, 111680
- Abowarda, A.S., Bai, L., Zhang, C., Long, D., Li, X., Huang, Q., & Sun, Z. (2021). Generating surface soil moisture at 30 m spatial resolution using both data fusion and machine learning toward better water resources management at the field scale. *REMOTE SENSING OF ENVIRONMENT*, 255, 112301
- El Hajj, M., Baghdadi, N., & Zribi, M. (2019). Comparative analysis of the accuracy of surface soil moisture estimation from the C- and L-bands. *International Journal of Applied Earth Observation and Geoinformation*, 82, 101888
- Jiang, Y., Yang, K., Shao, C., Zhou, X., Zhao, L., Chen, Y., & Wu, H. (2021). A downscaling approach for constructing high-resolution precipitation dataset over the Tibetan Plateau from ERA5 reanalysis. *ATMOSPHERIC RESEARCH*, 256, 105574
- Karthikeyan, L., & Mishra, A.K. (2021). Multi-layer high-resolution soil moisture estimation using machine learning over the United States. *REMOTE SENSING OF ENVIRONMENT*, 266, 112706
- Liu, Y., Qian, J., & Yue, H. (2021). Combined Sentinel-1A With Sentinel-2A to Estimate Soil Moisture in Farmland. *IEEE Journal of Selected Topics in Applied Earth Observations and Remote Sensing*, 14, 1292-1310
- Nguyen, T.T., Ngo, H.H., Guo, W., Chang, S.W., Nguyen, D.D., Nguyen, C.T., Zhang, J., Liang, S., Bui, X.T., & Hoang, N.B. (2022). A low-cost approach for soil moisture prediction using multi-sensor data and machine learning algorithm. *SCIENCE OF THE TOTAL ENVIRONMENT*, 833, 155066
- Wei, Z., Meng, Y., Zhang, W., Peng, J., & Meng, L. (2019). Downscaling SMAP soil moisture estimation with gradient boosting decision tree regression over the Tibetan Plateau. *REMOTE SENSING OF ENVIRONMENT*, 225, 30-44
- Zhang, Y., Liang, S., Zhu, Z., Ma, H., & He, T. (2022). Soil moisture content retrieval from Landsat 8 data using ensemble learning. *ISPRS JOURNAL OF PHOTOGRAMMETRY AND REMOTE SENSING*, 185, 32-47

# Assessment of water stress of major river basins in China for Sustainable Development Goals

Jing Lu, Li Jia,

*State Key Laboratory of Remote Sensing Science, Aerospace Information Research Institute, Chinese Academy of Sciences, Beijing 100101, China*

lujing@aircas.ac.cn; jiali@aircas.ac.cn

**ABSTRACT** - Based on FAO's water stress definition, this study constructed a method to disaggregate water stress's spatial and temporal distribution in China by combining multi-source data, including statistical, remote sensing and model-simulated data. The remote sensing data and the model-simulated data provided the spatial and temporal proxies for the renewable water resource and freshwater withdrawal to disaggregate the statistical values at the provincial administrative units. The disaggregated data at the grid scale were used to calculate water stress in China's major river basins and to evaluate their spatial and temporal changes and drivers. Among China's ten first-class water resources regions, Haihe River holds the highest water stress, followed by Huaihe River and Northwest Rivers, with water stress larger than 100% (the extreme water stress level). The water stress in each water resource region is spatially heterogeneous, but the extreme and high water stress level means that the available water resources cannot meet the demands of water use and it is in an unsustainable status. From 2002 to 2020, the water stress in Haihe River, Pearl River, and Southeast Rivers were significantly declining because of increasing precipitation and decreasing water use. However, attention should be paid to the significant increasing trend of water stress in Huaihe River and Northwest Rivers due to declining available water resources and increasing water use.

## 1 INTRODUCTION

Water, the source of life, is vital to human health and well-being. Water scarcity can hamper the sustainable development of the economy, society, and human beings. Ensuring availability and sustainable management of water and sanitation for all is the key content of the Sustainable Development Goal 6 (SDG 6) in the United Nations 2030 Agenda. Water stress level of the SDG 6.4.2 indicator provides a measure of water scarcity by considering the environment flow requirement (EFR) (FAO, 2018, 2019). High levels of water stress can lead to competition increases and potential conflicts among water use sectors, which is adverse to sustainable development.

The Food and Agriculture Organization of the United Nations (FAO), as the custodian agency of SDG 6, proposed a global framework for evaluation of water stress levels at the national scale by using the statistical data from FAO Global Information System on Water and Agriculture (AQUASTAT) (FAO, 2018). The water stress in China in 2018 was reported as 43% in the report on level of water stress issued by FAO and UN-WATER in 2021 (UN-WATER, 2021). China was cataloged as a country with a low water stress level. However, China is a large country with 1.4 billion population and unevenly distributed water resources in time and space. As the population grows, rapid economy development and global climate change, the shortage of water resources will be a more serious problem, especially in northern China. The

supply of water resources cannot meet the demand for water use in many regions of China. Therefore, it is necessary to take an in-depth analysis of water stress at the sub-national scale, which is helpful to formulate water management policies and ensure the sustainable utilization of water resources. The water stress monitoring at the national scale cannot reflect regional and sub-regional differences within countries. Meanwhile, the information of temporally dynamic change of water stress is also lacking due to the limitations of data and methods (UN-WATER, 2021).

Understanding spatial and temporal changes of water stress plays a critical role in the sustainable utilization of water resource. For the regional assessment of water stress in China, Zhang et al. (2020) analyzed China's water stress and its drivers at the provincial administrative unit by calculating the water stress indicator. Pan et al. (2018) used the Falkenmark index and water stress indicator to quantitatively evaluate water resource pressure in China's first-grade districts of water resources. The water stress indicator calculated in Zhang's and Pan's studies didn't consider EFR, differing from the one defined by the SDG 6.4.2 indicator. Environment flow reservation is essential for the sustainability of water resources. Ma et al. (2020) reported a comprehensive nationwide water scarcity assessment in China at multiple temporal and geographic scales by considering the water quality and defining 80% of the total freshwater resources as EFR. However, EFR

changes with regions rather than a fixed ratio, and the water stress level is related to how much water is reserved for the environment (Vanham et al., 2021). Vanham et al. (2018) discussed that some essential elements including temporal and spatial disaggregation should be considered in SDG 6.4.2 indicator. The development of remote sensing technology can provide a large number of data on the Earth's surface information. The advantages of high spatial and temporal resolution and quasi-real-time monitoring by remote sensing data have not been effectively placed in the assessment of water stress of SDG 6.4.2 indicator. Therefore, the purpose of this work is to disaggregate water stress level indicator by combing multi-source data including remote sensing data and to evaluate the spatial and temporal changes of water stress and the drivers in China.

## 2 METHOD

### 2.1 Water stress indicator

The level of water stress of SDG 6.4.2 indicator is defined as the ratio between total freshwater withdrawn (TFWW) by all major sectors and total renewable freshwater resources (TRWR) after deducting EFR (UN-WATER, 2021), and calculated as:

$$\text{Water stress (\%)} = \text{TFWW} / (\text{TRWR} - \text{EFR}) \times 100 \quad (1)$$

TFWW is usually calculated as the sum of withdrawal from renewable freshwater resources and fossil groundwater for agriculture, industries, and services minus the direct use of non-conventional water as wastewater, the direct use of agricultural drainage water and the use of desalinated water. TRWR is the sum of internal renewable freshwater resources generated from endogenous precipitation and external renewable freshwater resources (flows entering the country, taking into consideration of the quantity of flows reserved to upstream and downstream countries through agreements or treaties). EFR refers to the quantity and change of freshwater flows required to sustain freshwater ecosystems and the human livelihoods and well-being. Water-stress values are categorized into five levels:

- 0-25%, no water stress;
- 25%-50%, low water stress level;
- 50%-75%, medium water stress level;
- 75%-100%, high water stress level;
- >100%, extreme water stress level.

High water stress level negatively affects social and economic development. Water stress level >100% indicates that environmental water or non-renewable water (such as groundwater) is being used, which is undesirable and unsustainable.

### 2.2 Spatial and temporal disaggregation of TRWR and TFWW

TRWR and TFWW are usually obtained from statistical data at national or provincial level. Many assessments of water stress in China mainly depended on this data. The spatial and temporal disaggregation of TRWR and TFWW requires the gridded remote sensing data and simulated data as the proxy. In this work, remote sensing-based precipitation - evapotranspiration - the change of terrestrial water storage provides the spatial and temporal proxy for TRWR, while model-simulated water use based on the remote sensing data provide the proxy for TFWW. The principle of spatial disaggregation is that TRWR (TFWW) in a given region is the sum of values of all grids in the region. The temporal disaggregation implies that the yearly TRWR (TFWW) is the sum of all monthly values. The schematic diagram of the spatial and temporal disaggregation of TRWR and TFWW is shown in Figure 1. The weight on the grid scale or the monthly scale is calculated by the proxy of TRWR (TFWW) and then is multiplied by the statistical regional yearly TRWR (TFWW) to obtain the gridded or monthly values. Spatial disaggregation and temporal disaggregation are two independent processes. If the temporal disaggregation follows the spatial disaggregation, the gridded water resources and freshwater withdrawal at the monthly scale can be obtained. The water stress in different river basin scales can be calculated based on the gridded data.

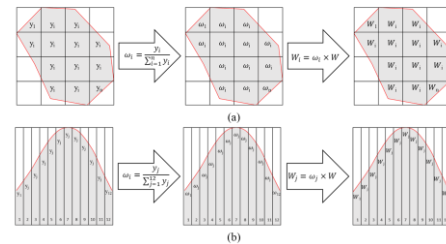


Figure 1. The (a) spatial and (b) temporal disaggregation process of total renewable freshwater resources or total freshwater withdrawal ( $y$  is the data reflecting the temporal and spatial changes of total renewable freshwater resources or total freshwater withdrawal, which can be from remote sensing data or model-simulated data;  $w$  is the weight;  $W$  is the target variable of total renewable freshwater resources or total freshwater withdrawal from the statistical data;  $i$  is the pixel contained in the corresponding region;  $j$  is the period from January to December)

## 3 DATA AND MATERIALS

According to Equation (1), the estimation of water stress mainly involves three variables: TFWW, TRWR, and EFR. The Annual China Water Resources

Bulletin provides the TFWW and TRWR data of each province in China. The GPM (Global Precipitation Measurement mission) precipitation, ETMonitor evapotranspiration, and GRACE (Gravity Recovery and Climate Experiment) terrestrial water storage anomaly (TWSA) as the remote sensing data sources together provide the proxy of the spatial distribution of TRWR. The GPM Precipitation data integrated the multi-source satellite remote sensing data and the meteorological site observations, with the temporal and spatial resolution of 0.1°/month, downloaded from <https://disc.gsfc.nasa.gov>. ETMonitor is a remote sensing-based ET model driven by multi-source data and can generate the global daily ET (Zheng et al., 2022). Daily ET data in 1km resolution can be obtained from <https://data.casearth.cn>. GRACE TWSA data is from JPL Mascon products (<http://grace.jpl.nasa.gov>), with a spatial and temporal resolution of 0.5°/month. WaterGAP (Water-global Assessment and Prognosis), a Global hydrological model that quantifies human use of groundwater and surface water, provided the spatial proxy for TRWR (Hannes et al., 2021). The the monthly simulated data with 0.5°×0.5° spatial resolution released by the latest version of WaterGAP 2.2d (Hannes et al., 2020) are used in this work.

Although International Water Management Institute gave the global scheme to estimate the EFR, it is very different from the actual situation of water resources in China. The difference between TRWR and EFR (TRWR – EFR) expresses the available water resources. Wang et al. (2006) obtained the ratio of available water resources of the ten first-class river basins in China by the in-situ observation from about 144 stations over 115 rivers. The value of (TRWR – EFR) was calculated by TRWR multiplying the ratio of available water resources in this work.

## 4 RESULTS AND DISCUSSION

### 4.1 Water stress and change of whole China

The average water stress in China from 2002 to 2020 was 67%, ranging from a maximum of 73% to a minimum of 58% (Figure 2), in a medium water stress level, which is different from the results reported by the UN-WATER. This discrepancy is mainly from the calculation of EFR, while the ratio of available water resources used in this work can reflect the available water resources in China better. The water stress in China initially increased and then decreased from 2002 to 2020, the maximum in 2008, and the minimum in 2020. Both TFWW – EFR and TFWW showed a significant increasing trend, indicating the rising wetness of climate and the growing demand for water use due to population growth and social and economic development during the past 20 years.

Before 2008, the increasing water use and declining available water resources together contributed to the increase of water stress in China. The decrease in water stress since 2008 is mainly attributed to the increase in available water resources. The decrease in water use after 2013 due to the implementation of the strictest water resources management policy also contributes to the decrease in water stress.

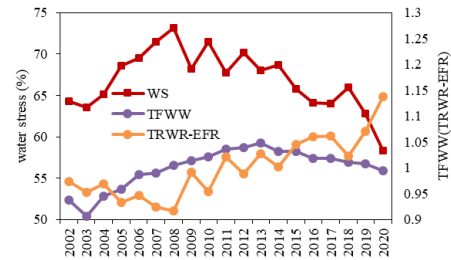


Figure 2. The water stress (WS) in China from 2002 to 2020 (TRWR – EFR is the available renewable water resources). The right y-axis is the ratio of TFWW or TRWR – EFR to their mean values in 2002–2020, respectively.

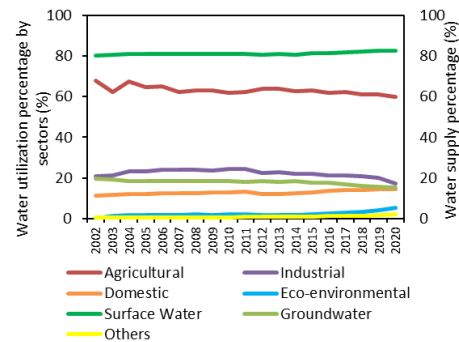


Figure 3. The water use by different sectors and water supplies in China from 2002 to 2020

Agriculture is China's dominant water use sector, accounting for 63% of total water withdrawal on average and showing a significant decline during the past 20 years (Figure 3). Therefore, the improvement of agricultural water use efficiency to reduce agricultural water use is critical to alleviate the water stress in China. Industrial water use accounts for 22% on average, showing an initially increasing and then decreasing trend, reaching the maximum around 2010. Domestic and ecological water use accounts for 13% and 2%, respectively, showing a significant increasing trend from 2002 to 2020. Surface water is the main water supply in China, accounting for more than 80% of the total water supply and showing a significant increasing trend. Groundwater supply decreased significantly, especially since 2014, which reflected the depression of groundwater exploitation and the

increasing water supply to North China Plain due to the implementation of the Middle Route of the South-to-North Water Diversion Project (Long et al., 2020). The substantial increase in other unconventional water supplies demonstrates the improvement of wastewater reuse and seawater desalination capacity.

#### 4.2 Spatial distribution of water stress in basin scale

There are ten first-class water resource regions in China. Six regions including Songhua River, Liaohe River, Haihe River, Yellow River, Huaihe River, and Northwest Rivers locate in Northern China, while the other four regions of Yangtze River, Pearl River, Southeast Rivers, and Southwest Rivers in Southern China. Among the ten water resource regions, the Haihe River holds the highest water stress, followed by Huaihe River and Northwest Rivers. The water stress in the three regions is more than 100% (at the extreme water stress level) (Figure 4), indicating that the available water resource cannot satisfy the demands of regional water use after deducting considering the environmental flow requirement and the water resource exploitability. Yellow River and Liaohe River have a high level of water stress. The water stress of the Pearl River, Yangtze River, and Songhua River regions are at the medium level. Southeast Rivers region is in the low water stress level. There is no water stress in the Southwest Rivers region because of the abundant renewable water resource and less water use demand. The main river basins in the north except the Songhua River are all in high or extreme levels of water stress, which is consistent with the current situation of water shortage in Northern China. The water stress in northern China is generally higher than that in the South, which relates to the spatial distribution of precipitation. Precipitation is the main source of water resources.

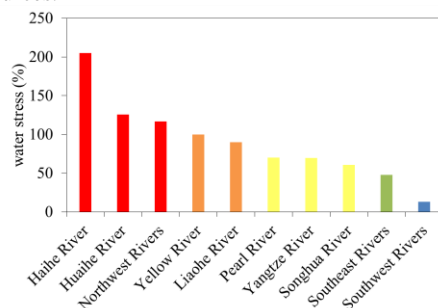


Figure 4. The water stress of the ten first-class water resources regions in China (the bar colors mean different levels of water stress: red is more stressed, blue is less stressed)

The water stress in each water resource region is spatially heterogeneous by the expression of water stress in China's third-class river basins (Figure 5). Almost all sub-river basins in Haihe and Huaihe water resources regions lie in the extreme water stress level. Only several sub-river basins in the mountain area of Haihe River show medium and low water stress levels. The Northwest Rivers region as a whole has an extreme water stress level, but the regions with the extreme level are mainly located in the northwest of Xinjiang Uygur Autonomous Region, and the Heihe river basin, Shiyanghe river basin, and Shulehe river basin, because the large amounts water are used by the agriculture. Agricultural water use accounts for larger than 90% of the total freshwater withdrawal in the Northwest region. These river basins are also the hot areas of water resources research in the arid and semi-arid regions because of the water shortage problem (Wang and Wei, 2019). Yellow River region is also confronting a serious water scarcity problem, especially in its middle and downstream with the extremely high level of water stress. The majority of sub-river basins in Liaohe River except for the part in the east are also in extreme water stress levels. The east of Pearl River because of the developed economy holds a higher water stress level than the west. The downstream of Yangtze River also lies in an extreme water stress level because of increasing water use demands with economic prosperity, higher than that in its upper and middle reaches. Although Songhua River keeps a medium water stress level, some sub-river basins in the central region have an extreme level of water stress. The water stress in the south and the north of Southeast Rivers is higher than that in the central region. In general, the water stress level in the east of China is higher than that in the West, relating to the developed economy and the dense population with more water use demands. The spatial distribution of water stress in Figure 5 is generally consistent with the results of Ma et al. (2020) and Wang et al. (2017).

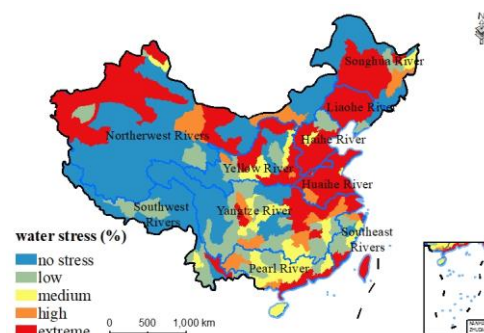


Figure 5. The spatial distribution of water stress level in the third-class river basins in China



#### 4.3 Water stress changes and drivers in the main river basins from 2002 to 2020

The Mann-Kendall (MK) test method is used to take the trend analysis. A negative (positive) MK value means a declining (increasing) trend. The absolute MK value greater than 1.96 means a significant change. Otherwise, it is nonsignificant. From 2002 to 2020, the water stress in Haihe River, Pearl River, and Southeastern Rivers regions significantly declined, while Liaohe River, Songhua River, and Yellow River regions showed a nonsignificant decreasing trend (Figure 6). The declining change in water stress is beneficial to water resources sustainability, especially to those regions with extreme or high water stress levels, such as Haihe River, Liaohe River, and Yellow River. Yangtze River and Southwest Rivers gave a slightly nonsignificant increasing trend. MK values in Huaihe River and Northwest Rivers are greater than 2, indicating that the two regions have had a significant increasing trend during the past 20 years. The significant increasing trend will further exacerbate the problem of water scarcity due to the extreme water stress level in these regions, which will not be helpful to sustainable development.

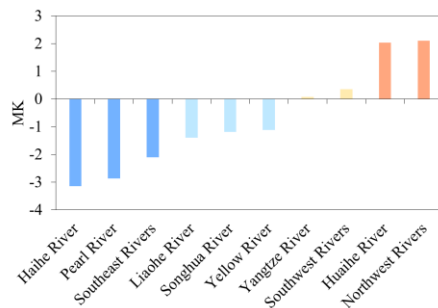


Figure 6. The change trends of water stress in the ten first-class water resources regions in China (Mann-Kendall (MK) value  $>0$  indicates an increasing trend of water stress, and vice versa.  $|MK|>1.96$  means the significant change in the 95% confidence interval.)

Consistent with the trend of the whole region, most sub-river basins in Haihe River, Pearl River, Southeast Rivers, Liaohe River, and Songhua River showed a declining trend, only several sub-river basins have an opposite trend (Figure 7). The upper stream of Yellow River shows a significant decrease, while some sub-river basins in the middle and downstream are increasing the water stress. A significant decrease is found in the upper stream of Yangtze River. Water stress in most regions in the west and the north of Yangtze River is increasing, but not significant. Almost all sub-river basins in Huaihe River have an increasing change in water stress, especially in the

west of this region, a significant increase be found. The increasing change of water stress in Northwest Rivers is mainly contributed by its northern regions with significant increasing.

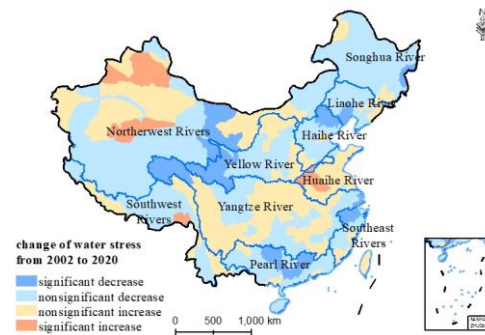


Figure 7. The spatial distribution of water stress change in the third-class river basins in China

Climate factors and water use changes together act on the change of water stress. A Logarithmic Mean Divisia Index (LMDI) method was used to calculate the contribution of climate factors and water use factors to the change of water stress from 2002 to 2020, and the results are shown in Figure 8. The negative value means the restrains to the increase of water stress, while the positive value promotes the increase of water stress. During the past 20 years, the decline in water stress at Haihe River, Pearl River, Southeast Rivers, and Liaohe River can be attributed to the combined effects of the wetting climate (increasing precipitation) and decreasing water use. The contribution from the climate wetting to water stress in Songhua River and Yellow River is greater than the contribution from the increased water use, which leads to a decreasing trend in water stress in these two regions. The increase in water use generally contributes to the increase of water stress in Yangtze River, Southwest Rivers, and Northwest Rivers, although the wetting climate can suppress some increase in water stress. The drying climate with less precipitation is the main reason for the increase in water stress in Huaihe River, and the increase in water use further intensifies the water stress increasing. Generally, the contribution of climate factors to the change of water stress is greater than that of the water use factor, and the regions affected by the wetting climate are more than that by the drying climate. The increase in water use is the dominant of the increase of water stress in the arid and semi-arid regions in Northwestern China.

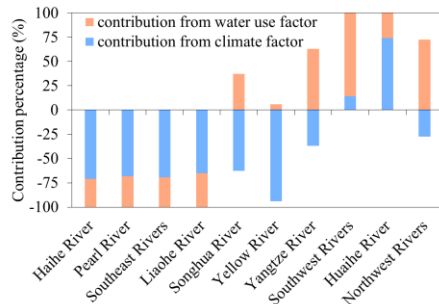


Figure 8. The contribution of climate factor and water use factor to the change of water stress in the ten first-class water resources regions

## 5 CONCLUSION

This study provides a method to obtain the temporal and spatial distribution of water stress at the gridded scale. Based on the gridded water stress data, water stress in China's river basin scale are calculated and evaluated. Water stress in the North of China is generally higher than in the South, and higher in the East than in the West. The spatial distribution of water stress is consistent with the natural endowment of China's water resources and the economic development level. The water stress of the whole China shows an initially increasing and then decreasing trend from 2002 to 2020, which is related to climate change and the implementation of water resources management policy. The assessment of water stress at China's river basins is generally reasonable, but it is still a challenge to estimate water stress accurately because of uncertainties in estimating water use, external renewable water resources, environmental flow requirements, etc.

## 6 ACKNOWLEDGEMENT

This work is supported by the Strategic Priority Research Program of the Chinese Academy of Sciences (Grant no. XDA19030203 and XDA19090120)

## REFERENCES

- FAO, 2018, Progress on level of water stress - Global baseline for SDG 6 Indicator 6.4.2.
- FAO, 2019, Incorporating environmental flows into "water stress" indicator 6.4.2 - Guidelines for a minimum standard method for global reporting.
- Hannes M., Denise C., Stephanie E., et al., 2020, The global water resources and use model WaterGAP v2.2d - Standard model output. *PANGAEA*, <https://doi.org/10.1594/PANGAEA.918447>.
- Hannes M., Denise C., Stephanie E., et al., 2011, The global water resources and use model WaterGAP v2.2d: model description and evaluation. *Geoscientific Model Development*, 2021, 14, 1037-1079.
- Long D., Yang W., Scanlon B., et al., 2020, South-to-North Water Diversion stabilizing Beijing's groundwater levels. *Nature Communications*, 11, 3665.
- Ma T., Sun S., Fu G., et al., 2020, Pollution exacerbates China's water scarcity and its regional inequality. *Nature Communication*, 2020, 11, 650.
- Pan H., Fu Y., 2018, An evaluation of the utilization of water resources based on water stress indicator. *China Rural Water and Hydropower*, 2018, 04, 53-56. (in Chinese)
- Vanham D., Hoekstra A., Wada Y., et al., 2018, Physical water scarcity metrics for monitoring progress towards SDG target 6.4: An evaluation of indicator 6.4.2 "Level of water stress". *Science of the Total Environment*, 2018, 613-614, 218-232.
- Vanham D., Alfieri L., Flörke M., et al., 2021, The number of people exposed to water stress in relation to how much water is reserved for the environment: a global modeling study. *Lancet Planet Health*, 5, e766-74.
- UN-Water, 2021, Progress on level of water stress - Global status and acceleration needs for SDG indicator 6.4.2.
- Wang J., Zhong H., Geng L., et al., 2006, Available water resources in China. *Advances in Water Science*, 17(4), 549-553. (in Chinese)
- Wang J., Zhong L., Iceland C., 2017, China's water stress is on the rise. *World Resources Institute*, <https://www.wri.org/insights/chinas-water-stress-rise>.
- Wang, S., Wei, Y., 2019, Water resource system risk and adaptive management of the Chinese Heihe River Basin in Asian arid areas. *Mitigation and Adaptation Strategies for Global Change*, 24, 1271-1292.
- Zhang Z., Ni H., Chen G., et al., 2020, Analysis on changing trend of regional water resources pressure and suggestions on dealing with differentiation. *Water Resources and Hydropower Engineering*, 2020, 51(11), 41-48. (in Chinese)
- Zheng C., Jia L., Hu G., 2022, Global Land Surface Evapotranspiration Monitoring by ETMonitor Model Driven by Multi-source Satellite Earth Observations. *Journal of Hydrology*, 128444.

# Retrieval of vegetation water content with multi-frequency passive microwave sensor AMSR-E data

Cunxin Cui<sup>1</sup> and Bo-Hui Tang<sup>1,\*</sup>

<sup>1</sup> Faculty of Land Resource Engineering, Kunming University of Science and Technology, 650031, Yunnan, China

\* Corresponding to Bo-Hui Tang, No. 68, Wenchang Road, 121 Street, Wuhua District, Kunming 650093, Yunnan, China. Email: tangbh@kust.edu.cn

**ABSTRACT** - Vegetation water content inversion is an important part of many key biogeochemical cycles. Conventional vegetation moisture monitoring is usually carried out in the visible/near-infrared spectral region band, which is mainly proposed based on the reflection characteristics of leaves. In order to avoid the frequent influence of extreme weather events such as haze, clouds, and rain, passive microwave data are used to retrieve vegetation moisture in this paper. In the first step, the Advanced Integral Equation Model (AIEM) is used to simulate the emissivities of L, C and X bands. It is found that the surface emissivity of bare soil at different frequencies can be characterized by linear functions whose parameters depend on the frequency pairs used. Secondly, based on the radiative transfer model ( $\omega$ - $\tau$  model) and passive microwave vegetation index (MVIs), the water content of vegetation under different vegetation cover conditions is calculated under large-scale observations. In the third step, in order to verify the inversion accuracy of vegetation water content, the normalized vegetation index (NDVI) data obtained from MODIS products are used as indirect comparison because it is difficult to obtain a large range of vegetation water content data. The results shows that the vegetation water retrieved by AMSR-E/AMSR2 has good consistency and correlation with NDVI at the spatial and temporal scales.

**Keywords:** Vegetation water content, Passive microwave, Microwave vegetation indices, AMSR-E/AMSR2, NDVI.

## 1 INTRODUCTION

Vegetation water content (VWC) is a major factor affecting photosynthesis and biomass of green plants, and an indispensable component in many key biogeochemical cycles. VWC is also an important parameter in soil moisture retrieval from active and passive microwave data, because it is directly related to microwave attenuation characteristics of the vegetation.

Remote sensing, as a comprehensive, macroscopic, rapid and real-time observation method, is one of the effective methods to monitor the surface parameters. Microwave remote sensing, as a tool that can penetrate clouds and is less affected by cloud and rain weather and light conditions, is an ideal method to retrieve the vegetation water content of long time series in southwest China where cloud and rain weather are more frequent. Microwave sensors are divided into active and passive. In passive microwave remote sensing, vegetation optical thickness is a key parameter for vegetation observation. In early studies, the linear relationship between vegetation water content and vegetation optical thickness proposed by Jackson et al. (Jackson and Schmugge 1991)(Equation (1)) has been widely accepted.

$$\tau = b \cdot w \quad (1)$$

Where:  $\tau$  represents the optical thickness of vegetation.  $w$  is the water content of vegetation, and the coefficient  $b$  is an empirical constant, which is determined by the observation frequency and vegetation type. Therefore, in passive microwave remote sensing, only the parameters of vegetation optical thickness and parameters are needed to retrieve vegetation water content.

Most of the previous studies on passive microwave inversion of vegetation optical thickness focused on AMSR-E sensor data. AMSR-E (Njoku 1999) officially generated the vegetation optical thickness product based on the brightness temperature data of AMSR-E sensor through iterative algorithm. However, the vegetation optical thickness product is a subsidiary product of soil moisture inversion, which sacrifices the accuracy of vegetation optical thickness product while improving the accuracy of soil moisture product. Therefore, the application of the optical thickness product in large-scale vegetation monitoring is greatly limited. In recent years, Zhao Tianjie et al. (Zhao et al. 2011) used the multi-frequency Microwave Vegetation Indices (MVIs) proposed by Shi Jiancheng et al. (Shi et al. 2008). The optical thickness of vegetation was

retrieved based on AMSR-E multi-frequency brightness temperature data. Since MVIs is not affected by soil signals, the proposed vegetation optical thickness inversion algorithm makes up for the shortcomings of previous works to a large extent.

In this paper, we propose a method of estimating VWC using MVIs, which depends on vegetation structure parameters and considers vegetation coverage. Vegetation water content in Asia is retrieved and its relationship with normalized difference vegetation index (NDVI) is discussed.

## 2 RADIATIVE TRANSFER THEORY

### 2.1 General model

It is necessary to consider the influence of atmospheric emission ( $T_{BP-SKY-U}$ ) and atmospheric attenuation ( $\tau_{ATM}$ ). When simulating the brightness temperature at the top of the atmosphere,

$$T_{BP} = T_{bp} \cdot \exp(-\tau_{ATM} \cdot \cos^{-1} \theta) + T_{BP-SKY-U} \quad (2)$$

Where:  $T_{BP}$  is the brightness temperature at the top of the atmosphere;  $T_{bp}$  is the brightness temperature at the surface of the vegetation that observed immediately above the canopy;  $\tau_{ATM}$  is the atmospheric attenuation factor;  $T_{BP-SKY-U}$  is the upward atmospheric radiation. The simple calculation method of  $\tau_{ATM}$  and  $T_{BP-SKY-U}$  can be found in Pellarin et al. (Pellarin et al. 2006) (Pellarin et al. 2006), as follows:

$$\tau_{ATM(1.4GHz)} = \exp[-3.8687 - 0.2294Z(km) - 0.00386T_{2m}(K)] \quad (3)$$

$$\tau_{ATM(6.6GHz)} = \exp[-4.0166 - 0.2227Z(km) - 0.00286T_{2m}(K) + 0.02330Q_{2m}(g \cdot kg^{-1}) + 0.3020R_{rate}(mm \cdot h^{-1})] \quad (4)$$

$$\tau_{ATM(10.7GHz)} = \exp[-4.1207 - 0.2271Z(km) - 0.00187T_{2m}(K) + 0.04610Q_{2m}(g \cdot kg^{-1}) + 0.5712R_{rate}(mm \cdot h^{-1})] \quad (5)$$

$$T_{BP-SKY-U}(f) = T_{ATMeq} \cdot \exp(-\tau_{ATM(f)} / \cos \theta) \quad (6)$$

Where:  $T_{ATMeq} = \exp[4.8716 + 0.002447T_{2m}(K)]$ ,  $Z(km)$  is the height from pixel to sensor.  $T_{2m}(K)$  is the temperature at 2 meters on the surface,  $Q_{2m}(g \cdot kg^{-1})$  is the surface air humidity ratio, and  $R_{rate}(mm \cdot h^{-1})$  is the rainfall rate. The modeling of vegetation is discussed below.

### 2.2 Vegetation model

The zero-order radiative transport model, also known as  $\omega$ - $\tau$  model, is the zero-order solution of the radiative transport equation of vegetation. It is widely used to simulate the brightness and temperature of the surface under vegetation cover, so as to invert the surface parameters. When vegetation coverage and atmospheric effects are not considered, two vegetation parameters, namely vegetation optical thickness  $\tau$  and vegetation canopy single albedo  $\omega$ , participate in the simulation of surface brightness temperature in the  $\omega$ - $\tau$  model. The  $\omega$ - $\tau$  model has the form:

$$T_{bp}(f) = F_v \cdot \varepsilon_p^s(f) \cdot L_p(f) \cdot T_s + (1 - F_v) \cdot \varepsilon_p^s(f) \cdot T_s + F_v \cdot \varepsilon_p^v(f) \cdot T_v + F_v \cdot (1 - \varepsilon_p^s(f)) \cdot \varepsilon_p^v(f, \theta) \cdot T_v \cdot L_p(f) \quad (7)$$

Where:  $T_{bp}$  represents the surface brightness temperature received by the radiometer under  $P$  polarization (V/H),  $F_v$  represents the vegetation coverage,  $\varepsilon_p^s$  represents the soil emissivity,  $\varepsilon_p^v = (1 - \omega) \cdot (1 - L_p)$  represents the emissivity of the vegetation layer,  $\omega$  represents the single scattering albedo of the vegetation canopy,  $L_p = \exp(-\tau / \cos(\theta))$  represents the vegetation transmittance,  $\tau$  and  $\theta$  represents the vegetation optical thickness and observation Angle, respectively.  $f$  represents the channel frequency.  $T_s$  and  $T_v$  represent soil temperature and vegetation canopy temperature, respectively.

### 2.3 Emissivity characteristics of bare soil at two adjacent frequency angles

Shi et al. (Shi et al. 2008) proposed the microwave vegetation index MVIs based on the setting of AMSR-E sensor (multi-frequency, dual-polarization, 55° observation Angle), which effectively removed the influence of soil information.

$$MVIs = (T_{Bv}(f_2) - T_{Bh}(f_2)) / (T_{Bv}(f_1) - T_{Bh}(f_1)) \quad (8)$$

In order to eliminate the influence of soil emissivity on vegetation information, the relationship between soil emissivity is found. Based on the Advanced Integrated Emission Model (AIEM), the V-polarized Emission and H-polarized surface emissivity of L-band (1.41GHz), C-band (6.925GHz) and X-band (10.65GHz) in microwave band were simulated in this paper. **Table 1** shows the parameter range of simulated emissivity of bare surface.

Table 1  
Parameters and their range used in AIEM simulations

parameter	min	max	Interval	unit
Incidence angle ( $\theta$ )	30	65	5	°
Soil moisture (Ws)	2	44	2	%
Rms height ( $\sigma$ )	0.1	4.5	0.2	cm
Correlation length (l)	2	40	2	cm

Total data:  $8 \times 22 \times 23 \times 20 = 80960$

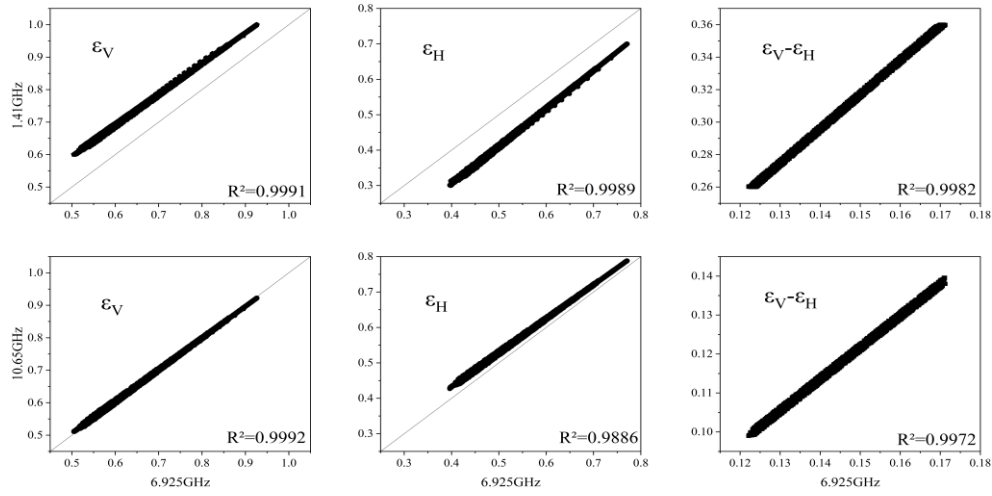


Fig.1. Relationships of AIEM simulated surface emissivity at 55° for the different frequencies.

As shown in Figure 1, the surface emissivity is simulated in the form of C-band (6.925ghz) as the X-axis, L-band (1.41ghz) and X-band (10.65ghz) as the Y-axis, respectively. It is not difficult to see that the surface emissivity between adjacent frequencies or incident angles has a linear relationship:

$$\varepsilon_p^s(f_2) = a(f_1, f_2) + b(f_1, f_2) \cdot \varepsilon_p^s(f_1) \quad (9)$$

Where: parameter is independent of polarization, but only related to the relationship between band frequency and adjacent incident Angle. The relationship between polarization difference ( $\varepsilon_v^s - \varepsilon_h^s$ ) of L-band, C-band and X-band simulated by AIEM model is as follows:

$$\varepsilon_v^s(6.925\text{GHz}) - \varepsilon_h^s(6.925\text{GHz}) = 0.4733 \cdot (\varepsilon_v^s(1.41\text{GHz}) - \varepsilon_h^s(1.41\text{GHz})) \quad (10)$$

$$\varepsilon_v^s(10.65\text{GHz}) - \varepsilon_h^s(10.65\text{GHz}) = 0.8112 \cdot (\varepsilon_v^s(6.925\text{GHz}) - \varepsilon_h^s(6.925\text{GHz})) \quad (11)$$

The root mean square error (RMSE) of the relative error expressed in Formula (7) is 0.44%, and the root mean square error (RMSE) of the relative error

expressed in Formula (8) is 0.10%. The error is small, does not affect the experimental results, can be ignored.

#### 2.4 Retrieval method of vegetation water content

The following assumptions are made in this paper:

- 1) It is assumed that vegetation signals are uniformly distributed and not affected by polarization differences,  $\omega_v = \omega_v$ ,  $\tau_v = \tau_v$ ;
- 2) Suppose that the soil temperature  $T_s$  is approximately equal to the vegetation canopy temperature  $T_v$ ,  $T_v = T_s = T$ ;
- 3) Assume that the single albedo of vegetation canopy  $\omega = 0$  (Zhao et al. 2011).

These assumptions have been widely used in passive microwave remote sensing to retrieve soil moisture and vegetation parameters (Njoku and Chan 2006; Owe et al. 2001; Paloscia et al. 2006; Van de Griend and Wigneron 2004).

By combining the previous two and three methods, the polarization difference ratio of radiometer brightness temperature at various observation frequencies can be stated as the following formula:



$$\frac{T_{Bv}(f_2) - T_{Bh}(f_2)}{T_{Bv}(f_1) - T_{Bh}(f_1)} = \frac{\left[ T_{bv} \cdot \exp(-\tau_{ATM}(f_2) \cdot \cos^{-1} \theta) + T_{BP-SKY-U}(f_2) \right] - \left[ T_{bh} \cdot \exp(-\tau_{ATM}(f_2) \cdot \cos^{-1} \theta) + T_{BP-SKY-U}(f_2) \right]}{\left[ T_{bv} \cdot \exp(-\tau_{ATM}(f_1) \cdot \cos^{-1} \theta) + T_{BP-SKY-U}(f_1) \right] - \left[ T_{bh} \cdot \exp(-\tau_{ATM}(f_1) \cdot \cos^{-1} \theta) + T_{BP-SKY-U}(f_1) \right]} \quad (12)$$

Where:  $T_{BP-SKY-U}(f) = T_{ATMeq} \cdot \exp(-\tau_{ATM}(f) / \cos \theta)$ , the formula can be simplified as:

$$\text{Take factor } \alpha = \frac{\exp(-\tau_{ATM}(f_2) \cdot \cos^{-1} \theta)}{\exp(-\tau_{ATM}(f_1) \cdot \cos^{-1} \theta)} \text{ as}$$

atmospheric influence factor, which represents the influence of atmosphere on microwave radiation transmission, and can be expressed by the following formula:

$$\frac{T_{Bv}(f_2) - T_{Bh}(f_2)}{T_{Bv}(f_1) - T_{Bh}(f_1)} = \alpha \frac{T_{bv}(f_2) - T_{bh}(f_2)}{T_{bv}(f_1) - T_{bh}(f_1)} \quad (13)$$

According to the above assumptions, when considering the surface vegetation coverage  $F_v$ , the vegetation model can be expressed as follows:

$$\frac{T_{Bv}(f_2) - T_{Bh}(f_2)}{T_{Bv}(f_1) - T_{Bh}(f_1)} = \frac{e^{-2\tau(f_2)/\cos \theta} \cdot F_v + 1 - F_v \cdot \varepsilon_v^s(f_2) - \varepsilon_h^s(f_2) \cdot T}{e^{-2\tau(f_1)/\cos \theta} \cdot F_v + 1 - F_v \cdot \varepsilon_v^s(f_1) - \varepsilon_h^s(f_1) \cdot T} \quad (14)$$

Where: let the parameter  $\beta = \frac{\varepsilon_v^s(f_2) - \varepsilon_h^s(f_2)}{\varepsilon_v^s(f_1) - \varepsilon_h^s(f_1)}$ , From equation (11), when  $f_2 = 10.65\text{GHz}$  and  $f_1 = 6.925\text{GHz}$ ,  $\beta = 0.8112$ .

Jackson and Schmugge(Jackson and Schmugge 1991) proposed the following formula for the parameters in equation (1).

$$b = c / \lambda = c \cdot f / 30, (\lambda < 5\text{cm}) \quad (15)$$

Where:  $\lambda$  represents the microwave wavelength. The  $b$  parameter in the formula above lowers as the wavelength increases. Only the type of plant is related to the  $b$  parameters. Equation (20) is applicable to both the C-band and the X-band in this work

The following expression is derived by combining equations (1) and (15):

$$\tau = b \cdot w = c \cdot f \cdot w / 30 \quad (16)$$

The above equations (14) and (16) are combined, and it is known that  $\theta = 55^\circ$ . The parameter  $F_v$  is calculated from the NDVI product of MODIS. Only WVC is an unknown variable. Use the iterative method to solve this function. Finally, the vegetation water content is obtained.

Figure 2 shows that when parameter  $c$  is determined, vegetation water content changes with the change of  $FVC$ . Figure 3 shows that vegetation water content changes with the change of  $c$  when determining parameter  $FVC$ .

As can be seen from Figure 3, this equation will encounter multiple solutions and no solutions when

solving. In view of the above situation, the WVC observed in the previous ten days in this area is used as the initial value for iteration to ensure a unique solution. The initial value is used as the solution value, when there is no solution.

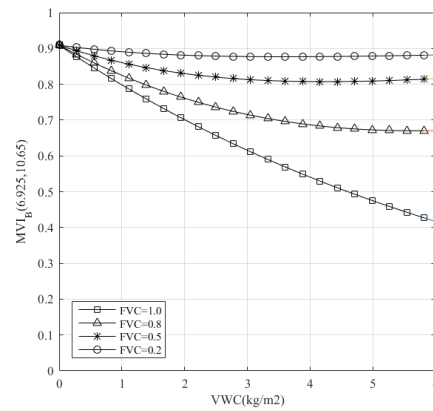


Fig.2. Theoretical relationship between MVI and WVC under different FV

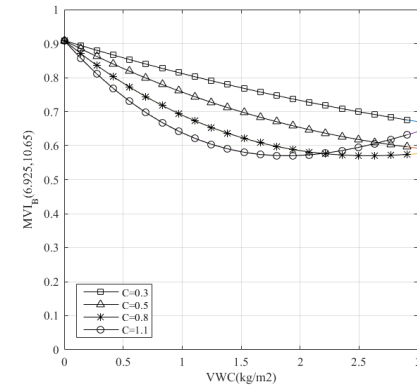


Fig.3. Theoretical relationship between MVI and WVC under different C conditions

### 3 RETRIEVALS OF WVC

#### 3.1 Region

China has a wide range of latitude and longitude. China's territory spans nearly 50 degrees of latitude from north to south. Most of it is in the temperate zone, and a small part is in the tropics. There is no cold zone. It's about the size of Europe. Traversing high, medium and low latitudes from north to south, the complex environment results in a variety of vegetation.



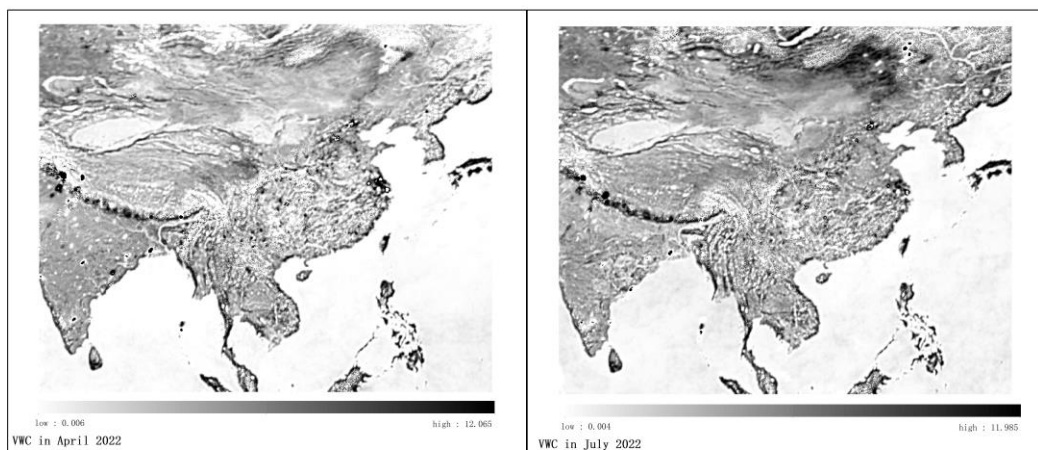


Fig.4 April monthly mean values for VWC in the left, July monthly mean values for VWC in the right .

### 3.2 AMSR-E/AMSR2 data

The Advanced Microwave Scanning Radiometer 2 (AMSR2) is a remote sensing sensor mounted on GCOM-W1, which is used to measure weak microwave radiation on the Earth's surface and atmosphere. AMSR2's antenna rotates every 1.5 seconds to obtain data over 1,450 kilometers long. This cone scanning mechanism enables AMSR2 to acquire a set of daytime and night time data covering more than 99% of the Earth every 2 days.

AMSR-E (2002-2011) and AMSR2 (2012-present) 12.5km and 10.0km gridded standard brightness temperature data have been publicly released by institutions and universities such as JAXA, NSIDC and Bremen University.

In this study, AMSR2 data products acquired in April and July 2022 were used as data sources. The selected bands are C band (6.9GHZ) and X band (10.65GHZ), and the polarization modes are vertical V polarization and horizontal H polarization. The resolution of the data product is 10KM.

### 3.3 Retrieval of vegetation water content

For the Chinese region, April represents the early spring (emergent vegetation) and July represents the summer (vegetation reaching its peak value in many places). The vegetation phenology of this period is quite obvious. So we take the remote sensing images in April and July of 2022 as raw materials for our experiments.

We retrieve the vegetation water content for April and July 2022. (April on the left, July on the right). According to the findings, high VWC values are found in densely forested areas, primarily in the Qinling Mountains and southeast Tibet, while low VWC values are found in desert and sparse grassland

regions. As demonstrated in Fig. 4, the distribution of VWC values increases from west to east and from north to south, which is consistent with China's shifting trend of vegetation distribution between April and July.

## 4 RESULTS AND DISCUSSION

Fig. 5 (April) and Fig. 6 (July) shows the scatter plots of NDVI and the VWC values for the global observations obtained during 2022.

As can be seen, the B-value (y-axis) can have a wide dynamic range for any particular NDVI observation (a given value on the x-axis). This range takes into account the variations in optical and microwave sensitivity for various vegetation characteristics. These variations are mostly brought on by inherent variations in the information collected by microwave and optical sensors, as well as those devices' sensitivity to various vegetational characteristics.

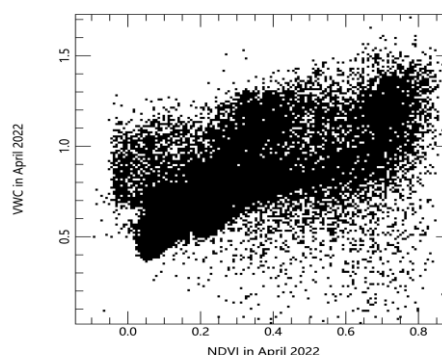


Fig.5 The scatter plots of NDVI and the VWC values in April 2022

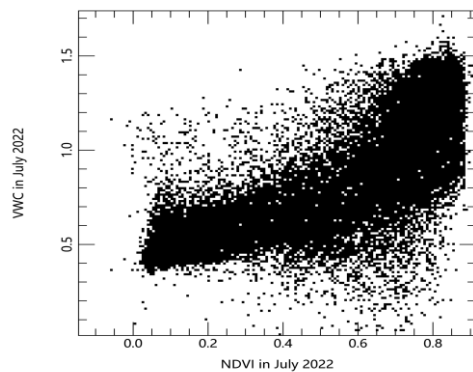


Fig.6 The scatter plots of NDVI and the VWC values in July 2022

## 5 CONCLUSIONS

In this paper, we proposed a method of estimating VWC using MVIs, which depends on vegetation structure parameters and considers vegetation coverage. Vegetation water content in Asia was retrieved and its relationship with NDVI was discussed.

The results showed that the VWC and normalised vegetation index (NDVI) from the AMSR2 inversions were in good agreement and correlated well at the spatial and temporal scales. The NDVI values were smaller or even negative in areas with less vegetation moisture in April at high latitudes, which is mainly caused by snow and vegetation dieback. During the vegetation growing season in July, NDVI values increased significantly, with a corresponding significant increase in vegetation moisture. The seasonal variation in vegetation moisture and NDVI is evident from April to July in the mid-latitudes. At lower latitudes, the range of variation was not significant and both showed high levels.

## REFERENCES:

- Jackson, T.J., & Schmugge, T.J., 1991, Vegetation effects on the microwave emission of soils. *REMOTE SENSING OF ENVIRONMENT*, 36, 203-212
- Njoku, E.G., 1999, *AMSR land surface parameters: Surface soil moisture, land surface temperature, vegetation water content*: Jet Propulsion Laboratory, Pasadena, CA
- Njoku, E.G., & Chan, S.K., 2006, Vegetation and surface roughness effects on AMSR-E land observations. *REMOTE SENSING OF ENVIRONMENT*, 100, 190-199
- Owe, M., de Jeu, R., & Walker, J., 2001, A methodology for surface soil moisture and vegetation optical depth retrieval using the microwave polarization difference index. *IEEE TRANSACTIONS ON GEOSCIENCE AND REMOTE SENSING*, 39, 1643-1654
- Paloscia, S., Macelloni, G., & Santi, E., 2006, Soil Moisture Estimates From AMSR-E Brightness Temperatures by Using a Dual-Frequency Algorithm. *IEEE TRANSACTIONS ON GEOSCIENCE AND REMOTE SENSING*, 44, 3135-3144
- Pellarin, T., Kerr, Y.H., & Wigneron, J., 2006, Global Simulation of Brightness Temperatures at 6.6 and 10.7 GHz Over Land Based on SMMR Data Set Analysis. *IEEE TRANSACTIONS ON GEOSCIENCE AND REMOTE SENSING*, 44, 2492-2505
- Shi, J., Jackson, T., Tao, J., Du, J., Bindlish, R., Lu, L., & Chen, K.S., 2008, Microwave vegetation indices for short vegetation covers from satellite passive microwave sensor AMSR-E. *REMOTE SENSING OF ENVIRONMENT*, 112, 4285-4300
- Van de Griend, A.A., & Wigneron, J., 2004, On the Measurement of Microwave Vegetation Properties: Some Guidelines for a Protocol. *IEEE Transactions on Geoscience and Remote Sensing*, 10, 2277-2289
- Zhao, T.J., Zhang, L.X., Shi, J.C., & Jiang, L.M., 2011, A physically based statistical methodology for surface soil moisture retrieval in the Tibet Plateau using microwave vegetation indices. *J. Geophys. Res.*, D08116

# Identification of tea plantations in plateau areas based on Sentinel-1/2 active and passive remote sensing data

Shanchuan Gao<sup>1</sup> and Bo-Hui Tang<sup>1,\*</sup>

<sup>1</sup> Faculty of Land Resource Engineering, Kunming University of Science and Technology, 650031, Yunnan, China

\* Corresponding to Bo-Hui Tang, No. 68, Wenchang Road, 121 Street, Wuhua District, Kunming 650093, Yunnan, China. Email: [tangbh@kust.edu.cn](mailto:tangbh@kust.edu.cn)

**ABSTRACT-** Efficiently and accurately identifying the spatial distribution of tea plantations is of great significance for ecological and environmental protection in Yunnan province, China. Since the study area is located in the subtropical plateau region of southwest China, the land is fragmented, the vegetation types are complex, and there are much cloudy and rainy weather, making it very difficult to identify tea plantations using only optical remote sensing data. In order to solve these problems, this paper uses Sentinel-1 (S1) Synthetic Aperture Radar (SAR) data and Sentinel-2 (S2) optical data to design 7 classification feature combinations to explore the influence of red edge features, radar features, and texture features on the identification accuracy of tea plantations. The feasibility of Jeffreys-Matusita distance (JM) feature selection and Recursive Feature Elimination (RFE) feature selection algorithm to find the optimal feature combination was verified, and the distribution of tea plantations in the study area was acquired by using the object-oriented random forest algorithm. The research shows that (1) the combination of SAR data and optical data can effectively improve the identification accuracy of tea plantations. (2) S2 red edge features and S1 radar features can significantly improve the accuracy of the identification results of tea plantations. (3) After applying the JM distance and RFE feature selection algorithms, the producer accuracy of tea plantations was improved by 1.39% and 2.38%, and the user accuracy was improved by 1.02% and 1.3%, respectively, compared with the identification of all features. The overall accuracy of the random forest algorithm combined with RFE is 93.43%. The producer accuracy of the tea plantations identification results is 91.07%, and the user accuracy is 89.47%. This study provides an effective approach to identify tea plantations in cloudy and rainy areas in the subtropical plateau of southern China.

**Keywords:** Sentinel-1/2, Tea plantations, Feature selection, Plateau areas, random forest, Jeffries-Matusita distance, Recursive feature elimination.

## 1 INTRODUCTION

Tea is an economically significant crop in global agriculture, China is now the world's largest tea producer (Yang et al. 2015). Tea is part of the Yunnan plateau characteristics of modern agriculture, the local implementation of rural revitalization, promote industrial prosperity with very important. In recent years, the rapid expansion of tea plantations has brought about a decline in the quality of forest resources, reduction of arable land area, loss of biodiversity and ecosystem services in tea growing areas (Xu et al. 2020; Liu et al. 2016). In order to effectively supervise tea plantations, protect the red line of cultivated land, and avert natural disasters, it is crucial for government departments to have quick and accurate access to the distribution range of tea plantations.

Remote sensing is frequently utilized to gather crop information, and there are limited studies on the use of remote sensing images for tea plantation

identification and classification. Tea is an evergreen perennial plant, which makes it challenging to identify tea plantations on remote sensing images (Xu et al. 2018). Currently, the primary solution is to use the spectral contrast between various time periods or the contrast of vegetation index features for extraction (Zhu et al. 2019). However, tea is mainly grown in the tropical subtropical highland region, where there is a higher probability of cloudy and rainy weather. Additionally, there is a problem with the lack of optical remote sensing data, making it difficult to identify tea plantations using only spectral features or vegetation index features (Yusoff et al. 2017). Tea plantations are fragmented and complex, and the identification results often differ greatly from the field. In the research of remote sensing identification and classification, increasing the dimension of feature variables can improve the classification accuracy, but too many feature variables will cause information redundancy and reduce the classification accuracy (Wang et al. 2019). In this paper, to address some

existing problems, Sentinel-1 and Sentinel-2 images were used as data sources, and object-oriented random forest algorithm was used to identify and extract tea plantation areas in Shuangjiang County, Yunnan Province, China. Seven feature combinations were designed to explore the influence degree of red edge features, radar features and texture features on the identification accuracy of tea plantations, to verify the feasibility of Jeffries-Matusita distance and recursive feature elimination feature selection algorithm, and to acquire the distribution of tea plantations in the study area.

## 2 STUDY AREA AND DATA

### 2.1 Study Area

Lahu-Va-Blang-Dai Autonomous County of Shuangjiang, Lincang City, Yunnan Province is located in Yunnan-Guizhou Plateau of China with geographic coordinates of 99°35'15"E – 100°90'33"E and 23°11'58"N – 23°48'50"N. The climate of Shuangjiang County is subtropical monsoon climate, with an average annual temperature of 20.2°C, an average annual rainfall of 1000~1200 mm, and an annual sunshine time of 2222 hours. The natural conditions of the study area are very suitable for the development of tea planting, and it was selected into the "China's Top 100 Tea Counties List" in 2020. The study area is a typical plateau agricultural area with highland mountainous terrain, complex crop cultivation structure and finely divided plots.

### 2.2 Data

The Sentinel-1 (S1) and Sentinel-2 (S2) data used in this study were downloaded from Copernicus Open Access Hub (<https://scihub.copernicus.eu/>). A total of six Sentinel-1A interferometric wide-field imaging mode (IW) GRD images were selected from March to August 2021, with dual polarization of VV and VH. The Sentinel-2B Level-2A four cloud-free images covering the study area on February 23, 2021 was selected. The SNAP software was used for pre-processing. The processed S1 and S2 data were resampling to 10m resolution, UTM 47N was selected as the projection coordinate system, and the S1 and S2 data were registered, clipped, stacked and extracted features in ENVI. The data list of this study is shown in Table 1.

Table 1. Remote sensing data and sensing times

Platform	Sensing data
Sentinel-2	2021-02-23
Sentinel-1	2021-03-11, 2021-04-16,
	2021-05-22, 2021-06-15,
	2021-07-09, 2021-08-14

The training and validation samples were selected based on the surface coverage classification data and Google high-resolution images as the basis for classification and accuracy verification. The land cover data was adopted from Global 30-m land-cover dynamic monitoring products with fine classification system released by Aerospace Information Research Institute, Chinese Academy of Sciences, and the data was acquired from the Big Earth Data Science Engineering Program website (<http://data.casearth.cn/>). Google high-resolution images were acquired from Google Earth, and the sensing time is February 2021.

## 3 METHODS

This study aimed to acquire the distribution of tea plantations in the study area. The study methods included the construction of the feature combination, classification algorithm, feature selection algorithm, sample selection and accuracy evaluation. The flowchart for the tea plantation identification method of this study is shown in Fig1.

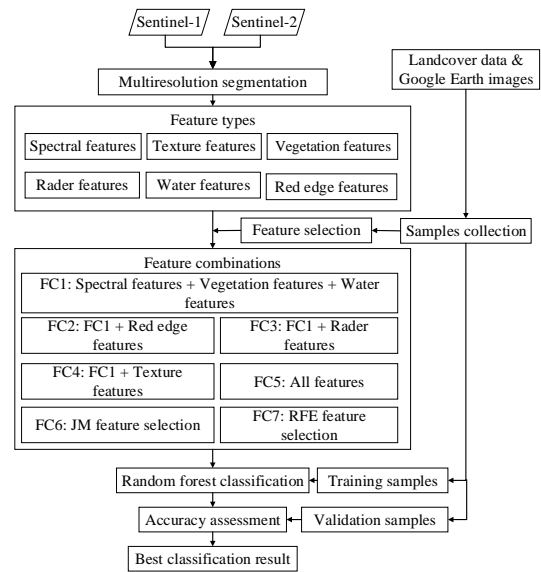


Fig.1 Flowchart for the tea plantation identification method.

### 3.1 Feature Combination

We acquired 53 feature variables from the processed S1 and S2 data, including spectral features, vegetation features, water features, red-edge features, texture features, and radar features.

The spectral features include B1-B4, B8-B12 of S2. The vegetation features include: normalized difference vegetation index, enhanced vegetation

index, modified soil adjusted vegetation Index, green normalized difference vegetation index (Frampton et al. 2013). Water features include: modified normalized difference water index, normalized difference water index (Zhang et al. 2021). Red-edge features include: B5-B7 of S2, normalized difference vegetation index red-edge 1, normalized difference vegetation index red-edge 2, normalized difference vegetation index red-edge 3, MERIS terrestrial chlorophyll index, chlorophyll index red-edge, modified simple ratio red-edge, red-edge position index (Fernandez-Manso et al. 2016; Frampton et al. 2013). B5, B6, and B7 of S2 are added to the red-edge features in order to examine the effect of red-edge features on classification accuracy. For texture features, we calculated the gray-level co-occurrence matrix (Qu et al. 2022) of the S1 and S2 image with a  $3 \times 3$  filtering window to acquire 16 texture features. The radar features consist of the VV and VH polarizations in six images of S1, for a total of 12 features. Seven feature combinations were designed to identify and compare the identification results, including FC1: Spectral features + Vegetation features + Water features; FC2: FC1 + Red edge features; FC3: FC1 + Radar features; FC4: FC1 + Texture features; FC5: All features; FC6: JM feature selection; FC7: RFE feature selection.

### 3.2 Classification Algorithm

The random forest algorithm is a machine learning algorithm based on CART decision trees (Breiman, 2001). When the RF algorithm classifies, a randomly drawn sample from the sample set with put-back builds a decision tree constituting a random forest, and the classification result of the object to be classified is decided by multiple decision trees voting. The object-oriented classification method requires segmentation of images before classification. A multiresolution segmentation algorithm (Baatz et al, 2000) is used to segment the image in eCognition 9.0 software, with a segmentation scale of 60.

In a process of RF classification, two basic parameters are required to generate a prediction model (Gao et al. 2015), the number of trees in a forest (*ntree*) and the number of prediction variables for use at each split to grow a decision tree (*mtry*). The random forest model was established and optimized based on the python open source toolkit scikit-learn. In this paper, *mtry* selects the default value, the square root of the number of features. 5-Fold cross-validation was used to evaluate the best parameters to improve the efficiency of the RF classifier when constructing the RF algorithm. We verified 7 feature combinations of features separately and averaged the results acquired, and finally acquired the most appropriate *ntree* value of 73.

### 3.3 Feature Selection Algorithm

In random forest classification, adding features can improve the classification accuracy, but too many features added can cause information redundancy to reduce the classification accuracy, so it is important to control the number of features to reduce information redundancy. In this study, we use J-M distance and recursive feature elimination algorithm for feature selection.

#### 1) Jeffries-Matusita Distance

The Jeffries-Matusita (JM) distance is used to statistics separability criterion, and determine the best feature combination based on the results (Cheng et al, 2022). The definition of the JM distance is as follows:

$$JM = 2(1 - e^{-B}) \quad (1)$$

In the formula,  $B$  represents the Bavian distance between two categories on a feature. The definition of the Bavian distance is as follows:

$$B = \frac{1}{8}(e_1 - e_2)^2 \frac{2}{\delta_1^2 + \delta_2^2} + \frac{1}{2} \ln \left[ \frac{\delta_1^2 + \delta_2^2}{2\delta_1 \cdot \delta_2} \right] \quad (2)$$

In the formula,  $e_1$  and  $e_2$  represents the feature value mean of the two categories,  $\delta_1$  and  $\delta_2$  represent the feature value standard deviation of the two categories. The main purpose of this paper is to identify tea plantations, so only the JM distances between tea plantations and other land cover types are calculated.

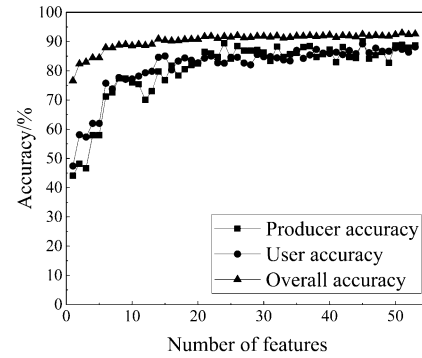


Fig.2 Variation of accuracy with increasing features (JM distance).

According to formula (1) and (2) to calculate the JM distance of all features, according to the JM distance value of the features in decreasing order into the RF classification model for the identification of tea plantations, to observe the changes in user accuracy and producer accuracy of tea plantations (Fig2). The accuracy reached the highest when the number of features is 45, after which the accuracy will not exceed this value as the number of features continues to increase. Therefore, the 45 features with higher JM distance were added to FC6.

## 2) Recursive Feature Elimination

The Recursive Feature Elimination (RFE) is trained on the initial feature space in the classification algorithm model, evaluates the importance of the features involved in the training, repeatedly builds the model to exclude the least important features until the optimal feature space is filtered (Qu et al. 2022). In random forest classification, the Gini coefficient can usually be used to evaluate feature importance. The average change in the node-splitting Gini index of the corresponding feature in each tree is used as a scoring indicator (Raschka, 2015).

In this study, the Gini coefficient is used to evaluate the importance of feature variables, and the definition of the Gini coefficient is as follows:

$$Gini = 1 - \sum_c p^2(C / N) \quad (3)$$

where  $C$  is the number of classes,  $N$  is the number of trees, and  $p$  represents the probability of belonging to  $C$ .

FC7 was determined with RFE, and the prediction accuracy of the classifier is evaluated using 5-fold cross-validation, as shown in the Fig.3, when the number of features equals to 40, the prediction accuracy of the classifier reaches the highest, and then decreases as the number of features continues to increase. Therefore, after the RFE feature selection algorithm, a feature combination with 40 features is acquired.

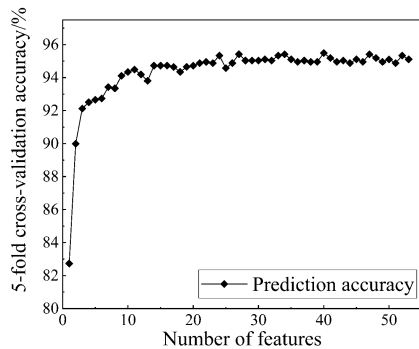


Fig.3 Variation of accuracy with increasing features (RFE).

## 3.4 Sample Selection and Accuracy Evaluation

In the study area, samples were selected for classification and validation by combining surface coverage fine classification data, Google high-resolution images and Sentinel-2 images. The study area was classified five land cover types: build-up land, forest, tea plantations, cropland, and water body. We randomly selected a total of 1309 segmentation objects as training samples based on the distribution of land cover types in the study area, with 158223 pixels

for the tea plantation. The validation samples were generated using ArcGIS 10.8 to generate 3500 random points in the study area and visually interpreted to assign feature attributes, of which 504 points were validated for the tea plantation. We use confusion matrix to verify the classification accuracy, and the evaluation indexes were overall accuracy (OA), kappa index of agreement (KIA), producer accuracy (PA) and user accuracy (UA).

## 4 RESULTS

### 4.1 Comparison and Analysis

The classification accuracies of the seven feature combinations are shown in Table 2. It can be seen that a good classification results can be acquired by just constructing a features combination of spectral features, vegetation features, water features, but it cannot effectively identify tea plantations. The results of FC1-FC4 showed that: the addition of red-edge features and radar features improved the PA and UA of tea plantation identification by 13.69%, 5.25% and 11.9%, 2.14%, respectively, compared with FC1; the feature combination constructed from spectral features, vegetation features, water features, and red-edge features can greatly improve the identification ability of tea plantations; the combination of radar data and optical data can effectively improve the identification accuracy of tea plantations, and to a certain extent overcome the shortcomings of insufficient optical images in cloudy and rainy areas, and the accuracy of identifying tea plantations is better than using optical data only; affected by the inconspicuous texture due to the over-planting of tea trees in the study area, the texture features have a negative impact on the identification accuracy of tea plantations.

Both feature selection algorithms can significantly improve the classification accuracy. The PA and UA of tea plantation identification after feature selection based on JM distance were 90.08% and 89.19%, respectively; the PA and UA of tea plantation identification after feature selection based on RFE algorithm were 91.07% and 89.47%, respectively. In contrast, the PA and UA of tea plantation identification with all 53 feature bands included in FC5 was 88.69% and 88.17%. The identification accuracy of the feature combination after the RFE selection was higher, and the information redundancy problem generated by too many features was effectively avoided. Therefore, RFE algorithm is a more appropriate feature selection algorithm for tea plantation identification. The classification results of FC7 were used as the final result of this study.



Table 2 Comparison of the accuracy assessment of seven feature combinations

Combinations	OA/%	KIA		Build-up	Tea plantation	Cropland	Forest	Water body
FC1	88.03	0.8	PA/%	89.05	72.62	87.97	91.54	98.75
			UA/%	89.16	75.31	82.78	92.81	100.00
FC2	90.86	0.85	PA/%	89.53	86.31	89.47	92.22	100.00
			UA/%	90.59	80.56	86.44	95.18	100.00
FC3	89.94	0.83	PA/%	88.37	84.52	88.97	91.44	97.50
			UA/%	95.00	77.45	83.24	95.82	100.00
FC4	88.66	0.81	PA/%	93.02	63.10	90.48	93.70	98.75
			UA/%	91.95	81.33	83.08	91.80	100.00
FC5	92.6	0.88	PA/%	97.67	88.69	90.73	93.80	100.00
			UA/%	96.55	88.17	86.81	95.68	100.00
FC6	92.49	0.87	PA/%	96.51	90.08	90.10	93.55	100.00
			UA/%	94.32	89.19	85.60	95.86	100.00
FC7	93.43	0.89	PA/%	95.35	91.07	91.48	94.44	100.00
			UA/%	97.62	89.47	87.53	96.48	100.00

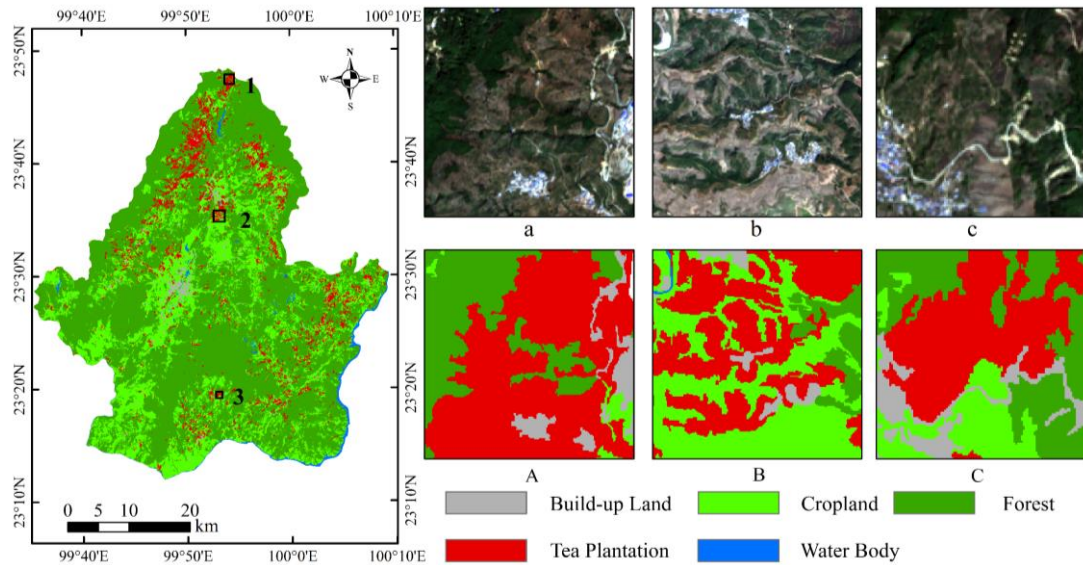


Fig.4 The spatial distribution map and details of enlarged areas of land cover in this study area. (a, b, c) are the S2 image enlargements of the three regions marked as 1, 2, 3 in this map, respectively. (A, B, C) are the corresponding tea plantation identification results.

#### 4.3 Tea Plantation Identification Results

Fig.4 shows the classification results of this study, and the identification results of tea plantations are randomly selected for detailed display. It can be seen that after multiresolution segmentation, a satisfactory segmentation result is achieved for forest, cropland and tea plantation, merging similar small areas and having clear boundaries with other vegetation types.

Most of the tea plantation identification results basically match with the actual situation, and these results show that the feature combination after feature selection of RFE algorithm is effective in the classification of complex vegetation types in the southwest plateau region of China. This study provides a reference for remote sensing tea plantation identification in cloudy and rainy areas of southwest plateau of China.

## 5 DISCUSSION

In this study, we used S1 SAR images and S2 optical images to identify the tea plantations. The addition of SAR images made up for the shortcomings of optical images, complemented the image information, and improved the classification accuracy. Red-edge features had an excellent effect on the identification accuracy of tea plantations. Using the object-oriented classification method, the images were segmented before classification. It effectively avoided the phenomenon of fragmentation of land cover type's boundaries and made the boundaries between land cover types clear and more consistent with the real surface conditions. Compared to JM distance, RFE was more suitable for feature selection in tea plantation identification. In the subsequent research, image data with higher spatial resolution will be used to reduce the negative impact of texture features on tea plantation identification.

## REFERENCES

- Yang, X., Yu, Z., Zhang, B., Huang, J., Zhang, Y., Fang, F., Li, C., Zhu, H., & Chen, Y., 2015, Effect of fluoride on the biosynthesis of catechins in tea [*Camellia sinensis* (L.) O. Kuntze] leaves. *Scientia Horticulturae*, 84, 78-84.
- Xu, W., Huang, S., Wu, C., Xiong, Y., Wang, L., Lu, N., & Kou, W., 2020, The Pruning Phenological Phase-based Method for Extracting Tea Plantations by Field Hyperspectral Data and Landsat Time Series Imagery. *Geocarto International*, 37, 1-18.
- Liu, Y., Feng, Y., Zhao, Z., Zhang, Q., & Su, S., 2016, Socioeconomic drivers of forest loss and fragmentation: A comparison between different land use planning schemes and policy implications. *Land Use Policy*, 54, 58-68.
- Xu, W., Qin, Y., Xiao, X., Di, G., Doughty, R.B., Zhou, Y., Zou, Z., Kong, L., Niu, Q., & Kou, W., 2018, Quantifying spatial-temporal changes of tea plantations in complex landscapes through integrative analyses of optical and microwave imagery. *International Journal of Applied Earth Observation and Geoinformation*, 73, 697-711.
- Zhu, J., Pan, Z., Wang, H., Huang, P., Sun, J., Qin, F., & Liu, Z., 2019, An Improved Multi-temporal and Multi-feature Tea Plantation Identification Method Using Sentinel-2 Imagery. *Sensors*, 19, 2087.
- Yusoff, N.M., Muharam, F.M., Takeuchi, W., Darmawan, S., & Razak, M.H.A., 2017, Phenology and classification of abandoned agricultural land based on ALOS-1 and 2 PALSAR multi-temporal measurements. *International Journal of Digital Earth*, 10, 155-174.
- Wang, B., Li, J., Jin, X., & Xiao, H., 2019, Mapping Tea Plantations from Multi-seasonal Landsat-8 OLI Imageries Using a Random Forest Classifier. *Journal of the Indian Society of Remote Sensing*, 47, 1315-1329.
- Baatz, M., & Schape, A., 2000, Multiresolution segmentation: an optimization approach for high quality multi-scale image segmentation. *Angewandte Geographische Information Sverarbeitung*, 12, 12-23.
- Frampton, W.J., Dash, J., Watmough, G., & Milton, E.J., 2013, Evaluating the capabilities of Sentinel-2 for quantitative estimation of biophysical variables in vegetation. *ISPRS Journal of Photogrammetry and Remote Sensing*, 82, 83-92.
- Zhang, J., Zhou, J., Zhang, G., Ji, Y., Zeng, Y., Fan, W., & Aikelamu, A., 2021, Climate- and human-driven variations in lake area and number in North Xinjiang, China. *International Journal of Remote Sensing*, 42, 469-485.
- Fernandez-Manso, A., Fernandez-Manso, O., Quintano, C., 2016, SENTINEL-2A red-edge spectral indices suitability for discriminating burn severity. *International Journal of Applied Earth Observation and Geoinformation*, 50, 170-175.
- Breiman, L., 2001, Random forests. *Machine Learning*, 45, 5-32.
- Gao, T., Zhu, J., Zheng, X., Shang, G., Huang, L., & Wu, S., 2015, Mapping Spatial Distribution of Larch Plantations from Multi-Seasonal Landsat-8 OLI Imagery and Multi-Scale Textures Using Random Forests. *Remote Sensing*, 7, 1702-1720.
- Cheng, L., Li, Y., Zhang, X., & Xie, M., 2022, An Analysis of the Optimal Features for Sentinel-1 Oil Spill Datasets Based on an Improved J-M/K-Means Algorithm. *Remote Sensing*, 14, 4290.
- Qu, X., Shi, D., Gu, X., Sun, Q., Hu, X., Yang, X., & Pan, Y., 2022, Monitoring Lodging Extents of Maize Crop Using Multitemporal GF-1 Images. *IEEE Journal of Selected Topics in Applied Earth Observations and Remote Sensing*, 15, 3800-3814.
- Raschka, S., 2015, *Python Machine Learning*. Birmingham: Packt Publishing.

## The use of temporal sample migration to explore crop type from remotely sensed data

Shibo Zhang<sup>1</sup>, Jingya Yang<sup>1</sup>, Jing Sun<sup>1</sup>, Qiong Hu<sup>2\*</sup>, Pei leng<sup>1</sup>, Miao Lu<sup>1</sup>, Yuman Ma<sup>1</sup>, Hongyang Wang<sup>1</sup>, Wenbin Wu, Qian Song<sup>1\*</sup>

<sup>1</sup>Key Laboratory of Agricultural Remote Sensing, Ministry of Agriculture and Rural Affairs/Institute of Agricultural Resources and Regional Planning, Chinese Academy of Agricultural Sciences, Beijing 100081, China

<sup>2</sup>Key Laboratory for Geographical Process Analysis & Simulation of Hubei Province/School of Urban and Environmental Sciences, Central China Normal University, Wuhan 430079, China

Correspondence: songqian01@caas.cn; huqiong@mail.ccnu.edu.cn

**ABSTRACT-** Accurate and timely crop mapping is crucial for various agricultural production and monitoring. Current supervised classification methods based on remote sensing heavily rely on ground-truth samples collected at high cost, and the years without sampling highly limits the classification work. To address such challenge, we proposed a time-migration method based on historical all-season training samples (2017, 2018, 2020) to conduct supervised crop classification mapping in the target year (2021) without ground-truth samples. We chose Hailun City, Heilongjiang Province of northeastern China as study site, whose major crop production include corn, soybeans, and rice. We reconstructed the time-series Sentinel-2 data, and selected the optimal spectro-temporal features based on the Gini coefficient to construct standard crop phenological curves. We calculated the similarity between the reference spectral and image spectral and designed the rules for tag matching by dynamic time warping algorithm and designed the rules for the label matching to detect and identify the change state of training sample pixels. We obtained the crop types of historical samples in the target year by this method. The results showed that the migration accuracy of the samples can reach 90%, used these samples as training data for the random forest to classify the target year, the overall accuracy can reach 93%. We proposed a new sample time migration method in this study, which can achieve efficient and mass migration of historical samples, which greatly reduced the cost in ground-truth sampling work. (Smith, 1987)

### 1. INTRODUCTION

Crop spatial distribution information is an important basis of crop growth monitoring, yield estimation and disaster assessment, as well as a significant support for the optimization and adjustment of regional crop cultivation structure and the government's macro decision making. Recently, remote sensing technology has become the main technical method for crop spatial distribution mapping. Currently, supervised classification strategies are mainly crop classification methods, which means that model training must use sample data. The ground samples are important inputs of the spectral and temporal characteristics in different bands of remote sensing images, their quality, quantity and spatial distribution directly affect the classification result (Maxwell A E, 2019). However, those ground samples only apply train classifier in the mapping year. In previous agricultural mapping studies, very few classifiers could be applied to multiple years without year-to-year retraining and so the frequency of crop mapping was limited by reference data availability.

Therefore, when cropland maps are needed, we need to recollect ground samples, which will cost considerable cost in time and labor resources. How to improve the efficiency of using historical samples to achieve sustainable classification tasks for other seasons without ground-truth samples is a hot topic of current research.

There were many scholars has explored that using historical all-season training samples to conduct supervised crop classification mapping in the target year without ground-truth samples. Hao used immune neural network (ABNET) to construct the crop reference NDVI time series, and used ABNET to achieve the target year crop classification of Bole and Manas in Xinjiang, and the overall classification accuracy reached 87.13% and 83.48% (Hao, 2016). Zhang used the random forest classifier to classify historical years with ground-truth samples, and extracted the pixels with the same in all historical years as potential samples. The result showed that the average classification accuracy was about 80% (Zhang, 2019). Friesz used over 11 million samples to train a

classification tree algorithm and develop a crop classification model (CCM). The CCM performed well against a withheld test data set with a model prediction accuracy of over 90% (Friesz,2017). However, there are still some problems, on the one hand, the crop sowing time has changed between years due to climate and the crop weather curve has shifted, on the other hand, in some areas with frequent crop rotation are limited.

The objective of this study was to present a robust automated classification approach to map soybean and corn repeatedly, consistently and efficiently at low cost. We used phenological metrics in crop classification for cross-year classifier extension, which applies a universal set of rules to multiple years.

## 2 STUDY AREA AND DATA

### 2.1 Study area

Our study area is Hailun, where is located in the Songnen Plain (46°58′~47°52′N, 126°14′~127°45′E) in the north-central part of Heilongjiang Province, with an area of 4667 km<sup>2</sup> and 31.67 hm<sup>2</sup> of arable land. The crop cultivation structure of Hailun is relatively stable, with the main production of soybean, corn and rice. According to the statistics in 2020, the sown area of the three crops accounted for 97.8% of the total grain sown area, and the planting area of other crops was very small, so this crop distribution in Hailun city is very similar to the planting structure of Heilongjiang province. Due to temperature conditions, crops in the study area are usually grown one season per year. Rice is mostly cultivated in the main season between the spring and summer, approximately from April to October. Corn is mainly sown in the first half of May and harvested in the first half of October. Soybeans and corn are harvested at the same time, but soybeans are planted about ten days later than corn. The rotation between soybean and corn is very common in the croplands. Other crops include wheat, peanut ,vegetables, and so forth. Rice, soybean and corn comprise over 95% of the total area of annual crops.

### 2.2 Data and processing

#### 2.2.1 Satellite images

To further reduce cloud pollution, we screened the images for cloudiness <30% on the GEE platform and chose a time interval from late April to late October each year, covering the entire growing period of major crops. In order to eliminate noise and obtain images at equal time intervals, we used the traditional 10-day maximum synthesis method to ensure that the different stages of the crop growth period are covered with corresponding images.

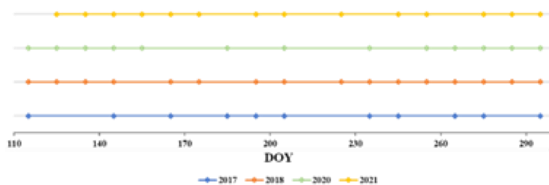


Figure1 S2-A/B Data distribution

#### 2.2.2 Ground reference data

In order to obtain the main types of crop mapping in the study area, a ground-based field survey was conducted in 2017, 2018, 2020, 2021. We measured by handheld Global Positioning System(GPS) and recorded the crop type by taking pictures with our smartphones. In addition, we also selected some non-arable samples on Google Earth to facilitate the work of our classifier, such as water bodies, buildings, woodland and roads. Our main purpose is to focus on cultivated land samples, and these non-cultivated land samples are only used as auxiliary data to make our classification results more consistent with the real situation.

The survey contains mainly rice, corn, soybean and other crops. Since this study focuses on the mapping of main crops in Hailun, various other crop types were merged into a class called “other”.

Rice, corn and soybeans are the main crops, and other crops contain small crops such as wheat and peanuts. The largest number of samples collected in 2018 reached 647, and the smallest was 490 samples in 2020.

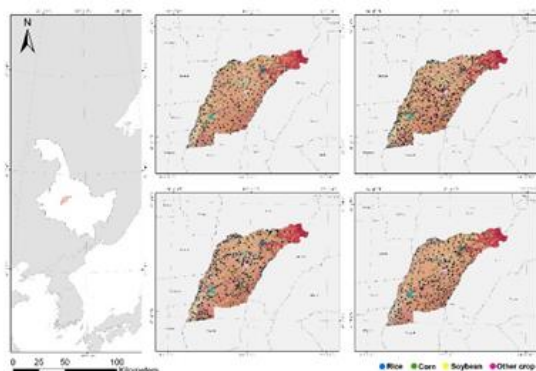


Figure 2 Study area and sample distribution

## 3 METHODS

A viable approach is to distinguish crop types based on seasonal characteristics of crop growth indicated by satellite-based vegetation indices (Dong,2020). Among the many ways to deal with time series data, there is increasing evidence that the classic DTW measure is the best measure in most domains. DTW is a measure of

the similarity of two time series of different lengths, using dynamic programming techniques to find the minimum distance between two time series, where the series are distorted by stretching or shrinking the time dimension. Annual changes of phenological cycles caused by weather or by variations in the agricultural practices. DTW proved to be an efficient solution to handle this challenge (Sakoe,1978).

We first constructed multiple feature curves and extracted the standard curves of major crops as the reference curves respectively, and then extracted the curve of that sample in the target year as the target curve.

The distance between the two was calculated by DTW for label matching, and the smaller the distance is, the greater the similarity between the two curves.

Unlike the conventional setting of threshold classification, we focused on considering relative values when performing matching, so that we can ensure that enough samples have labels, and also set up a voting mechanism to ensure the correct rate of sample migration. Due to the small and diverse area of other crops, it was too difficult to extract the standard curve of this category, and we set the threshold and extracted it based on its maximum cumulative distance and low consistency with the curves of rice, corn, and soybean

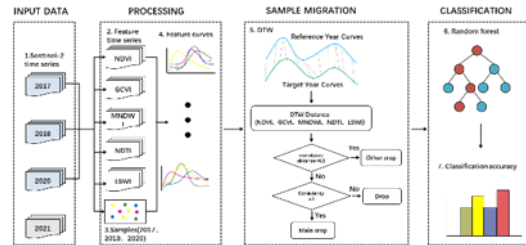


Figure 3 Sample migration and classification process

## 4 RESULT

### 4.1 Classifier Comparison

We have selected random forests and support vector machines among the commonly used machine learning models for comparison. We conducted a comparison experiment for each year separately to test which model performed better and then used it as our subsequent choice. In the experiment, 70% of the samples were used as the training set and 30% as the validation set, and the overall accuracy and kappa were used to evaluate the classification results.

The results showed that random forest accuracy was the highest and stable, with OA above 98%. SVM has poor classification accuracy, especially in 2020, which was only 66.4%. (Table 1)

Table 1 Accuracy of SVM and RF classification for different years

Year	SVM		RF	
	OA	Kappa	OA	Kappa
2017	83.78%	0.80	99.72%	0.99
2018	80.71%	0.75	99.21%	0.99
2020	66.4%	0.56	98.13%	0.98

### 4.2 Comparison of single year curves and multi-year convergence curves

The extracted crop phenology curves for each year were used as reference curves respectively, and the curves extracted from the real samples in 2021 were used as target curves, and the real labels to verify the accuracy of our method. We examined the migration accuracy of various crops by F1-Score. It was verified that the single-year curves had the best migration accuracy of the questions in 2017 and the worst in 2020.

Different types of crops have different levels of recognition difficulty. Rice has the highest recognition accuracy, with scores above all 0.91, and the highest was 2020 (0.98). The recognition accuracy of other crops was generally lower, all between 0.65-0.8. The identification accuracy of corn and soybean was relatively close, but the 2020 curve did not perform well in distinguishing between the two, while the accuracy was more stable in all other years above 0.9.

The migration accuracy of the fused multi-year curves obtained by linear interpolation was generally higher than that of the single-year curves. The accuracy was above 0.95 for rice, corn and soybean recognition, and can reach 0.72 for other crops. The fused curves take into account more physical information and are better matched with the target curves after linear interpolation.

### 4.3 Classifier classification

Our method has been tested with good results. Next, we migrated all our existing samples to the target year (2021) for classification. Due to cloud pollution, we were not able to migrate all the samples completely, but these samples were sufficient to support our next classification task. The entire real sample of 2021 will be used to verify our classification accuracy. We also designed the effect of the combination of single-year and multi-year sample approaches on classification accuracy.

In the single-year comparison, the 2018 migrated samples had the highest classification accuracy (87.32%) and also the highest number of samples migrated. The accuracy is obviously higher when we input all the migrated samples into the classifier, which we can achieve an accuracy of 91.56%.



Table 2 Classification results of sample migration in different years

Sample Source	Number of valid samples	OA	Kappa
2017	166	86.55	0.83
2018	216	92.61	0.91
2020	186	68.47	0.65
2017、2018、2020	568	91.13	0.90

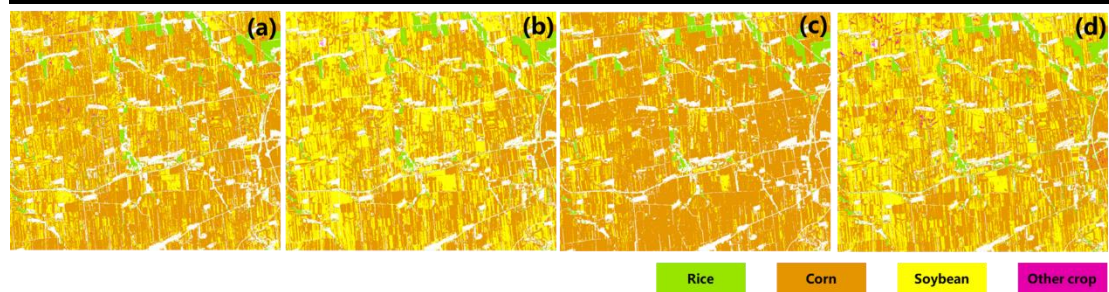


Figure 4 Classification accuracy of random forest for samples of different years (2017,a), (2018,b), (2020,c), (2017、2018、2020,d)

## 7 References

- Maxwell A E, Warner T A, Fang F. Implementation of machine-learning classification in remote sensing: An applied review[J]. International Journal of Remote Sensing, 2018, 39(9): 2784-2817.
- Hao P, Wang L, Zhan Y, et al. Using moderate-resolution temporal NDVI profiles for high-resolution crop mapping in years of absent ground reference data: a case study of bole and manas counties in Xinjiang, China[J]. ISPRS International Journal of Geo-Information, 2016, 5(5): 67.
- Zhang L, Liu Z, Liu D, et al. Crop mapping based on historical samples and new training samples generation in Heilongjiang Province, China[J]. Sustainability, 2019, 11(18): 5052.
- Friesz A M, Wylie B K, Howard D M. Temporal expansion of annual crop classification layers for the CONUS using the C5 decision tree classifier[J]. Remote Sensing Letters, 2017, 8(4): 389-398
- Dong, J., Liu, W., Han, W., Xiang, K., Lei, T., & Yuan, W. (2020). A phenology-based method for identifying the planting fraction of winter wheat using moderate-resolution satellite data. International Journal of Remote Sensing, 41(18), 6892-6913.
- Sakoe, Hiroaki, and Seibi Chiba. "Dynamic programming algorithm optimization for spoken word recognition." IEEE transactions on acoustics, speech, and signal processing 26.1 (1978): 43-49.



# Estimation of gross primary productivity of Xishuangbanna tropical seasonal rainforest based on VPM correction model

Siqi Feng<sup>1</sup> and Bo-Hui Tang<sup>1\*</sup>

<sup>1</sup> Faculty of Land Resource Engineering, Kunming University of Science and Technology, 650031, Yunnan, China

\* Corresponding to Bo-Hui Tang, No. 68, Wenchang Road, 121 Street, Wuhua District, Kunming 650093, Yunnan, China. Email: tangbh@kust.edu.cn

**ABSTRACT**—Vegetation photosynthesis model (VPM) is a widely used model for calculating Gross Primary Productivity (GPP). Many studies have shown that it has a good effect in calculating GPP for most Vegetation types. However, the estimation accuracy of the VPM model is not high for regions with long cloudy weather, such as Xishuangbanna tropical seasonal rainforest. This paper develops a VPM model for estimating GPP under cloudy conditions, which mainly corrects the two parameters,  $W_{\text{scalar}}$  and EVI, which are greatly affected by clouds in the model. First, the water stress factor  $W_{\text{scalar}}$  is replaced by Evaporation Fraction (EF). Secondly, using the good correlation between near surface temperature and EVI, the conversion coefficient between near surface temperature and EVI is fitted to achieve the effective reconstruction of EVI polluted by clouds. The correction of the two factors improves the estimation accuracy of the VPM model, and the comparison with GPP 4-year site observations shows that the correction of EVI have a better improvement, with an increase of 0.22 in  $R^2$  compared with the pre-correction, and the correction of  $W_{\text{scalar}}$  is increased by 0.11 in  $R^2$ . In order to verify the proposed method, the in-situ observation data of the Xishuangbanna flux site from 2007 to 2010 are used. The results show that the proposed method effectively improves the accuracy of GPP estimated by the VPM model, especially in 2007, when the sky is heavily contaminated by clouds, and the improvement is significant, with  $R^2$  increases from 0.2 to 0.82. In general, the accuracy of GPP estimated by the proposed method has been significantly improved, with RMSE ( $\text{gC}\cdot\text{m}^{-2}\cdot\text{d}^{-1}$ ) decreases from 15, 14.4, 18.1, 14.2 to 8.07, 6.56, 10.33, 11.44, respectively. Therefore, the proposed method can be used to estimate GPP of tropical seasonal rainforest in Xishuangbanna.

**Keywords:** Gross primary productivity, Tropical seasonal rainforest, Vegetation photosynthesis model, Eddy covariance.

## 1 INTRODUCTION

The gross primary productivity (GPP) of terrestrial ecosystems is a key parameter to quantitatively characterize carbon sink/carbon source. It represents the productivity of a specific region or ecosystem, and also reflects the growth characteristics and health status of regional vegetation or ecosystem. Therefore, accurate estimation of GPP is of great significance for providing data basis for carbon balance study of a region or ecosystem. Tropical rainforests account for 12% of the terrestrial ecosystem carbon cycle (Lieth and Whittaker, 1975; Malhi et al., 1998) is an important part that cannot be ignored, and its species quantity and biological productivity are more abundant than other ecosystems. Therefore, accurate GPP inversion can provide a data basis for the study of the carbon budget of the tropical seasonal rainforest ecosystem, which is of great significance.

At present, all models have poor estimation performance in tropical rainforests (Lin et al., 2018), the estimated GPP correlation  $R^2$  of savannas, shrubs,

and evergreen broad-leaved forests distributed in tropical areas are generally lower than 0.3, and RMSE is about  $3\text{gC}/\text{m}^2/\text{d}$  (Huete et al., 2008; Ma et al., 2014; Sjöström et al., 2013). The unique climate of Xishuangbanna tropical seasonal rainforest makes it have an obvious dry season and rainy season within a year. In the dry season, the cold air from the north can hardly reach Xishuangbanna due to the blocking effect of Ailao Mountain and Wuliang Mountain. Therefore, in the dry season (November to April of the following year), the air is dry, the rainfall is scarce, and the sky is clear. (Ham, 1982). Although there is forest fog, it can completely dissipate before noon. Continuous rain cumulus clouds during the rainy season cause excessive errors in optical remote sensing. In this case, based on the existing remote sensing data and flux data, this paper improves the vegetation photosynthesis model (VPM) model suitable for Xishuangbanna tropical rainforest, eliminates the errors of optical remote sensing in the rainy season, improves the accuracy of evaluation, and aims to

improve the accuracy of estimating GPP in tropical rainforest and provide accurate evaluation of terrestrial ecosystem carbon cycle.

## 2 STUDY AREA

The research area is located in Xishuangbanna National Nature Reserve in Mengla County, Dai Autonomous Prefecture of Xishuangbanna, Yunnan Province. This area is located on the northernmost edge of the tropical rainforest in Southeast Asia and is also an important tropical rainforest concentrated distribution area in China. The climate is affected by the geographical location and is subject to the risk control system of the Southwest season all year round. It belongs to the north tropical monsoon climate (Zhang et al., 2006). The climate in the study area is highly seasonal, with distinct dry and wet seasons. The precipitation in the rainy season (May to October) is concentrated, and 87% of the annual precipitation occurs in this season. The precipitation in the dry season is less, but the phenomenon of forest fog is obvious, fog and fog water greatly make up for the lack of rainfall (Liu et al., 2005). Therefore, due to the influence of forest fog, the dry season can be further divided into the fog-cool season (November to February) and the dry-hot season (March to April). The unique climate resulted in the unique phenology of deciduous canopy in April and new leaves before July in the study area (Tan et al., 2014).

## 3. DATA AND METHOD

### 3.1 Data and Processing

The meteorological data and flux data used in this study are obtained from the Xishuangbanna station through the National Ecological Science Data Center (<http://www.cnern.org.cn/>). The flux data set has been processed by unified quality control and data interpolation, which has high reliability. In order to match the remote sensing data used in the model (MODIS, 8D time resolution), the daily latent heat (LH), daily sensible heat ( $H$ ), daily photosynthetically active radiation (PAR), daily ecosystem respiration (Re), daily net ecosystem exchange (NEE), daytime half-hour PAR and daytime half-hour NEE data are accumulated into the sum of 8 days, and the average temperature of 8 days is obtained from the daily average temperature. MODIS data are used to calculate enhanced vegetation index (EVI) and normalized difference vegetation index (NDVI) in four bands: blue (459-479 nm), red (620-670 nm), near infrared (841-875 nm), and shortwave infrared (1628-1652 nm) in MOD09A1 product provided by google earth engine (GEE) platform. Additionally, the HANTS filter is used to eliminate noise from the downloaded remote sensing data.

### 3.2 Brief Introduction of the VPM Correction Model

VPM model is a combination of eddy flux observation data and remote sensing data ecosystem primary productivity estimation model (Xiao et al., 2004), it assumes that the blades and the forest canopy by active photosynthesis of vegetation (PAV, mainly chloroplasts) and non-vegetation photosynthesis (NPV, mainly aging leaves, branches, and stem) of (Li et al., 2007). The general form of the VPM model is as follows:

$$GPP = \varepsilon_g \times FAPAR_{PAV} \times PAR \quad (1)$$

$$\varepsilon_g = \varepsilon_0 \times T_{scalar} \times W_{scalar} \times P_{scalar} \quad (2)$$

$$T_{scalar} = \frac{(T - T_{min})(T - T_{max})}{[(T - T_{min})(T - T_{max})] - (T - T_{opt})^2} \quad (3)$$

$$W_{scalar} = \frac{1 + LSWI}{1 + LSWI_{max}} \quad (4)$$

$$P_{scalar} = \frac{1 + LSWI}{2} \quad (5)$$

where PAR is the photosynthetically active radiation ( $\mu\text{mol}/\text{m}^2/\text{s}$ , photosynthetic photon flux density, PPFD),  $FAPAR_{PAV}$  is the fraction of PAR absorbed by PAV (chloroplasts),  $\varepsilon_g$  is the light use efficiency ( $\text{gC}/\text{mol PAR}$ ). The parameter  $\varepsilon_0$  is the apparent quantum yield or maximum light use efficiency ( $\text{gC}/\text{mol PAR}$ ), and  $T_{scalar}$ ,  $W_{scalar}$ , and  $P_{scalar}$  are the down-regulation scalars for the effects of temperature, water, and leaf phenology on the light use efficiency of vegetation, respectively.  $T_{min}$ ,  $T_{max}$ , and  $T_{opt}$  are minimum, maximum, and optimal temperatures for photosynthetic activities, respectively.

This paper develops a VPM model for estimating GPP under cloudy conditions, which mainly corrects the two parameters,  $W_{scalar}$  and EVI, that are greatly affected by clouds in the model. First, the water stress factor  $W_{scalar}$  is replaced by Evaporation Fraction (EF). Secondly, using the good correlation between near surface temperature and EVI, the conversion coefficient between near surface temperature and EVI is fitted to achieve the effective reconstruction of EVI polluted by clouds. In addition, new leaves are growing in Xishuangbanna tropical seasonal rainforest all year round, so  $P_{scalar}$  is set to 1. The form of the VPM correction model is as follows:

$$GPP = \varepsilon_g \times EVI_{cor} \times PAR \quad (6)$$

$$\varepsilon_g = \varepsilon_0 \times T_{scalar} \times EF \quad (7)$$

$$EF = \frac{LE}{LE + H} \quad (8)$$

where LE is latent heat flux ( $\text{W m}^{-2}$ ) measured by the eddy covariance (EC) tower, and  $H$  is sensible heat flux ( $\text{W m}^{-2}$ ).

### 3.3 Parameter Estimation of the VPM Correction Model

1) Estimating canopy-level light use efficiency ( $\varepsilon_g$ ) parameter

NEE and PAR conform to the Michaelis-Menten function. The maximum light use efficiency ( $\varepsilon_0$ ) of vegetation can be obtained by estimating linear or nonlinear models between them. Common nonlinear models include the rectangular hyperbola model, non-rectangular hyperbola model, and hyperbola modified model. According to the light response curve, light is the main limiting factor of photosynthesis under non-strong light conditions, and the linear relationship is obvious. Therefore, in this study, half an hour of daytime data under non-strong light conditions ( $0 < \text{PAR} < 1200 \mu\text{mol/m}^2/\text{s}$ ) is selected for monthly linear model fitting, and the month with the best fitting effect is selected in the growing season (From May to October every year) to obtain  $\varepsilon_0$  parameters (Table 1):

$$\text{NEE} = \alpha \times \text{PPFD} - R \quad (9)$$

where  $\alpha$  is the slope of linear fitting, and its value represents maximum light use efficiency, PPFD is photosynthetic photon flux density, and  $R$  is ecosystem respiration. According to Table 1, Xishuangbanna tropical seasonal rainforest is best fitted in June 2009, with a maximum light use efficiency of 0.54  $\text{gC/mol PAR}$ .

The temperature stress factor and water stress factor are calculated according to Equation (3) and Equation (8), respectively.

Table 1 Comparison of the maximum light use efficiency ( $\varepsilon_0$ ,  $\text{gC/mol PAR}$ ) fit for each growing season (May to October) from 2007 to 2010

	2007		2008		2009		2010	
	$\varepsilon_0$	$R^2$	$\varepsilon_0$	$R^2$	$\varepsilon_0$	$R^2$	$\varepsilon_0$	$R^2$
May	0.47	0.22	0.52	0.26	0.43	0.29	0.40	0.15
June	0.49	0.19	0.55	0.24	0.54	0.42	0.45	0.12
July	0.72	0.30	0.64	0.29	0.61	0.41	0.60	0.28
August	0.54	0.16	0.68	0.32	0.59	0.35	0.63	0.37
September	0.57	0.27	0.60	0.35	0.47	0.39	0.62	0.39
October	0.61	0.3	0.53	0.29	0.36	0.33	0.60	0.36

#### 2) Correction of EVI

The correlation factors used for EVI fitting must not be affected by rainy season clouds, so clear-sky data (dry season) from 2007 to 2010 are chosen for the fitting. Therefore, four years (2007 to 2010) of EVI, PAR, EF, and near surface temperature  $T_{\text{air}}$  are selected for Pearson correlation analysis, and the results are shown in Fig.1.

As shown in Fig. 1, the best correlation between  $T_{\text{air}}$  and EVI is obtained under clear sky conditions. Therefore,  $T_{\text{air}}$  and EVI for the 4-year dry season were used to construct fitting equations and interpolate EVI for the rainy season. Fig.2 shows the fitting results and Fig.3 shows the interpolation replacement results.

EVIHANTS	1	0.11	0.081	0.52
PAR/mol	0.11	1	-0.24	0.45
EF	0.081	-0.24	1	0.03
Tair/°C	0.52	0.45	0.03	1

Fig.1 Pearson correlation of EVI and different correlation factors under clear sky.

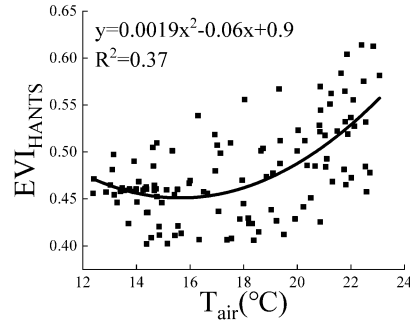


Fig.2 Fitted curves of EVI and near surface air temperature under clear sky.

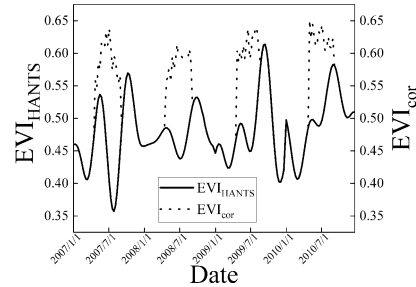


Fig.3 Comparison of EVI time series curves before and after interpolation. The solid line represents the original EVI time series filtered by HANTS, and the dashed line represents the EVI time series after fitting replacement.

**Table 2**

Comparison of dry/rainy seasons and full year before and after model correction for different years  
(RMSE unit:  $\text{gC}\cdot\text{m}^{-2}\cdot 8\text{day}^{-1}$ )

	dry season				rainy season				full year			
	$R^2$		RMSE		$R^2$		RMSE		$R^2$		RMSE	
	VPM	VPM <sub>cor</sub>	VPM	VPM <sub>cor</sub>	VPM	VPM <sub>cor</sub>	VPM	VPM <sub>cor</sub>	VPM	VPM <sub>cor</sub>	VPM	VPM <sub>cor</sub>
2007	0.43	0.64	10.72	6.98	0.05	0.40	19.52	10.06	0.17	0.77	15.00	8.07
2008	0.63	0.80	10.99	6.18	0.08	0.20	16.10	7.63	0.33	0.82	14.4	6.56
2009	0.52	0.56	14.53	10.54	0.03	0.30	23.04	9.56	0.33	0.70	18.10	10.33
2010	0.73	0.60	6.77	6.92	0.03	0.14	19.94	9.53	0.37	0.63	14.20	11.44

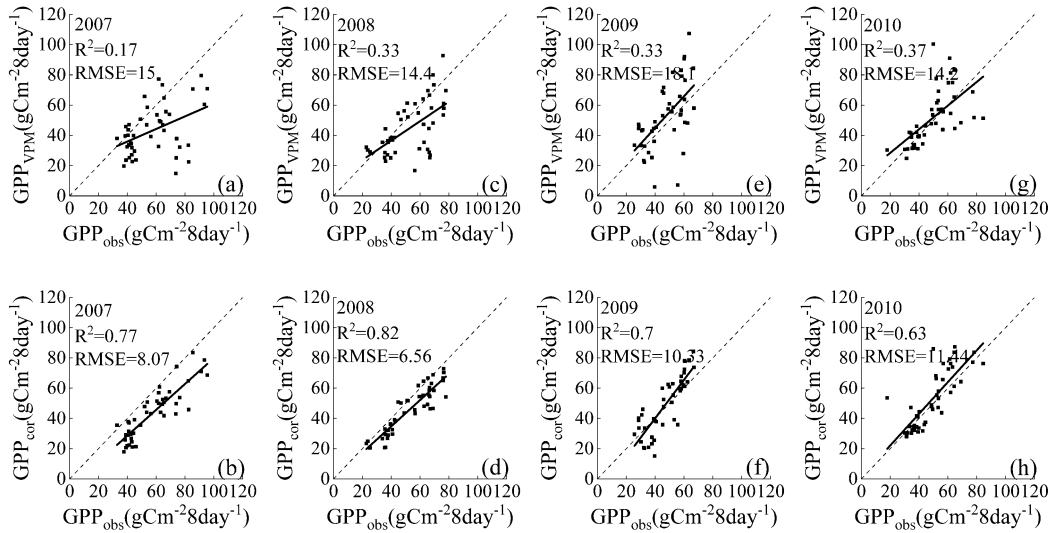


Fig.4 Comparisons of  $GPP_{VPM}$  (first row),  $GPP_{cor}$  (second row) at 8-day time scales for Xishuangbanna site observations. Dashed lines are 1:1 lines. Solid lines are linearly-fitted lines.

## 4 RESULTS AND DISCUSSION

### 4.1 Comparison of VPM Model and VPM Correction Model

Comparing the estimation accuracy of two models in different years and dry/rainy seasons, the results are shown in Table 2 and Fig.4. The GPP estimated by the VPM model is denoted as  $GPP_{VPM}$ , the GPP estimated by the correction model is denoted as  $GPP_{cor}$ , and the measured value of GPP is denoted as  $GPP_{obs}$ .

From Table 2, the effect of the dry season estimation is better than the rainy season. In the dry season, the difference between the two models is not significant, and  $GPP_{VPM}$  even outperformed  $GPP_{cor}$  in 2010, which indicates that the VPM model can accurately reflect the GPP of vegetation in most cases.

$GPP_{VPM}$  is significantly lower than  $GPP_{cor}$  in the rainy season, with  $R^2$  no greater than 0.1 and extremely poor correlation, which proves that the influence of clouds in the rainy season is not negligible.  $GPP_{cor}$  significantly improved this phenomenon, and its  $R^2$  improved to 0.2 - 0.3 in the rainy season. In general,  $GPP_{cor}$  can better simulate the seasonal variation phenomenon of low GPP values in spring and winter and high GPP values in summer. The 4-year  $R^2$  is 0.77, 0.82, 0.7, and 0.63, which are 0.6, 0.49, 0.37, and 0.26 higher than  $GPP_{VPM}$ , respectively. The  $R^2$  of the GPP estimated by the corrected model is 0.6 - 0.8, indicating that the model can eliminate the influence of rainy season clouds to a certain extent and reasonably estimate the GPP of Xishuangbanna tropical seasonal rainforest.

As shown in Fig. 4, the accuracy of GPP estimated by VPM<sub>cor</sub> in the Xishuangbanna tropical seasonal rainforest is higher than that of the VPM model compared with the observed GPP<sub>obs</sub>. The GPP<sub>VPM</sub> distribution was more dispersed, especially when GPP<sub>obs</sub> are higher than 50 gC·m<sup>-2</sup>·8day<sup>-1</sup>, which is the main reason for the lower overall R<sup>2</sup> of GPP<sub>VPM</sub>. These points correspond to the rainy season of the Xishuangbanna tropical seasonal rainforest, when GPP<sub>obs</sub> reaches its peak and GPP<sub>VPM</sub> is at a low value, so GPP<sub>VPM</sub> appears significantly dispersed. When GPP<sub>obs</sub> are higher than 50 gC·m<sup>-2</sup>·8day<sup>-1</sup>, GPP<sub>cor</sub> still maintains a good linear relationship, proving a significant improvement to the VPM model.

#### 4.2 Comparison of Correction Effect of Two Factors

Comparing the effect of two corrections on the accuracy improvement of VPM models for different years and 4 years.

Table 3 Comparison of the effect of correction of two factors on the accuracy improvement of VPM model in different years and 4 years (RMSE unit: gC·m<sup>-2</sup>·8day<sup>-1</sup>)

	VPM		W <sub>scalar</sub>		EVI <sub>cor</sub>	
	R <sup>2</sup>	RMSE	R <sup>2</sup>	RMSE	R <sup>2</sup>	RMSE
2007	0.17	15.02	0.39	11.78	0.52	11.89
2008	0.33	14.36	0.50	10.59	0.58	11.52
2009	0.33	18.09	0.40	14.64	0.61	13.05
2010	0.38	15.31	0.44	12.21	0.60	13.29
4years	0.20	17.49	0.31	13.84	0.42	15.09

As shown in Table 3, both corrections improve the estimation accuracy of VPM model in Xishuangbanna tropical seasonal rainforest to different degrees. The accuracy improvement effect fluctuates in different years due to different hydrothermal and meteorological conditions. The two correction effects are most significant in 2007, with model R<sup>2</sup> improving by 0.22 and 0.35, respectively. The correction effects of water stress factors are not significant in 2009 and 2010, with model R<sup>2</sup> improving by 0.06 and 0.07, while the correction effect for EVI improves steadily in each year. In general, the accuracy improvement of EVI correction is stable and significant, while the accuracy of the model corrected for water stress factor improved somewhat but fluctuated depending on the hydrothermal and meteorological conditions of the year. The four-year data also confirm the above findings, with the two correction models improving R<sup>2</sup> by 0.25 and 0.11, respectively. Therefore, improving optical remote sensing data is the key to improving the accuracy of VPM model estimation in Xishuangbanna tropical seasonal rainforest.

## 5 CONCLUSIONS

In this study, the VPM model has been corrected to improve the estimation accuracy of the VPM model in the Xishuangbanna tropical seasonal rainforest, in order to address the issue of GPP excessive estimation errors caused by cloud influence. The specific correction methods included water stress factor replacement and EVI fitting replacement. The accuracy of the corrected model have been greatly improved in four representative years. The results showed that 1) the influence of clouds in the rainy season in Xishuangbanna tropical seasonal rainforest is the main reason for the excessive estimation errors of the VPM model, and how to eliminate the influence of clouds is the key to improve the accuracy of the model with optical remote sensing as the input parameter. 2) The accuracy of the VPM model was improved by two correction processes. The 4-year R<sup>2</sup> increases by 0.6, 0.49, 0.37, and 0.26, respectively, and the 4-year RMSE decreases by 6.93, 7.84, 7.77, and 2.76, respectively. These results indicated that the corrected model has a better ability to estimate the GPP of Xishuangbanna tropical seasonal rainforest, and can better reflect the changes of GPP<sub>obs</sub>.

## REFERENCES:

- Ham, R.D., 1982, FOG DRIP IN THE BULL RUN MUNICIPAL WATERSHED, OREGON. *Journal of the American Water Resources Association*, 18, 785-789.
- Huete, A.R., Restrepo-Coupe, N., Ratana, P., Didan, K., Saleska, S.R., Ichii, K., Panuthai, S., & Gamo, M., 2008, Multiple site tower flux and remote sensing comparisons of tropical forest dynamics in Monsoon Asia. *Agricultural and Forest Meteorology*, 148, 748-760.
- Li, Z., Yu, G., Xiao, X., Li, Y., Zhao, X., Ren, C., Zhang, L., & Fu, Y., 2007, Modeling gross primary production of alpine ecosystems in the Tibetan Plateau using MODIS images and climate data. *Remote Sensing of Environment*, 107, 510-519.
- Lieth, H., & Whittaker, R., 1975, Primary productivity of the biosphere.
- Liu, W.J., Zhang, Y.P., Li, H.M., & Liu, Y.H., 2005, Fog drip and its relation to groundwater in the tropical seasonal rain forest of Xishuangbanna, southwest China; preliminary study. *Water research (Oxford)*, 39, 787-794.
- Ma, X.L., Huete, A., Yu, Q., Restrepo-Coupe, N., Beringer, J., Hutley, L.B., Kanniah, K.D., Cleverly, J., & Eamus, D., 2014, Parameterization of an ecosystem light-use-efficiency model for

- predicting savanna GPP using MODIS EVI. *Remote Sensing of Environment*, 154, 253-271.
- Malhi, Y., Nobre, A.D., Grace, J., Kruijt, B., Pereira, M.G.P., Culf, A., & Scott, S., 1998, Carbon dioxide transfer over a Central Amazonian rain forest. *Journal of Geophysical Research: Atmospheres*, 103, 593-612.
- Lin, S., Li, J., & Liu, Q., 2018, Overview on estimation accuracy of gross primary productivity with remote sensing methods. *Journal of Remote Sensing*, 22, 234-252.
- Sjöström, M., Zhao, M., Archibald, S., Arneth, A., Cappelaere, B., Falk, U., D Grandcourt, A., Hanan, N., Kergoat, L., Kutsch, W., Merbold, L., Mougin, E., Nickless, A., Nouvellon, Y., Scholes, R.J., Veenendaal, E.M., & Ardö, J., 2013, Evaluation of MODIS gross primary productivity for Africa using eddy covariance data. *Remote Sensing of Environment*, 131, 275-286.
- Tan, Z., Zhang, Y., Song, Q., Yu, G., & Liang, N., 2014, Leaf shedding as an adaptive strategy for water deficit: a case study in Xishuangbanna's rainforest. *Journal of Yunnan University (Natural Sciences Edition)*, 89, 273-280.
- Xiao, X., Zhang, Q., Braswell, B., Urbanski, S., Boles, S., Wofsy, S., Moore, B., & Ojima, D., 2004, Modeling gross primary production of temperate deciduous broadleaf forest using satellite images and climate data. *Remote Sensing of Environment*, 91, 256-270.
- Zhang, Y., Sha, L., Yu, G., Song, Q., Tang, J., Yang, X., Wang, Y., Zheng, Z., Zhao, S., Yang, Z., & Sun, X., 2006, Annual variation of carbon flux and impact factors in the tropical seasonal rain forest of xishuangbanna, SW China. *Science in China. Series D, Earth sciences*, 49, 150-162.



# Estimating the downwelling surface longwave radiation under all-sky conditions from FengYun-4A Data

Yun Jiang<sup>1, 2</sup>, Bo-Hui Tang<sup>1, 3, \*</sup> and Huanyu Zhang<sup>1, 2</sup>

<sup>1</sup>State Key Laboratory of Resources and Environment Information System, Institute of Geographic Sciences and Natural Resources Research, Chinese Academy of Sciences, Beijing 100101, China;

<sup>2</sup>College of Resources and Environment, University of Chinese Academy of Sciences, Beijing 100049, China;

<sup>3</sup>Faculty of Land Resource Engineering, Kunming University of Science and Technology, Kunming 650093, China

\*Correspondence: tangbh@kust.edu.cn

**ABSTRACT** – Fengyun-4A (FY-4A) is the latest generation of China's geostationary satellite, the Advanced Geosynchronous Radiation Imager (AGRI) on it can provide high-precision, high-frequency observation data, which provides new possibilities for the downwelling surface longwave radiation (DSLRL) estimation with the high spatial and temporal resolution, but it only provides DSLRL product under clear sky conditions. This work presents a new method for estimating DSLRL under all-sky conditions using a genetic algorithm–artificial neural network (GA-ANN) algorithm based on brightness temperature (BT) from the FY-4A AGRI infrared channels and near-surface air temperature and dew point temperature from ERA5 reanalysis data. According to the verification results of two independent observation sites, it is shown that the bias and RMSE are  $-4.31 \text{ W/m}^2$  and  $35.28 \text{ W/m}^2$ , respectively, which is better than the accuracy of clear-sky DSLRL product provided by the FY-4A satellite. Compared with the CERES SYN all-sky DSLRL product, the DSLRL estimated by the new method is in good agreement with it, the bias and RMSE are  $0.86 \text{ W/m}^2$  and  $26.87 \text{ W/m}^2$ , respectively, and the new method has a higher spatial resolution (4 km), which can display more details of spatial variation.

**Keywords:** downwelling surface longwave radiation; FY-4A; ERA5; all-sky

## 1 INTRODUCTION

The downwelling surface longwave radiation (DSLRL) is the driving force of the surface energy transport and exchange process and vitally important for the earth-atmosphere energy exchange and the formation and change of climate. Accurately estimating the DSLRL is of great significance to the research fields of meteorology, hydrology, ecology and so on (Tang and Li 2008; Trenberth et al. 2009). DSLRL can be obtained from site observations or inversion using remote sensing data. With the development of remote sensing satellite technology, remote sensing satellites can provide data with high temporal and spatial continuity and spatial uniformity, which provides a new way for the inversion of DSLRL at the regional and global scales. Therefore, satellite data are used for DSLRL estimation, such as Moderate Resolution Imaging Spectroradiometer (MODIS), Cloud and Earth Radiant Energy System (CERES), etc., and a variety of DSLRL estimation algorithms and products have been developed. A lot of attempts have been made to DSLRL inversion methods based on remote sensing satellite data, but most of these methods focus on clear sky conditions and are relatively mature. At the same time,

many algorithms have been developed for DSLRL estimation under cloudy sky conditions, but due to the complexity of cloudy sky conditions, there are still large uncertainties in the DSLRL estimation.

The methods of DSLRL estimation using remote sensing data under clear sky conditions are divided into parametric methods and hybrid methods. The parametric method uses the radiative transfer equation and statistical data to establish the mathematical relationship between the radiance at the top of the atmosphere (TOA) and the DSLRL (Tang and Li 2008; Wang et al. 2017; Wang et al. 2014; Yan et al. 2016; Zhou et al. 2019a). The hybrid algorithm establishes the statistical regression relationship between meteorological parameters (such as air temperature and water vapor content) and DSLRL (Nussbaumer and Pinker 2012; Yu et al. 2012; Yu et al. 2019; Zhou et al. 2019b). For DSLRL estimation under cloudy sky conditions, there are mainly two methods: one is an empirical algorithm by correcting or adding cloud parameters (Cheng et al. 2019; Liu et al. 2020; Rooney 2005; Zhong et al. 2019); the other is using different cloud parameters (cloud base height, cloud base temperature, cloud top temperature) to establish a parameterized estimation algorithm or use a single-

layer cloud model to estimate DSLR (Jiang et al. 2022; Wang et al. 2020; Wang et al. 2018; Yang and Cheng 2020; Yang et al. 2022). In general, due to the large uncertainty in the estimation of cloud base height and cloud base temperature, DSLR estimation under cloudy sky conditions is still challenging.

Most of the DSLR estimation methods mentioned above are developed based on polar-orbiting satellite data, but polar-orbiting satellites have low temporal resolution. At the same time, although geostationary satellites have high temporal resolution, there are few studies on DSLR estimation using them. As a geostationary satellite, Fengyun-4A (FY-4A) satellite can provide data with 1h time resolution, which provides new possibilities for DSLR estimation. However, the products provided by the FY-4A satellite only include DSLR products under clear sky conditions, and lack of DSLR products under all-sky conditions. Therefore, this study proposed a genetic algorithm-artificial neural network (GA-ANN) -based DSLR estimation method under all-sky conditions using the brightness temperature (BT) data of the FY-4A thermal infrared channels and the near-surface air temperature and dew point temperature from the ERA5 reanalysis data.

## 2 DATA

### 2.1 Satellite Data

The FY-4A AGRI L1 Full Disk Data provides the reflectance (Channels 1-6) and BT (Channels 7-14) at 0 min and 45 min of each hour, the band ranges, and primary purpose of channels 7-14 are detailed in Table 1. In this study, we employed the BT observed by eight infrared channels (channels 7-14) as the input data to train and validate the new proposed DSLR estimation model. The CERES Single Scanner Footprint (SSF) product provides cloud products and radiation flux products in each CERES field of view (approximately 20 km). In this study, we employed the calibrated CERES SSF FOV all-sky DSLR product as the reference data to train the machine learning model.

### 2.2 Reanalysis Data

ERA5 is a fifth-generation atmospheric reanalysis of the global climate launched by the European Center for Medium-Term Weather Forecasts (ECWMF). ERA5 reanalysis data provides aggregated values for seven parameters: 2-m air temperature, 2-m dew point temperature, total precipitation, mean sea level pressure, surface pressure, 10-m u-component of wind, and 10m v-component of wind. This study employed 2-m air temperature and 2-m dew point temperature from ERA5 hourly data on single levels as input data to estimate DSLR.

### 2.3 Site Observations

This study selected three observation network sites to calibrate the CERES SSF FOV all-sky DSLR reference products to build a training dataset. Based on the quality control documents of the observation sites, six sites were used to validate and calibrate the CERES SSF FOV all-sky DSLR products including the Arou Observation Site in the WATER, the Daxing Observation site, and Miyun Observation site in the HAIHE, the Dunhuang Observation Site, Linze Observation Site and Xiyinghe Observation Site in the CARN. Meanwhile, the Dashalong Observation Site and Huazhaizi Observation Site in the Water were used to validate the estimated DSLR under all-sky conditions.

## 3 METHOD

The goal of this study is to estimate DSLR under all-sky conditions from BT data of FY-4A AGRI and near-surface air temperature ( $T_a$ ) and dew point temperature ( $T_d$ ) of reanalysis data using the GA-ANN model. First, determine the training data set of the model, in which the input data are the BT data of FY-4A AGRI and  $T_a$  and  $T_d$  in the reanalysis data and the output data are field observations. However, due to the limited number of observation sites, we use the CERES SSF FOV all-sky DSLR product corrected by field observations as the output data to train the model. Second, the GA-ANN algorithm is used to train the model, and the cross-validation method is used to verify the accuracy of the trained model. Finally, the DSLR under all-sky conditions is estimated using the trained model, and the estimated all-sky DSLR was validated with in situ measurements.

This study used the observation data of six field sites to correct the CERES SSF FOV all-sky DSLR products within the range of observation sites (30°N to 47°N, 90°E to 117°E), which was used as the input data of the training dataset. The calibration formula can be expressed as:

$$\text{DSLR}_{\text{cal}} = a * \text{DSLR}_{\text{org}} + b \quad (1)$$

Where:  $\text{DSLR}_{\text{cal}}$  is the calibrated DSLR,  $\text{DSLR}_{\text{org}}$  is the original DSLR,  $a$  is the calibration parameter,  $b$  is the offset. To ensure the representativeness of the sample, we selected the CERES SSF FOV all-sky DSLR product on the first day of each month for the two years (2019 and 2020) that matched the FY-4A data as the output data of the GA-ANN model. There were 206870 samples, with 105434 from Terra and 101436 from Aqua, paired and selected as the output training dataset.

To maintain the simplicity of the model and reduce the uncertainty caused by redundant parameters, this study decided to use the BT of the FY-4A AGRI thermal infrared channels (channels 7~14) and the  $T_a$  and  $T_d$  in the ERA5 reanalysis data as input data, use the corrected CERES SSF FOV all-sky DSLR product as output data, DSLR under all-sky conditions can be expressed as:

$$DSLRL_{all-sky} = f(BT_i, T_a, T_d) \\ i = 7, 8, 9, 10, 11, 12, 13, 14 \quad (2)$$

Where  $DSLRL_{all-sky}$  is the estimated DSLR under all-sky conditions,  $BT_i$  is the brightness temperature of FY-4A AGRI band  $i$ . Finally, the node values in the hidden layer are iteratively simulated to determine the optimal neural network.

## 4 RESULT

### 4.1 Validation Using in Situ Measurements

In this study, the proposed new method was trained and validated on independent sites (no overlap sites exist between the training and testing data) as DSLR estimation. Two independent sites were used to validate the proposed new algorithm, they are the Dashalong and Huazhaizi sites of WATER. The BT data from FY-4A AGRI and the  $T_a$  and  $T_d$  from ERA5 reanalysis data were extracted at each site, and then these parameters were input into the established DSLR estimation model. We estimated DSLR under all-sky conditions for the first day of each month in 2020, and then used two independent sites (Dashalong and Huazhaizi sites) to field-validate the estimates. Note that due to the different spatial resolution of the FY-4A satellite data and the ERA5 reanalysis data, we used the nearest neighbor method to match the two data. If the DSLR product with the same resolution as the FY-4A satellite data is produced, the reanalysis data needs to be downsampled to the same resolution.

Figure 4 shows a scatterplot of the estimated values vs. the measured values at the two sites. The results showed that the estimated DSLR agrees well with ground measurements, which demonstrates the new proposed algorithm can produce a reasonable DSLR under all-sky conditions. The validation accuracy estimated all-sky DSLR at all sites with a bias of  $-4.31 \text{ W/m}^2$  and an RMSE of  $35.28 \text{ W/m}^2$ . Overall, similar accuracy was observed at each site.

### 4.2 Comparison with FY-4A Product

Since the FY-4A satellite lacks DSLR products under cloudy sky conditions, this study only compares and analyzes the DSLR products under clear sky conditions.

As in Section 4.1, we used the measurement data of the two sites (Dashalong and Huazhaizi) for the first day of each month in 2020 to verify and compare the FY-4A DSLR product.

The evaluation results of the FY-4A DSLR against ground observations at all sites are shown in Figure 5, it can be shown that the FY-4A clear-sky DSLR exhibits a relatively large bias ( $-16.27 \text{ W/m}^2$ ) and RMSE ( $41.68 \text{ W/m}^2$ ). The new method proposed in this study estimates DSLR under all-sky conditions with higher accuracy than the FY-4A clear-sky DSLR product.

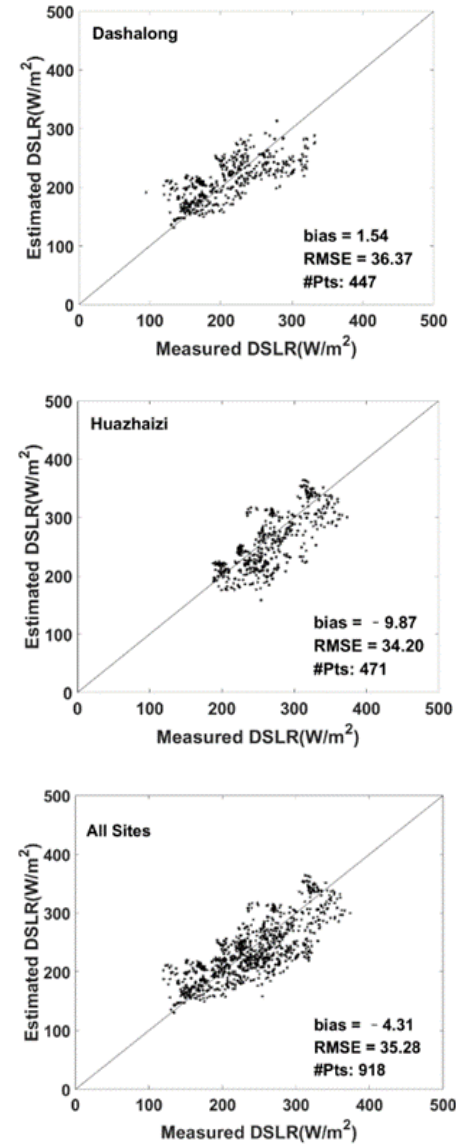


Figure 4. Scatterplot of the estimated all-sky DSLR vs. ground DSLR measurements.

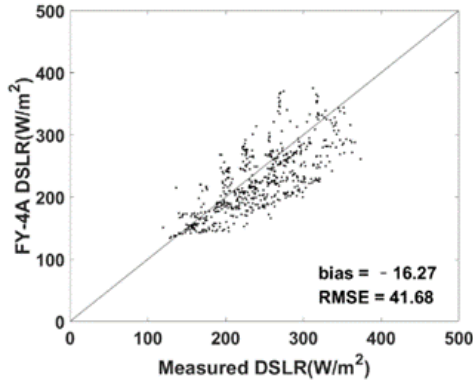


Figure 5 Scatterplot of the FY4A clear-sky DSLR vs. ground DSLR measurements at all two sites.

#### 4.3 Comparison with CERES Product

To further evaluate the performance of the newly proposed DSLR estimation method, the Clouds and the Earth's Radiant Energy System Synoptic (CERES-SYN), Edition 4A, DSLR product was employed for comparison. The CERES-SYN provides global hourly  $1^\circ \times 1^\circ$  gridded top of the atmosphere, in-atmospheric (profile), and surface fluxes, the surface fluxes are produced using the Langley Fu-Liou radiative transfer model based on inputs from MODIS, geostationary (GEO) imagers, and the Goddard Earth Observing System (GOES) Data Assimilation System reanalysis (Doelling et al. 2016). In this study, the all-sky hourly DSLR from CERES-SYN products was compared with the newly proposed DSLR estimation method.

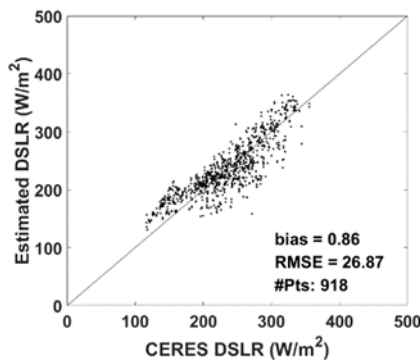


Figure 6 Scatterplot of estimated all-sky DSLR vs. CERES SYN 1deg DSLR product.

Figure 6 shows the comparison results of the newly proposed method estimated DSLR and CERES-SYN DSLR at two sites in 2020. The comparison analysis result shows that the estimated DSLR from the proposed method has a good agreement with the CERES-SYN DSLR product, the bias and RMSE are  $0.86 \text{ W/m}^2$  and  $26.87 \text{ W/m}^2$ , respectively.

## 5 DISCUSSION

This study develops a DSLR estimation method for all-sky conditions based on the BT data of the FY-4A AGRI and the  $T_a$  and  $T_d$  from the ERA5 reanalysis data. The FY-4A AGRI infrared channel (bands 7 ~ 14) provides BT data, which can be used to reflect information such as water vapor, clouds, and land surface temperature. In addition, the  $T_a$  and  $T_d$  were added in this study to improve the performance of the model. In order to reflect the importance of each variable, we used principal component analysis to analyze the contribution ratio of each variable. The results show that infrared channels (bands 7 ~ 14) have a similar contribution ratio. We also analyzed the correlation between each variable and DSLR and found that the correlation is similar, so we take the BT of infrared channels (bands 7 ~ 14) as the input parameter. Due to the limitation of FY-4A satellite data download and its short in-orbit time (launched in December 2016), it is impossible to use the measured site data to establish an estimation model.

We use the corrected CERES SSF FOV all-sky DSLR data to replace the measured data, although the corrected DSLR has good accuracy compared with the measured data (bias is  $-0.06 \text{ W/m}^2$ , RMSE is  $17.68 \text{ W/m}^2$ ). However, there is a certain gap with the measured data, which will inevitably lead to estimation errors. By comparing the estimated DSLR and CERES SYN products, it is found that the two products have high consistency, which shows that the algorithm proposed in this study can achieve high accuracy. If the long-time series of FY-4A observation data and measured data can be downloaded to establish an estimation model, a higher estimation accuracy can be obtained. Meanwhile, the spatial resolution of CERES SSF FOV all-sky DSLR data used to build the estimation model is  $20 \text{ km}$ , while the spatial resolution of FY-4A AGRI BT data is  $4 \text{ km}$ . When the model is established, in order to ensure the consistency of the data, we aggregate the BT data to a spatial resolution of  $20 \text{ km}$ , which leads to uncertainties in the estimation of DSLR.

## 6 CONCLUSIONS

This study developed a new method for estimating DSLR under all-sky conditions by using the BT observations from FY-4A AGRI thermal channel data along with the  $T_a$  and  $T_d$  from ERA5 reanalysis data, the estimation model was established based on the GA-ANN algorithm. Due to the small number of observation sites and the limitation of FY-4A data download, the calibrated CERES SSF FOV all-sky DSLR product was used instead of site measured data as the targets, the BT,  $T_a$  and  $T_d$  are used as inputs.

Cross-validation was used to verify the performance of the new proposed estimation model, the bias and RMSE estimated by the new proposed method were  $-0.03 \text{ W/m}^2$  and  $15.81 \text{ W/m}^2$ , respectively.

The new proposed method estimated all-sky DSLR are validated by the two independent observation sites. The all-sky DSLR retrieval accuracy in terms of bias and RMSE are  $-4.31 \text{ W/m}^2$  and  $35.28 \text{ W/m}^2$ , respectively, which is comparable and even better than the FY-4A clear-sky DSLR product. In addition, the estimation results were compared with CERES SYN all-sky DSLR products, and the results showed that the bias and RMSE of the two products are  $0.86 \text{ W/m}^2$  and  $26.87 \text{ W/m}^2$ , which indicates that the estimated DSLR is in good agreement with the CERES product. Compared with the  $1^\circ$  spatial resolution of the CERES SYN all-sky DSLR product, the product estimated in this study has a spatial resolution of  $4 \text{ km}$ , which has better spatial and temporal resolution and can show more detailed spatial variation.

## REFERENCES

- Cheng, J., Yang, F., & Guo, Y. (2019). A Comparative Study of Bulk Parameterization Schemes for Estimating Cloudy-Sky Surface Downward Longwave Radiation. *Remote Sensing*, 11
- Doelling, D.R., Sun, M., Nguyen, L.T., Nordeen, M.L., Haney, C.O., Keyes, D.F., & Mlynczak, P.E. (2016). Advances in Geostationary-Derived Longwave Fluxes for the CERES Synoptic (SYN1deg) Product. *JOURNAL OF ATMOSPHERIC AND OCEANIC TECHNOLOGY*, 33, 503-521
- Jiang, Y., Tang, B.-H., & Zhao, Y. (2022). Estimation of Downwelling Surface Longwave Radiation with the Combination of Parameterization and Artificial Neural Network from Remotely Sensed Data for Cloudy Sky Conditions. *Remote Sensing*, 14
- Liu, M., Zheng, X., Zhang, J., & Xia, X. (2020). A revisiting of the parametrization of downward longwave radiation in summer over the Tibetan Plateau based on high-temporal-resolution measurements. *Atmospheric Chemistry and Physics*, 20, 4415-4426
- Nussbaumer, E.A., & Pinker, R.T. (2012). Estimating surface long-wave radiative fluxes at global scale. *Quarterly Journal of the Royal Meteorological Society*, 138, 1083-1093
- Rooney, G.G. (2005). Modelling of downwelling long-wave radiation using cloud fraction obtained from laser cloud-base measurements. *Atmospheric Science Letters*, 6, 160-163
- Tang, B., & Li, Z.-L. (2008). Estimation of instantaneous net surface longwave radiation from MODIS cloud-free data. *Remote Sensing of Environment*, 112, 3482-3492
- Trenberth, K.E., Fasullo, J.T., & Kiehl, J. (2009). Earth's Global Energy Budget. *Bulletin of the American Meteorological Society*, 90, 311-324
- Wang, C., Tang, B.-H., Wu, H., Tang, R., & Li, Z.-L. (2017). Estimation of Downwelling Surface Longwave Radiation under Heavy Dust Aerosol Sky. *Remote Sensing*, 9
- Wang, J., Tang, B.-H., Zhang, X.-Y., Wu, H., & Li, Z.-L. (2014). Estimation of Surface Longwave Radiation over the Tibetan Plateau Region Using MODIS Data for Cloud-Free Skies. *IEEE Journal of Selected Topics in Applied Earth Observations and Remote Sensing*, 7, 3695-3703
- Wang, T., Shi, J., Ma, Y., Letu, H., & Li, X. (2020). All-sky longwave downward radiation from satellite measurements: General parameterizations based on LST, column water vapor and cloud top temperature. *ISPRS Journal of Photogrammetry and Remote Sensing*, 161, 52-60
- Wang, T., Shi, J., Yu, Y., Husi, L., Gao, B., Zhou, W., Ji, D., Zhao, T., Xiong, C., & Chen, L. (2018). Cloudy-sky land surface longwave downward radiation (LWDR) estimation by integrating MODIS and AIRS/AMSU measurements. *Remote Sensing of Environment*, 205, 100-111
- Yan, G., Wang, T., Jiao, Z., Mu, X., Zhao, J., & Chen, L. (2016). Topographic radiation modeling and spatial scaling of clear-sky land surface longwave radiation over rugged terrain. *Remote Sensing of Environment*, 172, 15-27
- Yang, F., & Cheng, J. (2020). A framework for estimating cloudy sky surface downward longwave radiation from the derived active and passive cloud property parameters. *Remote Sensing of Environment*, 248
- Yang, F., Cheng, J., & Zeng, Q. (2022). Validation of a Cloud-Base Temperature-Based Single-Layer Cloud Model for Estimating Surface Longwave Downward Radiation. *IEEE Geoscience and Remote Sensing Letters*, 19, 1-5
- Yu, S., Xin, X., & Liu, Q. (2012). Estimation of clear-sky longwave downward radiation from HJ-1B

- thermal data. *Science China Earth Sciences*, 56, 829-842
- Yu, S., Xin, X., Liu, Q., Zhang, H., & Li, L. (2019). An Improved Parameterization for Retrieving Clear-Sky Downward Longwave Radiation from Satellite Thermal Infrared Data. *Remote Sensing*, 11
- Zhong, L., Zou, M., Ma, Y., Huang, Z., Xu, K., Wang, X., Ge, N., & Cheng, M. (2019). Estimation of Downwelling Shortwave and Longwave Radiation in the Tibetan Plateau Under All-Sky Conditions. *Journal of Geophysical Research: Atmospheres*, 124, 11086-11102
- Zhou, W., Shi, J., Wang, T., Peng, B., Zhao, R., & Yu, Y. (2019a). Clear-Sky Longwave Downward Radiation Estimation by Integrating MODIS Data and Ground-Based Measurements. *IEEE Journal of Selected Topics in Applied Earth Observations and Remote Sensing*, 12, 450-459
- Zhou, W., Shi, J.C., Wang, T.X., Peng, B., Husi, L., Yu, Y.C., & Zhao, R. (2019b). New Methods for Deriving Clear-Sky Surface Longwave Downward Radiation Based on Remotely Sensed Data and Ground Measurements. *Earth and Space Science*, 6, 2071-2086



## Estimation of all-weather land surface temperature based on deep neural network by combining AMSR2 and MODIS data

Zhong Peng<sup>1, 2</sup>, Ronglin Tang<sup>1, 2, \*</sup>, Yazhen Jiang<sup>1, 2</sup>, Meng Liu<sup>3</sup>, Zhao-Liang Li<sup>1, 2, 3</sup>

<sup>1</sup> State Key Laboratory of Resources and Environment Information System, Institute of Geographic Sciences and Natural Resources Research, Chinese Academy of Sciences, Beijing 100101, China;

<sup>2</sup> University of Chinese Academy of Sciences, Beijing 100049, China;

<sup>3</sup> Key Laboratory of Agricultural Remote Sensing, Ministry of Agriculture and Rural Affairs/Institute of Agricultural Resources and Regional Planning, Chinese Academy of Agricultural Sciences, Beijing 100081, China;

\* Authors to whom correspondence should be addressed: tangrl@reis.ac.cn;

**ABSTRACT** – Land surface temperature (LST) is an important physical variable at the land surface-atmosphere boundary and a key input parameter for many geochemical models. All-weather LST products can be beneficial for enhancing the temporal resolution of remote sensing products of surface evapotranspiration, soil moisture, and net radiation. Through combining MODIS data and microwave AMSR2, the 10 km daily LST estimation models were constructed by using the deep neural network (DNN) algorithm for cloud and cloud-free conditions. In-situ observations of 143 sites in the AmeriFlux and FLUXNET networks were used to evaluate the accuracy of LST estimation by the DNN model. The results demonstrated that the DNN model could effectively establish the relationship between satellite data (AMSR2 and MODIS) and LST. Compared with the in-situ observations of LST, the estimated LST under clear sky and cloudy sky presented a root mean square error (RMSE) of 2.4 °C and 3.07 °C, respectively, which could explain 94%-97% of the LST variation.

## INTRODUCTION

Land surface temperature (LST) model based on thermal infrared remote sensing cannot effectively retrieve the LST under cloudy sky, and thereby is greatly limited in many applications, especially for those that require both high temporal resolution and dense spatial coverage of the LST (Li et al. 2013).

Presently, LST can be retrieved by three main approaches, including those from in-situ measurements, from satellite observations, and by model simulations (Phan and Kappas 2018; Yan et al. 2020; Yu et al. 2022). In-situ measurements are not influenced easily by weather and can provide continuous observation of LST variations, but do not provide extensive spatial coverages (Ermida et al. 2019). The model simulation approaches can estimate LST at a global level with a continuous spatio-temporal scale, but are typically outputs at a coarse resolution and the models are generally complex with a large number of input parameters, thus requiring considerable computational cost (Liu et al. 2021). The development of regional or global scale LST models based on satellite remote sensing technology can achieve continuous spatial and temporal LST estimations that have a broader application in practice than observations from in-situ

sites (Yu et al. 2022). As the thermal infrared radiation cannot penetrate the clouds, the LST models based on thermal infrared remote sensing cannot effectively retrieve the LST in the cloudy sky, and thus cannot meet the demand of its all-weather application. The passive microwave remote sensing can reduce atmospheric influence, and the surface microwave radiation can be likely to transmit through the clouds, which has obvious advantages to retrieve LST when using remote sensing datasets (Mo et al. 2021). Recently, machine learning techniques have been widely applied in hydrological process models, energy balance models, and climate forecasting systems with their robustness in solving complex nonlinear structures (Peng et al. 2022). The commonly applied machine learning techniques include the Random Forest (RF), Artificial Neural Network (ANN), Deep Neural Network (DNN), Convolutional Neural Network (CNN), etc.

This paper aims to combine MODIS and AMSR2 remote sensing data to retrieve high-accuracy LST separately in the clear and cloudy skies by the DNN technique. There are 143 in situ sites from the AmeriFlux network and FLUXNET network used to construct the DNN model for estimating LST and to evaluate the accuracy of the model.

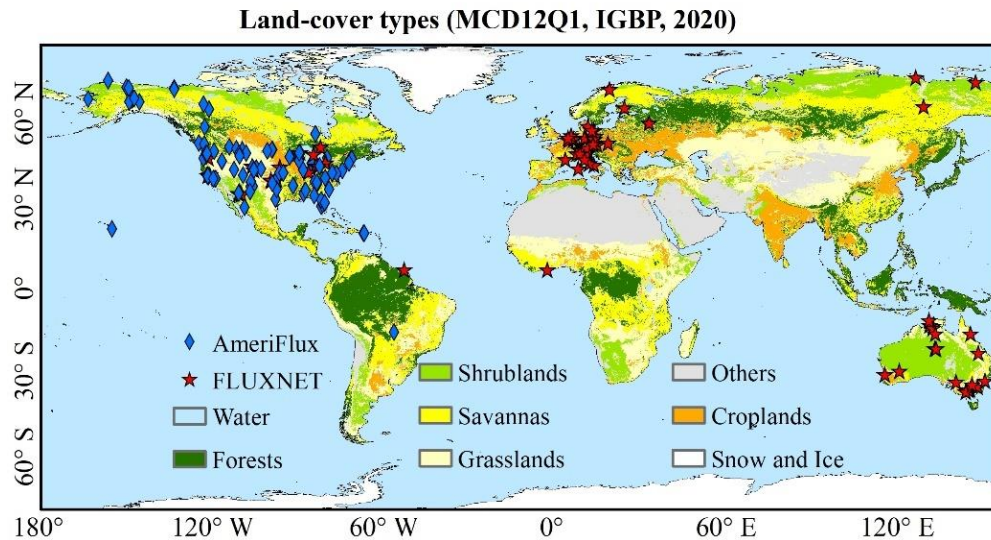


Fig 1. Locations of in-situ sites of AmeriFlux network and FLUXNET Network, and the land cover types in 2020 (background colored) extracted from the MCD12Q1

## 2. DATA SOURCES

### 2.1. In-situ observations

In situ observations of 143 sites from the AmeriFlux network (2012-2020) and FLUXNET network (2012-2014) networks were used to construct the DNN model for estimating LST and to evaluate the accuracy of the model (Fig. 1). These sites are located mainly in North America, Europe, and Asia, and less frequently on other continents, and the site observations are usually recorded every half hour. All in-situ site observations are publicly accessible and free to download (AmeriFlux network: <https://AmeriFlux.lbl.gov>, FLUXNET network: <https://FLUXNET.fluxdata.org>).

### 2.2. Satellite datasets

The remote sensing datasets used in the study mainly included the MODIS datasets and AMSR2 datasets. The MODIS datasets included the MODIS/Terra+Aqua annual 500 m land cover type product (MCD12Q1), the MODIS/Terra 16-day 500 m vegetation index (MOD13A1), the MODIS/Terra+Aqua daily LST and Emissivity products (MOD11A1 and MYD11A1), and the global MODIS/Terra annual 250 m surface vegetation cover product (MOD44B). All products were accessed for free from the MODIS website (<https://adsweb.modaps.eosdis.nasa.gov/search/>). The AMSR2 dataset primarily included the vertical polarization bands of L3 brightness temperature (BT) products, namely three bands with center frequency of 23.8 GHz, 6.5 GHz, and 89 GHz that are very relevant

to LST (<https://gportal.jaxa.jp/-gpr/>). The brightness temperature product has a spatial resolution of 10 km and a temporal resolution of daily scale. In addition, a 1 km DEM product from GMTED2010 was selected as auxiliary data for the study.

## 3. METHODS

### 3.1. Data preprocessing

The data pre-processing process in this study included pre-processing of in-situ observations and pre-processing of remote sensing data. The pre-processing of in-situ observations included data quality-control and time zone conversion. Quality-control was designed to remove the interpolated data and observed invalid (values of -9999) data in the in-situ measurements. The time zone conversion was made to convert the local time of the in-situ site observations to local solar time so that it could be directly matched with satellite observations. The pre-processing of remote sensing data focused on interpolating and smoothing the image data. Because the Normalized Difference Vegetation Index (NDVI, MOD13A1) was at daily scale and had some quality problems, this study first obtained the daily NDVI by temporal interpolation and then smoothed by Savitzky-Golay (Chen et al. 2004) method.

### 3.2. In-situ LST derivation

The in-situ observed LST can be inferred from the measured long-wave radiation combined with the

surface emissivity retrieved from the satellite based on the radiation balance (Liang 2005), which is used as the training target and validation data for the DNN model, as expressed :

$$T_s = \left( \frac{R_{lu} - (1 - \varepsilon)R_{ld}}{\varepsilon\sigma} \right)^{1/4} \quad (1)$$

$$\varepsilon_s = 0.273 + 1.778\varepsilon_{31} - 1.807\varepsilon_{31}\varepsilon_{32} - 1.037\varepsilon_{32} + 1.774\varepsilon_{32}^2 \quad (2)$$

where  $T_s$  is the land surface temperature,  $R_{lu}$  and  $R_{ld}$  are the upswelling and downswing longwave radiations, respectively,  $\sigma$  is the Stefan Boltzmann constant ( $5.67 \cdot 10^{-8} \text{ Wm}^{-2}\text{K}^{-4}$ ) is the land surface emissivity, and  $\varepsilon_{31}$  and  $\varepsilon_{32}$  are the emissivities of band 31 and band 32, respectively.

### 3.3. DNN model building

Combined with the MODIS and AMSR2 remote sensing data, the DNN was used to directly establish the relationship between remote sensing data and in-situ LST. In reference to existing studies, variables that may be closely related to LST were used as input data for the DNN model, which came from MODIS including percent tree cover (PTC, MOD44B), NDVI, and emissivity ( $\varepsilon_{31}$  and  $\varepsilon_{32}$ ), sensor zenith angle (SZA), and MODIS LST ( $LST_{modis}$ ) product from MOD11A1 and MYD11A1. Here, the ( $LST_{modis}$ ) was taken as input to improve the accuracy of the DNN model. The data from AMSR2 included brightness temperature products with center frequency of 23.8 GHz, 6.5 GHz, and 89 GHz. In addition, DEM was also considered as an input parameter for the DNN model. The DNN model expressions for estimating the clear sky LST ( $LST_{clear}$ ) and cloudy sky LST ( $LST_{cloudy}$ ) are:

$$LST_{clear} = f(DEM, PTC, NDVI, SZA, \varepsilon_{31}, \varepsilon_{32}, BT23.8, BT36.5, BT89, LST_{modis}) \quad (3)$$

$$LST_{cloudy} = f(DEM, PTC, NDVI, SZA, \varepsilon_{31}, \varepsilon_{32}, BT23.8, BT36.5, BT89) \quad (4)$$

The sample data extraction of DNN models required matching the longitude and latitude information of the sites with the remote sensing data according to time, thereby obtaining the image pixel values at the corresponding spatial locations of the images. Note that all image pixel values were extracted from the original resolution images and the image pixel with inhomogeneous land cover types in the 3\*3 grid were removed according to the IGBP classification of MCD12Q1. Total sample data of 168,652 samples were obtained in this study, and the time coverage of the data ranged from May 2012 to December 2020. The sample data was then split into training data and validation data by 3:1 using random sampling, with the training data

used to train the DNN model and optimize the model hyperparameters, and the validation data used to evaluate the model accuracy. Considering the stability of the model and the estimation accuracy, we determined the optimal neural network structure and hyperparameters in this study as shown in Table 1.

Table 1 Deep neural network (DNN) structure and hyperparameters

Hyperparameters	Value
hidden layers	100-80-40-20-10
activation function	Rule
batch-size	256
max epoch	15000

## 4. RESULTS AND DISCUSSION

Fig.2 (APPENDIX) shows the scatter density plots of the LST estimated by the DNN model against in-situ observations under clear sky and cloudy sky. The results indicated that the LST estimated by the DNN model under clear sky and cloudy sky agreed well with the in-situ observations, which were located near the 1:1 line and could explain 94%-97% of the LST variations. The root mean square error (RMSE) in the validation of the DNN model estimated LST under clear sky and cloudy sky was 2.4 °C and 3.07 °C, respectively, and the mean absolute error (MAE) was 1.8 °C and 2.32 °C, respectively. The mean bias error (MBE) could be ignored in both cloudy and clear sky. Note that the overall validation accuracy of the estimated LST under clear sky outperformed that of the estimated LST under cloudy sky. The worse results of cloudy-sky DNN model were probably caused by the complex atmospheric conditions, while the clear sky DNN model had the MODIS LST product as input that could improve the accuracy.

Fig 3. (APPENDIX) presents the temporal trend of the estimated LST from the DNN model versus in-situ observations for different land cover types (recording time > 5 years) under clear sky and cloudy sky. The temporal trend diagram demonstrated that the LST estimated by DNN was consistent with the variation of in-situ observations, and the LST during clear sky was significantly higher than that under cloudy sky. The LST exhibited significant seasonal variations in interannual cycle, with the LST peaking at 60°C in summer and decreasing to less than 0°C in winter, with lower LST in areas with higher vegetation cover or sufficient water supply (e.g., forest or wetland).

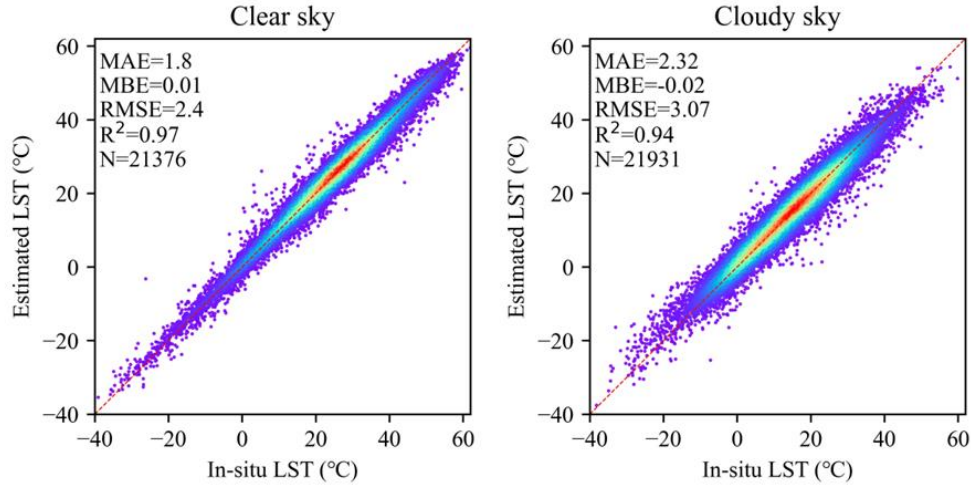


Fig 2. Scatter density plots of estimated LST by deep neural network (DNN) model against in-situ observations of LST under clear sky and cloudy sky

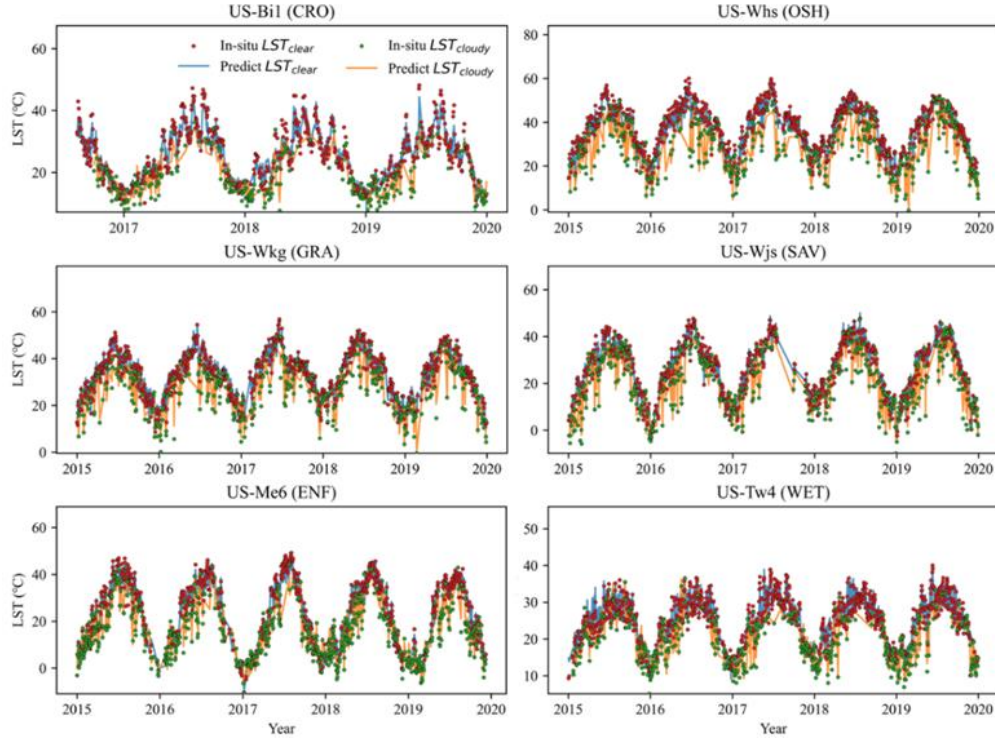


Fig 3. Temporal trend of estimated LST for different land cover types from the deep neural network (DNN) model with in-situ observations of LST under clear sky and cloudy sky

## 5. CONCLUSIONS

The DNN model could effectively construct the relationship between satellite data (AMSR2 and MODIS) and LST, and obtain better accuracies. The DNN model combining thermal infrared remote

sensing and microwave remote sensing data may overcome the deficiency of the former in retrieving LST under cloudy sky and achieve all-weather LST estimations, which will facilitate the continuous monitoring of the Earth's LST.

## REFERENCES

- Chen, J., Jönsson, P., Tamura, M., Gu, Z., Matsushita, B., and Eklundh, L. 2004. A simple method for reconstructing a high-quality NDVI time-series data set based on the Savitzky–Golay filter. *Remote Sensing of Environment*, 91, 332-344
- Ermida, S.L., Trigo, I.F., DaCamara, C.C., Jimenez, C., and Prigent, C. 2019. Quantifying the Clear-Sky Bias of Satellite Land Surface Temperature Using Microwave-Based Estimates. *Journal of Geophysical Research-Atmospheres*, 844-857
- Li, Z., Tang, B., Wu, H., Ren, H., Yan, G., Wan, Z., Trigo, I.F., and Sobrino, J.A. 2013. Satellite-derived land surface temperature: Current status and perspectives. *Remote Sensing of Environment*, 131, 14-37
- Liang, S. 2005. *Quantitative remote sensing of land surfaces*: John Wiley & Sons
- Liu, J., Hagan, D.F.T., and Liu, Y. 2021. Global Land Surface Temperature Change (2003–2017) and Its Relationship with Climate Drivers: AIRS, MODIS, and ERA5-Land Based Analysis. *Remote Sensing*, 13, 44
- Mo, Y., Xu, Y., Chen, H., and Zhu, S. 2021. A Review of Reconstructing Remotely Sensed Land Surface Temperature under Cloudy Conditions. *Remote Sensing*, 13, 2838
- Peng, Z., Tang, R., Jiang, Y., Liu, M., and Li, Z. 2022. Global estimates of 500 m daily aerodynamic roughness length from MODIS data. *Isprs Journal of Photogrammetry and Remote Sensing*, 183, 336-351
- Phan, T.N., and Kappas, M. 2018. Application of MODIS land surface temperature data: a systematic literature review and analysis. *Journal of Applied Remote Sensing*, 12, 1
- Yan, Y., Mao, K., Shi, J., Piao, S., Shen, X., Dozier, J., Liu, Y., Ren, H., and Bao, Q. 2020. Driving forces of land surface temperature anomalous changes in North America in 2002–2018. *Scientific Reports*, 10
- Yu, P., Zhao, T., Shi, J., Ran, Y., Jia, L., Ji, D., and Xue, H. 2022. Global spatiotemporally continuous MODIS land surface temperature dataset. *Scientific Data*, 9

# Influence of hyperspectral thermal infrared sensor channel selection on land surface temperature and emissivity inversion accuracy

Xiujuan Li <sup>a,b</sup>, Hua Wu <sup>a,b,\*</sup>, Zhaoliang Li <sup>a,b,c</sup>, Ni Li <sup>d</sup>

<sup>a</sup>. State Key Laboratory of Resources and Environmental Information System, Institute of Geographic Sciences and Natural Resources Research, Chinese Academy of Sciences, Beijing 100101, China

<sup>b</sup>. University of Chinese Academy of Sciences, Beijing 100049, China

<sup>c</sup>. Key Laboratory of Agri-informatics, Ministry of Agriculture/Institute of Agricultural Resources and Regional Planning, Chinese Academy of Agricultural Sciences, Beijing 100081, China

<sup>d</sup>. Key Laboratory of Digital Earth Science, Aerospace Information Research Institute, Chinese Academy of Sciences, Beijing 100094, China

\* Corresponding author: Hua Wu, Phone: +86 13810811395, Email: wuh@lreis.ac.cn

**ABSTRACT:** Hyperspectral thermal infrared (HTIR) remote sensing data offers a wealth of spectral information, which is getting more and more attention. However, there must be redundant information because of the significant connections between HTIR channels. And there are few channel selection methods for retrieving land surface parameters. Therefore, we employ the stepwise iteration methodology based on information content (SIIC) to choose the channels more sensitive to land surface parameters. Based on the selected channels, land surface temperature (LST) and emissivity (LSE) are synchronously inversed using machine learning method and get satisfactory accuracy. Consequently, the findings of this research can be used to guide the channel selection of a HTIR sensor for land surface observation.

## 1. INTRODUCTION

Thanks to the various channels of Hyperspectral thermal infrared (HTIR) remote sensing data, it is feasible to extract land surface temperature (LST) and emissivity (LSE) at the same time. However, there must be redundant information because of the significant connections between HTIR channels. Therefore, channel selection is one of the key problems in the research of hyperspectral remote sensing inversion (Li, et al., 2013). For hyperspectral remote sensing data, the widely used channel selection methods include stepwise iteration method (Rodgers, 1996; Crevoisier, 2003), Jacobian method (Aires, et al., 2002), Manually selected method (Fourrié and Thépaut, 2002) and so on. Moreover, the stepwise iteration methodology based on information content (SIIC) is considered to be the best method for channel selection (Rabie F, 2002). However, the above channel selection methods mainly serve the inversion of atmospheric profile. So far, there are few methods to select the channels for surface information retrieval. The majority of channel selection methods for retrieving land surface parameters still rely on the prior knowledge and choose channels that are mainly in the atmospheric window, which lacks a quantitative representation of the land surface information.

Therefore, we employ the SIIC to choose the channels more sensitive to land surface information in this study. In addition, the simultaneous inversions of LST and LSE are effectively accomplished from the simulated on-board radiance data using Artificial Neural Network (ANN). Based on this study, a reasonable channel selection scheme is provided for LST and LSE inversion.

## 2. DATA AND METHODOLOGY

The radiative transfer equation at the thermal infrared band is shown in Equation 1.

$$L_{\lambda} = \varepsilon(\lambda)\tau(\lambda)B(\lambda, T_s) + (1 - \varepsilon(\lambda))L_{\downarrow}(\lambda)\tau(\lambda) + L_{\uparrow}(\lambda) \quad (1)$$

Where,  $L_{\lambda}$  is the at-sensor radiance at wavelength  $\lambda$ .  $\varepsilon$  is the LSE.  $\tau$  is the atmospheric transmittance.  $L_{\downarrow}$  and  $L_{\uparrow}$  are the atmosphere downwelling radiance and upwelling radiance. And  $B(\lambda, T_s)$  is the Planck function at land surface temperature  $T_s$  and wavelength  $\lambda$ .

Based on equation (1), the HTIR data are simulated in this study. The atmospheric simulation data are generated by using TIGR database and MODTRAN 5.2. Based on ASTER spectral library, the emissivity



spectrum curves of 100 typical ground objects were selected. The spectral range is 8-12.5  $\mu\text{m}$ , and the channel interval is set to 0.05  $\mu\text{m}$ , and a total of 91 channels are generated. Combined with the LST generated by perturbation and the channel response function, the simulated data of HTIR data are obtained. Based on the simulated data, the channel subsets are further selected. The channel numbers and locations were determined when the information content is saturated based on SIIC method. Further, the information content is defined as the entropy difference between the states before and after observation:

$$H = S(P1) - S(P2) = \frac{1}{2} \ln|S_a| - \frac{1}{2} \ln|\hat{S}| = -\frac{1}{2} \ln|\hat{S}S_a^{-1}| \quad (2)$$

Where,  $\hat{S}$  is the post-observation covariance matrix,  $S_a$  is background field covariance matrix. In this experiment, US76 standard atmospheric profile is used to generate background field data. And  $\hat{S}$  can be calculated from the background field covariance matrix:

$$\hat{S} = S_a - S_a K^T (K S_a K^T + S_e)^{-1} K S_a \quad (3)$$

Where,  $K$  is the weight function matrix.  $S_e$  is the observation error covariance matrix. The information content of a single channel is calculated instead since computing the information content of all combinations would need too much computing power. Remember that a row vector  $k$  in the weight function matrix  $K$  is the weight function corresponding to the channel, and  $s_e$  is the diagonal element of the corresponding position in  $S_e$ , which represents the observation error variance of the channel. And then, the post-observation error covariance matrix of one channel is calculated:

$$\hat{S} = S_a - S_a K^T (k S_a k^T + s_e)^{-1} k S_a \quad (4)$$

Where,  $k S_a k^T + s_e$  is a single value. So the information content of a single channel can be calculated by the following formula (5).

$$H = -\frac{1}{2} \ln \left| I - \frac{(k S_a)^T k}{s_e + k S_a k^T} \right| \quad (5)$$

The channel with the maximum  $H$  is to be selected in each iteration.

In order to bypass the atmospheric correction, some scholars have successfully used regression method (Zhou, et al., 2002, 2011; Goldberg, 2003), multi-channel method (Zhong, et al., 2016), machine learning or deep learning methods (Wang, 2013; Wang, et al., 2022; Aires, 2001, 2002; Lan, et al., 2020) to directly retrieve LST from hyperspectral data. Machine learning can deal with high complexity and nonlinear ill-

conditioned inversion problems, which can bypass the complex computation process and obtain satisfactory inversion results. For parameters inversion study, neural network has been widely used in thermal infrared remote sensing. Research shows that in most cases, the inversion accuracy of neural network is better than that of traditional linear regression model, and the inversion feasibility is high. Therefore, Artificial Neural Network (ANN) is selected for synchronous inversion of LST and LSE.

### 3. RESULTS

Based on the SIIC, we calculated the information content of the 8-12.5  $\mu\text{m}$  spectrum. Figure 1(a) showed the process of calculating the information content. The channel corresponding to the highest point of each information spectrum is the channel selected in one iteration. The information spectrum closer to the top is calculated earlier. The pink curve represents the information spectrum when the first channel is selected. For the 8-12.5  $\mu\text{m}$  spectrum segment, the maximum information content is 3.1015 at 9.1945  $\mu\text{m}$ . Then, on the basis of the first channel selected, the information content of the next channel is calculated, that is, the yellow curve. By comparing the first and second information spectrum curves, it can be seen that after a certain channel is selected, the information contents of other channels near this channel are significantly reduced due to their high similarity with the selected channel, and the information content of other channels is also reduced accordingly. Therefore, it can provide a certain reference for the selection of inversion channels of LST and LSE. Finally, the first 47 channels, which accounts for 85% of the total information content of all channels, are selected to retrieve LST and LSE.

Based on the simulated data, the LST and LSE were retrieved from the on-board radiance using ANN methods. Figure 2 shows the performance of the ANN model on the training and test sets. As a result, the RMSE of the retrieved LSTs is 1.917K in the training set and 1.922K in the test set, and the RMSEs of the retrieved LSEs are both 0.011 in the training set and the test set. The training set and test set keep the same precision level, which shows that the model has great stability and robustness.

To verify the sensitivity of the ANN model to different noises, we add two kinds of white gaussian noises to the data: noise-equivalent temperature difference (NEAT) of 0.1K and absolute calibration error of 1K. The results are shown in Table 1. After adding the NEAT, the RMSE increases by 0.08K for LST, and 0.001 for LSE. After adding the calibration noise, the RMSE increases by 0.08K for LST, and 0.001 for LSE. Comparatively speaking, ANN is not very sensitive to NEAT and calibration noise.

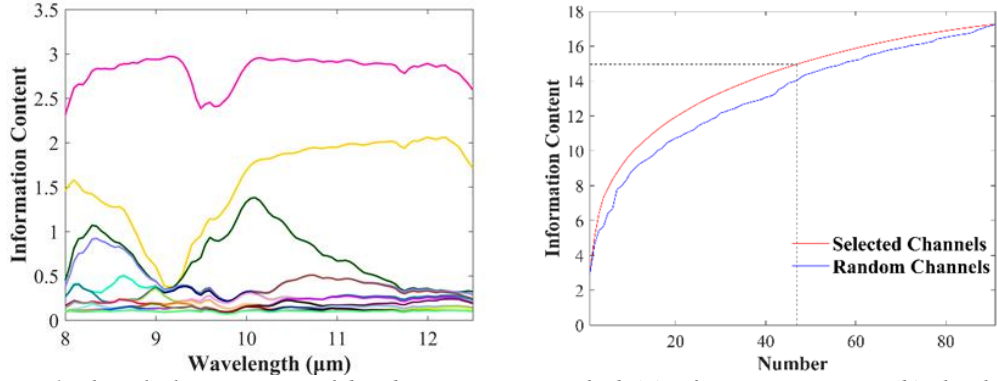


Figure 1. The calculation process of distribution iteration method. (a) Information spectrum. (b) The change of the information with the number of selected channels by SIIC and randomly selection.

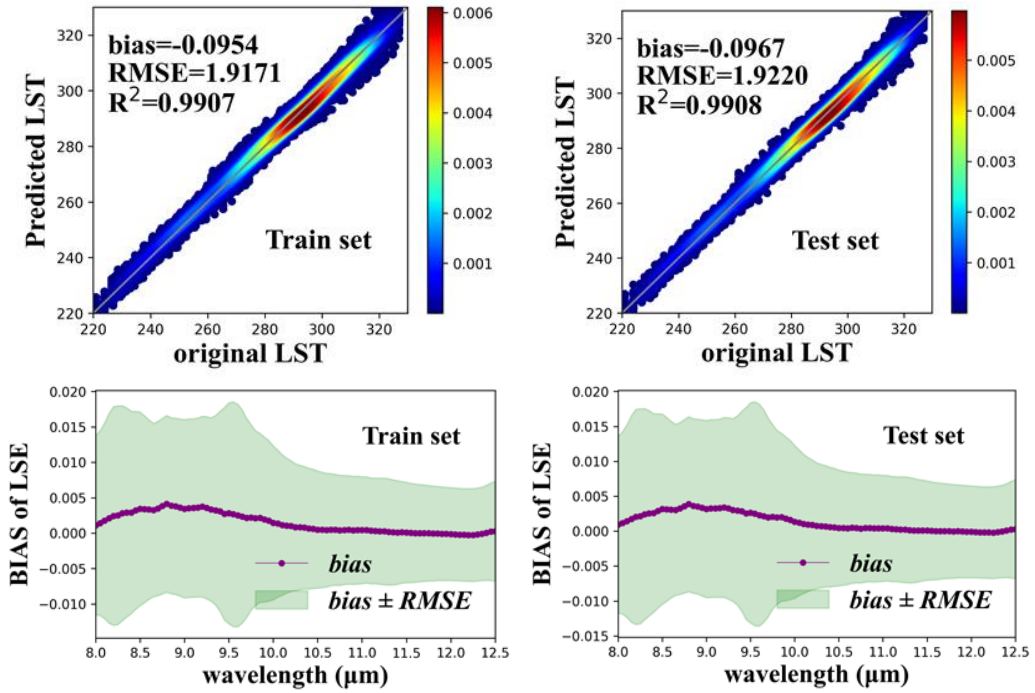


Figure 2. Model Result of ANN.

Table 1. the RMSEs for the ANN model

Parameter	Dataset	Without noise	NEAT	Calibration noise
LST	Train	1.9171	1.9993	2.4683
	Test	1.9220	2.0033	2.4778
LSE	Train	0.0106	0.0117	0.0110
	Test	0.0107	0.0118	0.0110

#### 4. CONCLUSIONS

Based on the SIIC, the channels for retrieving land surface parameters from hyperspectral thermal infrared data are selected in this paper. The first 47 channels with the highest information content are selected. And then the integrated inversion models of LST and LSE were constructed based on the machine learning method, ANN. According to the results, the selected channels can be used as the optimal channel for surface parameters inversion, which can achieve inversion accuracy of 1.9K for LST and 0.01 for LSE. And the model has certain anti-noise property.

## 5. ACKNOWLEDGEMENTS

This work was supported in part by the National Key R&D Program of China under Grant 2018YFB0504800, and in part by the National Natural Science Foundation of China under Grants 42071319, 41871267 and 42071331.

## 6. REFERENCE

- Aires F., Prigent C., Rossow W. B. et al., 2001. A new neural network approach including first guess for retrieval of atmospheric water vapor, cloud liquid water path, surface temperature, and emissivities over land from satellite microwave observations. *Journal Of Geophysical Research-atmospheres*, 106(14): 14887-14907.
- Aires, F., Chédin, A. and Scott, N. A., 2002. A regularized neural net approach for retrieval of atmospheric and surface temperatures with the IASI instrument. *Journal of Applied Meteorology*, 41(2): 144-159.
- Crevoisier C., Chedin A. and Scott N. A., 2003. AIRS channel selection for CO<sub>2</sub> and other trace-gas retrievals. *Quarterly Journal of the Royal Meteorological Society*, 129(593): 2719-2740.
- Fourrié N. and Thépaut J. N., 2002. Validation of the NESDIS Near-Real-Time AIRS Channel Selection. Reading: European Centre for Medium Range Weather Forecasts.
- Goldberg M. D., Qu Y., McMillin L. M., et al. 2003. AIRS near-real-time products and algorithms in support of operational numerical weather prediction. *IEEE Transactions on Geoscience and Remote Sensing*, 41(2): 379-388.
- Lan X. Y., Zhao E. Y., Li Z. L., et al., 2020. Deep mixture model-based land surface temperature retrieval for hyperspectral thermal IASI sensor. *IEEE Access*, 8: 218122- 218130.
- Li Z.-L., Tang B.-H., Wu H., et al., 2013. Satellite-derived Land Surface Temperature: Current status and perspectives. *Remote Sensing of Environment*, 131: 14–37.
- Rabier F., Fourrié N., Chafäi D. et al., 2002. Channel selection methods for infrared atmospheric sounding interferometer radiances. *Quarterly Journal of the Royal Meteorological Society*, 128 (581): 1011-1027.
- Rodgers C. D., 1996. Information content and optimization of high spectral resolution measurements//*Proceedings of SPIE 2830, Optical Spectroscopic Techniques and Instrumentation for Atmospheric and Space Research II*. Denver, CO, United States: SPIE: 136-147.
- Wang N., Li Z.-L., Tang B.-H., et al., 2013. Retrieval of atmospheric and land surface parameters from satellite-based thermal infrared hyperspectral data using a neural network technique. *International Journal of Remote Sensing*, 34(9-10): 3485-3502.
- Wang X., Zhong L., and Ma Y. M., 2022. Estimation of 30 m land surface temperatures over the entire Tibetan Plateau based on Landsat-7 ETM+ data and machine learning methods.
- Zhou D. K., Smith W. L., Li J., et al., 2002. Thermodynamic product retrieval methodology and validation for NAST-I. *Applied Optics*, 41(33): 6957.
- Zhou D. K., Larar A. M., Liu X., et al., 2011. Global land surface emissivity retrieved from satellite ultra-spectral IR measurements. *IEEE Transactions on Geoscience and Remote Sensing*, 49(4): 1277-1290.
- Zhong X., Huo X., Ren C., et al., 2016. Retrieving land surface temperature from hyperspectral thermal infrared data using a multi-channel method. *Sensors*, 16(5): 1-14.

## Retrieval of apparent fluorescence quantum efficiency from FLEX–FLORIS 500-780 nm

Shari Van Wittenberghe<sup>1</sup>, Ana Belen Pascual<sup>1</sup>, Adrian Perez<sup>2</sup>, Eatidal Amin<sup>1</sup>, Carolina Tenjo<sup>1</sup>, Neus Sabater<sup>3</sup>, Jose Moreno<sup>1</sup>

*1 Laboratory for Earth Observation, Image Processing Laboratory, University of Valencia*

*2 Image and Signal Processing Group, Image Processing Laboratory, University of Valencia*

*3 Finnish Meteorological Institute*

Email: Shari.Wittenberghe@uv.es

**ABSTRACT** - The solar-induced vegetation fluorescence, emitted by the Chlorophyll *a* molecules as a small radiative flux in the 650–850-nm range has become new quantitative information in the understanding of vegetation status from the leaf to the landscape and global scales. However, to quantitatively exploit the obtained fluorescence signal and obtain the link between vegetation fluorescence and the core photosynthetic light reaction dynamics, advanced signal processing is required. Full spectral information in the region 500-800 nm is hereby used as input for the processing of the top-of-canopy fluorescence emission from a bottom-up leaf level approach. As part of the FLEX L1B-to-L2 Algorithm Retrieval and Product Development Study, retrieval strategies for photosynthesis-related products are being developed based on the synergistic FLEX–FLORIS and Sentinel 3–OLCI spectral information. One of these products is the fluorescence quantum efficiency which is the ratio between the emitted fluorescence and the absorbed radiation that triggers the emission. Retrieved FQE values at the canopy level are small (1-2%) but promising validation results are achieved. The apparent FQE indicates the downregulation of the excitation pressure on the Chlorophyll molecules and the energy provided to the final reaction centres. Hence, FQE provides a first proxy for the photosynthetic efficiency of the vegetation surface. Despite the relationship tends to be more complex due to the activation of non-photochemical quenching mechanisms which changes the qualitative coupling between fluorescence and photosynthesis, FQE is a first proxy of the downregulation of harvested light.

### 1 INTRODUCTION

Solar-induced vegetation fluorescence, emitted by the Chlorophyll *a* molecules as a small radiative flux in the 650–850-nm range is providing new quantitative information in the understanding of vegetation status from the leaf to the landscape and global scales. The goal is to use the canopy-leaving fluorescence signal as an unbiased estimate of the photosynthetic activity of the underlying vegetation.

As part of ESA's Fluorescence Explorer (FLEX) L1B-to-L2 Algorithm Retrieval and Product Development Study, retrieval strategies for photosynthesis-related products are being developed based on the synergistic FLEX–FLORIS and Sentinel 3–OLCI spectral information. For an overview of the FLEX mission, the reader is referred to Moreno et al. (2016) and Drusch et al. (2017). The Fluorescence Imaging System (FLORIS) imaging instrument onboard FLEX will cover the wavelength range from 500 to 780 nm with a spectral sampling ranging from 0.1 to 2 nm and a spectral resolution of 0.3 within the

O2 absorption bands and up-to 3 nm within the full region (Coppo et al. 2017). The spectral band characteristics and region will allow the disentanglement of the vegetation fluorescence (F) flux (often referred to as solar-induced fluorescence, or SIF) from the reflected radiance. However, interpreting the retrieved fluorescence signal at any remotely observed scale, and additionally contextualizing it within the origin of the photosynthetic light reactions, is not a straightforward task. To improve the estimation of actual photosynthesis from the future spaceborne mission based on the retrieved top-of-canopy F information, additional steps are required. The primary requirements are the quantitative description of (1) the real surface emission, accounting for all the photon losses along the path between the sites of emission and detection, and (2) the real surface absorbed energy triggering this emission. Resolving these quantitative components will enable the calculation of the actual quantum yield of the fluorescence emission process, an essential step to get to photosynthesis (Van Wittenberghe et al., 2021). The goal of this work is to

propose an algorithm for the quantitative retrieval of the fluorescence quantum efficiency, based on the essential retrieval of the photosynthetically absorbed photons from FLORIS LR data, to supplement the solar-induced fluorescence retrieval from the FLORIS HR data of the future FLEX mission.

## 2 MATERIAL AND METHODS

### 2.1 Product definition: apparent or TOC fluorescence quantum efficiency

The (Apparent) Fluorescence Quantum Efficiency (FQE) of the Chl *a* molecules, expresses the fate of an absorbed photon to be eventually (apparently, at the TOC) emitted as an F photon, requiring the quantification of the number of absorbed photons triggering the emission (APAR Chl product). FQE is a unitless parameter based on the ratio of the fluoresced to absorbed photon flux, expressed as  $J_F$  and  $J_A$ , integrated over wavelength ( $\lambda$ ) and angle ( $\omega$ ):

$$FQE = (\text{number of photons emitted}) / (\text{number of photons absorbed}) \quad (1)$$

$$= \frac{\int_{\lambda} \int_{\omega} J_F d\lambda d\omega [\text{photons m}^{-2} \text{s}^{-1}]}{\int_{\lambda} \int_{\omega} J_A d\lambda d\omega [\text{photons m}^{-2} \text{s}^{-1}]} \quad (2)$$

### 2.2 Step 1: fitting retrieval of fAPAR Chl

The total amount of light energy absorbed by the leaf/vegetation and its fraction (fAPAR<sub>total</sub>, -) is composed of both photosynthetic and non-photosynthetic absorbed fractions (Figure 1). Only the photosynthetic light absorption relates to the energy absorbed by the antenna complexes, which is further (fully or partly) used for driving the carbon reactions. Here, we are interested in the energy absorbed by the Chlorophyll (Chl) pigments, the main photosynthetic light absorbing pigment. In a first approach to extract the absorption coefficient  $\mu$  for Chl (a+b), and in particular the red tail part of it, a power function was applied to the absorbance (A) spectra of leaves with variable ratios of Chl *a*/Chl *b* contents:

$$\mu = A \left( \frac{1}{n} \right) \quad (3)$$

Where  $n$  is a positive number.

This average pigment absorption coefficient was further used in a non-negative least squares fitting algorithm whereby the fitted absorbance spectrum  $A(\lambda)$  is estimated by the power function model  $F(x(\lambda))$  using weighted factors  $b_1$  and  $b_2$  applied to the pigment component spectra  $x_i$ :

$$\hat{A} = (b_1 * x_i(\lambda))^{b_2} \quad (4)$$

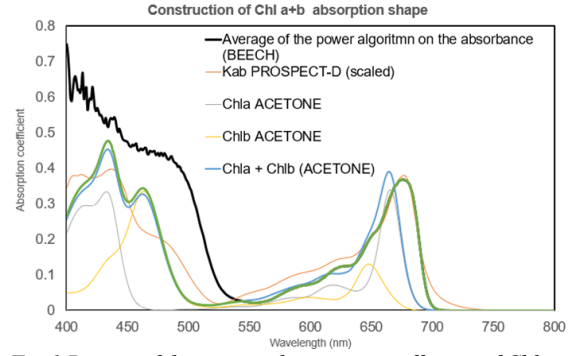


Fig.1 Design of the *in vivo* absorption coefficient of Chl *a* + *b* as a combined spectrum based on (i) *in vitro* absorption shapes of Chl *a* and Chl *b* and (ii) the *in vivo* absorbance shape of the red-edge

The error between the fitting of the observations  $y$  and the model  $F(x(\lambda))$  is hereby minimized through the parameters  $a_i$  and  $b_i$  by a least square function:

$$\min_x \|F(x, xdata) - ydata\|_2^2 = \min_x \sum_i (F(x, xdata_i) - ydata_i)^2 \quad (5)$$

Hereby we test the fitting algorithm first on leaf spectra using the FLORIS LR  $\lambda = [500-780 \text{ nm}]$  range. Using the solved weighted factors  $b_1$  and  $b_2$ , the modelled absorbance is converted to the full photosynthetically active region, based on the pigment absorption for the full PAR range,  $x_i [400-800 \text{ nm}]$  (Fig. 2).

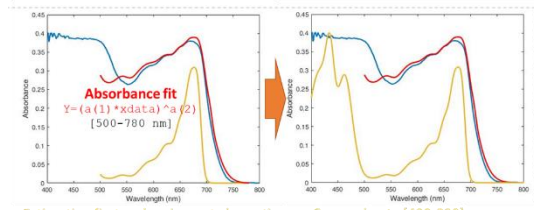


Fig.2 Measured (blue line) and fitted absorbance (red) based on the absorption feature for Chl (yellow), first for the FLORIS LR range (left), and further for the full PAR range (right)

### 2.2 Step 2: retrieval of APAR Chl

In a second step, the intermediate fAPAR product, obtained from step 1, is used to calculate the APAR product. To do so, the vector of the fraction of absorbed light obtained in the first step is multiplied by the incoming at-surface irradiance  $[400-780 \text{ nm}]$ , and converted to photon units:

$$apar(\lambda) = fAPAR(\lambda) * PAR \quad (6)$$

These radiometric units are further converted to photon flux units and integrated over the full PAR range (400-

750 nm). Note that currently there is no distinguishing between the diffuse and direct irradiance for the APAR calculation. We calculate the APAR for Chl, respectively as:

$$apar\_photons(\lambda) = 1/(h * c) \int_{400}^{700} \lambda * apar(\lambda) d\lambda \quad (7)$$

The final product is given as the PAR integrated sum of the photons absorbed (Table 1).

Parameter/variable	Units	Spectral integral?	Product
Estimated total TOC absorbance	[-]	no	intermediate
Absorption weight of Chl, result from the <i>apar</i> fitting module	[-]	no	intermediate
Absorbed radiation by Chl in the region 400-780 nm	[W m <sup>-2</sup> sr <sup>-1</sup> nm <sup>-1</sup> ]	no	intermediate
Spectrally resolved photon flux by Chl in the region 400-780 nm	[photons m <sup>-2</sup> s <sup>-1</sup> nm <sup>-1</sup> ]	no	intermediate
Integrated photon flux by Chl in the region 400-780 nm	[photons m <sup>-2</sup> s <sup>-1</sup> ]	yes	Final product: APAR_Ch

Table 1 Design of the in vivo absorption coefficient of Chl a + b as a combined spectrum based on (i) in vitro absorption shapes of Chl a and Chl b and (ii) the in vivo absorbance shape of the red-edge

### 2.3 Step 3: Calculation of FQE based on full range Fluorescence and APAR Chl

In a last step we calculate the ratio between the full-range Chl fluorescence emission, a product of the earlier steps in the L2 processing chain, and the developed APAR Chl product, according Eq. 2.

### 2.4. End-to-end scene generation and validation of FQE

The generation of synthetic scenes is one of the core parts of an End-to-End Simulator (E2ES), providing scenes (ground truth) as would be observed by satellite instruments and used as reference against simulated retrieved mission products (Tenjo et al., 2018). For FLEX, an E2ES has been developed to generate appropriate scenes that allow assessing the performance of the ground data processing chain. As a component of the E2ES, a surface definition module provides in the forward modelling scheme a TOC reflectance, fluorescence and temperature. As part of this module the SCOPE model is used to simulate the surface fluorescence properties (Vilfan et al., 2016). Fluorescence quantum efficiency is an input parameter of the forward modelling, with typical values in the range of [0-0.015] at the leaf level.

## 3 RESULTS

### 3.1 Leaf fitting of fAPAR Chl

The fAPAR fitting algorithm was developed and tested for pure leaf reflectance spectra, using a single species

dataset of beech leaves (n=76), obtained with an integrating sphere set-up (Figure 3). Fitting the Chl absorption feature used results in a mean RMSE obtained of  $0.0261 \pm 0.0071$  (Figure 4).

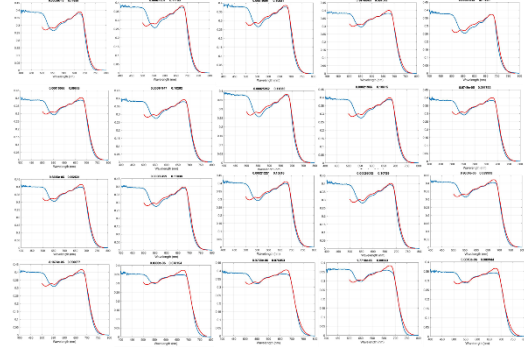


Figure 3. Example subset results of the absorbance fitting (red solid line) of the FLORIS LR bands based on transformed reflectance spectra (blue solid line)

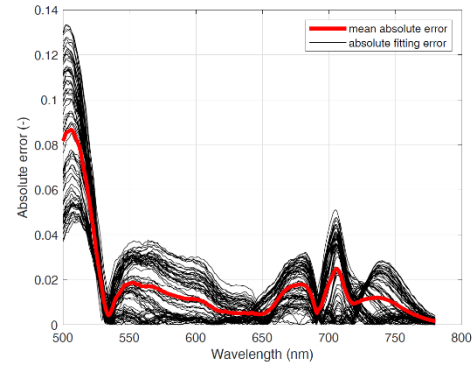


Figure 4. Absolute error of the spectral fitting at leaf level for the entire FLORIS LR spectral range

The absolute error for the fitted band range shows higher errors in the PRI range (500-550 nm) and still some error of 0.02 around the red-edge. These higher errors can possibly be devoted to (1) missing absorption features in the fitting algorithm, such as carotenoid contributions or dry matter effects, (2) lacking description of the Chl a and Chl b absorption features, and (3) incomplete description of the Chl a absorption behaviour, especially in the region beyond 700 nm.

### 3.2 FQE Validation of FLEX E2E scene

Retrieved (apparent) FQE values at the canopy level are small, in the order of 1-2%. These values are in the same range as the reference values of the forward simulation, which contain four groups of values: 0, 0.52%, 0.9% and 1.25% (Figure 5). Being so low values, the relative absolute error can reach high values, above 50% (Figure 6).

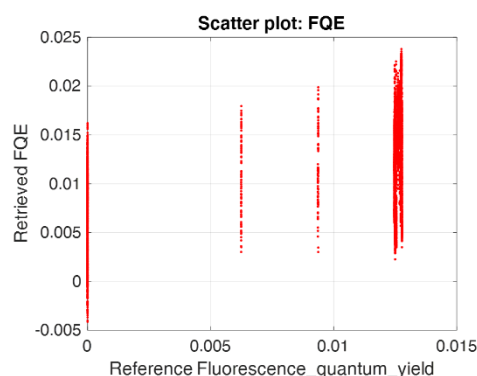


Figure 5. FQE retrieved values versus E2ES input values

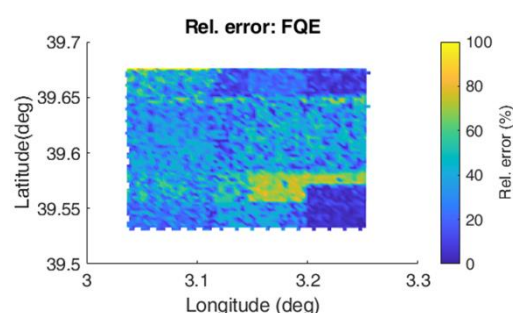


Figure 6. Relative error map of the FQE retrieval

#### 4 CONCLUSIONS

Disentangling the absorption of the overlapping pigments is shown based on the spectral fitting of the FLORIS HR 500-780 nm reflectance product using individual pigment absorption features and a non-negative least squares fitting approach. The spectrally-resolved fAPAR contribution for Chlorophyll a is retrieved. The apparent fluorescence quantum efficiency (FQE) is calculated as the ratio of the spectrally-integrated fluorescence emission and the PAR absorbed by Chl, both converted to photon flux units. With these advances in the quantitative interpretation of the vegetation fluorescence signal the actual light use through photosynthesis and vegetation growth with carbon assimilation will be better quantified. Hence, by the retrieval of FQE, combined with additional information on the dynamic regulation of the energy pathways in the light reactions, promising opportunities are presented to improve our understanding of the vegetation dynamics in the global carbon cycle.

#### 5 REFERENCES

- Coppo P., et al., 2017. Fluorescence imaging spectrometer (FLORIS) for ESA FLEX mission. *Remote Sensing* 9: 649, 2017.
- Drusch M., Moreno J., Del Bello U. et al., 2017. The Fluorescence EXplorer Mission Concept – ESA's Earth Explorer 8. – *IEEE Transactions on Geoscience and remote sensing* 55, 1273-1284.
- Moreno J.F., al., 2016. Very high spectral resolution imaging spectroscopy: The Fluorescence Explorer (FLEX) mission. *IEEE International Geoscience and Remote Sensing Symposium (IGARSS)*, 264-267.
- Tenjo et al., 2018, Design of a Generic 3-D Scene Generator for Passive Optical Missions and Its Implementation for the ESA's FLEX/Sentinel-3 Tandem Mission. *IEEE Transactions on Geoscience and remote sensing*, 56 (3), 1290-1307.
- Van Wittenberghe et al., 2021, Towards the quantitative and physically-based interpretation of solar-induced vegetation fluorescence retrieved from global imaging. *Photosynthetica*, 59 (SI), 438-457.

#### 6 ACKNOWLEDGEMENTS

This work is funded by the “Algorithm retrieval and product development study for the future Fluorescence Explorer/Sentinel-3 (FLEX-S3) tandem mission” project from the European Space Agency (ESA contract no. AO/1-8897/17/NL/MP). S. Van Wittenberghe is supported by the European Research Council (ERC) under the ERC-2021-STG PHOTOFLUX project (grant agreement 101041768).





## AUTHOR INDEX

---

### A

Acuña-Ruz, T., 39  
Amézquita, L., 39  
Amin, Eatidal, 176  
Arce, S., 39  
Asam, Sarah, 93  
Áviles, F., 39

### B

Bai, Xiangtian, 104  
Ben Achhab, N., 52, 58  
Boccia, V, 20  
Bono, L., 39  
Burchard-Levine, Vicente, 12

### C

Cadau, E., 20  
Calleja, Javier F., 89  
Camacho, Fernando, 26  
Campos-Taberner, Manuel, 16, 26, 30, 85  
Chen, Yunlong, 116  
Chiesi, M., 16  
Cintas, J., 69  
Corbea-Pérez, Alejandro, 89  
Cotlier, G., 48  
Cristóbal, Jordi, 34  
Cui, Cunxin, 139

### D

Debaecker, V., 20  
De Los Reyes, R., 20  
de Pablo, Miguel Ángel, 89  
Díaz-Delgado, Ricardo, 34  
Domingo, C., 74

### E

Engdahl, Marcus, 98  
Ezzaher, F-E., 52, 58

### F

Fei, Chen, 104  
Feng, Siqi, 155  
Fernández, Cristina, 63  
Fernández, Susana, 89  
Fernández-Alonso, José M., 63  
Franch, B., 20, 48, 69, 74

### G

Gao, Ya, 128  
Gao, Shanchuan, 145  
Garate, P., 39  
García, S., 48  
García-Haro, Francisco Javier, 16, 26, 30, 85  
García-Monteiro, S., 1, 7  
Gascon, F, 20  
Geng, Xiaowei, 111, 116, 122  
Gessner, Ursula, 93  
Gilabert, María Amparo, 16, 26, 30, 85  
Gómez-Giráldez, Pedro J., 34  
González-Cascón, Rosario, 12  
Guo, Li, 104, 111, 116, 122

## H

Holzwarth, Stefanie, 93  
Hu, Qiong, 151  
Huo, Hongyuan, 104, 111, 116, 122

## J

Jia, Li, 133  
Jiang, Yun, 161  
Jiang, Yazhen, 167  
Jimenez, J.C., 48  
Julien, Y., 1, 7, 44, 48

## K

Kuenzer, Claudia, 93

## L

Leng, Pei, 151  
Li, Zhao-Liang, 104, 116, 122, 167  
Li, Xiujuan, 172  
Li, Zhaoliang, 172  
Li, Ni, 172  
Liu, Meng, 167  
Llorens, Rafael, 48, 63  
Lopez-Sanchez, Juan M., 69, 98  
Louis, J., 20  
Lu, Jing, 133  
Lu, Miao, 151

## M

Ma, Yuman, 151  
Martín, M. Pilar, 12  
Martínez, Beatriz, 16, 26, 30, 85  
Martínez-Sánchez, Enrique, 26  
Maselli, F., 16  
Mattar, C., 39  
Moletto-Lobos, I., 20, 39, 69  
Mollà-Bononad, B., 69  
Moreno, Jose, 176  
Muñiz, Rubén, 89  
Muñoz, R., 39

## N

Naciri, H., 52, 58  
Navarro, Francisco, 89  
Neira, H., 39  
Nieto, Héctor, 34

## O

Olea-Encina, P., 39  
Otero, Jaime, 89

## P

Pacheco-Labrador, Javier, 12  
Pascual, Ana Belen, 176  
Peng, Zhong, 167  
Perez, Adrian, 176  
Pflug, B., 20

## **R**

Raissouni, N., 52, 58  
Reijmer, Carleen, 89  
Reiners, Philipp, 93  
Riaño, David, 12  
Rubio, C., 69, 74

## **S**

Sabater, Neus, 176  
Salinas-González, Daniel, 80  
San Bautista, A., 69, 74  
Sánchez-Ruíz, Sergio, 16, 26, 30, 85  
Sánchez-Torres, M. J., 69, 74  
Sánchez-Zapero, Jorge, 26  
Sanyer, W., 39  
Saunier, S., 20  
Skokovic, Drazen, 48, 80  
Sobrinho, J. A., 1, 7, 44, 48, 52, 58, 63, 80  
Song, Qian, 151  
Sòria, G., 48  
Sun, Jing, 151

## **T**

Tang, Bo-Hui, 139, 145, 155, 161  
Tang, Ronglin, 167  
Tao, Jing, 104, 111, 122  
Tenjo, Carolina, 176  
Troncoso, R., 39

## **V**

Van Wittenberghe, Shari, 176  
Vega, José A., 63  
Villarroya-Carpio, Arturo, 98

## **W**

Wang, Zhaofang, 104  
Wang, Liguó, 128  
Wang, Yitong, 128  
Wang, Hongyang, 151  
Wu, Wenbin, 151  
Wu, Hua, 172

## **Y**

Yang, Jingya, 151

## **Z**

Zhang, Wenzhi, 111, 116, 122  
Zhang, Shibo, 151  
Zhang, Huanyu, 161  
Zhong, Geji, 128  
Zhou, Ping, 111

